Northumbria Research Link

Citation: Hosseinibiroun, Mehdi Hosseini (2021) Numerical and experimental investigation of droplet actuation by surface acoustic waves. Doctoral thesis, Northumbria University.

Numerical and experimental investigation of droplet actuation by surface acoustic waves

Mehdi H. Biroun

PhD

2021

Numerical and experimental investigation of droplet actuation by surface acoustic waves

Mehdi H. Biroun

A thesis submitted in partial fulfilment of the
requirements of the
University of Northumbria at Newcastle for the
degree of Doctor of Philosophy

Department of Mechanical and Construction
Engineering

May 2021

Abstract

Surface acoustic waves (SAWs) technology for manipulating small volumes of liquids has received much attention in recent years. SAW-based manipulation can be used for different bio-sampling functions, such as mixing, heating, pumping, jetting, separation, and atomization of droplets with volumes in the scale of microliters. Most studies in recent years have mainly focused on investigating SAW potential in different real-world microfluidics applications. However, the underlying physics of the droplet deformation by SAW still remains controversial.

This thesis aims to investigate droplet deformations subjected to SAWs using both numerical and experimental methods. Different types of SAW devices with various resonant frequencies and different substrates are fabricated to carry out droplet actuation experiments. The experimental models are developed for three main reasons. First, to analyse the droplet deformation; second, to accurately define the contact angle boundary condition needed for simulations; and third, to validate the computational model.

A Coupled Level Set Volume of Fluid (CLSVOF) mathematical model is developed to investigate the large deformation of sessile droplet induced by SAWs. A dynamic contact angle boundary condition is implemented to model the droplet three-phase contact line (TPCL) movement.

The numerical and experimental results are quantitatively and qualitatively compared, and a remarkable agreement is achieved, which proves that the developed computational model can be used to simulate different droplet actuation scenarios. After validation of the computational model, it is used for analysing the physics of the droplet jetting and pumping. The effects of important factors such as droplet volume and SAW frequency and power on droplet pumping are investigated. Moreover, the model is used to analyse the energy budget of a droplet jetting. An investigation into the optimization of the interdigital transducers (IDT) location of the SAW devices for different microfluidic applications is also carried out using the computational model.

The experimental and computational models are then employed to investigate a novel application of SAW devices to control the droplet impact. SAWs devices are used to manipulate and control the droplet dynamics. The experimental results revealed that characteristic impact parameters such as impact regime, contact time, maximum spreading and re-bouncing angle could be modified and controlled by SAWs. By changing the SAW direction and power, droplets impact behaviour can be altered. The maximum reduction of contact time up to $\sim$50% can be achieved, along with alterations of droplet spreading, re-bouncing angle, and movement along the inclined surfaces.

On the other hand, numerical results revealed that the SAWs could be used to modify and control the internal velocity fields inside the droplet. By breaking the symmetry of the internal recirculation patterns inside the droplet during the impact on flat surfaces, the kinetic energy recovered from interfacial energy during the retraction process is increased, and the droplet can be entirely separated from the surface with a much shorter contact time. Also, numerical results revealed that applying SAWs modifies the energy budget inside the liquid medium on both flat and inclined surface, leading to different impact behaviours. This innovative paradigm opens up new opportunities to actively program and controls the droplet impact on smooth or planar and curved surfaces, as well as rough or textured surfaces.

List of publications

List of journal papers

- **Mehdi H. Biroun**, Mohammad Rahmati, Ran Tao, Hamdi Torun, Mehdi Jangi, Yongqing Fu (2020) Dynamic behaviour of droplet impact on inclined surfaces with acoustic waves, Langmuir, 36, 34, 10175–10186. doi.org/10.1021/acs.langmuir.0c01628
- **Mehdi H. Biroun**, Jie Li, Ran Tao, Mohammad Rahmati, Glen McHale, Linxi Dong, Mehdi Jangi, Hamdi Torun, YongQing Fu (2020) Acoustic waves for active reduction of droplet impact contact time, Phys. Rev. Applied 14, 024029. doi.org/10.1103/PhysRevApplied.14.024029
- Jie Li, **Mehdi H. Biroun**, et al. (2020) Wide range of droplet jetting angles by thin-film based surface acoustic waves. J. Phys. D: Appl. Phys., 53, 355402. doi.org/10.1088/1361-6463/ab8f50.
- **Mehdi H. Biroun,** Rahmati, M. T., Jangi, M., Tao, R., Chen, B. X., & Fu, Y. Q. (2019). Computational and experimental analysis of droplet transportation/jetting behaviours driven by thin-film surface acoustic waves. Sensors and Actuators A: Physical, 299, 111624. doi.org/10.1016/J.SNA.2019.111624.
- **Mehdi H. Biroun**, Rahmati, M. T., Jangi, M., Chen, B. X., & Fu, Y. Q. (2020). Numerical and experimental investigations of electrode configurations for efficient droplet streaming and jetting induced by surface acoustic waves, Int. J. Mul. Flow, 136, 103545. doi.org/10.1016/j.ijmultiphaseflow.2020.103545
- **Mehdi H. Biroun**, Luke Haworth, Prashant Agrawal, Bethany Orme, Glen McHale, Hamdi Torun, Mohammad Rahmati, YongQing Fu (2021). Droplet Impact onto Superhydrophobic and Slippery Liquid-Infused Porous Surfaces under Surface Acoustic Waves, Submitted to ACS Applied Materials & Interfaces.

List of conferences and SIG meeting presentations

- **Mehdi H. Biroun**, M.T. Rahmati, M. Jangi, Y. Q. Fu “Droplet Impact Control by Surface Acoustic Waves” Acoustofluidics, 2020, Glasgow, UK, (Online Conference).
- **Mehdi H. Biroun**, M.T. Rahmati, M. Jangi, Y. Q. Fu "A Coupled Level Set and Volume of Fluid Method for Droplet Actuation by Surface Acoustic Waves." Acoustofluidics, 2019, Enschede, Netherlands.
- **Mehdi H. Biroun,** "computational and experimental analysis of a sessile droplet pumping by surface acoustic waves." 2019, Fifth SIG Meeting of acoustofluidics in UK fluid Network (UKFN), Heriot-Watt University, Edinburg, UK.
- **Mehdi H. Biroun** "Experimental study of the dynamic behaviour of droplet impact on hydrophobic surfaces of SAW device" Acoustofluidics Forum and Olympics, 2019, Bristol University, Bristol, UK.
- **Mehdi H. Biroun** "Numerical simulation of droplet jetting by SAW" Acoustofluidics Forum and Olympics 2018, Northumbria University, Newcastle upon Tyne, UK.

Contents

List of figures

List of tables

Nomenclature

Latin *Symbols*

A	Wave amplitude (m)
a	Dynamic contact angle coefficient
b	Dynamic contact angle coefficient
c	Stiffness Tensor (Nm^{-1})
Ca	Capillary number
D_0	Initial diameter (m)
D_n	Needle inner diameter (m)
E_{dis}	Viscous dissipation (kgm^{2}s^{-2})
E_{SAW}	Applied SAW energy (kgm^{2}s^{-2})
E_t	Total energy (kgm^{2}s^{-2})
E_0	Initial energy (kgm^{2}s^{-2})
e	Piezoelectric Tensor (CN^{-1})
$\boldsymbol{F}$	SAW force (N)
F_{adh}	Adhesion force (N)
$\boldsymbol{F}_{\sigma}$	Surface tension force (N)
f	Wave frequency (s^{-1})
$\boldsymbol{g}$	Gravitational acceleration (ms^{-2})
H	Smoothed Heaviside function
h	Droplet release height (m)
K	Kinetic energy (kgm^{2}s^{-2})
K_L	Wavenumber of the LSAW (s^{-1})
K_i	Wave number (s^{-1})
$L_{cl\ ,max}$	Maximum spreading width (m)
$\boldsymbol{n}$	Normal vector
Oh	Ohnesorge number
PE	Gravitational energy (m^2)
P	Power (W)
p	Pressure (pa)
Re	Reynolds number
R_0	Initial droplet radius (m)

$\boldsymbol{S}$	Strain rate tensor (s−1)
SE	Surface energy (kgm^{2}s^{-2})
SN	Swirl number
s	Area (m^2)
u	Velocity (ms^{-1})
T	Period of the harmonic
t	Time (s)
$\acute{t}$	Artificial time (s)
U_0	Impact velocity (ms^{-1})
$\boldsymbol{u}$	Velocity vector (ms^{-1})
V	Volume (m^3)
V_{Dr}	Droplet volume (m^3)
v	Sound velocity (ms^{-1})
W_{adh}	adhesion force work (N.m)
We	Weber number
x, y, z	Coordination directions
x_i	Displacement (m)
Z	Droplet tip height (m)

Subscripts Symbols

c	Interface
$cell$	cell
$final$	Final
g	Gas
l	Liquid
lg	Liquid-Gas
s	Solid
sl	Solid-Liquid
sg	Solid-Gas
$TPCL$	Three-phase contact line
w	The direction of the interface parallel to the wall
$wall$	Wall
0	Hydrostatic

1	Acoustic
2	Hydrodynamic

Greek Symbols

α	VOF function
$\acute{\alpha}$	Attenuation coefficient
α^{-1}	Solid attenuation length (m)
β	Normalized contact width
β_{Max}	Maximum spreading radius ratio
β^{-1}	Liquid attenuation length (m)
Γ	Coupling constant
γ	Surface tension coefficient (Kg.s^{-2})
Δx	Mesh size (m)
δ	Contact width (m)
ε	Dielectric permittivity (Fm^{-1-})
ϵ	Interface thickness (m)
ζ	Attenuation length (m)
θ_a	Advancing contact angle
θ_R	Rayleigh angle
θ_r	Receding contact angle
θ_s	Static contact angles
θ_0	Initial contact angle
Λ	Interface function
κ	Curvature of the interface
λ	Wavelength (m)
μ	Shear viscosity (m^{2}s)
μ'	Bulk viscosity (m^{2}s)
ϖ	Slip length (m)
ρ	Density (kg.m^{-3})
τ	Contact time (s)
τ_s	Spreading time (s)
$\acute{\varphi}$	Electrical potential (V)
ϕ	Level-Set signed distance function

ψ	Viscous dissipation function
ω	Angular frequency (Hz)

Abbreviations

ACA	Advancing Contact Angle
CAH	Contact Angle Hysteresis
CFD	Computational Fluid Dynamics
CICSAM	Compressive Interface Capturing Scheme for Arbitrary Meshes
CLSVOF	Coupled Level Set Volume of Fluid
CT	Contact Time
DC	Direct Current
DFI	Droplet Free Impact
DI	Deionised
DSAW	Downward Surface Acoustic Waves
ECA	Equilibrium Contact Angle
EMFPA-SIR	Edge-matched Flux Polygons and Spline-based Interface Reconstruction
ENO	Essentially Non-Oscillatory
FCT	Flux Correct Transport
FIDT	Focused Interdigital Transducer
GFM	Ghost Fluid Method
ICM	Interface Capturing Methods
IDT	Interdigital Transducer
ITM	Interface Tracking Methods
LN	Lithium Niobite
LOC	Lab on a Chip
LS	Level Set
LSAW	Leaky Surface Acoustic Wave
OTS	Octadecyl Trichlorosilane
PLIC	Piecewise Linear Interface Calculation
PVD	Physical Vapour Deposition
RCA	Receding Contact Angle

RF	Radio Frequency
SAW	Surface Acoustic Waves
SEM	Scanning Electron Microscope
SH-SAW	Shear Horizontal Surface Acoustic Waves
SPUDT	Single Phase Unidirectional Transducers
SSAW	Standing Surface Acoustic Waves
TH	Transverse Horizontal
TPCL	Three-phase contact Line
TSAW	Travelling Surface Acoustic Waves
TV	Transverse Vertical
TVD-RK	Total Variation Diminishing Runge-Kutta
USAW	Upward Surface Acoustic Waves
USNT	Ultra-Smooth Nanocrystalline Diamond
VOF	Volume of Fluid
WENO	Weighted Essentially Non-Oscillatory
ZnO/Al	Zinc Oxide-Aluminium
ZnO/Si	Zinc Oxide-Silicon
2D	Two Dimensional
3D	Three Dimensional

Acknowledgements

Firstly, I would like to thank my first supervisor, Prof. Mohammad Rahmati, for his tremendous guidance and encouragement. I am also grateful for the excellent example he provided as a successful professor. I would also like to thank my second supervisor, Prof. Richard Fu, for his assistance and valuable experience. His encouragement and unwavering confidence in my abilities allowed me the freedom to explore my experimental ideas throughout the project. He was a consistent source of inspiration. My special thanks go to my third supervisor, Dr Mehdi Jangi, who gave me the opportunity to start my PhD at Northumbria University. His extensive numerical knowledge has been invaluable throughout this project. On a professional level, I am incredibly appreciative of the opportunities and guidance you all offered me during the last three years.

I owe the technical staff at Northumbria University, Paul Curran and Rebecca Payne, and Philip Donnelly, my thanks for their assistance in my experimental works. I also thank Jimmy Gibson, who provided me with support for the computational resources. My special thanks go to Prof. Glen McHale and Dr Hamdi Torun for their scientific advice during my research. I am also grateful to my friends in NBD209 to create a friendly environment in our office and mental and technical support during our PhD's highs and lows. I would also like to thank Northumbria University for funding this PhD.

To my parents: Fariba and Ghader to provide me with the chance to pursue my ambitions throughout my entire life. I could not have asked for more.

To my spouse, Solmaz, whose support made the last three years much easier than expected. Your love, laughter and empathy helped me keep sane during my PhD life. I know it is a cliché, but this thesis is dedicated to you.

Last but not least, to the people of Iran. I had the privilege of free education from my first day of elementary school until the end of my M.Sc with your tax money. I can never express my gratitude and appreciation adequately.

Declaration

I declare that the work contained in this thesis has not been submitted for any other award and that it is all my own work. I also confirm that this work fully acknowledges options, ideas and contributions from the work of others.

Any ethical clearance for the research presented in this thesis has been approved. Approval has been sought and granted by the Faculty Ethics Committee on 23/04/2018.

I declare that the Word Count of this Thesis is 37452 words.

Name: Mehdi H. Biroun

Signature: Mehdi H. Biroun

Date: 03/03/2021

Chapter 1. Introduction

1.1 Background and motivation

Microfluidics has been extensively researched during the development of diverse technologies such as printing, lab on a chip (LOC), DNA chips, micro propulsion and microthermal devices in the past thirty years[1–3]. Technical difficulties arise when performing microfluidic applications on microscale volumes of liquids. For example, pumping microscale liquids (both in closed channels or free surfaces) is challenging due to the significant viscous and capillary forces which resist liquid motion[4]. As a result of the small scales, the Reynolds number in most microfluidic systems is low, and the flow is laminar[5]. In such systems, diffusive mixing is challenging and inefficient since it needs large length scales and long durations, which are impossible in many biochemical and biological microfluidic applications[6]. A reliable method to actuate liquids in the microscale is essential for successful applications of microfluidics.

Surface acoustic waves (SAWs) has been introduced as a new technique to actuate small volumes of liquids (either in bulk or droplet shape) without any mechanical or moving parts[7]. It is well known that when a liquid medium is located on the SAW propagation path, the wave energy transfers into the liquid medium[8]. Depending on the SAW amplitude, frequency, and direction, as well as the surface properties of the SAW device, liquid mixing, jetting, pumping, patterning, atomization, particle sorting, separation, and concentration is attainable[9]. Moreover, SAW devices can be used for the actuation and manipulation of liquids in both closed microchannels and free surface droplets.

SAW application in acoustofluidics is increasing due to unique features associated with this technology, such as their simplicity (i.e., no moving parts), low production costs, multi-function for sensing and actuation, fast fluidic actuation, tuneable frequency response, small size, and capability for easy interaction with other microfluidic components[10–12].

After the turn of the century, the actuation of liquids by SAWs was experimentally and numerically investigated[7]. Due to the great potential of SAW in microfluidics, a large and growing part of the research has been focused on the potential applications of SAWs in microfluidics[8]. Besides, efforts have been made to understand the physics of the interaction between SAWs and liquids[13]. Many analytical and numerical methods have been developed to explain SAW-fluid interaction[13]. SAW technology has been used more commonly to handle liquids in microchannels. This is mainly due to the less complicated fabrication process and elimination of liquid evaporation. Closed channels reduce the contamination and provide rapid flow actuation, enabling fast track analysis of diverse samples. SAW devices have found vast applications in biochemical analysis, disease diagnosis, DNA sequencing, bioprinting, and drug delivery systems[14].

There are only a few computational investigations of droplet actuation by SAWs compared to the liquid actuation in microchannels. This is mainly because of the complexity of developing computational models capable of modelling complex wave-liquid interaction and the multiphase flow due to the rapid and dynamic changes of the solid-liquid and liquid-gas interfaces[15]. The most computational analysis of SAW-based droplet actuation assumes that the liquid interface remains undeformed. However, experimental results show that the droplet interface is considerably deformed in a wide range of applied SAW power[15]. Thus, the physics of droplet actuation by SAWs, considering the surface deformation, remains elusive.

1.2 Project aims and objectives

Understanding the physics of droplet actuation by SAWs can improve the SAW device efficiency for different applications and lead to entirely new potential applications of SAWs in the industry. In this thesis, the deformations of droplets subjected to SAWs will be numerically and experimentally investigated. This research focuses on developing and validating a high fidelity numerical model capable of simulating large deformations of droplet interface subjected to SAWs. The experimental results will be used to validate the numerical results. Then, the numerical model will be used to explore the physics of the droplet actuation by SAWs and the fluid flow details such as velocity and pressure, which cannot easily be measured using experiments.

Several objectives have been outlined in this research to achieve the above aims:

- A mathematical model will be developed to simulate the droplet actuation by SAWs considering the solid-liquid and liquid-gas interfaces deformations. A three-dimensional (3D) interface capturing mathematical model, based on coupled level set volume of fluid

(CLSVOF) method, will be developed to model wave-liquid interaction considering the liquid-gas interface deformation induced by SAWs.

- To accurately simulate the solid-liquid interface deformation, a dynamic contact angle boundary condition will be developed.
- SAW devices with various IDT designs on different substrates will be fabricated and characterized. Experimental setups will be designed and assembled to investigate different droplet actuation scenarios.
- The experimental results will be used to validate the numerical model and simulation cases. Additionally, these results will be used as an input for the boundary conditions to increase the simulation accuracy. Later the simulation results will be used to optimize the SAW device configuration.
- Droplet impact on the smooth solid surface of the SAW device will be manipulated and controlled by SAWs. The effects of various parameters, such as SAW frequency and power, surface treatment, and SAW direction on the droplet impact parameters will be thoroughly investigated.

1.3 Scope of thesis

This thesis will be divided into seven chapters:

Chapter 1 introduces the research motivation, project aims, and objectives and the scope of the thesis.

Chapter 2 presents a literature review of the research, which will be mainly focused on the importance of the SAW technology, basic principles, applications in acoustofluidics, different approaches and current challenges in mathematical modelling of SAW-liquid interaction. Various methods of numerical modelling for multiphase flows will be reviewed in chapter 2. Finally, a review of the droplet impact phenomena will be presented at the end of this chapter.

Detailed mathematical methods, including the governing equations, interface capturing method, and solid-liquid interaction modelling, will be explained in chapter 3.

Experimental methodologies such as thin film deposition, SAW device fabrication, droplet actuation experiments, and droplet impact investigation will be explained in chapter 4.

In chapter 5, the developed model and boundary conditions will be firstly verified and validated. Then, droplet pumping and jetting behaviour will be analysed, and the physics behind these phenomena will be explained. The key parameters affecting the droplet pumping behaviour will be examined. Furthermore, using the energy budget method, the SAW device design will be optimized for different microfluidic applications.

Using the models developing during the course of this study, two potential applications for SAW devices are demonstrated in Chapter 6. First, a new methodology to control the droplet impact on solid surfaces using SAWs will be introduced to reduce the droplet contact time during its impact onto a solid surface. The physics of the phenomena will be explained by computational analysis. Second, the droplet impact on inclined surfaces will be investigated numerically and experimentally, revealing the full potential of SAW devices for manipulating and controlling the droplet impact on inclined surfaces.

Finally, the major conclusions of this thesis and recommendations for future works are presented in chapter 7.

Chapter 2. Literature review

In this chapter, first, an overview of the fundamentals of surface acoustic wave generation and propagation and current research focus in this field is provided. Then, a review of previous experimental and numerical works on droplet actuation by SAWs is presented. Finally, the gap in knowledge and the main challenges in the numerical simulation of droplet actuation by SAWs are presented.

2.1 Surface acoustic waves

One year after the injurious earthquake in Colchester in 1884, Rayleigh[16] mathematically analysed the earthquake waves. He explained that the destructive power of the earthquakes is transported via surface waves rather than bulk waves. The SAWs energy is restricted in the area very close to the free surface of the elastic substrate. The whole SAW microfluidics is built on the same principle: SAWs propagate on the solid surface with very low attenuation, which allows them to strike a target more effectively. Rayleigh discovered that transverse-vertical (TV) longitudinal waves (Rayleigh waves) could only be transmitted on an elastic surface. In 1911, Love[17] disclosed a transverse-horizontal (TH) and longitudinal surface wave which could propagate on a piezoelectric surface. Principally, SAWs can be generated by applying an alternating electric field on a piezoelectric substrate by a pair of interdigital transducers (IDT). A detailed explanation of SAW excitation is presented in section 2.2. SAW-based technology has been used in many scientific and industrial applications since the 1940s[18]. These applications vary from filters and oscillators[19] to sensors[20] and microfluidics systems[20].

Considerable advances in the 1990s in microfluidic systems production enabled scientists to manipulate a small volume of liquid in a microlitre scale to nanolitre. Consequently, LOC technology emerged, enabling the application of microfluidic systems in life sciences[2]. A LOC device integrates numerous laboratory analyses onto a single chip. The fundamental roles of LOC systems are summarised as below[21,22]:

- Transporting the liquid droplet (such as blood sample or DNA, Protein or cell containing Bio-samples) into the examination area in which probe particles are deposited.
- Mixing and binding the reactants and take out the unbound species.

- Detecting any changes in chemical, physical, mechanical, magnetic, or electrical signals on the LOC.
- Clean up the LOC surface for the next tests.

In short, SAW devices can be used for mixing, separation, translation, jetting, heating, and atomisation of microfluid volumes of fluids for applications in biochemical analysis, disease diagnosis, DNA sequencing and drug delivery.

2.2 Principles of liquid actuation by SAWs

SAWs can manipulate a liquid droplet located on a piezoelectric substrate within its propagation path by fluid-SAW interaction[23]m. The difference between sound velocities in the fluid domain and piezoelectric substrate leads to SAW radiation into the fluid medium. A schematic view of the SAW and LSAW is illustrated in Figure 2-1. SAW propagates from left to right along the solid surface within the depth of a single wavelength[24]. The transmitted wave propagates inside the liquid medium along the Rayleigh angle, θ_R:

$$\theta_R = arcsin\,({}^{v_l}/_{v_s}) \qquad (2.1)$$

where v_l and v_s are the sound velocities in liquid and piezoelectric mediums, respectively. SAW decays by a factor of e along the surface of the piezoelectric device due to leakage of the SAW into the fluid medium (LSAW). This length is the attenuation length, α^{-1}[25]:

$$\alpha^{-1} = \frac{\rho_s v_s^2}{f \rho_l v_l} \qquad (2.2)$$

where f is the SAW frequency and ρ_l and ρ_s are the densities of the fluid and the solid, respectively. On the other hand, SAW propagates in the liquid medium along the Rayleigh angle with a distinctly higher attenuation length, β^{-1}[26]:

$$\beta^{-1} = \frac{\rho_l v_l^3}{4\pi^2 f^2 (\frac{4}{3}\mu + \mu')} \qquad (2.3)$$

where μ and μ' are the shear and bulk viscosities of the fluid, respectively.

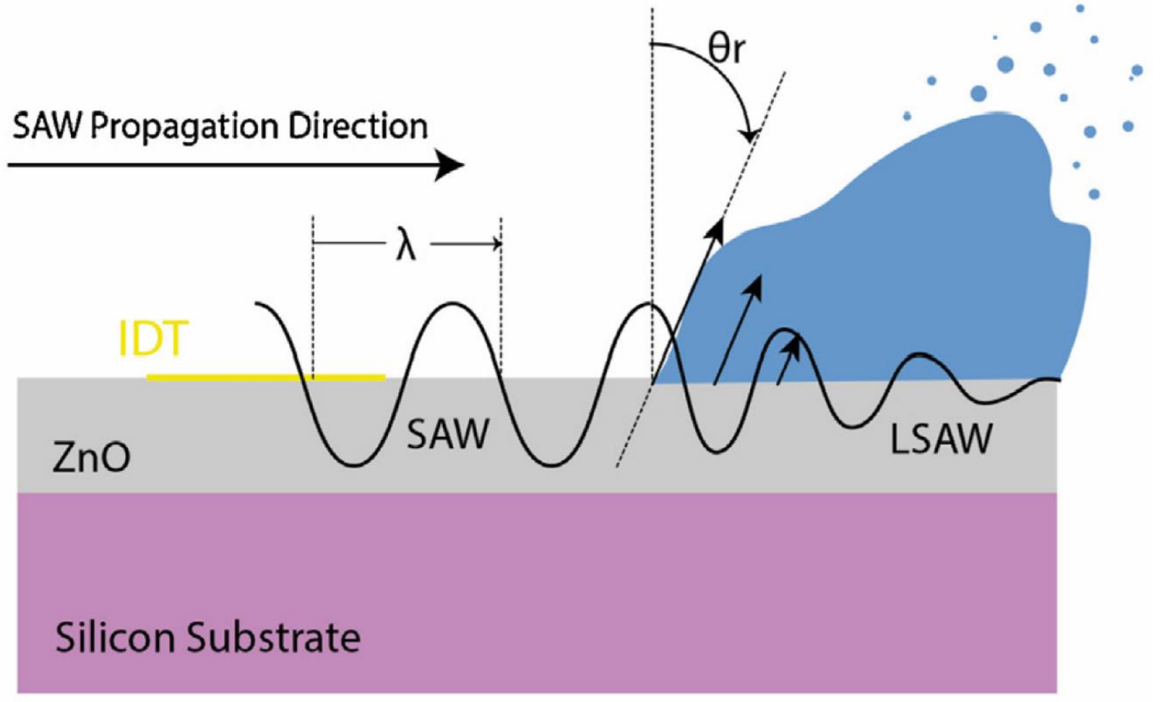

Figure 2-1: Schematic view of the SAW propagation mechanism along a piezoelectric substrate and actuation and deformation of the droplet free surface[27].

When acoustic energy is transferred to the liquid medium by the sound wave, a net pressure field is formed along the Rayleigh angle, which generates an internal streaming flow within the liquid. Sessile droplets have been successfully actuated by electrowetting, SAW, and even light using special photo-responsive surfaces[28]. However, only SAW is capable of all types of actuations on the droplets. At low applied RF powers, the SAW energy generates an internal recirculation in the liquid, and the droplet deforms into the asymmetrical conical shape and leans at the Rayleigh angle. By further increasing the power, capillary vibrations will appear in the droplet liquid-gas interface. As the power is increased, the applied SAW power can overcome the pinning force between the liquid and solid and droplet translation is achieved. Droplet jetting and atomization are also observed in the experiments at high applied RF (radio frequency) powers discussed in the next sections.

2.3 Droplet-based applications of SAWs

The radiation of SAWs inside the liquid medium when it reaches an area on which liquid is located was discovered by scientists in the 1960s[29]. Nevertheless, it seems that the idea of using

SAWs to actuate liquids by nonlinear acoustics only emerged in Shiokawa's researches during the late 1980s[30,31]. The Japanese research group reported jetting of droplets and liquid films by a 50MHz SAW device. In 1991, Moroney et al.[32] excited a thin membrane to generate Lamb waves and actuate liquids. His detailed and comprehensive results revealed the potential of SAW technology for microfluidics applications. The fundamentals of microfluidics at the time were not fully established, and the works of Moroney and Shiokawa failed to answer an engineering necessity. By the start of the century, the fast development of microfluidic chips and molecular biology led to the first realistic application of SAW technology in DNA hybridization and subsequently amplification by PCR (Polymerase chain reaction) by Wixforth et al.[6,33]. Since then, the field has grown fast as a branch of acoustofluidics. SAWs enable a whole new set of microfluidics functions on both droplets and confined liquids. Investigations of actuation in microchannels are out of the scope of this study scope and thus are not covered here. In the following, a review of experimental works to actuate droplets with SAWs is reported.

2.3.1 Streaming in droplets

Generation of high-speed internal streaming inside droplets in the scale on microlitre is challenging due to the low Reynolds number which leads to the domination of laminar flows. However, mixing, concentration and separation of liquid mixtures are essential in many microfluidic applications[28]. The diffusive internal streaming speed is too low for most LOC applications. Thus, researchers have used SAW-based internal streaming in droplets to increase the streaming speed significantly by generating chaotic advection. Initially, SAWs were used for internal streaming of droplets by Wixforth[34] almost twenty years ago. The idea of using acoustic waves for the actuation of droplets miniaturised the digital droplet LOC devices. This idea could effectively generate mixing in the droplet but was not suitable for concentrating and separating applications. Later, Li et al.[35] proposed several designs for the generation of swirl-like flow within the liquid (see Figure 2-2). They showed that an azimuthal flow with a vertical part could be induced by exposing asymmetric SAW on the droplet, pushing the vortex flow around the inclined axis.

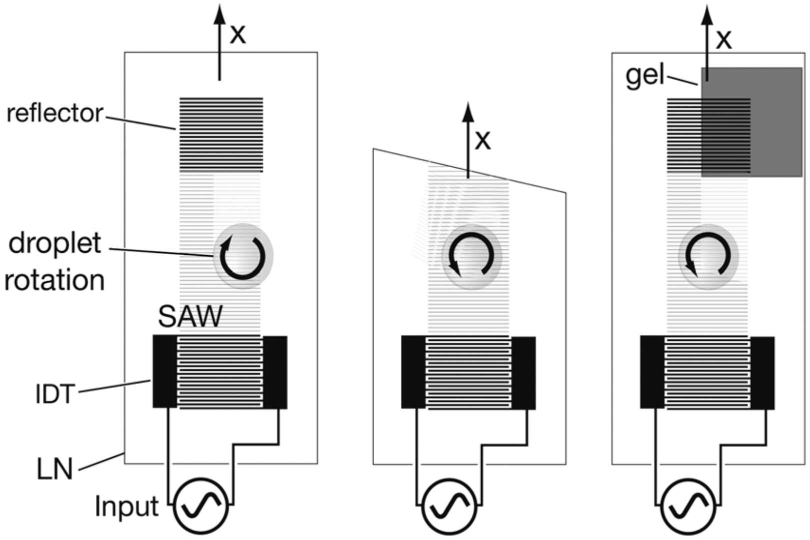

Figure 2-2: Three methods used to generate azimuthal flow by asymmetric SAW propagation. (Left) asymmetry is created by offsetting the drop from the centreline, (middle) symmetry is broken by the angled edge of the LN substratum, and (right) asymmetry is created by covering a part of the IDT with ultrasonic gel to absorb SAW in one area while reflecting it in another[35].

As shown in Figure 2-3, Shilton et al.[36] explored the liquid recirculation in a droplet by the generation of travelling surface acoustic waves (TSAWs, i.e., with waves propagating from one side of the droplet) by different types of single-phase unidirectional transducers (SPUDT). A more refined TSAW-based droplet mixing was demonstrated by Frommelt et al.[37] using a pair of tapered IDTs. By generating a narrow SAW beam with a variable launching point, they illustrated that the flow patterns could be modified and controlled by changing the input signals. They also controlled the mixing speed by modification of the SAW amplitude and frequency.

In general, for each SAW device, droplet manipulation operates under a critical input power necessary for droplet motion on the solid surface. This threshold power depends on the surface treatment (e.g., it is higher for superhydrophilic surfaces and lower for superhydrophobic surfaces[38]) and the three-phase contact line (TPCL) dynamics. For instance, Shilton et al.[36] reported that this critical power is 700 mW for their device. Recently, Lim et al.[39] used a dome-shaped chamber to optimize the mixing performance. They fabricated the chamber to avoid droplet interface instabilities at high applied powers, which enhanced the mixing performance.

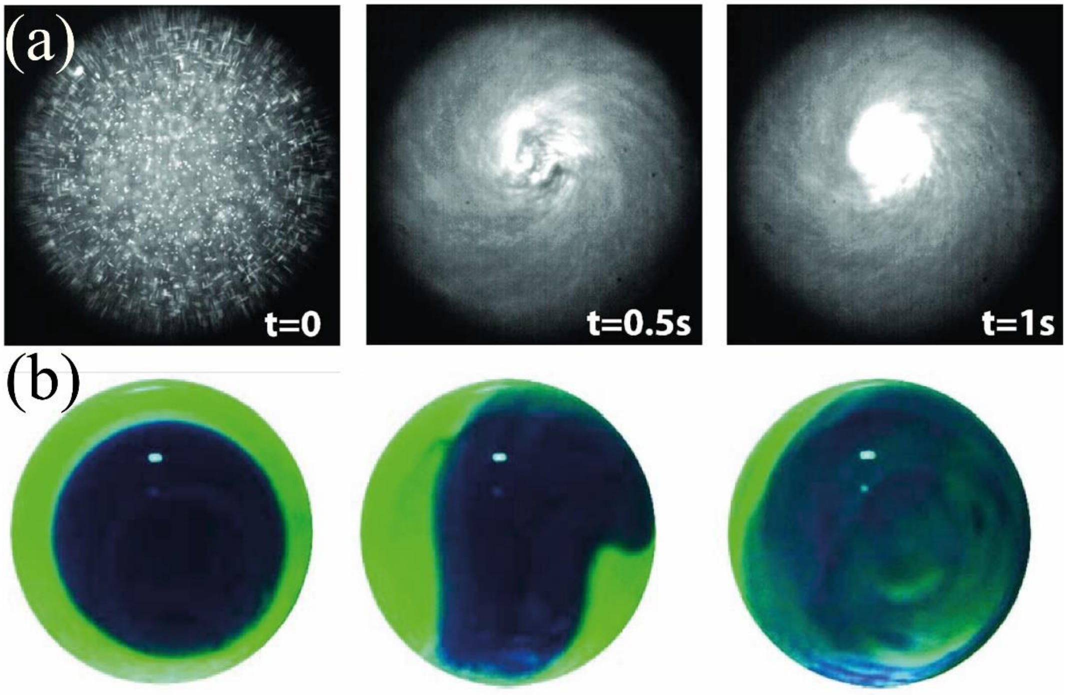

Figure 2-3: (a) SAWs induced by focused SPUDT is used for the concentration of particles in the 0.5 µl droplet (b) fast mixing water (blue) and glycerine (green) using concentric circular SPUDT designs[40].

Another key advantage of sessile drop microfluidics by SAWs is the possibility of generating internal flows in tiny sample volumes. For instance, Shilton et al.[41] reported regulated mixing of fluids within nanolitre order droplets, while Miansari et al.[13] were able to manipulate 10 fℓ droplets in a nanoslit using SAW. Additionally, liquid separation in immiscible mixtures is another application of SAW devices. For instance, Liang et al.[42] used SAW propagating on a glass substrate to separate water from a microlitre scale water/oil mixture. SAWs are vastly used for rapid concentration and separation of the particles inside the droplets[43–45]. This is extremely useful for many LOC functions, such as the separation of red blood cells[46].

2.3.2 Translation

Transportation (sometimes called pumping) of a sessile droplet in the microliter scale without evaporation is vital and challenging for LOC applications[47]. Microfluidic pumping is achieved typically by pumping in continuously filled channels; however, discrete liquid pumping (i.e., droplet translation) is achievable by applying SAW to the surface on which a droplet is located.

If the applied SAW power is higher than a limit, the internal streaming leads to a deformation in the droplet interface, which can eventually translate the droplet in the SAW propagation direction. The applied SAW power must overcome the forces aroused by contact line pinning and contact angle hysteresis.

Droplet pumping by SAW first was reported by Wixforth et al.[33] using a SAW driven microprocessor on a patterned surface (see Figure 2-4). Renaudin et al.[48] showed that droplet movement by SAW on a LiNbO3 piezoelectric substrate could be controlled by RF power and surface treatment. They showed that droplet pumping is achievable on hydrophobic surfaces by lower RF power. An experimental study of liquid droplet pumping by SAW generated on a 128º YX-LiNbO3 piezoelectric substrate was conducted by Beyssen et al.[49]. Results demonstrated that by increasing the droplet viscosity, pumping velocity significantly decreases. The pumping velocity dropped from 40 mm/s to 2 mm/s by changing the Water droplet by a water/glycerol droplet. Generally, most SAW microfluidic devices have been made up on bulk $LiNbO_3$ or quartz substrates; Du et al.[50] reported the fabrication of a SAW device using a thin-film piezoelectric material for droplet pumping with volumes up to 10 µl. The surface of the device surface was treated with a self-assembled monolayer of octadecyl trichlorosilane (OTS), which made the device surface hydrophobic to promote the pumping.

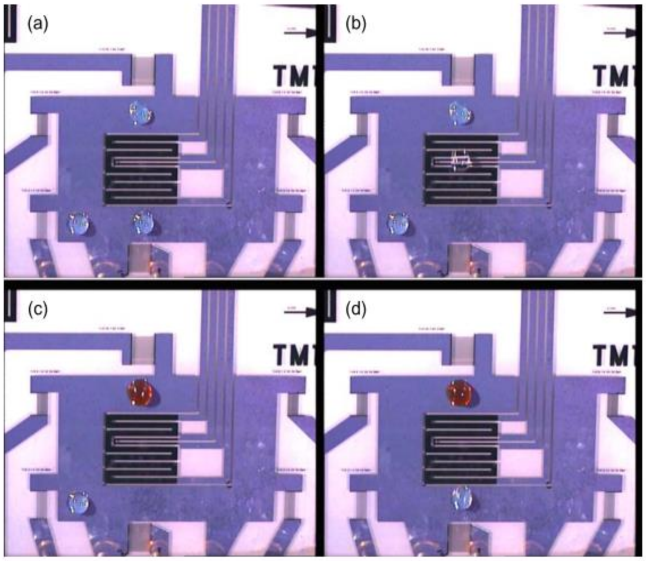

Figure 2-4: microfluidic SAW-based microprocessor designed by Wixforth et al. to mix, move and merge nanodroplets[33]. Snapshots (a) to (d) show the motion and mixing of the droplets.

The authors also experimentally studied the droplet size effect and applied RF voltage on droplet pumping velocity. Their results showed that droplet with lower volumes at higher applied RF voltages moved with higher velocity on hydrophobically treated surfaces.

Brunet et al.[51] experimentally explored the effect of the SAW amplitude, droplet volume, and fluid viscosity on the droplet pumping with the LiNbO3-based SAW device. Their results showed that maximum droplet velocity occurs when the solid-liquid interface diameter is equal to the attenuation length. At smaller diameters, the whole SAW energy was not absorbed by the droplet. However, droplets with greater solid-liquid interface diameter moved slower because the same amount of applied SAW energy was used to move a higher mass of liquid.

The actuation of stationary droplets by low power SAWs was investigated by Baudoin et al.[52]. Their results demonstrated that the necessary power to deform and move a sessile droplet could be reduced through vibrating the droplet. They showed that inertia-capillary oscillations effectively decrease the SAW power for internal streaming and pumping. The minimum required SAW power to move the droplet was reduced between 50 and 75 per cent using this method. This method is vital for cases where the droplet temperature needs to be kept constant during the mixing or pumping process.

To use the SAW technology as a LOC platform, these devices must handle droplet merging, splitting, and controllable translation. In 2012, Travagliati et al.[53] reported a method to detect and manipulate the droplet. They designed a SAW device with a cavity with a specific resonant frequency. The resonant frequency was shifted when the droplet reached the cavity; consequently, the SAW was reflected, and the droplet was stopped.

Ai and Marrone[54] used the focused SAW for droplet translation. Their results showed that by placing a droplet on the focal distance of the FIDTs, the droplet could be moved approximately five times faster than a straight IDT. Laterally offset modulated SAWs were used by Collignon et al.[55] for droplet merging and splitting applications. They showed that droplets with a volume of 0.5 to 6 μl could be symmetrically divided into two equal-size droplets. They also studied the effect of the liquid physical properties on merging and dividing the droplet. The snapshots of droplet dividing by SAW is shown in Figure 2-5.

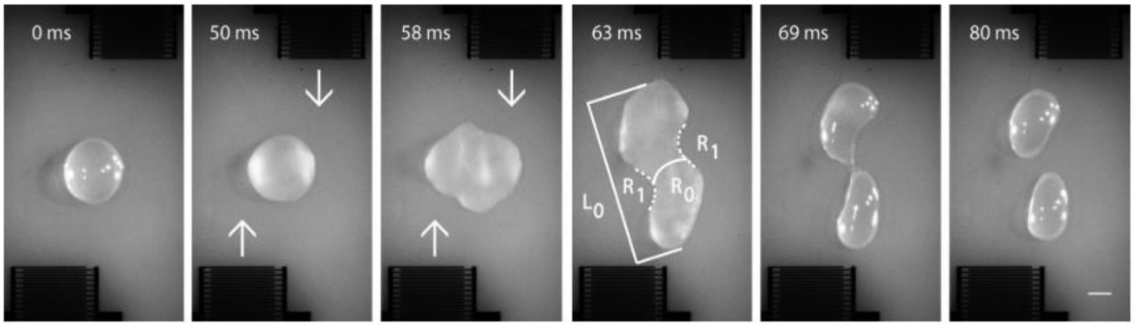

Figure 2-5: Splitting of a 3 µl droplet using a 0.5 mm thick 128° Y–X single-crystal lithium niobate substrate[55].

Bussonniere et al.[56] investigated the oscillation and translation of the droplets and three-phase contact line dynamics through high-speed camera imaging. They observed that the front and rear TPCL displacement occurs during droplet oscillation, as shown in Figure 2-6. They suggested that the maximum droplet speed is given by the product of droplet displacement per oscillation and the oscillation frequency.

A few studies have reported droplet transportation and mixing using SAW. For instance, Zhang et al.[57] reported the transfer of droplets with different colours from a glass substrate onto the piezoelectric surfaces and mixing the droplets in less than 7 s. Fu et al.[7] also reported translating a smaller droplet by SAW and mixing it into a bigger droplet. The snapshots shown in Figure 2-7 show that the smaller droplet is transported by sliding and rolling mechanism toward the bigger droplet and deforms before merging. The mixing efficiency depends on droplets contact angles, applied RF power, frequency, and droplet volume.

Recently, Wang et al.[58] Reported droplet translation on the inclined surfaces by AlN/Si SAWs. They showed that droplets with volumes smaller than 3 µl could be effectively transported on arbitrary inclined surfaces.

f

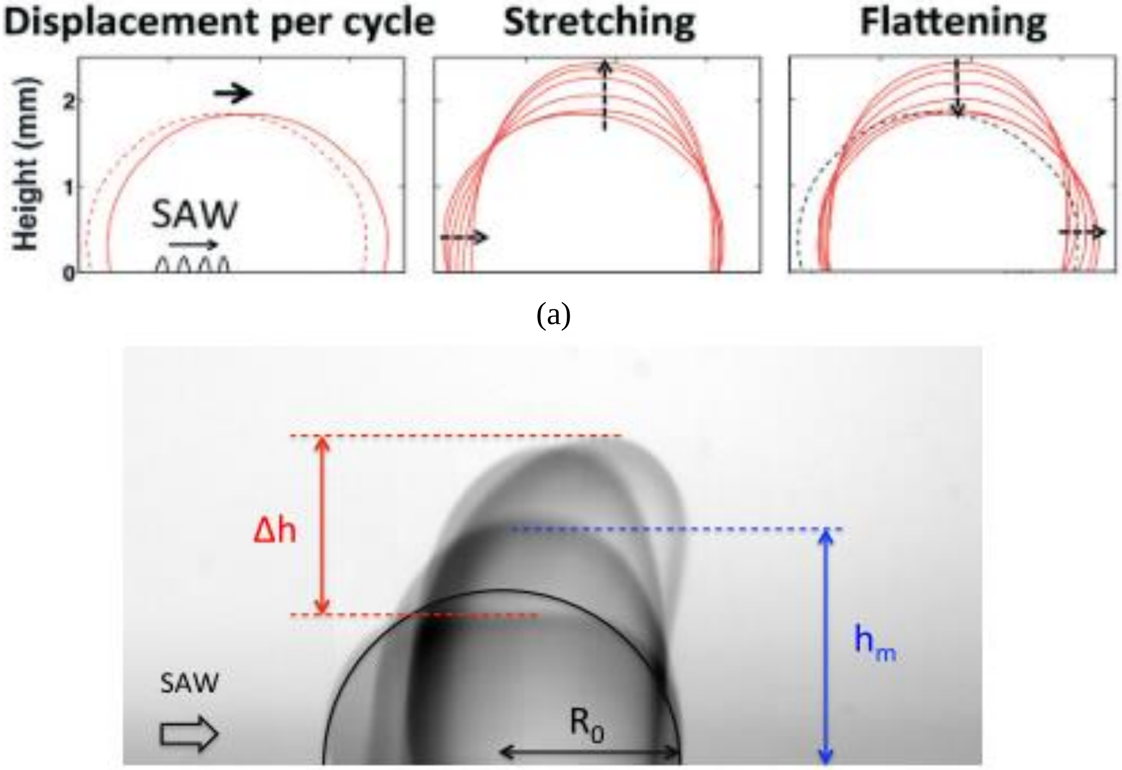

(a)

(b)

Figure 2-6: a) Oscillation of the droplet producing movement of the rear three-phase contact line during stretching and then the front three-phase contact line movement during flattening. b) Consecutive deformations of the droplet excited by SAW, leading to both pumping in SAW prorogation direction and oscillations of amplitude Δh[56].

Surface properties play an important issue that can affect the droplet pumping velocity by SAW. The superhydrophobic surface would minimize the solid and liquid contact area and thus minimize the pinning force and create a slippery surface. However, this minimized interaction area limits the amount of energy transferred by SAW to the liquid medium. On the contrary, hydrophilic surfaces generate a large pinning force that refrains the droplet from smooth translation. Most of the literature has used hydrophobic coatings such as CYTOP for smooth droplet translation. Innovatively, Lou et al.[59] reported droplet pumping on a slippery layer of lubricating oil-filled on a hydrophobic layer, making the surface superhydrophobic. The threshold power to pump the droplet on a ZnO/Si SAW device is significantly reduced (up to 85%) by using this method. Moreover, Tao et al.[38], proposed droplet pumping on curved flexible surfaces. They reported that changing the surface treatment, changing the contact angle hysteresis and receding contact angle droplet motion on inclined and curved surfaces can be modified.

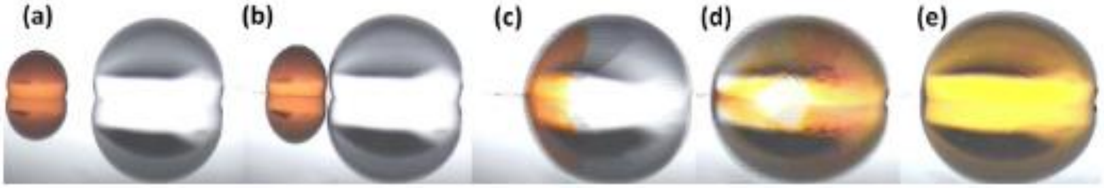

Figure 2-7: Snapshots of Pumping and mixing of two water droplets by SAW[7]. The dye colours the smaller droplet. (a) separated droplets before applying SAW, (b) the dye droplet is transported towards the large droplet at t = 0.4. (c) droplet merging and internal flow creation by Rayleigh angle inside droplet at t = 0.44. (d) internal streaming patterns at t = 0.45. (e) a homogeneously mixed droplet at t = 0.5.

2.3.3 Jetting

Generally, jetting of liquid occurs at the liquid-gas interface when external energy sources generate inertial pressure that overpowers surface tension. A nozzle is typically required to generate enough pressure and velocities to overcome the large surface tension of small liquid droplets[60]. Principally, significant shear stress appears in the fluid medium using a nozzle to create a jet[61]. Consequently, in bioprinting applications, the cell mortality percentage is increased, and as a result, clogging can occur. This leads to a significant drop in performance for the device[62]. Therefore, many nozzleless droplet jetting approaches, such as thermocavitation laser-generated bubble production[63] and spark-generated cavitation bubbles [64] inside the liquid, have been introduced lately. Compared with these methods, droplet jetting by SAW has advantages, including high-energy efficiency, lower possibility of damage to biological entities in the liquid, and high biocompatibility[65]. Additionally, SAW-based droplet jetting eliminates the need for various mechanical components, making the setup simpler, more reliable and reducing maintenance costs.

SAW-based jetting can happen when the transferred energy of SAW into the liquid medium is high enough to create a pressure field, which can overcome the surface tension at the liquid-air interface. SAW energy could create a large velocity field, which deforms the interface droplet, leading to a jet beam. Liquid jetting by SAW was debuted by Shiokawa et al.[66]. They showed that by applying a relatively high RF power to a SAW device, discrete liquid droplets were ejected continuously along the Rayleigh angle from the liquid film on the surface.

Later, Bennes et al.[67] reported the jetting phenomenon dependency on surface treatment. While on a hydrophobic surface, the contact angle was higher than 90° and a narrow bands of the water jet was extracted from the liquid by SAW, a spray of multi water jets with an increased number of tiny droplets were observed by applying the RF power on a SAW device with a hydrophilic surface. Tan et al.[68] investigated SAW excited droplet jetting using two opposite focused interdigital transducers (IDTs) fabricated on a 128° YX- $LiNbO_3$ piezoelectric substrate with a wavelength of ~ 200 µm. They derived a straightforward equation for jet velocity calculation based on the momentum balance. Bhattacharjee et al.[69] utilized the SAW-based jetting method to extend a pendulous droplet to form a liquid bridge with a second substrate underneath it. This simple method made it possible to build capillary bridges for low viscosity liquids, such as water, to investigate their capillary-thinning behaviour. Pang et al.[70] fabricated and tested SAW devices by deposition of Ultra-smooth nanocrystalline diamond (UNCD) and ZnO with various thicknesses on Silicone substrate. Their results showed that the droplet jetting efficiency is improved by introducing the UNCD interlayer to the ZnO/Si device. They reported that the UNCD layer helped increase the amount of the SAW energy transferred from the solid surface to the liquid medium.

Guo et al.[71] reported droplet jetting by both bulk (i.e., 128° YX $LiNbO_3$) and thin-film (ZnO/Si) piezoelectric materials. They reported the microfluidic performance of the SAW devices in a range of applied powers and frequencies. Their results showed that for SAW devices with higher resonant frequencies, jetting threshold power is increased. The increased thresholds are attributed to the smaller attenuation length and, in turn, lower acoustic energy transferred to the liquid medium. Darmawan and Byun[72] reported the effects of substrates wettability (i.e., hydrophobic and superhydrophobic) on droplets jetting and explained the resulting unique jetting behaviour. In an analysis of jetting behaviour, they found that the detachment time for the superhydrophobic surfaces is slightly higher than hydrophobic surfaces related to the SAW propagation area.

Zhou et al.[73] also reported the jetting phenomena achieved using the AlN/Si SAW device. Their systematic investigation of the effect of RF power and droplet size on the microfluidic applications showed that at lower droplet volumes, the threshold from RF power to observe jetting in experiments decreased. Jetting by shear horizontal SAWs (SH-SAWs) on 36^{o} YX LiNbO3 was first reported by Fu et al.[10]. Lee et al.[62] used a 128◦-rotated YX-cut LiNbO3 substrate to manufacture a focused SAW device and demonstrated its interfacial jetting characteristics and thermal stability. In 2018, Castro et al.[61] introduced a method to eject single or multiple droplets using pulsed SAWs continuously. They showed that by changing the pulse duration, the ejected droplet size could be controlled. Recently, Lei et al.[74] used travelling SAWs to perform single droplet jetting from a vertical capillary tube. They thoroughly analyzed the jetting characterization parameters such as applied RF power threshold, SAW device frequency, liquid volume, and pinch off droplet size (See Figure 2-8).

Although extensive work has been carried out to explore droplet jetting by experiments, far too little attention has been paid to understanding the physics of droplet jetting (and pumping).

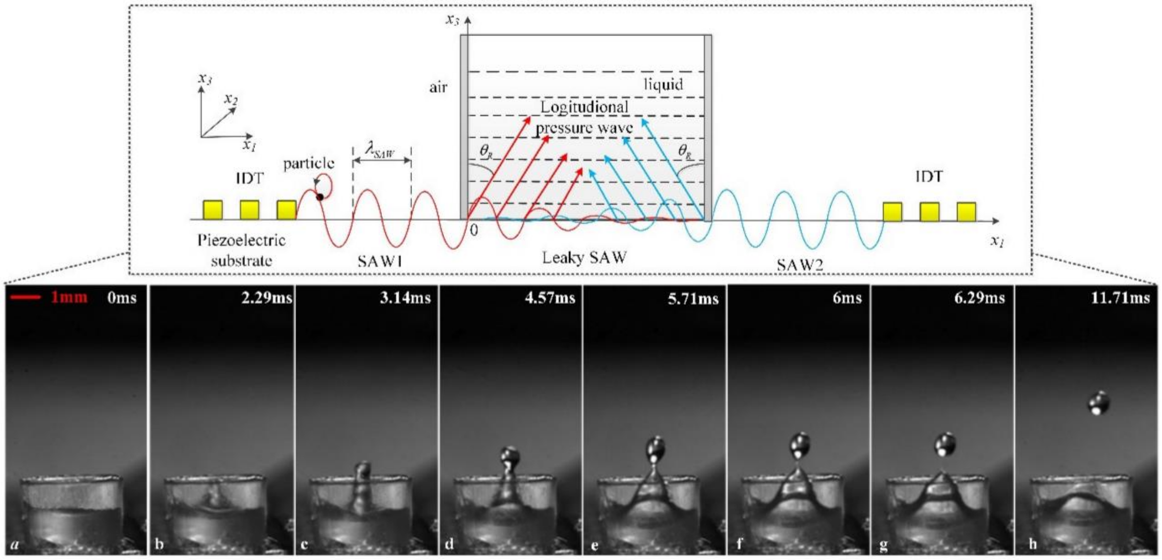

Figure 2-8: Snapshots of droplet generation in a vertical capillary tube by SAWs. The schematic figure in the dashed box illustrates the interaction principles between the SAW and liquid medium[75].

2.3.4 Atomization

In recent years, atomization has gained ample attention due to its interesting physics and many industrial applications. Liquid atomization typically occurs in SAW devices at considerably higher applied RF powers than the one used for jetting. Atomization creates a continuous flow of several tiny droplets with rather similar sizes, and most of the research is focused on optimising and predicting the parameters of the characteristics[13]. The basic theory for SAW atomization is not still well understood, and yet several studies have recently been conducted to investigate the effects of viscosity, SAW frequency, fluid dynamics and applied SAW power. Moreover, device engineering improvements is needed to reliably generate SAW atomization at lower input power[76]. Considering that this thesis aims not to investigate SAW liquid atomization, a detailed review of this phenomena is avoided.

2.4 Droplet impact phenomena

In past decade, the phenomenon of liquid droplet impact on solid surfaces has been extensively studied because of its significance in science and industrial applications, including anti-fogging[77], anti-acing[78–80], inkjet printing[81–84], agriculture[85,86], spray cooling[87,88], self-cleaning[89–91], anticorrosion[92–94], internal combustion engines[95,96], optical devices[97] and anti-bacterial surfaces[98]. Inspired by nature, diverse techniques have been invented to manipulate the droplet impact dynamics[99–102]. For instance, textured superhydrophobic surfaces are used to manipulate and promote the droplet rebouncing from the surface; topological heterogeneity is used for droplet rebouncing direction control[103–106]; high[107,108] and freezing[109] temperature surfaces are utilized to enhance complete bouncing of the liquid droplet. Droplet impact regimes, such as deposition, rebound, break-up, jetting and splash, can happen depending on the fluid properties. These include surface tension and viscosity, kinematics related to droplet size, impact velocity and direction, and structural and chemical properties of the solid surface[110–112]. Droplet impact dynamics have been investigated extensively in terms of many characteristic parameters such as contact time, maximum spreading diameter, droplet tip height and velocity during the impact, and rebouncing direction[113]. However, because of the millisecond-scale interaction and the liquid deformability, it is still challenging to control the characteristic impact parameters effectively within the context of different real-world applications.

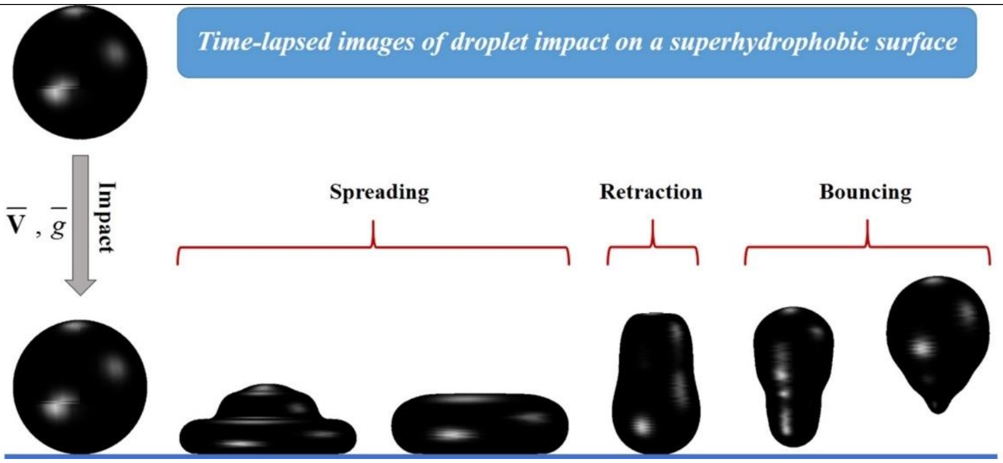

Figure 2-9: Snapshots of the complete droplet rebound from the surface[114].

The Reynolds number ($Re = \frac{\rho D_0 U_0}{\mu}$, where μ is liquid viscosity) denoting the ratio of inertial force to the viscous force, the Weber number ($We = \rho {U_0}^2 D_0 / \gamma_{lg}$, in which ρ, U_0, D_0, γ_{lg} are density, impact velocity, initial diameter, and surface tension of the droplet correspondingly) indicating the fraction of inertial force to surface tension and the Ohnesorge number ($Oh = \mu / \left(\rho \gamma_{lg} D_0\right)^{1/2}$) representing the ratio of viscous force to the inertial and capillary forces are three dimensionless numbers that are characteristically used to describe the droplet impact dynamics on solid surfaces.

After the droplet impact on solid surfaces and in the absence of splashing, the droplet spreads on the solid surface to a maximum spreading diameter and them depending on the surface and liquid physiochemical properties, and the droplet can retract or permanently remain spread on the surface (See Figure 2-9)[115]. The droplet dynamics are controlled by the interaction between kinematic, surface and potential energy and viscous dissipation[116]. Precisely, when the solid surface is (super)-hydrophobic, less energy is dissipated during the spreading phase and droplet detachment from the surface even as a jet can be observed[117]. By altering the wettability of the solid surface, the dynamics of spreading and retracting can be controlled.

During the spreading phase, ~75 % droplet kinetic energy is dissipated[118], and simultaneously the rest of the initial kinetic energy is converted to surface energy. After reaching the maximum diameter, potential surface energy starts to convert back to kinetic energy, and the droplet starts to retract. If the converted kinetic energy is high enough during the retraction process, the droplet will detach from the surface[118]. The contact time between the droplet and solid surface affects the amount of energy transferred between the liquid and solid and is favourable to be minimized for a wide range of real-world applications such as anti-icing, dropwise condensation, anti-corrosion, anti-fouling and self-cleaning surfaces[119,120]. Various methods have been reported to decrease contact time using textured surfaces with post arrays to achieve pancake-bouncing [121], ridge to break the symmetry[122], cylindrical macrostructures[123], or curved surfaces[124].

A few passive techniques have been developed and applied to reduce the droplet contact time on surfaces inspired by nature. For instance, Regulagadda et al. proposed texturing the substrate with a triangular ridge to realize droplet ski-jumping from the surface, thus leading to a contact time reduction of ~65%. Zhang et al. reported a 10%-30% contact time reduction using substrates patterned with varied posts and coated with nanoparticles for oblique droplet impact[125]. However, the efficiency, practical fabrication and applications of these proposed methods are still controversial. Hitherto, there is no report for an active method that can change the droplet impact regime, contact time, and rebouncing angle on an inclined surface for any random impact scenario.

2.5 Numerical models of droplet actuation by SAWs

Accurate computational modelling of the interaction between SAWs and droplets can be used to understand the underlying physics and improve the SAW device design and fabrication. Pioneer works of Rayleigh[16] and Eckart[126] revealed that acoustic streaming inside the liquid exposed the transfer of the momentum from the wave to the liquid by sound attenuation. Most of the researchers have distinguished two types of flow depending on whether the flow is generated by shear stress on the solid boundary (oscillation driven streaming) or from the dissipation of the sound momentum by viscosity (Eckart or bulk streaming)[26,127–131]. One of the initial works on acoustic streaming was carried out by Nyborg[127], who neglected the nonlinear hydrodynamics term (fluid inertia on streaming motion) in the Navier Stokes equation. Nyborg believed that both acoustic streaming and subsequent fluid velocity were second-order phenomena, and thus, the nonlinear hydrodynamics, which was fourth-order, could be neglected. Lighthill argued, in the 1970s, that the fluid inertia was only negligible for slow streaming velocities. He developed a mathematical model which provided a body force expression for the bulk streaming[26]. Analytical studies of droplet actuation by SAWs started by seminal papers of Shiokawa et al.[31,66]. By neglecting the acoustic waves' internal reflections at the liquid-gas interface, they followed Nyborg's approach to developing an analytical body force for calculating the streaming velocity[66].

As a result of advanced numerical methods and high-performance computing (HPC), several numerical models were developed to explicitly simulate the interaction of SAWs and liquid and internal streaming in droplets. These numerical works are mainly divided into two general sets:

- Separation of scales
- SAW as a body force

2.5.1 Separation of scales

In this method, the acoustic wave propagation is modelled inside the droplet, considering the viscous damping. The main challenge in this method is significantly different time scales for wave propagation (i.e., time discretization on the order of 10^{-8} s) and liquid streaming (i.e., 10^{-3} to 10^{-1})[132]. Generally, in this method, the wave propagation and microfluidics equations are modelled through two sets of equations followed by a perturbation expansion. Each physical quantity in this method is resolved into three contributions: hydrostatic (i.e., the system at rest), acoustic (i.e., oscillation part of the perturbation) and hydrodynamic (i.e., time-averaged part of perturbation during an acoustic period) [26,133].

$$p = p_0 + p_1 + p_2 \tag{2.4}$$

$$\rho = \rho_0 + \rho_1 + \rho_2 \tag{2.5}$$

$$\hat{u} = \hat{u}_1 + \hat{u}_2 \tag{2.6}$$

where p, ρ, and u are the pressure, density, and velocity, respectively. Also, since the droplet is at rest before SAW propagation, $u_{i,0} = 0$. Subscripts 0, 1, 2 refer to the hydrostatic, acoustic, and hydrodynamic terms, respectively[132]. The coupled acoustic wave is treated as a first-order perturbation into the fluid by using the first-order approximation to simplify and reduce the computational costs. The governing equations of the wave propagation become[4]:

$$\frac{\partial \rho_{1f}}{\partial t} + \rho_{0f}(\nabla . \hat{u}_1) = 0 \tag{2.7}$$

$$\rho_{0f}\frac{\partial \hat{u}_1}{\partial t} = -\nabla p_1 + \mu\nabla^2\hat{u}_1 + \left(\mu' + \frac{\mu}{3}\right)\nabla\nabla.\hat{u}_1 \tag{2.8}$$

$$p_1 = v_l^2\rho_{1f} \quad ,\hat{u}_1 = \frac{\partial x_i}{\partial t} \tag{2.9}$$

where $\acute{v}_l$ is the mechanical displacement of a Rayleigh wave (SAW). To derive the above set of equations, it is assumed that the flow is compressible and isentropic, and the thermal effects of wave damping and fluid heating are neglected. Assuming that the droplet is in contact with elastic walls partially traversed by SAWs the mechanical displacement of the wave can be calculated by the wave equations[134,135]:

$$\rho_s\frac{\partial^2 x_i}{\partial t^2} - c_{jk}\frac{\partial^2 x_i}{\partial x_j \partial x_k} - e_{jk}\frac{\partial^2 \acute{\varphi}}{\partial x_j \partial x_k} = 0, \tag{2.10}$$

$$e_{jk}\frac{\partial^2 x_i}{\partial x_j \partial x_k} - \varepsilon_{jk}\frac{\partial^2 \acute{\varphi}}{\partial x_j \partial x_k} = 0 \tag{2.11}$$

where, $i, j,$ and k indexes refer to the cartesian direction. c_{jk} is the stiffness tensor of the piezoelectric material, x_i is the displacement component along the corresponding Cartesian axes. $\acute{\varphi}$, e_{jk}, and ε_{jk} are electrical potential, the piezoelectric tensor, and dielectric permittivity tensor respectively[136]. SAWs have only two displacement components, the longitudinal component along the propagation direction, $\hat{u}_1$, and transverse displacement in the direction perpendicular to the surface, $\hat{u}_3$. Solution of the wave equations (i.e., Equations 2.10 and 2.11) gives the mechanical displacements of the SAWs which can be used in Equation 2.9 [44]. The results of Equations 2.9 can be used as a boundary condition to solve the mass and momentum conservation equations (i.e., Equations 2.7 and 2.9).

Using this method, Köster developed an algorithm to compute the internal streaming flow and small deformations of the surface for a two-dimensional (2D) droplet induced by SAWs. In the simulations, the droplet interface was considered a free capillary fluid boundary that simulates small deformations of the surface. Köster's 2D simulations did not provide any validation against the experimental data. Moreover, the numerical study was limited to one droplet size excited at a specific frequency. Antil et al.[137] simulated the wave propagation and the induced internal streaming flow using the separation of scales method. The obtained results were used to optimize the SAW devices. However, like the work of Köster, the obtained 2D results simulated the internal streaming flow in a channel and were not compared to the experimental results. Raghavan et al.[44] also used this method to reproduce the internal streaming flow induced by asymmetrical SAWs in 3D. Although the method predicted the flow patterns precisely, the reported internal streaming velocities was one order of magnitude smaller than the experimental velocities. Tan et al.[136] presented a numerical study of liquid actuation by SAW using the separation of scales method. Their two-dimensional numerical model focused on the dynamics of the liquid-gas interface in the low amplitude flow patterns. Their results, confirmed by experimental results, showed that at lower applied SAW amplitudes (i.e., acoustic Reynolds number lower than 1, $\frac{\rho_l v_l \lambda_{SAW}}{2\pi\mu'} < 1$) a fundamental resonant frequency and a superharmonic frequency was found in free surface vibrations. They also showed that the liquid-gas interface vibrations are comparable to the Rayleigh wave displacements. Their analysis was used to predict the vibration of the liquid-air interface for a 2D droplet and did not predict the large deformations of the free surface.

Vanneste and Bühler[138] developed a numerical algorithm of acoustic streaming based on the separation of scales method, inducing viscous dissipation and vortex generation. They spotlighted that Reynold stress and pressure gradient would cancel each other without viscous dissipation, and no mean flow would not be generated in the streaming. Furthermore, they proved that in cases for millimetric droplets actuated by SAWs with resonant frequencies higher than 10 MHz, the Eckart streaming dominates over the oscillation driven streaming. This method was applied to different geometries; however, the solutions were in 2D, and the authors neglected the internal reflections at the liquid-gas interface. They also considered the fluid medium as a square box placed on the surface of the SAW device. Riaud et al.[133] developed a cost-effective numerical method based on Vanneste and Bühler to investigate the effect of liquid viscosity of the internal streaming in a droplet induced by SAWs. They showed that liquid viscosity strongly affects the Eckart streaming inside the liquid and thus should be considered in the mathematical modelling. The developed model reproduced the experimental results of internal droplet streaming by SAWs. They also showed that the acoustic streaming patterns in a semi-spherical sessile droplet are dependent on both sound wave propagation and hydrodynamic flow motion. Chen et al.138 performed a 3D simulation of boundary-driven streaming induced by SAWs in highly viscous oil. They assumed that a water droplet is stationary inside the oil medium. They defined their method as the slip velocity method, which was developed based on the separation of scales method. Specifically, in the viscous boundary layer, the 1st-order and 2nd-order equations were solved with the surface displacement equations in the solid-liquid interface as the actuation source. Their experimentally validated results showed that there is a stagnation point in the simulations. Their results showed that after this point, the droplet stops moving; however, acoustic streaming inside the oil medium continues.

2.5.2 SAW as a body force

High fidelity simulation of fully coupled compressible Navier-Stokes and wave propagation equations is complex, expensive, and sometimes inaccessible. Consequently, to simplify the numerical models, most of the numerical works on droplet streaming by SAWs have replaced the effect of surface vibrations with a body force term to the Navier-Stokes equation. In fact, this method is a particular case of the separation of scales method in which only the incident acoustic field is considered, and the acoustic propagation within the liquid and reflections are neglected. Using this method can significantly reduce the computational costs allowing 3D simulations of complex cases. However, since acoustic propagation is neglected, viscous damping of the flow is not considered in the simulations, and thus local vorticity generation cannot be simulated.

Within this framework, Schindler et al.[139] numerically studied droplet deformation due to high-intensity surface acoustic waves, but they ignored the SAW radiation specifics in the drop and performed their simulations in 2D. Sankaranarayanan et al.[140,141] calculated the streaming force applied to a droplet by focused IDTs. Alghane et al.[142] performed a 3D simulation of liquid mixing by SAW. The nonlinear hydrodynamic term was included in the Navier-Stokes equation using a body force term. As a function of input power, they experimentally determined the SAW amplitude and additionally calculated the streaming velocity as a function of applied power. Using numerical simulations, they calculated all three components of the streaming velocity as a function of SAW amplitude. The comparison between the simulation and experiments results showed some simple flows under relatively low power (up to 0.025 W) in relatively large drops (30 μL). Ai and Marrone[54] investigated the droplet translation by focused surface acoustic waves. A part of their research was to numerically simulate the acoustic streaming force on the hemispherical droplet on the surface. In their 2D simulations, they mostly focused on the comparison between focused and straight IDT effect on the streaming force and did not consider the liquid-gas interface deformation.

Shah et al.[143] numerically investigated the interaction between SAW and droplets using a body source term, and they also reported a linear relationship between the input power and mixing velocity. However, they did not compare their results with experimental results and did not consider the deformation of the droplet interface. The first experiment regarding the simulation of droplet deformation by SAWs was most likely performed by Jangi et al.[15], who simulated the droplet vertical jetting using this approach. They developed a multiphase flow model to capture the large deformations of the droplet induced by circular and focused SAWs. However, they did not consider the dynamics of the three-phase contact line in their simulations. In another recent study, Noori et al.[144] simulated the droplet jetting by TSAW with the Lattice Boltzmann method. Their results could reproduce the droplet jetting, but they were performed in 2D, and the effect of contact angle hysteresis was not considered in the simulations.

2.6 Numerical modelling of multiphase flow

Computational resources and numerical methods development have made it possible to investigate the liquid-gas interface shape change by Computational Fluid Dynamics (CFD). Since 1980, numerous numerical methods have been developed for capturing the interface in two-phase flow in CFD[145]. In many cases, the experimental investigation of two-phase flow is challenging and expensive. On the other hand, numerical modelling can simulate a variety of cases in details economically. Numerical modelling of one phase flow aims to calculate the velocity, pressure, and temperature (for non-isothermal cases) for discrete points in the domain. Because of the two-phase flow complexity, the interface between two fluids, its movement and deformation, must be considered in the simulations by defining a proper boundary condition.

The interface is tracked by explicit methods in Interface Tracking Methods (ITM)[146]. A stationary fixed mesh is used to discretize to the domain, while a Lagrangian grid tracks the interface between two fluids such that its velocity should be equal to surrounding fluid at any time. Theoretically, the results provided by this method must be accurate. These methods are computationally costly since they require mapping of the interface from one grid to another. Besides, some numerical difficulties may arise for large deformation of the interface[147].

On the other hand, Interface Capturing Methods (ICM) consider the two phases of the fluid as one mixture and solve the problem on a fixed mesh. A phase function is used in ICMs to identify the interface between two phases at each time step. These methods are the most popular methods for multiphase problems in CFD and are considerably less expensive and can provide accurate results[147]. Among all ICM methods, Volume of Fluid (VOF) and Level Set (LS) methods have been vastly developed and used in two-phase flow problems. The coupling between VOF and LS (CLSVOF) has recently been developed to combine the advantages of both methods[148].

Since the approach used in this thesis is CLVOF, this review is concentrated principally on explaining the most frequently used methods of capturing interfaces (i.e., VOF, LS, and CLSVOF). Nevertheless, other methods are also present in the literature for two-fluid flow studies. In the following, a brief outline of the main important features of each approach is provided. Later, a more detailed explanation of VOF and LS methods is presented.

2.6.1 Boundary Integral Method

The liquid-gas interface of the flow is captured by solving the integral of the liquid-gas interface boundary equation in the Boundary Integral Method[149,150]. This approach only investigates the interface between the gas and liquid and thus is an effective and computationally cheap method. The main disadvantage of this methodology is the lack of viscosity simulation since the integral boundary methodology assumes that the solution is governed by potential flow in each fluid. More complex methods should be applied for large interface deformations, such as combining and breaking up the interface.

2.6.2 Diffuse Interface method

In the Diffuse Interface technique, the liquid-gas interface is smoothed to a particular thickness over several cells[151,152]. A narrow miscible field separating the two fluids is known to be the diffuse interface layer. In this approach, to differentiate between the two fluids in the domain, the volume fraction C is used, while C = 1 in the cells occupied by one of the fluids, C = 0 in the cells occupied by the other fluid. Using the convective Cahn-Hilliard equation, this scalar field is advected[153]. The key advantage of this approach is its applicability to the two-fluid flow problems with solid boundaries since it allows the interface to move by convection or diffusion along the solid walls due to the chemical gradient potential.

2.6.3 Lattice Boltzmann method

The Lattice Boltzmann method is a mesoscopic scale technique for computationally explaining the fluid flow based on the kinetic energy of the gases[154]. A density distribution function evaluates the particles' density in the computational domain, and then the fluid density is calculated as a function of the molecular mass of these particles. Interaction potential parameters are defined and used in this approach to model the liquid-gas and solid-liquid interfaces and interactions. One of the key benefits of the Lattice Boltzmann approach is that the boundary conditions are applied at the boundary particles instead of the domain itself[155]. This allows the simulation of the liquid-gas interface and solid boundaries without any additional requirements compared to other methods.

2.6.4 VOF method

Hirt and Nichols[156] developed the VOF method for the first time. This method solves a full Navier-Stokes equation for mass and momentum conservation in connection with the advection of a scalar called colour function, α. The colour function is defined as the percentage of each computational cell volume filled by the liquid phase. If the cell volume is only filled by gas, α is zero, and it is 1 when the cell is entirely covered by liquid[157]. The interface is defined among the cells where α is between 0 and 1. This method generally conserves the mass. The fluids physical properties are calculated using the colour function[157]. A numerical error is created due to the discrete interface representation. Unphysical flows around the interface represent this error (see Figure 2-10). The algorithm proposed by Hirt and Nicholas is summarized as below:

(1) Initialize pressure, velocity field and colour function in all the cells

(2) All cells which are partly filled are marked as boundary cells.

(3) Velocity in a new time step is predicted using old-time pressure

(4) Generally, predicted velocities do not satisfy the continuity equation. Pressure in the interior cells is changed, and the velocity change due to pressure change is added to initial velocities. Iterations are done until the continuity equation is satisfied.

(5) Using new calculated velocities, the advection equation is solved by an explicit scheme.

(6) Go to the second step until the end time or steady-state.

If negative or higher than one values are enhanced for colour function during the solution, they are simply reset to 0 or 1, respectively. This resetting is one of the main reasons for the mass error. All the developments enhanced for this method aimed to reconstruct the interface accurately and with less possible errors for different meshes types. A summary of essential developments is presented in the following.

While the amount of the fluid in each grid cell is calculated by the colour function, the gradient of this function is also needed to determine the interface direction. VOF technique is generally composed of two main steps, (i) interface position and slope determination by discretization scheme (ii) the time integration algorithm for advecting the colour function. The first process obtains the fluid fluxes and flow fields through the mesh cell faces. These terms are required to solve the advection equation. Two main approaches to determine the interface can be defined; Geometrical reconstruction scheme[158] and algebraic discretization scheme[159]

According to the neighbour cells, the VOF method developed by Hirt and Nichols can reconstruct the interface line segment either horizontally or vertically. The interface normal components magnitude determine the interface direction[160]. The RIPPLE code was developed based on this algorithm[161]. Y-VOF is a more exact algorithm for interface reconstruction, which is developed by Young[162]. In the 2D case, a straight line is used to show the cells' interface to satisfy the colour function in each cell. The fluxes through the cell faces and colour function are updated by sweeping the grid in one direction, and then they are updated by sweeping the mesh in the other direction perpendicular to initial direction.

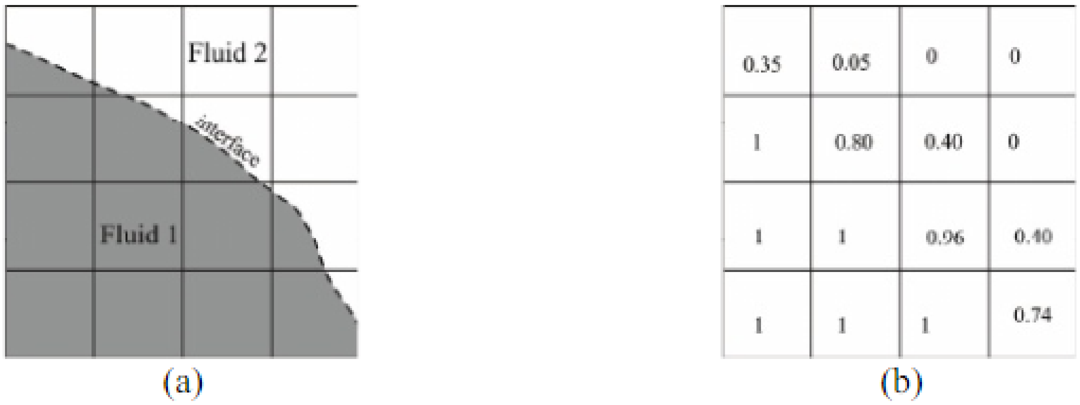

0.35	0.05	0	0
1	0.80	0.40	0
1	1	0.96	0.40
1	1	1	0.74

Figure 2-10: Two-phase flow schematics: (a) accurate interface position (b) Domain with VOF colour function [156]

Although these development methods were significant in multiphase modelling, they fail to simulate the interface accurately, especially in cases with large deformations with vorticity and shear near the interface. Most of these basic methods are no longer in use, and they are replaced by more accurate algorithms such as the Piecewise Linear Interface Calculation (PLIC) algorithm, which was developed by Rider and Kothe[158]. In this method (in 2D simulations), the slope of the line (which defines the interface) is determined by the gradient of a colour function. Since 1998, the PLIC algorithm has been developed, implemented and used in various CFD codes.

Aulisa[163] presented another algorithm for interface reconstruction and advection for 2D cases. In this method, the interface is reconstructed using a colour function and surface markers. Following the streamlines, the colour function field and markers are advected. A continuous chain of segments connects surface markers to build the interface. Using Edge-matched Flux Polygons and Spline-based Interface Reconstruction techniques (EMFPA-SIR), Lopez et al.[164] upgraded the Young's VOF method. The first step in this algorithm is to calculate the interface direction by the Y-VOF method, and then during the second step, it is corrected by cubic spline interpolation of the interface parts centre points.

Typically, in dispersed flows like fuel sprays, the cell size is much larger than the fluid part size. Consequently, reconstructions become more complicated, and the accuracy of the VOF method will decrease. In these cases, Ginzburg and Wittum[165] used an adaptive grid refinement of the interface. An alternative way to overcome this problem is to use a more accurate interface capturing algorithm. Lopez et al.[164] presented an improved algorithm to reconstruct the interface for cases where the fluid fields have a size less than the mesh size. They used markers to track the interface position and direction effectively.

In general, the essential advantage of geometrical reconstruction algorithms is that these methods assure linearity conservation with first and second-order accuracy. The initial reconstruction schemes were based on direction splitting techniques with first-order accuracy[166] [167]. More advanced and complicated schemes were developed to get second-order accuracy in reconstruction and advection[158,164,168].

However, the geometrical reconstruction schemes have two main disadvantages: high computational costs and their complexity for 3D cases. These schemes require determining the shape of the truncated area (volume for 3d cases) in each interface mesh cell and preserving the mass by detecting the accurate position of the interface. The focus of advances in geometrical methods in the last decade was developing schemes to preserve the linearity of the interface and be less computationally expensive[164,169–171].

An alternative approach to preserving the interface resolution with lower computational costs is Algebraic VOF, an ordinary and straightforward way to implement the VOF method. A convention term with a standard discretisation method is used to transport the VOF field. However, the accuracy of the interface definition is affected by numerical diffusion in the transport scheme. The initial algorithms of algebraic VOF methods are based on the scheme developed by Zalesak, named: Flux Correct Transport scheme (FCT)[172]. In this method, no explicit interface reconstruction is required. FCT has the advantage of stability because of the upwind method and interfaces sharpness, due to a downward method, through its mixed scheme. FCT is a faster method than geometrical reconstruction methods, but it has a lower accuracy than the Y-VOF scheme[166]. The FCT scheme is not diffusive, though tiny smears of fluid might separate from the interface to the gas phase[166].

Another algebraic method that depends on high-resolution discretization methods is Compressive Interface Capturing Scheme for Arbitrary Meshes (CICSAM), developed and presented by Ubbink and Issa[173]. This method keeps the interface sharps while it preserves the colour function bounded. “Counter gradient” is an additional term introduced to the VOF advection equation in an open-source library solver called “InterFoam” to maintain the sharpness of the interface. This term assures that the boundedness of the interface and conservativeness are preserved so that smears separated from the fluid interface are limited.

In short, since the early years of VOF method use, many advances in numerical modelling have been achieved. Most of the further research on this method focused on enhancing more accuracy and less computational costs. In the last decade, many efforts have been made to simplify implementing this method for various physical applications. During the VOF method improvements, a small number of benchmarking test cases have been used to compare these schemes' accuracy and mass conservation. Hollow square/circle of Rudman[166], single vortex and time reserved flows by Rider-Kothe[158], and Rayleigh-Taylor instabilities[161,166] are the most repeated tests in the literature. Lately, several hybrid methods have been developed and presented to combine the advantages of other interface capturing methods[174,175].

2.6.5 Level Set method

Osher and Sethian[176] developed the LS Method for the first time. Later this method was used for two-phase flow by Sussman[177]. A signed distance function, φ is defined to distinguish between two fluids in the mixture by providing the interface with a specific thickness. In one of the phases, φ is positive, and it is negative in the other phase. The physical properties change smoothly across the interface, which is defined as the area with $\varphi = 0$. To predict the interface deformation and move, the LS advection equation is solved. Sussman et al.[178] highlighted the most problematic point of the LS method, which is notable dissipation during discretization of the LS advection equation.

Additionally, because φ is not preserved during the solution, it has to be corrected at each time step, and this correction procedure leads to mass conservation issues[174]. After the first time step advection, the LS function ceases to act as a distance function. So, a “reinitialization” process is needed for distancing property recovery. Sussman has shown that the LS method does not preserve mass conservation because of the re-distancing process[177]. To elucidate about the importance of the reinitialization process, it should be explained that a steep and flat gradient of LS function is not desirable and can lead to numerical instabilities and accuracy loss. A smooth LS function with no unnecessary oscillations is desirable to determine the interface. In the last two decades, significant improvements to LS methods to achieve mass conservation have been presented. The objective of the LS method was to increase the accuracy of the technique while keeping it simple. These enhancements were achieved using higher order discretization schemes, improvements in the reinitialization process to preserve mass and coupling the method with other two-phase flow techniques.

The classic method for the reinitialization equation solving is using forward Euler time integration and spatial upwind scheme. This strategy leads to numerical dissipations as a loss of volume of the interface[179]. Shu and Osher [144] used a higher-order scheme called the Total Variation Diminishing Runge-Kutta scheme (TVD-RK) to overcome this problem. Using higher-order schemes were reported in many other references[180,181]. Essentially Non-Oscillatory (ENO) and the Weighted Essentially Non-Oscillatory (WENO) methods are other higher-order schemes that were suggested later[180,181]. ENO and WENO are high order schemes, combining low order upwind schemes[178,182]. A more detailed discussion about other spatial methods is presented by Losasso et al.[179].

Since higher-order schemes cannot solve the mass conservation problem, particularly for compressible flow[183], other solution strategies are required to improve the LS method. Many researchers have focused on reinitialization process improvement to reach this purpose so that a signed distance function is continuously attained near to surface.

In summary, because of its advantage in precisely evaluating the interface normal and curvature, the proposed Level Set approach for solving two-fluid flow problems is a workable option for many applications. The main disadvantage of this approach is the loss of mass (volume) during the advection of the smoothed LS function. A few techniques have been suggested to solve this problem, such as implementing high-order discretization schemes such as WENO and improving the reinitialization equation using a smooth Heaviside function. The volume conservation error was also minimised by refining the mesh in the under-resolved domains where significant interface distortion occurs.

2.6.6 Coupling level set and volume of fluid

A tremendous amount of attention has been paid over the last two decade to integrating the key basic benefits of both VOF and LS in a single approach to take advantage of both methods[184]. Fully coupled LS/VOF (CLSVOF) developed by Sussman and Puckett (2000) and then used by many researchers[184]. In this method, the transport equation is solved for both fields. The results are used together to build the interface. The LS builds a smoothly differentiable interface while the VOF makes sure that mass is conserved in all the field. In the coupled CLSVOF framework, Son and Hur (2002) created another technique for geometrical reconstruction of the interface[185]. This is done by adopting a configuration similar to the PLIC technique. The normal interface, in this method, is evaluated by using the LS smooth function.

Overall, to combine the advantages of both VOF and LS techniques, the coupled approach is developed. Implementation of the coupled approach is, however, more complicated than the standard VOF and LS techniques. This is associated with two major problems. First, in the CLSVOF method, a need to solve both VOF and LS advection equations is raised. A few approaches are recommended later to solve only the VOF advection equation and then initiate the LS field based on the VOF field. Second, to evaluate the interface slope and location in each interface cell, a geometrical reconstruction technique, like the PLIC method, must also be implemented. A few efforts have been made to create an analytical algorithm for determining the interface of the CLSVOF approach to reduce the difficulty of the geometrical reconstruction. To achieve continuous properties through the interface for solving the VOF and LS advection equations, the Ghost Fluid Method (GFM) has been used to develop the CLSVOF method. This technique adds virtual cells to the real cells around the interface, known as ghost cells, so that both virtual and actual regions are used to solve the problem of multiphase flow[185].

2.7 Final remarks

This chapter introduced the background of the experimental and numerical investigation of SAW-based acoustofluidics. A review on the SAW technology development is introduced, and the innovative SAW applications in the industry are highlighted. Additionally, applications of SAWs in droplet actuation are reviewed. Furthermore, a summary of analytical and numerical models, developed to investigate acoustic streaming and fluid actuation by SAW in a droplet, is presented. Moreover, a review of the literature of multiphase flow interface capturing methods has been presented.

It can be concluded from the literature that some studies have developed models for numerical investigations of deformations of droplets by acoustic waves. However, the literature review showed that most of the research, to date, has focused on internal streaming. However, a major problem with this kind of numerical simulations is the assumption of no liquid-gas interface deformation. What is known about the physics of SAW interaction with liquids is largely based upon numerical simulation of acoustic streaming.

In most of the SAW-based droplet actuation scenarios, interface deformations are observed. To date, the research has tended to focus on acoustic streaming rather than droplet deformation by SAWs. The present work will simulate the large deformations of the droplet interface subjected to SAWs. Furthermore, the interaction between the solid surface and the droplet will be taken into account in the simulations by developing a technique for accurate boundary condition treatments.

A thorough review of the droplet impact on a solid surface is also performed. Significant progress has recently been made using textured surfaces, surface treatment with nanoparticles, or sub-millimetric arrays to modify the droplet impact behaviour on solid surfaces. However, these processes are complicated, challenging, and sometimes expensive. It is also difficult to modify and control the impact dynamics in a programmable way actively and remotely. Up to date, there is little research on the implementation of active methods to control the droplet impact on demand.

Chapter 3. Numerical method

This chapter presents the mathematical formulation of the CLSVOF method and the dynamic contact angle models that will be used later to simulate the droplet actuation by SAWs. As explained in the previous chapter, the CLSVOF method is used to benefit both LS and VOF methods benefits' of capturing sharp interface and mass conservation. The described mathematical model is implemented in the OpenFOAM® computational fluid dynamics toolbox. The details of the boundary conditions and discretization schemes are also explained in this chapter.

3.1 Governing equations

Continuity (Equation 3.1) and momentum (Equation 3.2) equations for an isothermal, unsteady, single-phase, incompressible, and immiscible fluid in the absence of evaporation in cartesian coordinates are[186]:

$$\boldsymbol{\nabla}.\boldsymbol{u} = 0 \tag{3.1}$$

$$\frac{\partial(\rho\boldsymbol{u})}{\partial t} + \nabla.(\rho\boldsymbol{u} \otimes \boldsymbol{u}) = -\boldsymbol{\nabla}p + \boldsymbol{\nabla}.(2\mu\boldsymbol{S}) + \rho\boldsymbol{g} + \boldsymbol{F}_{\boldsymbol{\sigma}} + \boldsymbol{F} \tag{3.2}$$

where $\boldsymbol{u}$ is the velocity vector and $\otimes$ is the dyadic product. Additionally, p is static pressure, $\boldsymbol{g}$ is the gravitational acceleration, ρ and μ are liquid density and viscosity, respectively. $\boldsymbol{S} = \frac{1}{2}(\nabla\boldsymbol{u} + \nabla\boldsymbol{u}^T)$ is the strain rate tensor. $\boldsymbol{F}$ and $\boldsymbol{F}_{\boldsymbol{\sigma}}$ are the forces due to the SAWs and surface tension. The fluid density is constant in this modelling, and the multiphase methods calculate the density of the cells in the liquid-gas interface. To complete the model, closures are needed for SAW and surface tension forces.

3.2 SAW force closure

The magnitude of the SAW body force is calculated by Shiokawa's approach to close the momentum equation [66]. Shiokawa and co-workers considered SAWs to vary sinusoidally in time and took a time average of the Navier Stokes equation for the terms up to second order. For an incompressible fluid, the body force, F, the equation is given by[66]:

$$-F = \langle \rho_l(\acute{\boldsymbol{u}}.\boldsymbol{\nabla})\acute{\boldsymbol{u}} + \acute{\boldsymbol{u}}\boldsymbol{\nabla}.\rho_l\acute{\boldsymbol{u}} \rangle \tag{3.3}$$

where $\acute{u}$ represents the velocity of the particles in the liquid medium, and the brackets $\langle . \rangle$ are used to show time-averaged value. The time average operation is defined as[132]:

$$\langle O \rangle = \frac{1}{T}\int_{t_0}^{t_0+T} O(t)dt \tag{3.4}$$

where $T = 2\pi/\omega$ is the period of the harmonic SAW vibration, and ω is the angular frequency ($\omega = 2\pi f$, where f is the SAW frequency).

As shown in Figure 3-1, the SAW mode is changed to leaky SAW (LSAW) as soon as it reaches an area on which liquid is located. Like SAWs, LSAW propagates along the surface and excites a longitudinal wave into the liquid medium along the Rayleigh angle[66]. The particle displacement ($\acute{x}$ and $\acute{z}$) in the fluid medium ($z > 0$) can be calculated by[66]:

$$\begin{cases} \acute{x} = Aexp\, j\omega t.\, exp(-jK_L x)\, .\, ex\, p(-\alpha K_L z) \\ \acute{z} = -j\alpha Aexp\, j\omega t.\, exp(-jK_L x)\, .\, exp\, (-\alpha K_L z) \end{cases} \tag{3.5}$$

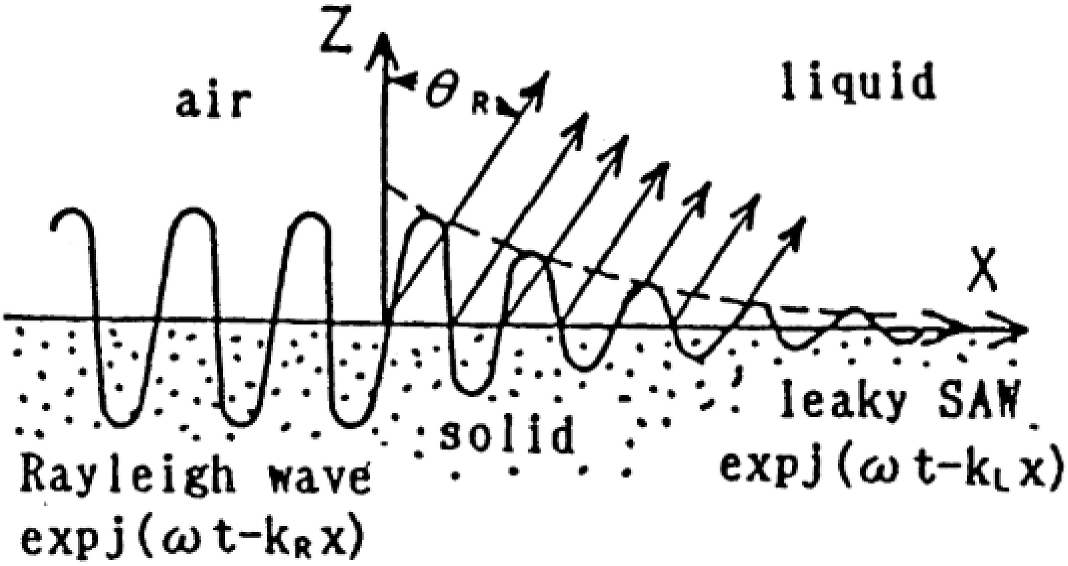

Figure 3-1: Schematic illustration of SAW radiation into liquid[66].

where A is equivalent to the SAW amplitude at the entrance to the liquid medium, j is the unit imaginary number and $\acute{\alpha}$, represents the attenuation coefficient of the LSAW:

$$\grave{\alpha}^2 = 1 - \left({}^{v_s}/_{v_l}\right)^2 \tag{3.6}$$

The wavenumber of the LSAW, K_L, can be calculated by extending the method of Campbell and Jones[187]. The effect of the vorticity generation by liquid viscosity is ignored in Equations 3.5. Particle displacements from Equations 3.5 is used to drive the velocity equations as follow:

$$\begin{cases} \acute{u}_x = d\acute{x}/dt \\ \acute{u}_z = d\acute{z}/dt \end{cases} \tag{3.7}$$

the components of the acoustic streaming body force for an incompressible fluid is given by[66]:

$$\begin{cases} F_x = -\rho_l(1+\alpha'^2)A^2\omega^2 K_i . exp\, 2(K_i x + \alpha' K_i z) \\ F_z = -\rho_l(1+\alpha'^2)A^2\omega^2 \alpha' K_i . exp\, 2(K_i x + \alpha' K_i z) \end{cases} \tag{3.8}$$

where $\alpha' = j\alpha$, and $K_L = K_r + jK_i$ is the propagation constant for leaky SAW, which is a complex number. In Equation 3.8, x and z are the tangential and normal positions based on the origin of the coordinates at the incidence point of the SAW and droplet on the device surface. As illustrated in Figure 3-2, in each XZ-plane, the SAW force is at its maximum at the SAW-droplet incident cell, and it attenuates exponentially in X and Z directions. Since SAWs do not have transversal vibrations, the y-component of the body force (perpendicular to the SAW propagation path on the surface) is zero. The direction of the body force in each cell is calculated using the Rayleigh angle (Equation 2.1).

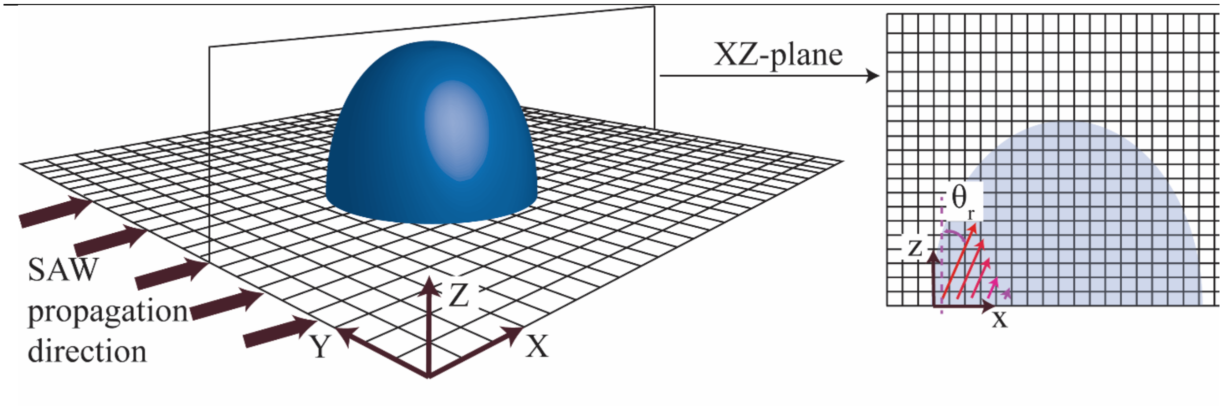

Figure 3-2: Definition of the coordinates for SAW body force calculation.

3.3 VOF method

In the VOF algorithm, both liquid and gas fields are defined by the volume fraction α, which is 1 at the liquid phase and 0 at the gas phase and lies between 0 and 1 at the interface. Note that flow is considered incompressible, and thus the density (and viscosity) of the fluid is constant. In the interface cells (where α is between 1 and zero), the density (and viscosity) of the cell is a function of α. An advection equation for the liquid volume fraction, α, is solved[188].

$$\frac{\partial \alpha}{\partial t} + \boldsymbol{\nabla}.(\boldsymbol{u}\alpha) = 0 \tag{3.9}$$

Density and viscosity in each cell are expressed by the volume fraction as:

$$\rho = \rho_l \alpha + \rho_g (1 - \alpha) \tag{3.10}$$

$$\mu = \mu_l \alpha + \mu_g (1 - \alpha) \tag{3.11}$$

where indices l and g indicate liquid and gas, respectively, Equations 3.10 and 3.11 ensure that the accurate liquid and gas properties are used in the areas far from the liquid-gas interface.

Additionally, F_σ in Equation 3.2 is calculated based on the approach of Brackbill[189]:

$$\boldsymbol{F}_\sigma = \gamma_{lg} \kappa(\alpha) \boldsymbol{\nabla}. \alpha \tag{3.12}$$

where γ_{lg} is the liquid-gas surface tension, and $\kappa(\alpha)$ is the curvature of the interface and is calculated by the method proposed by Brackbill et al.[189].

$$\kappa(\alpha) = -\boldsymbol{\nabla}. \frac{\boldsymbol{\nabla} \alpha}{|\boldsymbol{\nabla} \alpha|} \tag{3.13}$$

3.4 CLSVOF

In this method, the LS field, ϕ, is defined as a signed distance from the spatial interface. Thus, ϕ is 0 at the interface and determined to be positive at the continuous phase (liquid) and negative at the discrete phase (gas). Like the VOF field, the LS field is convected as following[178]:

$$\frac{\partial \phi}{\partial t} + + \boldsymbol{\nabla}.(\boldsymbol{u}\phi) = 0 \tag{3.14}$$

A re-initialisation step is applied at each time step to ensure that, $|\nabla \phi| = 1$ and to improve the computations of the interface curvature. Here the re-initialisation approach introduced by Sussman et al. is used[177].

$$\frac{\partial \phi}{\partial \acute{t}} + Sign(\phi_0)(|\boldsymbol{\nabla}\phi| - 1) = 0 \tag{3.15}$$

Here $S(\phi_0)$ is a sign function of the initial LS field, and $\acute{t}$ is a fictitious time and an equation was solved explicitly with a timestep of $\Delta\acute{t} = 0.1\Delta x$ which is considered to solve the re-initialisation equation explicitly. The density and viscosity of the mixture are then calculated by:

$$\rho(\phi) = \rho_g + (\rho_l - \rho_g)H(\phi) \tag{3.16}$$

$$\mu(\phi) = \mu_g + (\mu_l - \mu_g)H(\phi) \tag{3.17}$$

where $H(\phi)$ is a Heaviside function calculated by:

$$H(\phi) = \begin{cases} 0 & |\phi| < -\epsilon \\ \frac{1}{2}\left[1 + \frac{\phi}{\epsilon} + \frac{1}{\pi} sin\left(\frac{\pi\phi}{\epsilon}\right)\right] & |\phi| \leq \epsilon \\ 1 & |\phi| > \epsilon \end{cases} \tag{3.18}$$

where $\epsilon = 1.5\Delta x$ is the interface thickness and is defined so that the two-phase interface does not smear beyond a specific number of the cells. The key advantage of the LS method is to define the normal unit vector accurately as:

$$\boldsymbol{n_c} = \frac{\boldsymbol{\nabla}\phi}{|\boldsymbol{\nabla}\phi|} \tag{3.19}$$

Thus, the interface curvature is calculated more accurately with the LS field.

$$\kappa(\phi) = -\boldsymbol{\nabla}.\boldsymbol{n_c} \tag{3.20}$$

Since the surface tension has a significant impact in any multiphase flow, now it can be estimated more precisely.

$$\boldsymbol{F_\sigma} = \gamma_{lg}\kappa(\phi)\Lambda(\phi)\boldsymbol{\nabla}\phi \tag{3.21}$$

The interface function, Λ, is defined by[190]

$$\Lambda(\phi) = \begin{cases} 0 & |\phi| > \epsilon \\ \frac{1}{2\epsilon}\left(1 + cos\left(\frac{\pi\phi}{\epsilon}\right)\right) & |\phi| \leq \epsilon \end{cases} \tag{3.22}$$

Despite the mass conservative nature of the VOF method, since α is diffused along with the interface between 0 and 1, and the interface is smeared along this area, the VOF method is not capable of obtaining a sharp interface. The LS[182] and the VOF[174] methods are coupled to capture a sharp interface and smooth transition of the physical properties along with the liquid-gas interface. The algebraic VOF solver “interFoam” of the standard OpenFOAM toolbox (version

4.x.) has been used as a basis to develop the CLSVOF code in this study[27,191]. The first coupling step is to define the level set field using the VOF field. At each time step, the LS field is initialised by assuming that the interface is located at $\alpha = 0.5$.

$$\phi_0 = 0.75(2\alpha - 1).\Gamma \tag{3.23}$$

where $\Gamma = 0.75\Delta x$ is a non-dimensional small number, which is a function of the mesh size. This initial function, ϕ_0 is a signed function which is positive in the liquid phase and negative in the gas phase. The solution of the re-initialization equation, re-distances the value of ϕ_0:

$$\begin{cases} \dfrac{\partial \phi}{\partial \acute{t}} - S(\phi_0)(|\nabla \phi| - 1) = 0 \\ \phi(x, 0) = \phi_0(x) \end{cases} \tag{3.24}$$

The solution convergence starts from the interface and moves toward two phases. The artificial time step is set to be $\Delta \acute{t} = 0.1\Delta x$, to avoid any large changes in the LS function. Since VOF is capable of mass conservation, α is used to get the size of the cut in any interface cell, which is advected. Due to the accuracy of the LS method in calculating the normal unit vector at the interface, ϕ is used to calculate surface curvature and volumetric surface tension force. In the region in which solid, liquid and air are in contact, the normal interface vector should be corrected to satisfy the dynamic contact angle condition. This is discussed in detail in the next section.

3.5 Solid-liquid interaction

3.5.1 TPCL motion on the solid surface

The behaviour and the shape of the stationary droplets on solid surfaces are mainly determined by surface tension. The shape of a stationary droplet on a solid surface is defined by the equilibrium contact angle (ECA), θ_E, and determined by the surface wettability[192]. ECA is directly a function of three surface tension terms: (i) liquid-gas interface(γ_{lg}), (ii) solid-liquid interface(γ_{sl}), and (iii) solid-gas interface(γ_{gs})[193]. Young's law is illustrated in Figure 3-3 and states that the net force on the TPCL is zero when the droplet is stationary on the surface:

$$\gamma_{lg}\, cos(\theta_E) = \gamma_{sg} - \gamma_{sl} \tag{3.25}$$

The behaviour of the droplet on any solid surface is classified as hydrophilic ($\theta_E < 90°$) or hydrophobic ($\theta_E > 90°$).

Realistically, even the cleanest surfaces are not entirely homogeneous and show chemical or geometric heterogeneities. This eventually leads to contact angle hysteresis (i.e., the difference between advancing and receding contact angles), under which static contact angles, θ_s, can be obtained in the spectrum between advancing, θ_a, and receding, θ_r, contact angles ($\theta_r < \theta_s < \theta_a$). This indicates that the contact angle is chosen at the molecular scale and behaves as a macroscopic interface boundary condition[192].

The circumstance is completely different when the TPCL moves on the substrate, and the system is no longer at equilibrium. The ECA and contact angle hysteresis (CAH) are the key factors in TPCL motion on solid surfaces. An adhesion force, F_{adh}, is generated by contact angle hysteresis in the TCPL region, which opposes the TPCL motion [38]. It is well known that this adhesion force is lower for a droplet with a higher ECA and lower CAH[194,195]. A schematic illustration of the contact angles definitions and the direction of the adhesion force is shown in Figure 3-4.

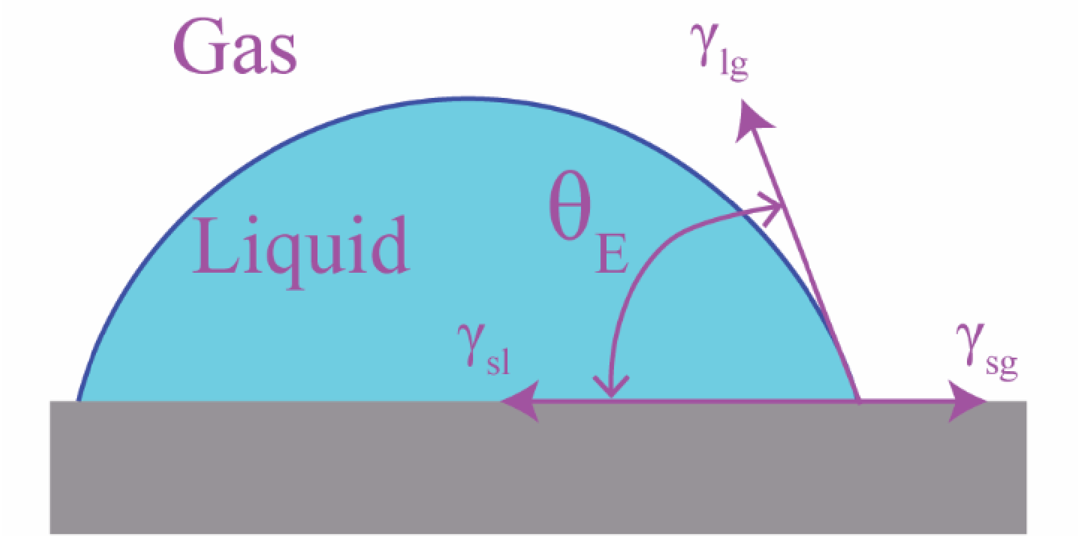

Figure 3-3: Three interfacial surface tension values, which together generate a zero net force on the TPCL, determine the equilibrium contact angle (θ_E) of a liquid droplet.

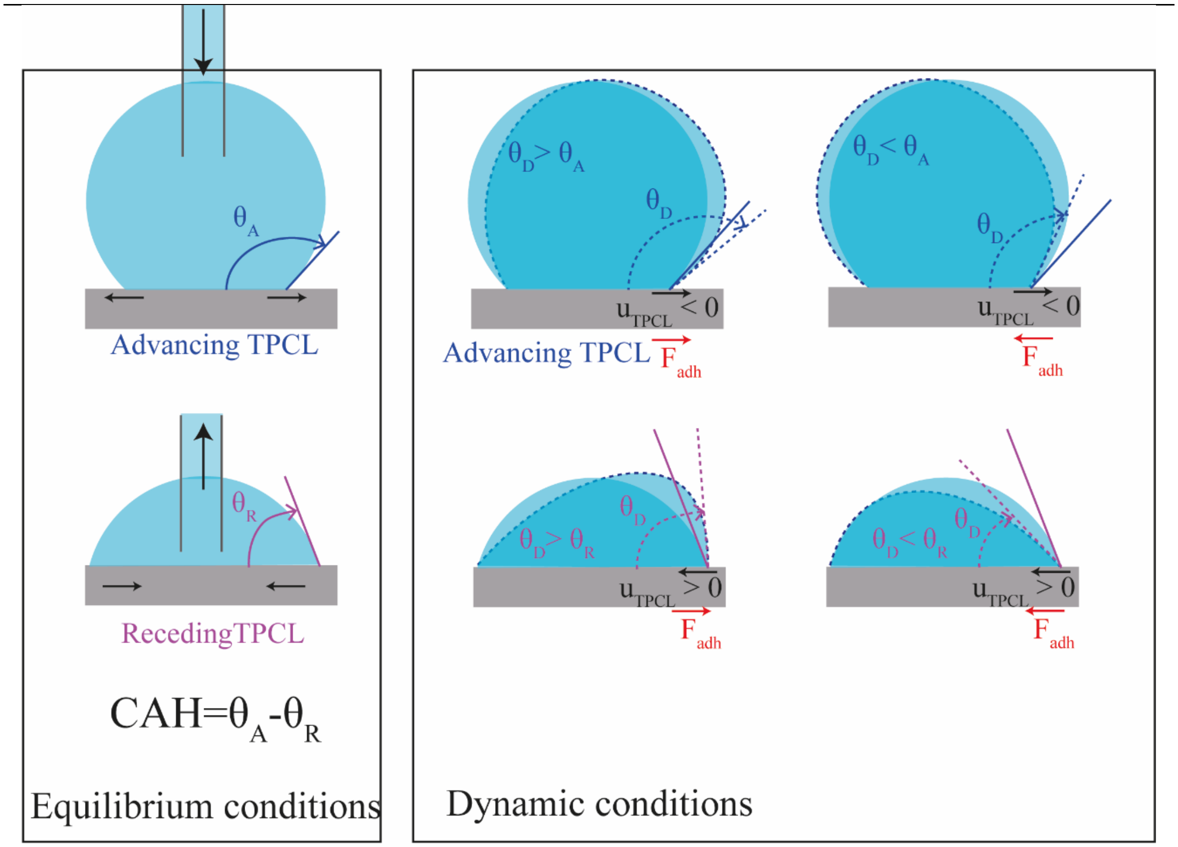

Figure 3-4: Definition of the contact angles and the direction of the resistance force at the TPCL: F_{adh} points to the left/right until θ_E is reached.

To have a high-fidelity model, the effect of this force should be considered in the modelling. In this dynamic contact angle method, instead of attempting to calculate the adhesion force at the TPCL region, a technique in which the contact angle is defined as a function of TPCL velocity and CAH is implemented. The calculated contact angle is used to change the curvature of the liquid-gas interface in the TPCL region (consequently the surface tension), which creates a local resistance against the TPCL motion in dynamic conditions. The developed DCA model is applied as a boundary condition to VOF and LS functions in the patches where a TPCL exists.

3.5.2 Contact angle treatment

The angle between the wall and normal interface vectors at the TPCL region, θ_0 is initially calculated by[196,197]:

$$cos(\theta_0) = \boldsymbol{n}_c.\boldsymbol{n}_{wall} \tag{3.26}$$

where $\boldsymbol{n}_c$ is calculated from the reconstruction algorithm and $\boldsymbol{n}_{wall}$ is the wall-normal vector. additionally, the normal interface vector at the TPCL region must be modified to the final normal vector, $\boldsymbol{n}_{final}$. At each moment, this final normal vector is equal to the dynamic contact angle, θ_d:

$$cos(\theta_d) = \boldsymbol{n}_{final}.\boldsymbol{n}_{wall} \tag{3.27}$$

Also, the plane in which the final normal vector lies must be defined by the normal interface vector, $\boldsymbol{n}_c$ and the wall-normal vector, $\boldsymbol{n}_{wall}$.

$$\boldsymbol{n}_{final} = a\boldsymbol{n}_c + b\boldsymbol{n}_{wall} \tag{3.28}$$

By merging Equations 3.26, 3.27, and 3.28, and solving the simultaneous set of equations for the values of a and b, the coefficients can be calculated as:

$$a = \frac{cos(\theta_d) - \ cos(\theta_0)\, cos(\theta_0 - \theta_d)}{1 - cos^2{}_{\theta_0}} \tag{3.29}$$

$$b = \frac{cos(\theta_0 - \theta_d) - \ cos(\theta_0)\, cos(\theta_d)}{1 - cos^2{}_{\theta_0}} \tag{3.30}$$

After calculation of a and b, the final normal vector, $\boldsymbol{n}_{final}$ is calculated and replaced with the initially calculated normal vector, $\boldsymbol{n}_c$ in all the domain cells in the TPCL area. The final normal vectors are used to calculate the curvature of the liquid-gas interface. Mathematically, the difference between the normal vectors generates a local surface tension force which considers the resistance force generated by the contact angle dynamics.

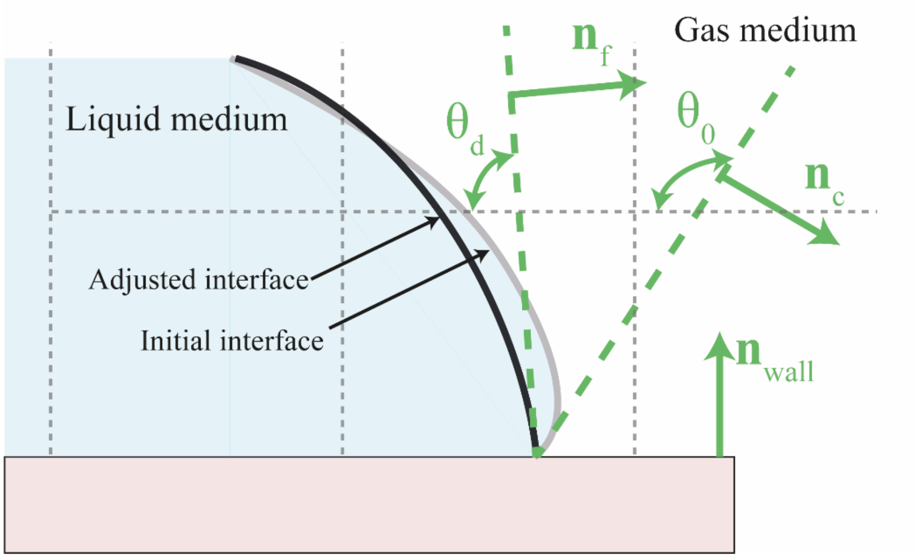

Figure 3-5: A Schematic view of the initial and adjusted liquid-gas interfaces and the dynamic contact angle.

The dynamic contact angle (DCA) must be calculated initially to calculate a and b,. The DCA is mostly derived in the literature as a function of the TPCL velocity. The velocity of the TPCL can be calculated as:

$$\boldsymbol{U}_{TPCL} = \boldsymbol{U}_{cell} - (\boldsymbol{U}_{cell}.\boldsymbol{n}_{wall}).\boldsymbol{n}_{wall} \tag{3.31}$$

where $\boldsymbol{U}_{cell}$ is the difference between the velocity of cell centre and velocity of cell face (the face which is in contact with the solid surface).

To know the direction of the TPCL, the direction of the interface parallel to the wall, $\boldsymbol{n}_w$, is calculated as:

$$\boldsymbol{n}_w = \boldsymbol{n}_c - (\boldsymbol{n}_c.\boldsymbol{n}_{wall}).\boldsymbol{n}_{wall} \tag{3.32}$$

The TPCL velocity along the solid surface can be calculated as:

$$u_{TPCL} = \boldsymbol{U}_{TPCL}.\frac{\boldsymbol{n}_w}{|\boldsymbol{n}_w|} \tag{3.33}$$

A negative value of u_{TPCL} means that TPCL is advancing, whereas a positive value of u_{TPCL} means that TPCL is receding. This is due to the direction of the $\boldsymbol{n}_c$ which is from the gas phase into the liquid phase (See Figure 3-5 for more details).

3.5.3 Dynamic contact angle calculation

When modelling moving contact lines, there are mainly two difficulties: definition of the DCA and the adjustment of the no-slip boundary condition to eliminate the contact line singularity. The DCA model is often chosen as a function of Capillary number Ca, the static contact angle θ_s and fitting parameter, k_i, which are used to fit the numerical results to the experiments[198].

$$\theta_d = f(Ca, \theta_s, k_i) \tag{3.34}$$

$$Ca = \frac{\mu . u_{TPCL}}{\gamma_{lg}} \tag{3.35}$$

One of the important approaches in modelling DCA is the Cox-Voinov model[199,200], which calculated the DCA from:

$$Ca = k(\ \theta_d - \theta_e)^3 \tag{3.36}$$

where k is a surface-related constant and is determined empirically[200]. Many empirical models for DCA have been developed based on Equation 3.36[198].

In this work, based on the DCA model proposed by the Afkhami et al.[201] a model is implemented to evaluate the DCA as a function of TPCL velocity:

$$cos\ (\theta_d) = cos(\theta_e) + C.Ca.ln\ (K/(\frac{\Delta x}{2})) \tag{3.37}$$

where $C = 8.45$ is an empirical fitting coefficient (See Appendix A), and $K = 0.2$ is a constant with a dimension of length, and Δx is the mesh size. The value of C is derived from the experimental data in chapter 5. Yokoi et al.[202] developed a model which is based on their finding that the DCA tends to increase, levelling off to a maximum limit eventually equal to Advancing contact angle (ACA) at high Ca numbers. Likewise, the DCA continues to decrease, reaching to receding contact angle (RCA). Based on the Yokoi method (and experimental observations), the DCA is limited by ACA and RCA:

$$\theta_d = \begin{cases} max[\theta_d, \theta_{adv}] & if \ \ u_{TPCL} < 0 \\ \theta_s & if \ \ u_{TPCL} = 0 \\ min[\theta_d, \theta_{rec}] & if \ \ u_{TPCL} > 0 \end{cases} \tag{3.38}$$

The current DCA boundary condition is developed base on the existing DynamicContactAngle boundary condition in OpenFOAM. The motion of the TPCL on a no-slip boundary causes a non-integrable stress singularity which can be calculated as $\tau_{xy} = \mu \frac{u_{TPCL}}{\Delta x}$. For the calculations using fine grids, this stress could hinder the motion of the TPCL[203]. It is suggested that applying the Navier-slip boundary condition near the three-phase contact line area, relaxes the local singularity and allows the contact line motion on the solid surface[201]. Thus, the Navier Slip boundary condition is implemented as:

$$\boldsymbol{u}|_{\boldsymbol{z=0}} - \boldsymbol{U_s} = \begin{Bmatrix} \varpi \dfrac{d\boldsymbol{u}}{dz}|_{z=0} & 0 < \alpha < 1 \\ 0 & \alpha = 0 \; or \; \alpha = 1 \end{Bmatrix} \tag{3.39}$$

At the solid boundary (z=0), where $\varpi = \Delta x/2$ is the slip length and $\boldsymbol{U_s}$ is the velocity of the solid surface[204].

3.6 Finite Volume discretization

A brief explanation of the discretisation procedures of OpenFOAM library, which is used in this modelling, is presented in this section. The governing equations should be discretized to achieve a numerical solution in CFD. The discretisation method implies how the partial and whole differential equations are translated into separate quantities and algebraic equations. It is then possible to resolve the discretized equations using linear solvers for the unknown variables. The solution domain is divided into a set of structured cells so that every two cells share one face. The normal vector of the face surface is illustrated in Figure 3-6.

All of the equations which are explained in this chapter are discretized following the finite volume technique. In OpenFOAM multiphase flow solvers, the modified pressure, p_{rgh} is used instead of static pressure, p. This modified pressure avoids the high differences across the liquid-gas interfaces.[205]. The relation between these two pressures is defined as:

$$p_{rgh} = p - \rho \boldsymbol{g}.\boldsymbol{x} \tag{3.40}$$

where $\boldsymbol{x}$ is the position vector. The integral form of the equations is solved in finite volume methods.

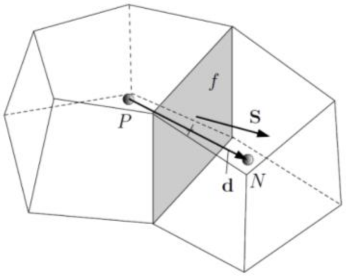

Figure 3-6: Solution domain discretization, from OpenCFD Ltd [205].

The integration is carried out over the mesh cells, but discretization usually depends on the surface integral to estimate diffusive and convective fluxes. The Gauss theorem is used to convert the terms, including spatial derivatives, into integrals over surfaces bounding each cell. The value of each cell centre should be interpolated at the face centres to perform spatial and temporal discretisation. The Linear Central Differencing scheme is the default scheme for the interpolation processes in this work unless a specific scheme is introduced precisely for a specific operation. The Gauss linear integration scheme is used to discretize the gradient terms. Like the gradient terms, convection term (e.g., $\boldsymbol{\nabla}.(\rho \boldsymbol{U} \otimes \boldsymbol{U})$) are discretized by the Gauss theorem. The implicit Euler scheme is used to discretize the time derivative terms. Although this scheme provides the first order of accuracy, it is entirely stable. In an effort to speed up the calculations, variable time step is used in this study through a user-defined function with a condition to keep the Courant number lower than 0.3.

The solution procedure of the CLSVOF method can be explained in the following steps

1. Scalar and vector fields ($\boldsymbol{U}, p_{rgh}, \rho, \mu, H, \delta, \alpha$) definition.
2. Numerical fields initialization, LS function reinitialization, then H and δ functions initial value calculation.
3. Calculation of the SAW force source term based on the SAW device properties and liquid phase location in the domain.

3.1. Evaluation of the Solid-liquid interface area and the mass centre of this area.

3.2. Calculation of TPCL area and the body force (depending on the IDT type).

4. Time loop start, interface correction and volume fraction correction at the liquid-gas interface.
5. Solution of the volume fraction advection equation, correction of VOF field (if required), and initialize LS field.
6. Solve the reinitialization equation, so that $S(\phi_0)$ is obtained. Then interface at the boundaries is corrected, and new values of H and δ functions and surface curvature are calculated.
7. Physical properties of the fluid and the fluxes are updated.
8. Navier-Stokes equation solution by PIMPLE algorithm to calculate velocity and pressure fields.
9. Go to the next time step (starting from step 4).

The PIMPLE algorithm, which is used to solve the momentum and pressure equations for time-dependent incompressible laminar or turbulent flows with large time steps, is the merged form of PISO-SIMPLE predictor-corrector solver (from OpenFOAM library). PISO (Pressure Implicit Split Operator) and SIMPLE (Semi Implicit Method for Pressure Linked Equations) are transient and steady-state solvers for incompressible flows. The PIMPLE algorithm is based on the iteration procedure for solving the Navier-Stokes equation. In this research, all the simulations are carried out on structured cells to decrease the computational costs and time. However, the developed method is capable of handling unstructured mesh.

3.7 Summary

In this chapter, the developed mathematical model to capture the liquid-gas interface is explained. In order to do so, An interface capturing method was developed based on the CLSVOF method to simulate the deformation of the droplet subjected to SAWs. A code was written to calculate the effect of SAW generated by various IDTs as a body force to consider the SAW effect. Furthermore, to accurately model the TPCL movement, a dynamic contact angle model is implemented. The dynamic contact angle model developed after testing a few models which were already in the literature and fitting the experimental data against simulation ones. The discretization methods are also explained in this chapter. In the next chapter, the experimental methods will be explained.

Chapter 4. Experimental methodology

This chapter explains the methods used to fabricate and characterise the SAW devices and the experimental procedures. First, the methods used to fabricate and characterize the various SAW devices used in this study are explained, and then the details of the carried out experiments are explained.

4.1 ZnO thin film deposition and characterisation

The first step in the fabrication of a thin-film SAW device is the deposition of a piezoelectric layer (ZnO in this study) on a substrate. Thus, using the physical vapour deposition (PVD) process, the ZnO thin film was deposited on different types of substrates such as silicon wafers and aluminium plates. A schematic illustration of ZnO deposition with a direct current magnetron sputter system is presented in Figure 4-1. As shown in Figure 4-2(a), a direct current magnetron sputter system (Nordiko Ltd.) was used to deposit a layer of ZnO piezoelectric film on the substrates using a pure zinc target (99.99%). 10×10 cm Aluminium plates with thicknesses of 0.5 and 1 mm and 3 inch single-sided polished monocrystalline silicon wafers with a thickness of 1 mm were used as the ZnO substrate deposition.

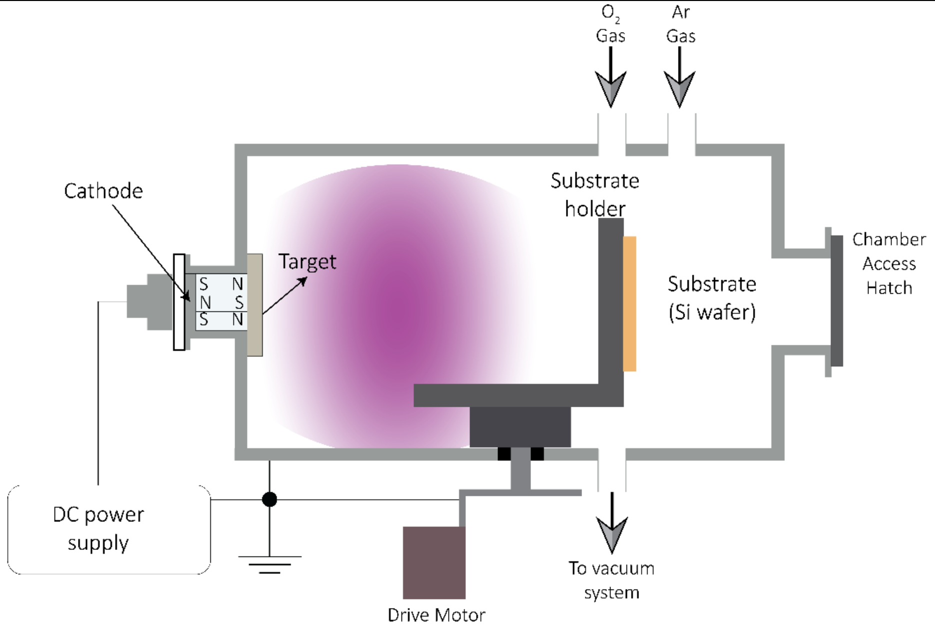

Figure 4-1: (a) A schematic illustration of a direct current magnetron sputter system.

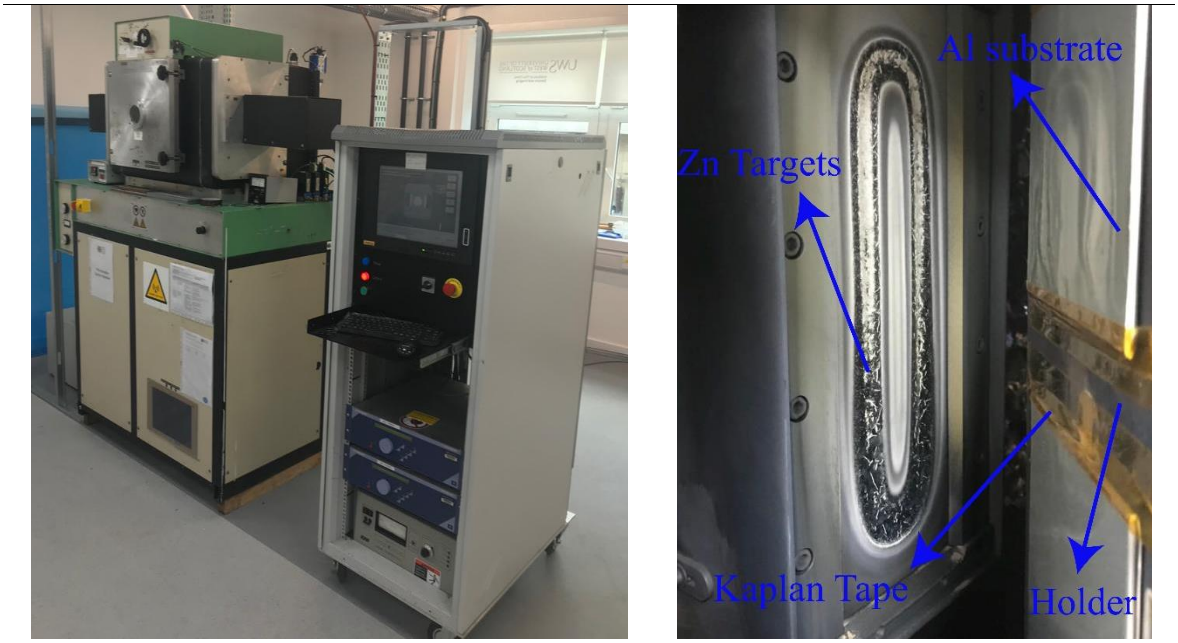

(a) (b)

Figure 4-2: (a) Nordiko sputtering machine. (b) Aluminium substrates fixed on the holders by Kaplan tape after eight hours of ZnO deposition.

Before the deposition, the substrate surfaces were cleaned with acetone and then by ethanol, and then the substrates were rinsed with deionised (DI) water and dried with nitrogen. These substrates were fixed on the holders with Kaplan tapes after a surface cleaning process (see Figure 4-2(b)). Six holders with mounted substrates were fixed with screws on a rotational hexagonal cylinder which was installed in the centre of the sputtering machine chamber. The minimum distance of the holders from the targets was 20.0 cm, and the holder was rotating at a speed of 4.0 rpm.

The vacuum pump was turned on, and during the deposition process, a chamber pressure of ~3.2 mTorr was maintained. The deposition parameters are as follows: a DC power of 400 *W* and an Ar/O_2 mass flow ratio of 10/15 SCCM (standard cubic centimetre per minute) without any external substrate heating. These parameters were selected after a few test runs and checking the film quality and thickness. The holders were not intentionally heated during the deposition. The achieved deposition rate was ~0.35 µm/hour and the total deposition time was 16 hours.

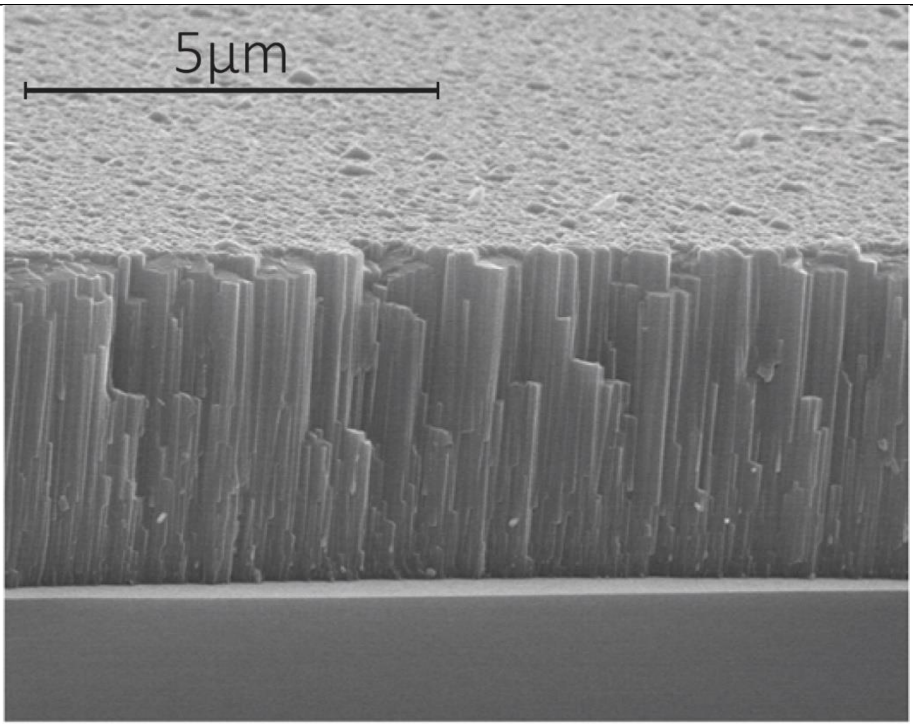

Figure 4-3: SEM image of the ZnO/Si SAW device surface.

A scanning electron microscope (SEM) was used for surface morphology and cross-section characterising of the ZnO thin film. An SEM image of the film/substrate is illustrated in Figure 4-3.

4.2 SAW device fabrication and frequency response characterisation

After thin-film deposition on substrates, interdigital transducers (IDTs) must be patterned on the SAW device surface. A characteristic SAW device consists of (minimum) one set of IDTs fabricated on the piezoelectric substrate surface. IDTs apply the electric field to the solid surface, and electrical energy is converted to mechanical stress and thus, SAW with displacement amplitude (in the order of 10 Å) is generated. The IDT design determines the characteristics of the SAW. By changing the profile, the number of fingers, spacing and aperture (overlap space) of the IDTs, the frequency, wave propagation path and mode of the SAW can be changed. For all the SAW devices fabricated in this research, straight IDTs were designed and patterned on the surface (see Figure 4-4).

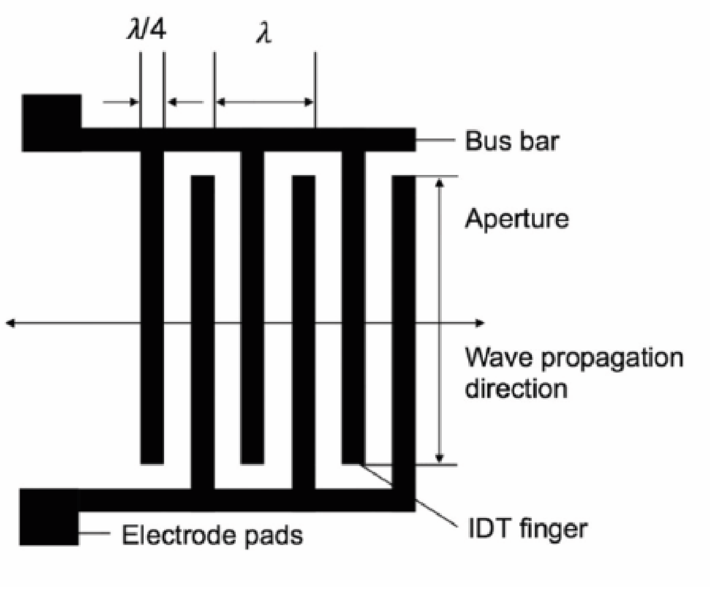

Figure 4-4: A schematic sketch of straight IDTs.

As shown in Figure 4-5, traditional photolithography and lift-off processes were used to pattern straight IDTs onto the ZnO film. After the surface cleaning process, A layer positive photoresist S1813 (Rohm and Haas) was coated onto the surface by a spin coating method (Laurell 650M spin coater). Spin coating was performed in two steps: first 10 seconds or rotation with 10 rpm, and second 60 seconds by a steady rotational velocity raise up to 3,700 rpm. To softly bake the samples, they were located on a hot plate with a temperature of 95 ^{o}C for 10 minutes. An EVG620 mask aligner was used to expose a dose of 90 mJ to the samples, and then they were immersed in the MF319 developer solution for 1 minute to develop the S1813 photoresist. The patterned Cr/Au IDTs had thicknesses of 20/100 nm and consisted of 30 pairs of fingers, with an aperture of 5 mm and different wavelengths of 64 to 300 µm.

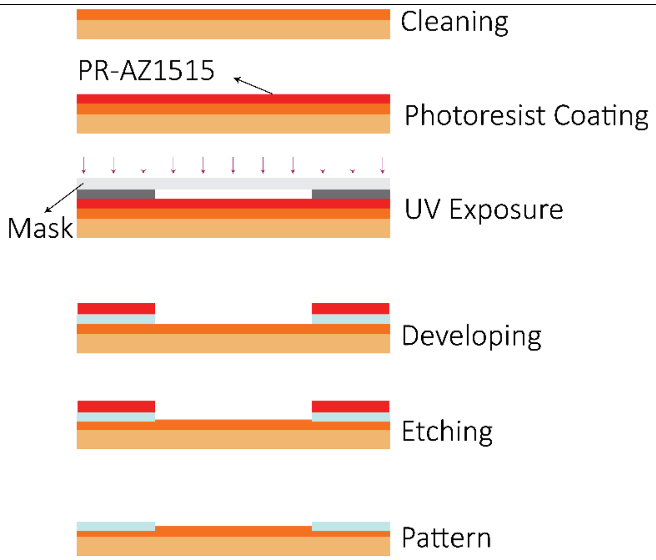

Figure 4-5: IDTs patterning process on the ZnO film using lithography and lift-off processes

The resonant frequency of each SAW device was measured using an RF network analyzer (HP8752A RF network analyzer). Table 4-1 list all the fabricated ZnO/Si and ZnO/Al SAW devices' measured resonant frequencies.

Constructive interference occurs while the frequency of the RF signal is set equal to v_s/λ_{SAW} (where λ_{SAW} is the wavelength, which is equal to the distance between two IDT fingers). A robust acoustic wave will be generated, travelling through the surface of the piezoelectric material[7]. The particles' motion in the solid surface is in two directions, A movement normal to the surface and a surface-tangential component of the motion with respect to the direction of the wave propagation (see Figure 4-6).

Table 4-1: Measured frequencies and calculated velocities of ZnO/Si and ZnO/Al devices

Wavelength (µm)	ZnO/Si		ZnO/Al	
	Frequency (MHz)	v_s (m/s)	Frequency (MHz)	v_s (m/s)
300	14.36	4310	9.00	2701
200	21.61	4322	13.74	2749
64	67.20	4301	42.87	2744
36	116.80	4205	75.72	2726
20	210.20	4204	136.55	2731
16	271.00	4336	169.50	2712

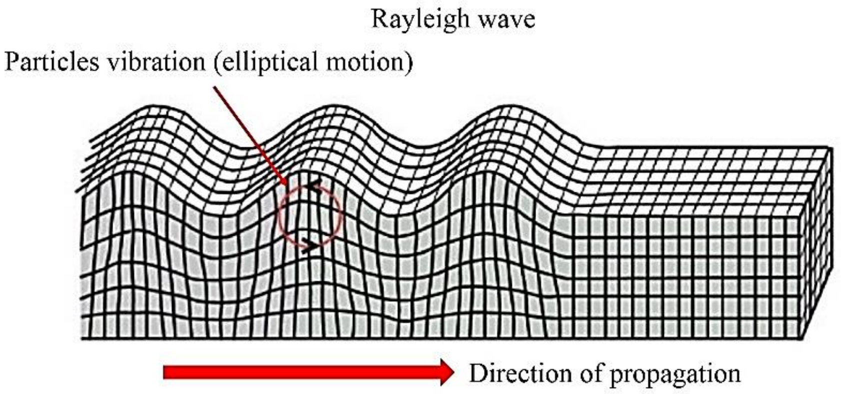

Figure 4-6: A schematic illustration of SAW propagation[4].

4.3 Stationary droplet actuation experimental setup

A schematic view of the experimental setup for jetting and pumping purposes is illustrated in Figure 4-6. To form a hydrophobic surface, the ZnO/Si SAW device's surface was coated with 1% CYTOP solution (Asahi Glass Co.) by drop coating and a post bake for 20 min at 150 °C. The hydrophobicity of the surface was characterised by measuring the static, advancing, and retracting contact angles during volume addition and withdrawal to a sessile droplet on a droplet shape analyser (Kruss DSA30S). Table 4-2 summarizes the ZnO/Si and ZnO/Al SAW devices' measured angles with and without CYTOP surface treatment.

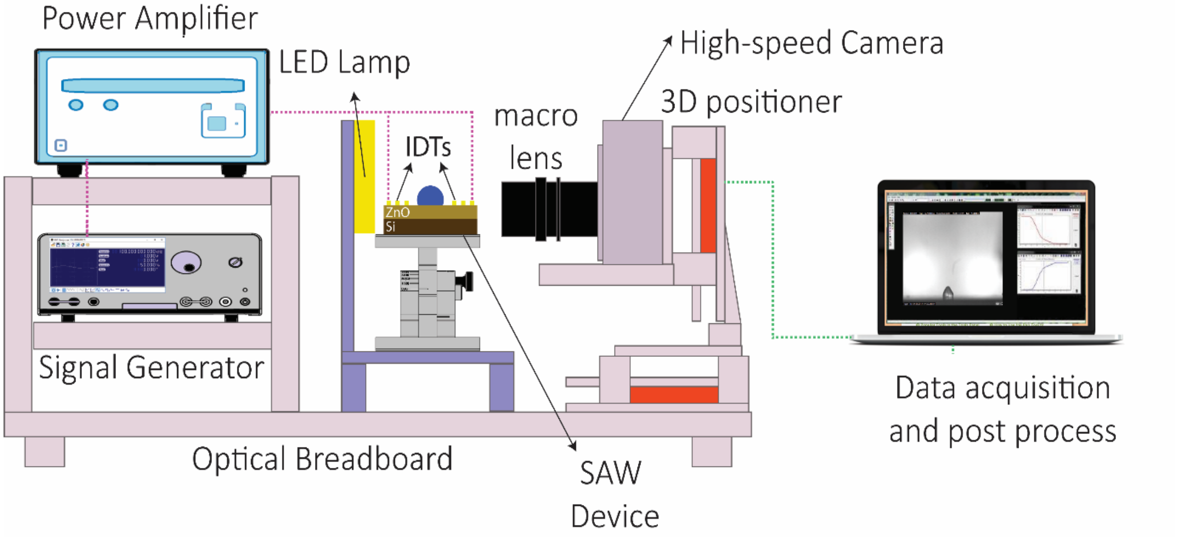

Figure 4-7: A schematic view of the experimental setup for droplet actuation by SAWs

Table 4-2: ECA, ACA, RCA and CAH for ZnO/Si SAW and ZnO/Al devices with and without surface treatment. In this table, ± sign shows the standard error.

SAW Device	ECA	ACA	RCA	CAH
ZnO/Si	86º±3º	90º±4º	27º±4º	63º±8º
CYTOP/ZnO/Si	122º±2º	123º±2º	95º±4º	28º±6º
ZnO/Al	98º±10º	111º±1º	49º±1º	63º±2º
CYTOP/ZnO/Al	114º±2º	114º±1º	105º±1º	9º±2º

RF signals with different powers (from -5 db to 12 db) were triggered by a signal generator (Marconi Instruments 2024) and amplified with an RF amplifier (Amplifier research, 75A250) before being applied to the IDTs to excite SAWs. The amplifier output power was measured using an RF power meter (RACAL Equipment, 9104). Droplet streaming and jetting experiments were carried out at an environment temperature of 20 ± 0.5 °C and 50 ± 5% relative humidity. At this temperature, the density, kinematic viscosity, and (water-air) surface tension of DI water are 998.2 kg.m^{-3}, 1.004×10^{-6} m^{2}s$^{-1,}$ and 0.072 N.m^{-1}, respectively. Droplets of deionised (DI) water with various volumes were located at the SAW device centre using a micropipette. The droplet deformation was captured using a high-speed camera (HotShot 1280CC) with a macro lens (120 mm-Nikon) at 2000-5000 frame per second (fps). A Matlab image processing tool was used to analyse the results. Each experiment was repeated three times to confirm the repeatability of the experiments. A schematic view of the experimental setup is illustrated in Figure 4-8.

4.4 Droplet impact experimental setup

Droplets of deionized water with an initial diameter of D_0= 1.9×10^{-3} m was generated from hypodermic needles (BD Microlance, inner diameter D_n=1.5×10^{-3} m) mounted on a 2D positioner using a syringe pump (Cellix, World Precision Instruments, UK). The calculation of the droplet volume, V_{Dr} was based on the numerical model proposed by Aminzadeh et al.[206]:

$$V_{Dr} = \frac{\gamma_{lg} \pi D_n}{\rho g} \tag{4.1}$$

The droplets were released from differently selected heights, H, with an initial velocity of zero, to reach the desired velocities before their impacts on the inclined solid surface. The inclination angle of the device surface was set to be 0°, 15°, 30°, 45°, and 60°.

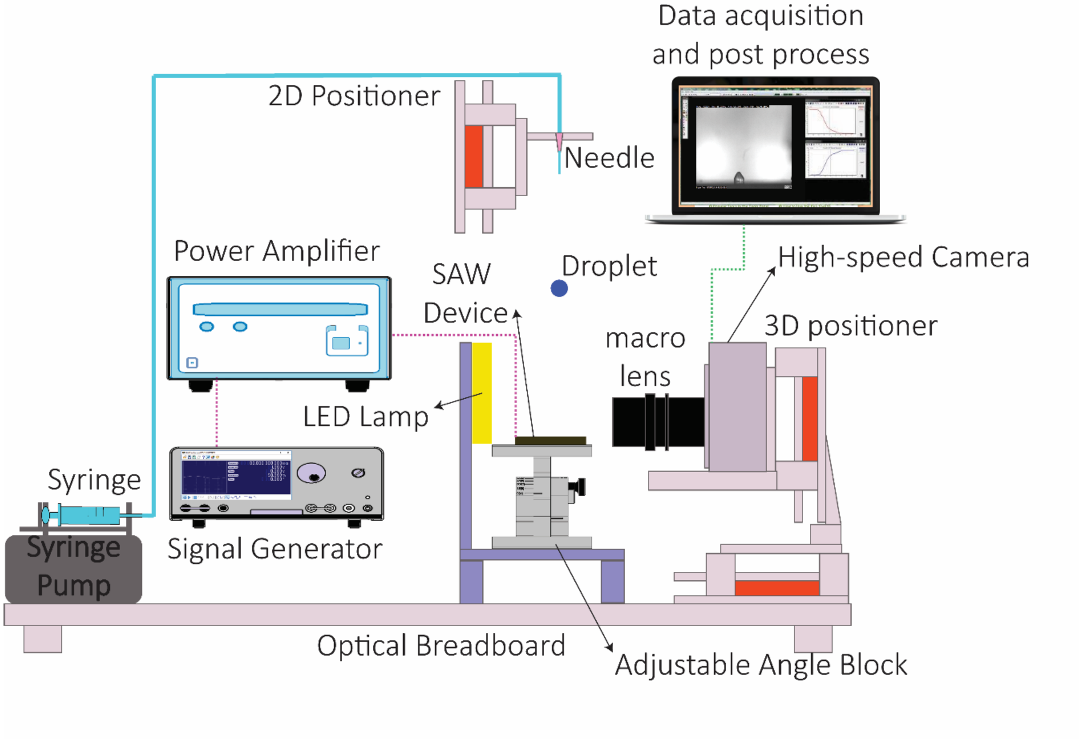

Figure 4-8: A schematic view of the experimental setup for droplet impact control by SAWs

The impact and rebouncing sequences were captured from a side view using a high-speed camera (HotShot 1280CC) with a macro lens (120 mm-Nikon) at 5000 frames per second (fps). MATLAB image processing tool was used to calculate the droplet impact velocity from two consecutive images just before its impact onto the device surface. To fully understand how the SAW can modify the droplet impact on inclined surfaces, a set of systematic experiments were performed to investigate the effects of inclination angle, impact velocity, and SAW direction and power, at a lab temperature of 21 ± 0.5 °C and 50 ± 5% relative humidity. Each test was repeated four times to confirm the repeatability of the experiments. A schematic illustration of the experimental setup is presented in Figure 4-8.

The diameter of the dispensing needle ($D_n=3\times10^{-4}$ m) was captured and measured, and the data were used to calibrate the images. A conversion factor of 40 µm/pixel was obtained. The optical imaging system resolution for observing droplets in our system was determined to be 120 µm based on edge detection methods corresponding to three pixels. On the other hand, the repeatability of the droplet diameter and impact velocity should be examined.

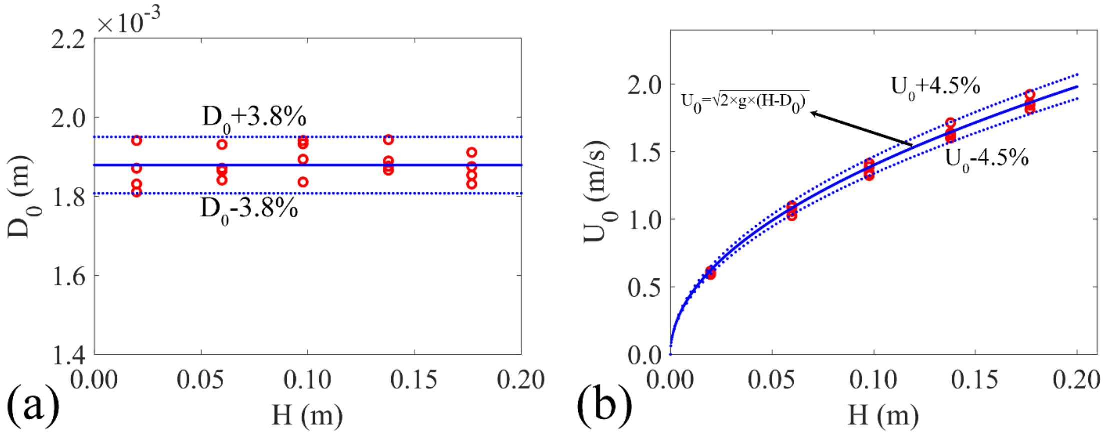

Figure 4-9: Uncertainty analysis for (a) Droplet initial diameter D_o; and (b) droplet impact velocity U_o for different experimental cases as a function of droplet release height, h.

Figure 4-9(a) shows that the uncertainty of the droplet diameter was ±3.8%. In principle, the impact velocity can be calculated by the equation, $U_0=\sqrt{2g(h-D_0)}$. Figure 4-9(b) shows that the uncertainty of the impact velocity was ±4.5%. This method is used to define the uncertainty because the number of the experimnts are limited and calculation of the standard deviation will not give reasonable ranges for error. The value of the relative error of the *We* number was calculated by the equation $\Delta We/We=\Delta D_0/D_0+2\Delta U_0/U_0$ to be 12.8%[207]. The angle deviation of the SAW device holder was ±0.3°.

4.5 Summary

In this chapter, the SAW device fabrication methodology was explained. Furthermore, the experimental setup and procedure for droplet actuation and impact experiments were described. Finally, an analysis of the experimental uncertainties was presented. Experimental observations and analysis showed that most of the parameters in the droplet-based experiments, such as internal pressure and velocity fields, are not easily measured by experimental results, and CFD simulations can give a better insight into the droplet dynamics. In the next chapter, the developed numerical model will be used to simulate droplet actuation by SAWs.

Chapter 5. Numerical investigation of droplets actuation by SAWs

In this chapter, first, the simulation setups and input parameters are explained. Then, two different droplet actuation scenarios are simulated with the developed method for model validation purpose. The simulation and experimental results are quantitatively and qualitatively compared to examine the capability of the CLSVOF method to reproduce the pumping and jetting phenomena by SAWs. Numerical and experimental results investigate droplet translation by SAWs. Initially, the developed model is used to explain the physics of pumping and then the effect of different variables such as SAW frequency and power and droplet volume on pumping behaviour is investigated.

Additionally, the developed model is used to investigate the droplet vertical jetting by SAWs. Moreover, the physics of droplet jetting and internal streaming by analysing the liquid medium's energy terms is investigated in this chapter. Finally, the numerical analysis is used to optimize the IDT positions to enhance optimum mixing, separation, and vertical jetting applications.

5.1 General simulation parameters and boundary conditions

In this section, all the simulation parameters which are similar for all the simulations are explained. Although the developed method can handle unstructured mesh, all the domains in this study are designed to lower the computational time and cost. Thus, the computational domain for all the simulations in this study is a rectangular box with fully Cartesian mesh. However, depending on the droplet size and microfluidic application, the dimensions of the boxes are determined for each case separately. To eliminate the boundary induced disturbances, a relatively large domain is chosen for all the cases.

Since all the experiments in this thesis are carried out for water droplet in atmospheric air at 20 ^{o}C and 20% humidity, the liquid properties are kept constant for all the simulations and presented in Table 5-1.

Table 5-1: Air and water properties

Properties	water	Air
Density	999.13 Kg.m^{-3}	1.1839 Kg.m^{-3}
Kinematic viscosity	8.917×10^{-7} m^2.s	15.52×10^{-6} m^2.s
Air-water Surface tension coefficient	0.0707106 Kg.s^{-2}	

The initial radius of the droplet is calculated as a function of droplet volume and ECA by:

$$R_0 = \sqrt[3]{\frac{-3V_{Dr}}{\pi(1-cos\theta_E)(cos^2\theta_E + cos\,\theta_E - 2)}} \tag{5.1}$$

where, θ_E is the equilibrium contact angle of the droplet on the surface. Interface thickness, ϵ is always equal to 1.5Δx and coupling parameter, Γ, is 0.75Δx in all the simulations.

The velocity boundary condition for all the solid surfaces is the Navier slip boundary condition. On these surfaces, the developed dynamic contact angle model is applied to both VOF and LS functions (See chapter 3 for definition) fields. The pressure boundary condition for such planes is fixedFluxPressure. This boundary condition (which is almost identical to zero gradient boundary condition) is generally used in OpenFOAM for pressure, where forces such as surface tension and gravity are added to the Navier-Stokes equations. The boundary condition adjusts the gradient accordingly.

For all other planes (i.e., sides and top), the velocity boundary condition is pressureInletOutletVelocity. This boundary condition assigns a zero gradient for the flow exiting the domain and a velocity field based on the flux in the patch-normal direction for the domain entering flow. On these patches (i.e., sides and top), the boundary condition for α and ϕ fields is zeroGradient. This boundary condition uses the value of the nearest cell to extrapolate the value of the fields to the patch. This means that the value on the patch is calculated in a way that its gradient in the direction perpendicular to the patch is equal to zero. The pressure boundary condition for all the patches (nonsolid surfaces) is totalPressure with total pressure, p, of zero. This boundary condition sets the patched pressure by the following equation:

$$\mathrm{p_p} = p - \frac{1}{2}(U_x^2 + U_Y^2 + U_Z^2) \tag{5.2}$$

The time of the simulations are varied for each case; however, to reduce the simulation time, adjustTimeStep function is used to vary the time step in a way that the Courant number ($\frac{\Delta t\sqrt{U_x^2+U_Y^2+U_Z^2}}{\Delta x}$) would not exceed 0.3. All the simulations are carried out in parallel. A Simple geometric decomposition method (from OpenFOAM standard library) is chosen to split the domain into pieces by direction (e.g., two pieces in the X-direction, one in Y). The number of subdomains is decided so that the number of cells in each domain would not exceed 10000 cells. All the calculations are performed on Dual Intel Xeon E5-2680 v4 14 core 2.4 GHz CPUs.

5.2 Droplet pumping

As discussed in chapter 2, droplet pumping by SAWs has not been numerically investigated. In this section, using the developed CLSVOF method, droplet pumping is investigated for the first time, and the key parameters affecting the pumping behaviour is analysed. Furthermore, droplet jetting behaviour at higher applied SAW power is simulated by the developed code. This results of this section are published as a research paper in Sensors and Actuators, A: Physical journal.

5.2.1 Model validation

Initially, a spherical droplet with a volume of 1 µl (droplet diameter on the surface is 1.37 mm) and equilibrium contact angle (ECA) of $\theta_E = 110^o$ is positioned on the left end of the bottom wall in the computational domain. In all the simulations, SAW is propagating from left to right. As simulation starts (t=0), SAW is propagated from the left edge of the computational domain in the X-direction. The XZ middle plane of the CFD mesh domain, droplet initial condition, and important boundary conditions are illustrated in Figure 5-1(a). The dimensions of the computational domain are selected after a series of test simulations for droplet moving area. Details of the input parameters are summarized in Table 5-2. The parameters used in the simulations of droplet pumping are fora ZnO/Si SAW device with a resonant frequency of 67.20 MHz and a Rayleigh angle of 19.23^o. The amplitude of the applied SAW is 400 Å.

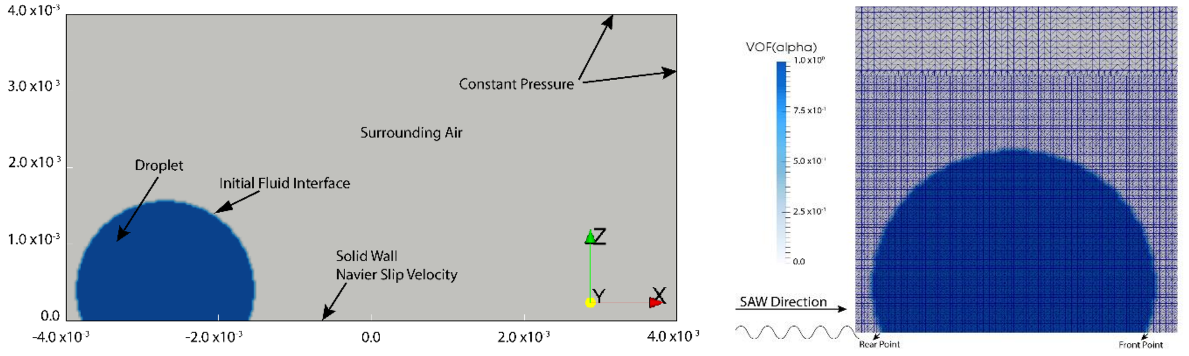

(a) (b)

Figure 5-1: Numerical setup (a) An isentropic view of simulation geometry with the droplet initial position. In all the simulations, the wave direction is from left to right, (b) A cross-section view of initial droplet condition and mesh refinement strategy. Rear point is defined as the point closer to the SAW device IDTs and vice versa.

Three mesh refinement strategies are defined to perform a grid independency test. In each mesh refinement step, each cell is divided to eight equal cells. To obtain a domain with different cell sizes, the cells in the area in which it is expected the liquid medium would move is refined one, two and three times along the Z-direction. A summary of all three computational domains is summarized in table 5-3. Note that for Δx larger than 6.75×10^{-5} m, convergence is not obtained.

To analyse the results, the average droplet velocity during the simulation is compared to experimental results. This parameter is chosen since measurement of droplet velocity from experimental results is possible with image processing methods. A comparison between these results shows that with 1 mesh refinement, the difference between the experimental and simulation results is high. By increasing the number of the mesh refinements along the Z-direction (i.e., smaller cell size), the results become closer to the experimental results. It is concluded from Table 5-3 that the droplet transportation velocity for domains with two and three mesh refinement steps has insignificant differences. Thus, to reduce the computational costs and time, all the computations for droplet pumping applications are performed in a domain with a droplet diameter to a minimum cell size ratio that is kept constant at ~60.

Table 5-2: Simulation parameter for droplet pumping by ZnO/Si SAW device

Input parameters	Value
Equilibrium contact angle	110°
Wave number[140]	-1813 m^{-1}
Attenuation coefficient	2.686

After mesh independency tests, the experimental data are compared with the simulation results in details to validate the CLSVOF solver. The computational domain is a rectangular box with a dimension of $8.0 \times 2.8 \times 4.0\ (mm)$ consisting of 3,476,480 hexahedral cells. Simulation has been performed for a droplet of water with a volume of 5 µl and an initial radius of 1.17 mm. The SAW with a frequency of 64.49MHz is applied to the liquid medium from the left side. A qualitative comparison between computational and experimental results of droplet transportation on a ZnO/Si SAW device is presented in Figure 5-2. A very close agreement is obtained between the computational and experimental results, which clearly shows that the CLSVOF method can be used to simulate the droplet deformation and transportation by the SAW.

Based on the simulation results, a comparison between the velocity of the front and rear points of the droplet (see Figure 5-1 for definition) is presented in Figure 5-3(a-b). The reasonably good agreement between the experimental and simulation results confirms that the numerical model can be used to simulate the droplet actuation by SAW. The difference between CFD and experiments between 0.018s and 0.032s is mainly because of the experimental setup. Since the surface treatment is not ideal at some positions the vaues of contact angles on the surface mihght change which leads to sudden movements of the TPCL.Since the TPCL motion is highly dependent on the dynamic contact angle model, the comparison between experimental and simulation results also validate the implementation of DCA boundary conditions.

Table 5-3: A comparison between the droplet transportation velocities for three different grid resolution strategies

Number of refine-ments	Δx ($m \times 10^{-5}$)	Number of cells in the domain	Cell numbers across the drop diameter	Simulation time (min)	Average droplet velocity (m/s)	Difference from experimental value
1	3.425	350446	40	~62	0.1552	+12.46%
2	2.30	115230	60	~240	0.1419	-1.44%
3	1.72	2767050	80	~1892	0.1418	-1.15%

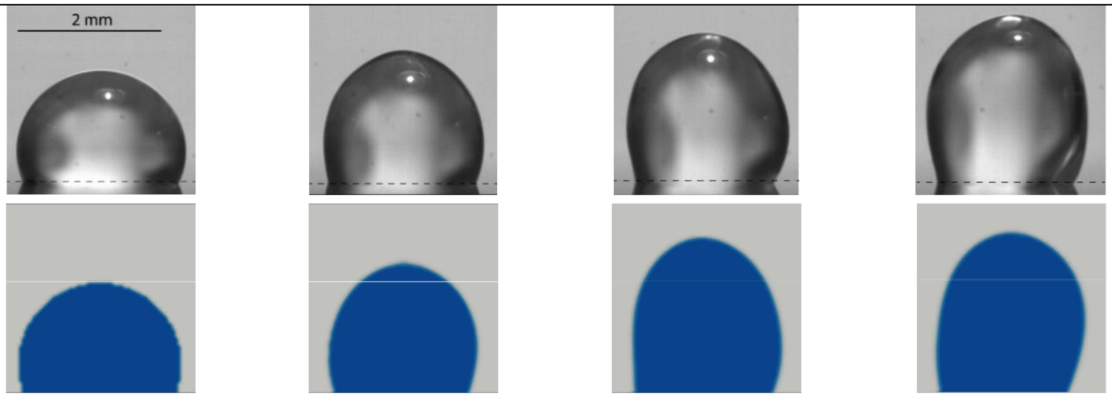

Time = 0 ms 12 ms 25 ms 37 ms

Figure 5-2: A comparison between experimental and simulation results of droplet shape variation.

5.2.2 Mechanisms of droplet pumping

As the precision of the CLSVOF method and contact angle model is confirmed, the mechanism of large deformations of the droplet and transportation are now investigated in this section using CFD results of the same case. When the SAWs hit the droplet medium on the solid surface, the SAW force is at its maximum value at the rear point (interact point) and decays exponentially along X and Z-directions. There are three key parameters in droplet behaviour during its pumping: (i) the SAW force which generates momentum inside the fluid, (ii) the liquid viscosity which dissipates the energy transferred by SAW into the fluid medium, and (iii) the interaction between the solid and liquid surfaces.

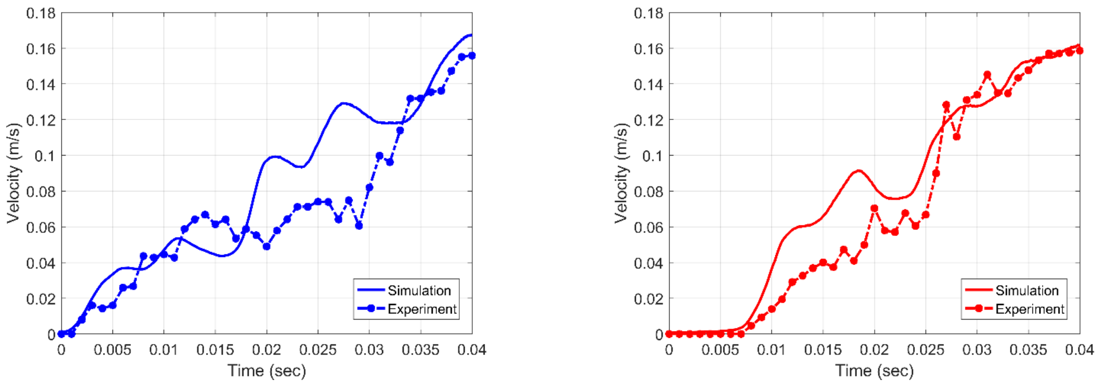

(a) (b)

Figure 5-3: A comparison between experimental and simulation results for droplet transportation velocity, (a) rear point (b) front point.

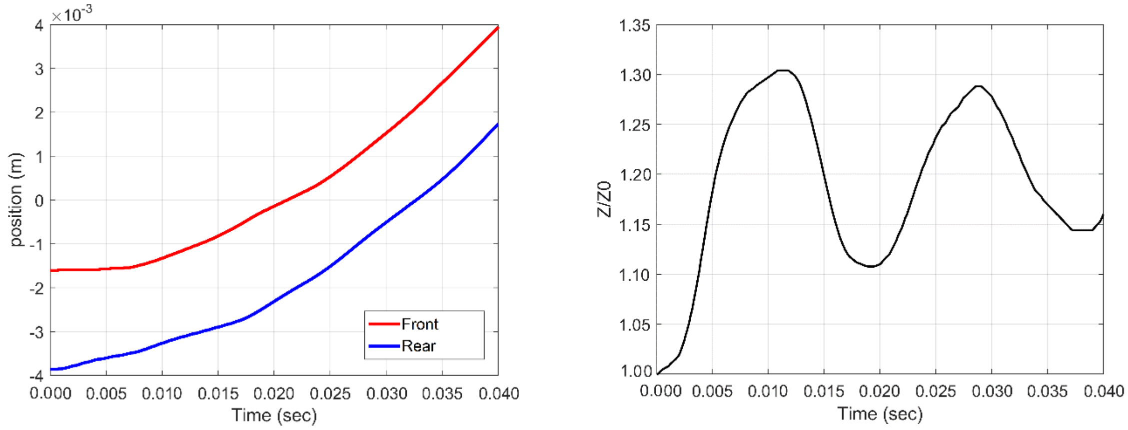

(a) (b)

Figure 5-4: Numerical simulation results of droplet transportation (c) droplet front and rear point position during the simulation. (b) Droplet tip position while pumping.

Before applying the SAW force, the TPCL is a circle. As shown in Figure 5-4(a), by applying the force for ~4.3 ms, the rear side of the TPCL shrinks toward the centre of the circle while the front side is motionless. The initial droplet deformation changes the contact angle. Meanwhile, the curvature at the droplet interface increases slightly. Equation 3.12 indicates that surface tension is proportional to the curvature of the droplet interface. Thus, the surface tension at the interface of the deformed droplet increases. During this time, the applied SAW force overcomes liquid inertia. After 4.3 ms, due to the momentum increase inside the droplet, the front side of the TPCL starts to move.

Consequently, the droplet tip is raised, and the solid and liquid contact area is decreased. After 12 ms, when the ratio of droplet tip height to its initial value (Z/Z_0) is equal to ~1.3 (see Figure 5-4(b)), the droplet tip starts to descend. The velocities of the rear and front points are also decreased due to the following two reasons (see Figure 5-3). Firstly, the surface curvature and surface tension are increased, which cancels the raise of the vertical momentum of the SAW force. Secondly, the lower contact area between the solid and the liquid reduces SAW energy transfer from the solid surface to the liquid medium. As soon as the ratio of Z/Z_0 reaches ~1.1, SAW energy transferred to the liquid medium is large enough to push the droplet tip upward again.

The total velocity of each cell centre in the liquid medium during the droplet transportation can be described as the sum of two velocities: (i) internal streaming velocity and (ii) translation velocity along the solid surface. Snapshots of the middle plane of the droplet overlaid by total velocity vectors are illustrated in Figure 5-5(a) to explain the air and liquid streaming patterns during the first 6 ms. As shown in Figure 5-5(a), during the initial 29 ms of droplet pumping, the slopes of droplet velocity in the two sides of the TPCL are not similar. These different velocity slopes from both sides create a wobbling movement. After this time, the velocities of two sides of the droplet tend to have the same trend, and the wobbling of the droplet starts to disappear. The droplet linear velocity (i.e., droplet pumping velocity in X-direction) is subtracted from the x component of velocity vectors to show the internal streaming patterns inside the droplet. Temporal evolutions of all the vectors inside the fluid medium are shown in Figure 5-5(b). Initially, the droplet is wobbling, and two annular vortexes can be observed inside the droplet. The lower vortex creates a rolling movement of the droplet, while the higher vortex creates a twin annular flow, which is the main reason for droplet tip wobbling. The higher vortex disappears after 26 ms, and the centre of the lower vortex moves toward the front point.

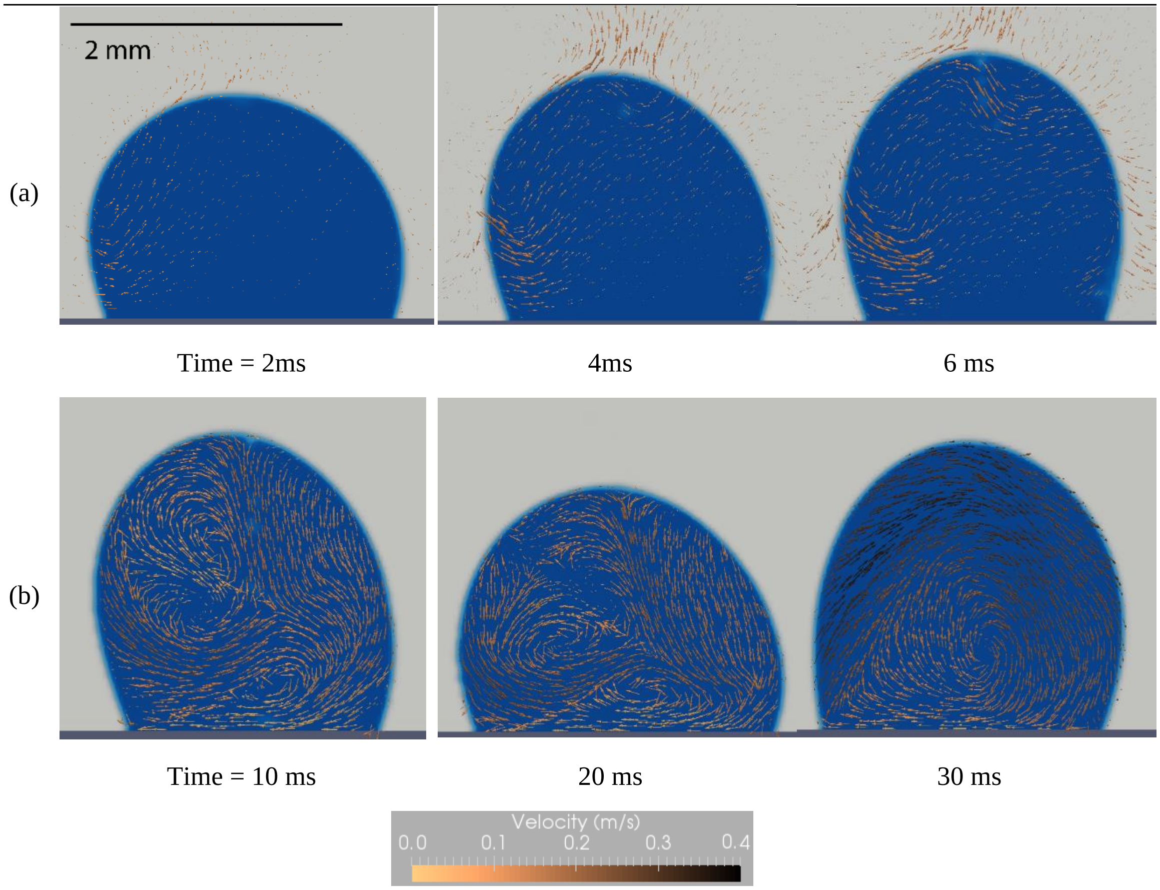

Figure 5-5: (a) Snapshots of droplet midplane overlaid by velocity vectors during the start of the droplet pumping. (b) Internal streaming development while pumping.

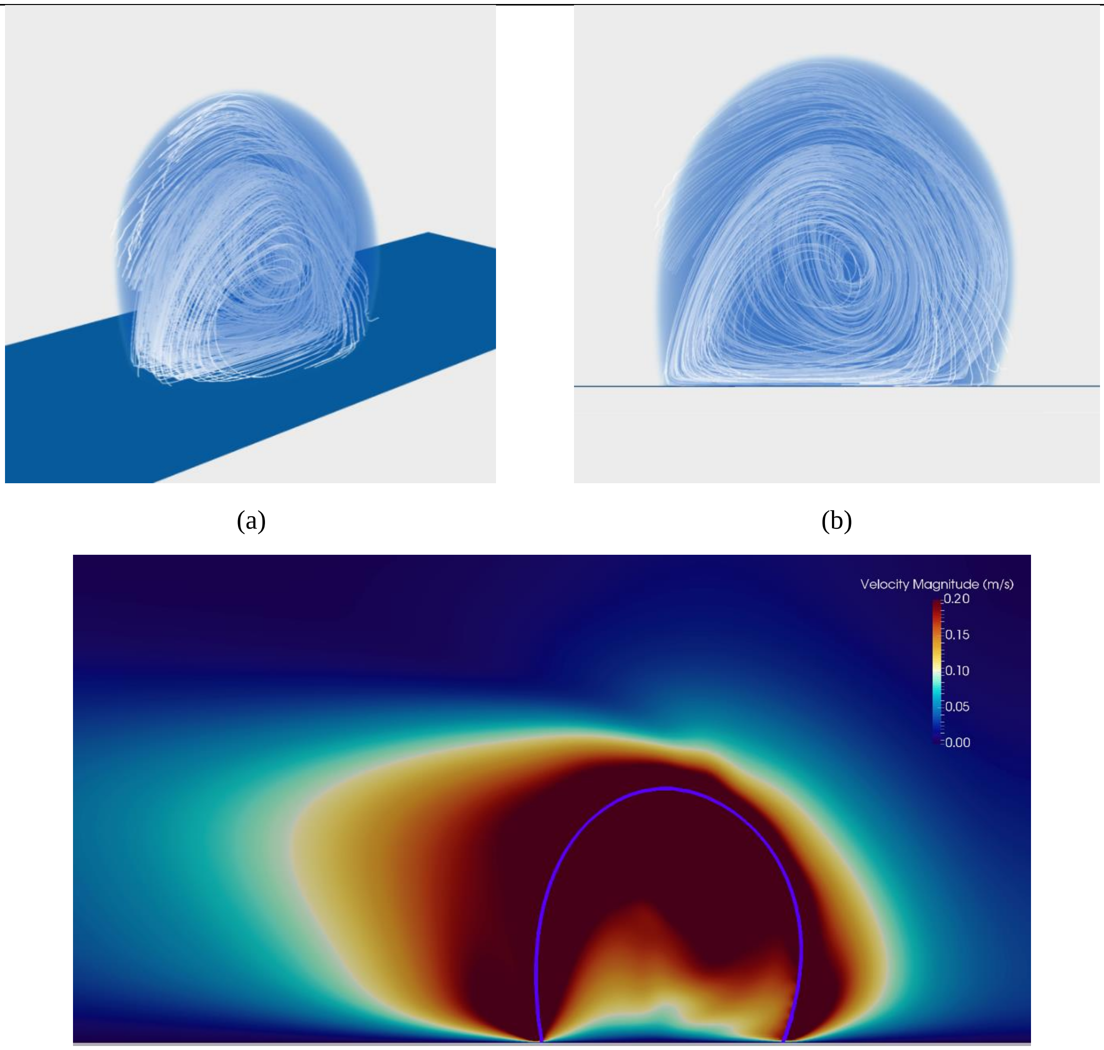

(a) (b)

(c)

Figure 5-6: (a-b) Numerical 3D illustrations of complex internal streaming pattern inside the droplet after 32 ms after applying SAW (a) Tilted view, (b) Cross-section view. (c) Velocity field for droplet and surrounding air of the droplet after 32 ms of calculation.

As time evolves, after 30 ms, a fully developed vortex can be observed inside the droplet, which corresponds to the rolling movement of the droplet on the solid surface. The 3D streamlines of internal streaming inside the droplet after 32 ms are presented in Figure 5-6(a-b). The corresponding magnitudes of velocity vectors at the same time are shown in Figure 5-6(c). The airflow velocities near the interface are relatively high.

5.2.3 Key parameters in droplet pumping

SAW power, droplet volume and SAW devide frequency are the three key parameters which are critical in SAW-based droplet pumping. Thus, the effect of these parameters on the droplet pumping is investigated by the developed numerical method in this section.

5.2.3.1 SAW power

Four cases were simulated to investigate the effect of the SAW power (i.e., wave amplitude) on transportation behaviour. For all the cases, the wave frequency was kept constant at 66.70 MHz. The water droplet has a volume of 5 µl with an initial contact angle of 110°. Wave amplitudes of 150, 250, 350, 420 (Å) were applied to change the wave powers for different cases. The CFD calculation was performed up to 45 ms.

Figure 5-7 illustrates the droplet velocity and Z/Z_0 results during the simulations for all cases. Experimental observations have shown that by increasing the SAW power at each frequency, different microfluidic functions such as internal streaming, transportation, and jetting can be obtained[71]. At each frequency, transportation occurs at a specific range of SAW amplitude, which is increased by increasing the resonant frequency of the device[141]. At SAW amplitudes between 30 to 200 Å, the amount of energy transferred from the solid surface to the fluid medium is low, and surface tension and viscous dissipation are large enough to keep the droplet in its initial spherical shape. With further increase of SAW amplitude, the SAW vertical momentum becomes high enough to reach the droplet surface, and thus the droplet is deformed.

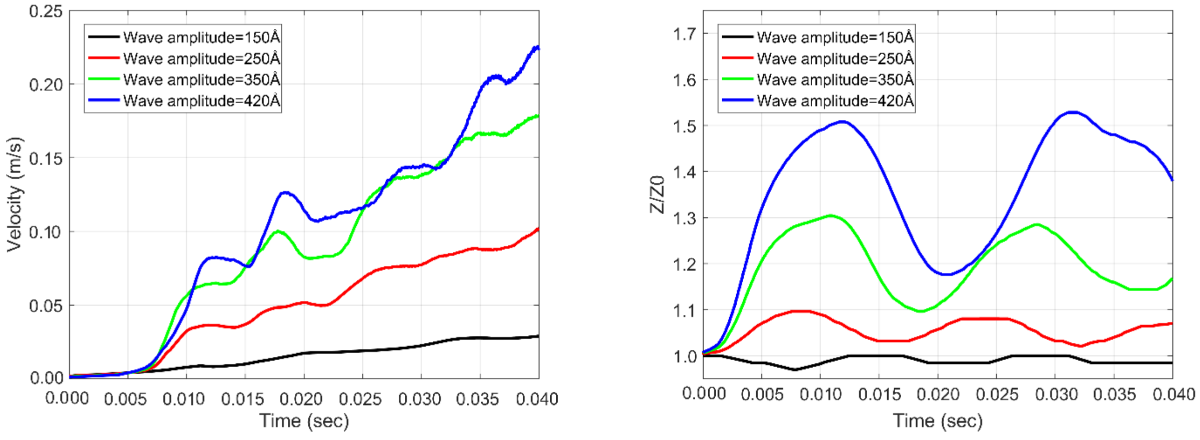

(a) (b)

Figure 5-7: Simulation results for droplet transportation with different wave power, (a) droplet front point velocity, (b) droplet tip height

5.2.3.2 Droplet volume

In this section, the effect of droplet volume on the transportation behaviour of the droplet is investigated. The SAW frequency is fixed at 66.70 MHz for all the cases, and the initial contact angle is 110°. If the same power is applied to the droplets with various volumes, due to the Newton's second law by increasing the droplet volume its velocity will decrease. To have a better insight of the effect of the volume on the pumping the applied SAW power is normilized with droplet diameter. Therefore, during the simulation, the ratio of the amount of SAW force to droplet volume constant is kept constant, and the ratio of SAW amplitude to droplet diameter is also kept constant. More details about the simulation parameters of this section are presented in Table 5-4.

The temporal evolution of Z/Z_0 is presented in Figure 5-8 to compare the droplet interface deformation. An interesting observation for the cases with droplet volumes of 1 and 2 µl is the effect of droplet diameter on interface deformation. For these cases, surface tension is high enough to resist the vertical momentum created by SAW force and avoid the significant deformation of the droplet.

As the droplet volume increases, droplet oscillation is more significant due to lower surface tension force at the liquid-gas interface. Some SAW energy is converted to surface energy by droplet deformation. Due to the liquid inertia, the droplet velocity is decreased for the larger droplets.

Table 5-4: simulation parameters to compare the effect of droplet volume in pumping

Droplet Volume (µl)	Wave Amplitude (A)	Droplet Diameter(mm)	CFD mesh size	Number of CFD mesh cells
1	204.61	0.684	$6.0 \times 1.6 \times 1.6(mm)$	~1.0 million cells
2	257.86	0.862	$6.0 \times 2.0 \times 2.0(mm)$	~1.5 million cells
5	350	1.17	$8.0 \times 2.8 \times 2.6(mm)$	~3.7 million cells
8	408.92	1.367	$12.0 \times 3.1 \times 3.0(mm)$	~5.0 million cells

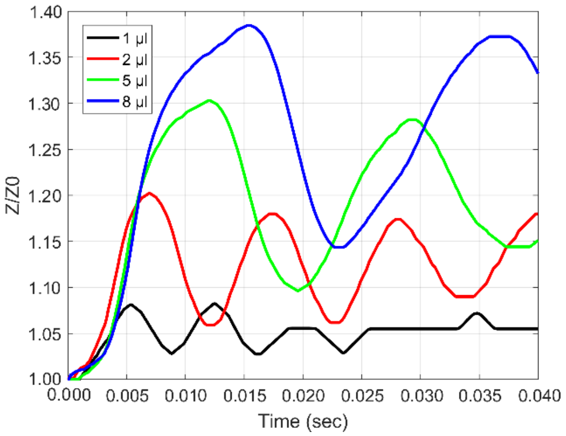

Figure 5-8: The ratio of droplet tip height to initial value during transportation with different droplet volume.

5.2.3.3 SAW resonant frequency

This section presents the simulation results in two parts to study the effect of resonant frequency on the droplet actuation. First, four different cases with different device resonant frequencies of 64.49, 116.96, 210.48 and 271.32 MHz were defined. The wave amplitude and initial contact angle are kept constants at 350Å and 110°, respectively. At higher frequencies, the solid-liquid interface area actuated by SAWs is limited to the rear edge area. However, the magnitude of the force in this area is larger (higher ω in the SAW body force equation). Droplet transportation velocities at different SAW frequencies are shown in Figure 5-9(a). The droplet front point velocity is decreased with the increase of the resonant frequency as the attenuation length of SAW decrease by increasing the frequency, and less energy is dispatched inside the fluid medium at a constant wave power. Second, to link the experimental and computational results, a set of simulations were performed to find the minimum wave amplitude to start droplet transportation or jetting. Experimental results show that by increasing the resonant frequency, the attenuation length is decreased, and thus, lower SAW energy is dispatched from the surface to the fluid medium[71]. As the wavenumber is a linear function of frequency, the wavenumber is increased by increasing the frequency, and the SAW force is attenuated in a shorter length among X and Z-directions. However, the magnitude of the force in the SAW agitated area is much larger. The total SAW momentum dissipated into the fluid medium, and its dissipation distance are significantly reduced by increasing the frequency.

It is vital to define a mathematical relationship between RF power and SAW amplitude to compare the simulation and experimental results of droplet transportation by SAW waves at different frequencies for ZnO/Si devices. Here, an empirical correlation between experimental and simulation results is introduced to identify the normalized SAW amplitude, A/λBy the RF power.

$$\frac{A}{\lambda} = 6.72 \times 10^{-6} P^{1.94} + 1.52 \times 10^{-6} P^{0.91} \tag{5.3}$$

where P is the applied RF signal power in Watts. This expression is enhanced by assuming that surface treatment quality is ideal for the experimental cases. The minimum power to enhance jetting and pumping at each wavelength is fitted with the simulation results with the same wavelength. Figure 5-9(b) shows the simulated minimum SAW amplitude normalized by wavelength to start droplet transportation and jetting at different frequencies. The comparison between the experimental and simulation results shows that the computational model can predict droplet behaviour. The mixing area is defined as an area where applied power creates internal streaming while the droplet is stationary.

The range of applied RF power to enhance internal streaming, transportation, or jetting is critical to design an optimum microfluidic SAW pump operated at a specific resonant frequency. The accuracy of the developed computational model can be used to predict the acoustofluidic behaviour at different RF power ranges. Comparing the minimum A/λ value to start jetting and transportation at different frequencies, the ratio between minimum power for jetting and transportation is decreased by increasing the frequency.

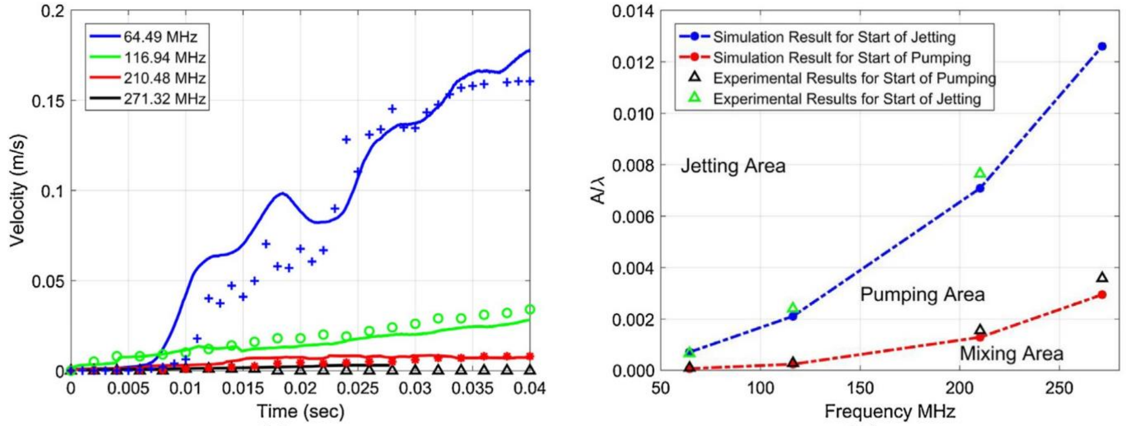

(a) (b)

Figure 5-9: (a) Droplet front point velocity at different resonant frequencies; discrete points are the experimental results (b) A comparison between simulation and experimental results for minimum A/λ to start transportation and jetting

5.2.4 One-sided jetting

Droplet jetting can happen when the SAW energy transferred from the solid surface to the liquid phase is large enough to overcome the surface tension and gravitational forces, and the droplet interface deforms until the droplet is separated from the surface along the Rayleigh angle[15]. The jetting phenomena are reproduced for a droplet of 5 µl on a SAW device with a resonant frequency of 271.32 MHz. The measured static contact angle for a sessile droplet on this device is 110°. Wavenumber and attenuation coefficient for this sample set at 425 and 2.47 consequently[142].

A comparison between experimental and simulation results is presented in Figure 5-10. The results clearly show that the developed code can capture the droplet interface during the jetting. The simulation results are overlaid by the velocity field inside the middle droplet plane. After 3 ms of simulation, Velocity vectors show that there is developing streaming at the left corner of the droplet. Droplet deformation is also pushing the surrounding air and creating an airflow around the droplet tip. After 11 ms, a strong flow pattern inside the droplet pushes the droplet upward. Furthermore, an air vortex can be observed on the left side of the droplet. Interestingly after the droplet separation from the surface, the internal streaming velocity is lower because of viscous dissipation.

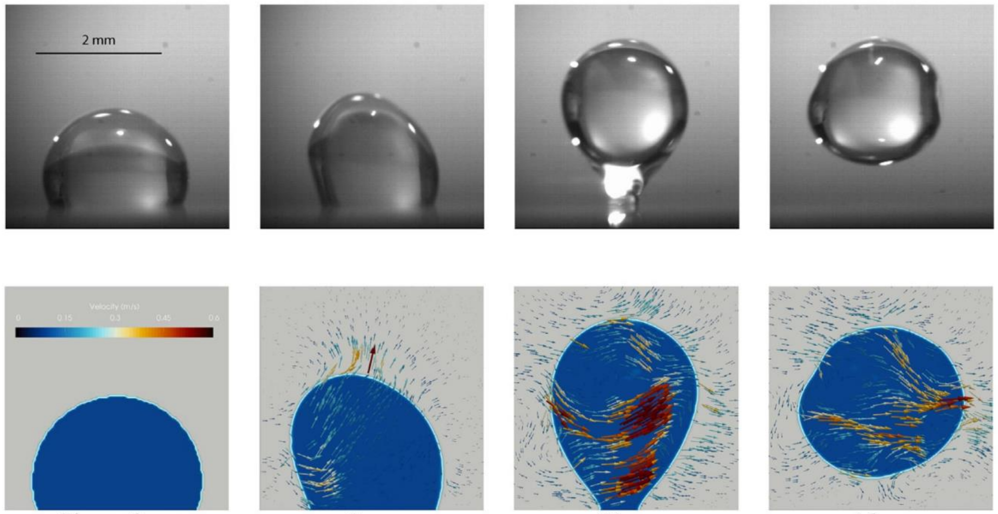

Time = 0 ms 3 ms 11 ms 16 ms

Figure 5-10: Comparing experimental and simulation results of droplet jetting by SAW device with a resonant frequency of 271.32 MHz. Scaled velocity vectors overlay simulation results.

5.3 Droplet jetting and internal streaming

In this section, the droplet actuation by a pair of IDTs is simulated to model the interactions between the solid and liquid phases and TPCL dynamics. After model validation by the experimental results, numerical results are used to analyse the energy budget of the droplet required for SAW induced internal streaming and jetting. Different energy terms, such as kinetic energy or viscous dissipation, are not easily measured experimentally. However, these energy terms and their effects on the physics of the flow can be investigated using the 3D numerical results, which are beneficial for designing and fabricating SAW devices for different LOC applications.

5.3.1 Model validation for droplet jetting

The computational domain for the droplet jetting cases is illustrated in Figure 5-11. For all the cases, a droplet at room temperature with an initial radius of 0.862 mm and a static contact angle of 110^{o} is set to be stationary in the bottom plane centre. The droplet contact angle and volume are equal to those of the experimental results. Grid dependency tests were carried out by defining three cases, e.g., with coarse, normal, and fine mesh sizes. The minimum cell size for each case is presented in Table 5-5. The simulation time is based on parallel simulation on 4 Dual Intel Xeon E5-2680 v4 14 core 2.4 GHz CPUs (224 cores).

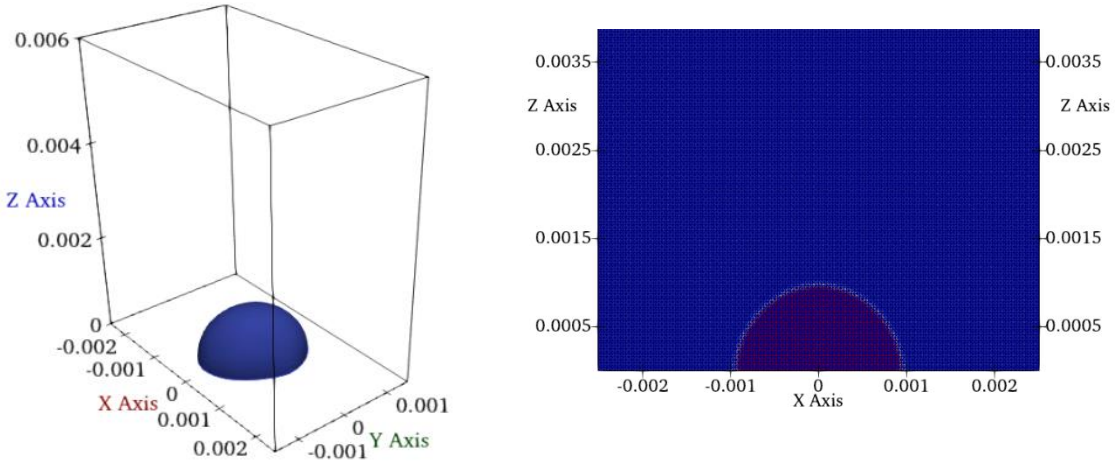

(a) (b)

Figure 5-11: (a) 3D view of the computational domain. (b) A cross-section of the XZ-plane to illustrate the mesh domain

Droplet jetting velocity, i.e., the droplet jet velocity in the Z-direction, is chosen to be compared with experimental results. As shown in Table 5-5, the average tip velocity (i.e., the average vertical motion of the droplet tip during 12 ms of the jetting) is 2% higher for the Coarse case than those of the Fine and Normal cases.

Moreover, a comparison between the temporal evolution of the droplet tip velocity (i.e., the droplet tip temporal velocity in Z-direction) has been made, as shown in Figure 5-12(a). For both the Fine and Normal cases, the tip velocity is nearly identical. However, the difference in results of the Coarse mesh case illustrates that mesh independency is not obtained with this mesh size. Overall, given that simulations with fine mesh size are computationally expensive, all the numerical cases of droplet jetting by SAWs are carried out with a mesh size of 2.50×10^{-5} mm.

Experimental and simulation results are quantitatively and qualitatively compared to validate the numerical model. A 2 µl Droplet is excited by a pair of aligned IDTs (e.g., forming a conventional SSAW) with applied SAW power and frequency of 12 *W* and 67.2 MHz, respectively. The applied SAW power to the IDTs in the experiments is 35 W. To tune the wave amplitude to SAW power, which is used in experiments, several simulations with various amplitudes were performed to achieve a close match between the simulation and experimental results. The applied SAW amplitude to the droplet is set to be 542 Å in numerical modelling. The computational domain is a rectangular box with a dimension of 5×5×6 mm^3. The temporal evolution of the droplet contact width in the X-direction, β_x, is compared with the experimental results shown in Figure 5-12(b). Moreover, the computational and experimental data of droplet tip velocities during the jetting are compared, as shown in Figure 5-12(c). Good agreements between the experimental and simulation results are obtained for these cases. Therefore, the numerical results can be used to analyse the droplet jetting by SAWs.

Table 5-5: Test cases for grid dependency analysis.

Case	Δx (mm)	Number of cells	Simulation time (min)	Average tip velocity (m/s)
Coarse	3.125×10^{-5}	1179648	~120	0.1447
Normal	2.50×10^{-5}	2304000	~390	0.1419
Fine	1.92×10^{-5}	5061888	~2880	0.1420

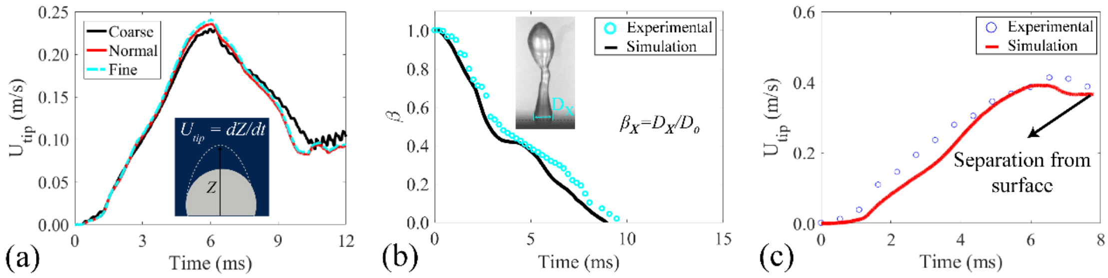

Figure 5-12: (a) Temporal evolution of droplet tip velocity during the jetting phenomena for different grids. (b) temporal evolution of droplet contact width in X-direction for a droplet induced by standing SAW with straight IDTs. The black line represents numerical results, and the cyan circles are obtained from experimental results. (c) A comparison between the tip velocity of the droplet for numerical and experimental results. For both cases, the droplet volume is 2μl.

As a case study, the numerical method and energy analysis is used to optimise the IDT positions of the SAW devices for microfluidic applications such as mixing, separation and jetting. Typically, internal droplet streaming and jetting are generated using SAW devices with one IDT or a pair of aligned IDTs. As explained in chapter 2, many studies applied standing surfaces acoustic waves (SSAW, i.e., a SAW is generated from both sides of the droplet by two aligned IDTs positioned precisely in front of each other) or travelling surface acoustic waves (TSAW, i.e., SAW is generated by one IDT) designs. In contrast, only a few studies have used two IDTs with an offset distance between them for internal droplet streaming and jetting. AS shown in Figure 5-13, it is hypothesised that by changing the relative positions of two opposite IDTs on the SAW device, the droplet dynamics would be significantly modified due to alteration in internal streaming and recirculation patterns. For example, it is expected by using offset IDTs (see Figure 5-13(b)), a swirling flow pattern would be generated within the droplet, which could increase the mixing efficiency. Here, an offset parameter, b, is defined as the ratio between the offset distance from the edges of two IDTs, d, to the IDT aperture, w, (see Figure 5-13 for a graphical illustration). For different LOC applications, a distinct type of flow is desired; therefore, this section aims to use the computational tool to find an optimum value of b for each microfluidic function (e.g., mixing, separation, jetting).

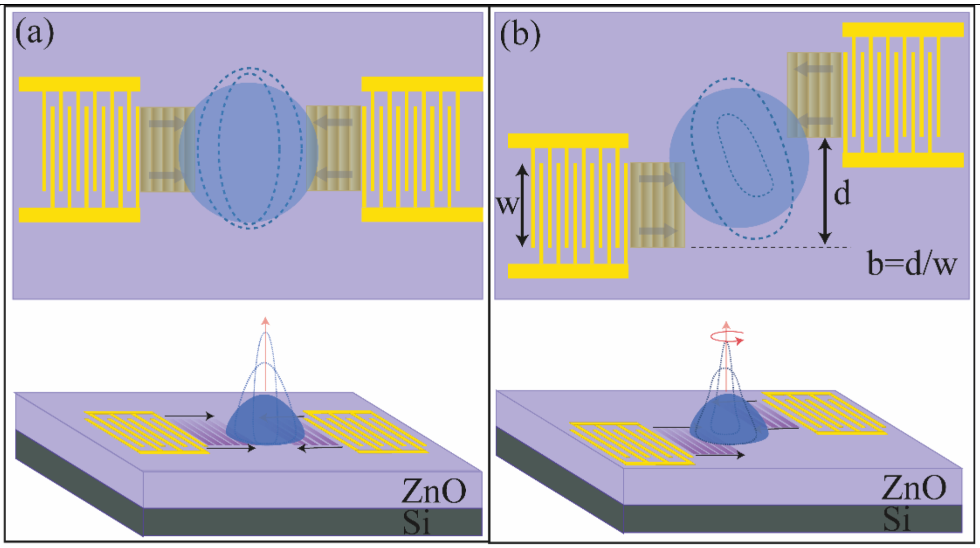

Figure 5-13: Schematic illustrations of droplet actuation with a ZnO/Si SAW device with (a) Aligned IDTs (b) IDTs with offset. The dashed lines illustrate the expected deformation in the liquid-gas and liquid-solid interface area.

5.3.2 Mechanism of droplet jetting

Figure 5-14(a) shows the experimental snapshots of the droplet jetting induced by SSAWs using two aligned IDTs. The applied SAW energy from both sides generates a flow along the Rayleigh angle. As a result of the generated flow, a liquid beam is formed. Meanwhile, the solid-liquid contact area is diminished until the droplet separation from the surface[15,208]. The time history of the snapshots of the XZ and YZ middle planes of the droplet overlaid by velocity vectors is shown in Figures 5-14(b) and 5-14(c), which are obtained from the simulation results. A quantitative comparison between Figures 5-14(a) and 5-14(b) shows an acceptable agreement between the numerical and experimental results.

The comparison between the intensities of the velocity vectors in the XZ and YZ midplanes shows that the flow patterns are stronger in the YZ midplane compared to the XZ midplane (see Figures 5-14(b) and 5-14(c)).

Based on the simulation results, by applying the SAWs, droplet contact width starts to decrease until the jetting is complete, and the droplet is separated from the surface after 7.5 ms. Due to the liquid inertia, at the start of the jetting and during the first 1 ms, the jet velocity is not significantly raised. During the next 5 ms, since the liquid-solid contact area is high, the SAW energy is quickly transferred into the liquid medium. The transferred energy can overcome the gravitational energy, and as a result, the jet velocity is increased significantly. As the time evolves, due to the decreased solid-liquid interaction area and jetting, the transferred SAW energy is diminished, and the droplet tip velocity is reduced.

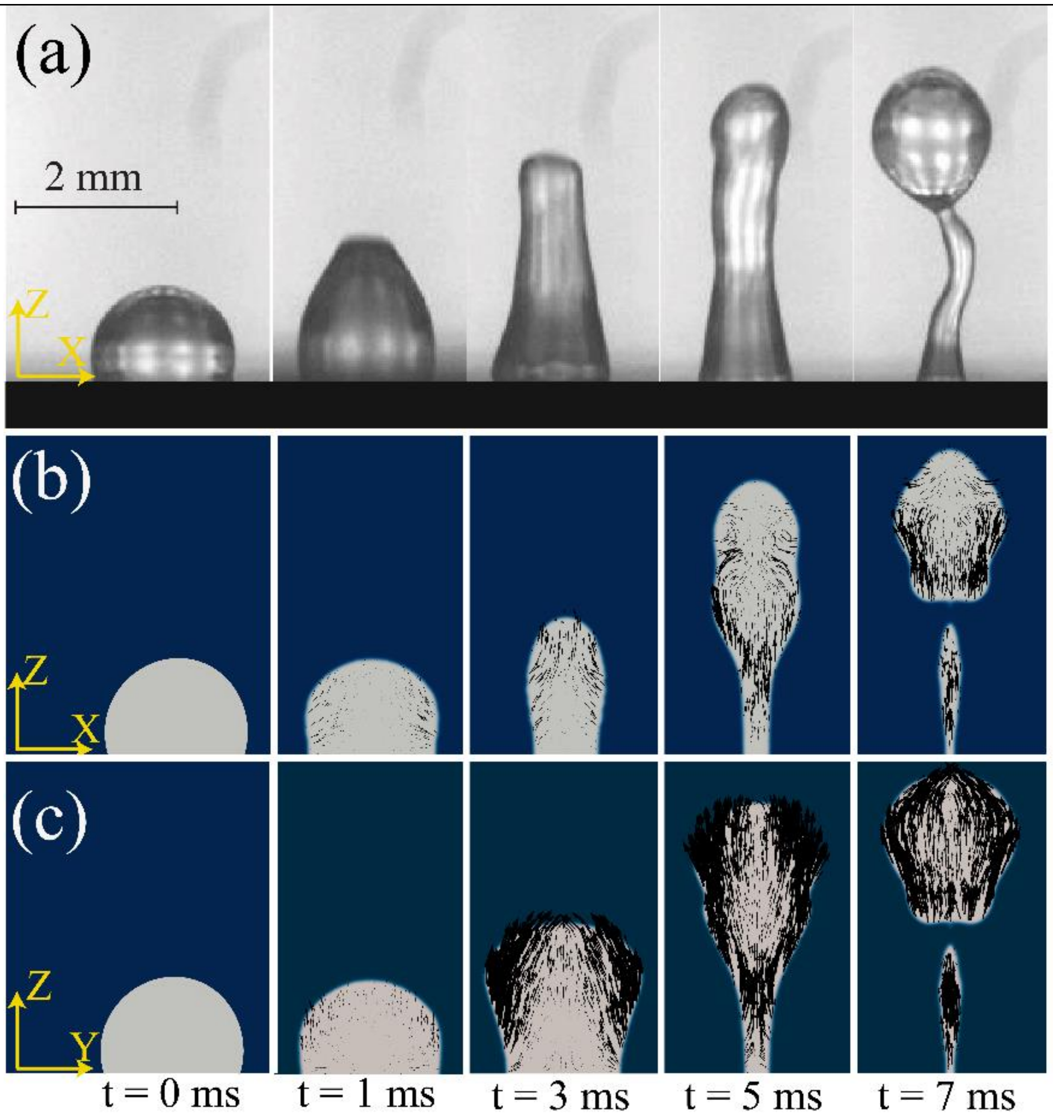

Figure 5-14: Experimental results of the temporal evolution of droplet jetting phenomena induced by SAWs. CFD snapshots of droplet interface overlaid by velocity vectors during the jetting process. (b) XZ middle plane, (c) YZ midplane. For both experimental and numerical results droplet volume is 2 µl. The applied SAW power to the IDTs in the experiments is 12 W. Amplitude of the applied SAW to the droplet is 360 Ǻ.

5.3.3 Energy analysis of jetting phenomena

To better understand the droplet jetting phenomena and further investigate the droplet vertical jetting induced by SAWs, the energy evolution during the jetting period is investigated in this section. During the jetting, the applied SAW energy, E_{SAW}, continuously changes the energy budget of the droplet. Here the cumulative applied SAW energy to the droplet at the given time, t_i, after the onset of SAW propagation, t_0, is defined as:

$$E_{SAW} = \int_{t_0}^{t_i} \int (\boldsymbol{F_{SAW}}.\boldsymbol{U}) dV dt \tag{5.4}$$

The applied SAW energy causes an increase in the kinetic energy K, surface energy, E_S, and gravitational energy, P, during the jetting process. However, part of this energy is dissipated due to liquid viscosity. Here the differences of these energies from their initial value at the stationary state can be calculated. It is assumed that the droplet kinetic energy before applying SAW is zero (i.e., assuming there is no movement or no internal recirculation within the liquid medium for the sessile droplet). The kinetic energy of the liquid can be defined as the volume integral of the kinetic energy of the infinitesimal volume element, V, within the liquid medium, e.g.,

$$K = \int \frac{1}{2} \rho_l u^2 dV \tag{5.5}$$

where u is the magnitude of the velocity vector. The surface energy SE is given by[209]:

$$SE = \gamma_{LV}(s_a - s_{a0}) + (\gamma_{SL} - \gamma_{SV})(s_s - s_{S0}) \tag{5.6}$$

where s_a and s_s are the areas of the droplet in contact with gas and solid medium, respectively. s_{a0} and s_{s0} are the droplet initial contact areas with the surrounding air and underneath the solid surface, respectively. The Gravitational energy, PE, is calculated from

$$PE = \int \rho_l g z dV - \int \rho_l g z_0 dV \tag{5.7}$$

where z and z_0 are the distances of each element in the Z-direction from the solid surface at a time of t_i and the stationary state, respectively. Due to the liquid viscosity, a part of the applied energy is continuously dissipated. The viscous dissipation function, ψ, is defined as:

$$\psi = \frac{\mu}{2}(S.\mathrm{S}) \tag{5.8}$$

Here, $S_{ij} = \left(\frac{\partial u_j}{\partial x_i} + \frac{\partial u_i}{\partial x_j}\right)$ is the strain tensor. The cumulative viscous dissipation at the given time, t_i can be calculated by:

$$E_{dis} = \int_0^{t_i} \int \psi \, dV \, dt \tag{5.9}$$

The results of the various energies for the simulated cases are presented in Figure 5-15. All the energies are normalised by the initial and total SAW energy applied to the droplet during the jetting process (7.58×10^{-7} J, calculated by Equation 5-4). It is apparent from Figure 5-15 that the viscous dissipation energy is two orders of magnitude lower than the other energies. Therefore, its effect on the jetting phenomena is insignificant, and thus could be neglected in jetting. As time evolves during the jetting, the solid-liquid contact area is diminished. Therefore, the transferred SAW energy, E_{SAW}, from the SAW device to the droplet is decreased. Consequently, during the first 4 ms of the jetting, E_{SAW} is increased sharply. After this period, because of rapidly reduced solid-liquid contact area, the rate of applied SAW energy is significantly reduced.

By applying SAW energy, and during the first 4 ms of the jetting, the droplet kinetic and surface energies are increased because of the generation of an internal streaming field (See Figure 5-15). Within this period, the surface and kinetic energies are continuously increased. However, after 4 ms, the surface and kinetic energies do not show significant changes, and the gravitational energy of the droplet is increased. Interestingly, the kinetic and surface energies of the droplet have similar values at its separation moment. In brief, the energy analysis indicates that a part of SAW energy is converted into kinetic energy which drives the droplet upward and another part of it is used to deform the droplet interface. The energy dissipation due to liquid viscosity is negligible during the jetting process.

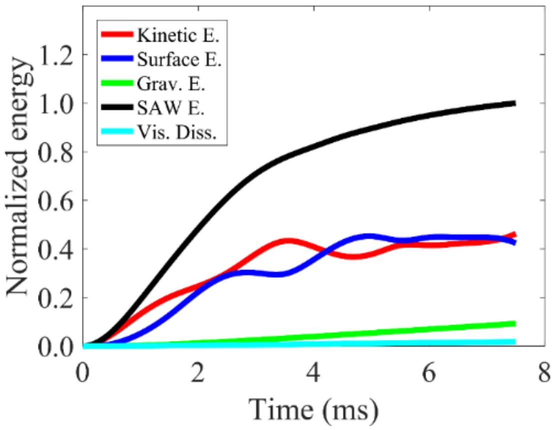

Figure 5-15: Temporal evolutions of the different energies obtained from CFD results. All the energies are normalised by the total amount of the SAW applied to the droplet during the jetting.

5.3.4 IDT location optimization by numerical results

Here, using different energy terms as the design variables for specific microfluidic applications, different IDT configurations is investigated with numerical simulations. The internal droplet streaming without significant interface deformation in the liquid-gas interface is first studied. In general, for mixing applications, by increasing the viscous dissipation, the time to achieve an efficient and fast mixing is reduced[210]. Therefore, it is ideal for SAW-based micromixer design to have the maximum viscous dissipation within the liquid medium. On the other hand, for the centrifugation applications such as microseparators, the optimum design should achieve the maximum internally circular streaming velocity. Therefore, the design criteria are to maximise the kinetic energy of the whole droplet.

The internal streaming patterns for SAW device with aligned IDTs (a standard SSAW); and SAW device with offset IDTs (See Figures 5-16(a-b) for illustrations) are compared. Figure 5-16(a) shows the 3D internal streaming pattern within the liquid medium induced by SAWs from two perfectly aligned IDTs. As shown in the XZ-view, the liquid is excited and pushed upward in the area close to the TPCL and then forms a relatively strong downward flow in the Z-direction at the centre of the droplet. The YZ-view illustrates the circular patterns which are created within the liquid medium. Four zones can be distinguished in the flow patterns at the XY-plane at the bottom of the droplet. The downward flow at the centre forms a circular flow pattern. The outward flow (red arrows) are redirected along the Rayleigh angle at the TPCL by the SAW force and surface tension. Thus four vortexes are created within the liquid, which is in a good agreement with the literature[133,211,212].

Whereas for the SAW device with offset IDTs (as shown in Figure 5-16(b)), the flow pattern within the liquid is changed to one circular flow around the Z-axis in the centre of the droplet. As shown in the first and second rows of Figure 5-16(b), a swirl-like circular flow is generated within the liquid[7,213]. Therefore, it is expected to have lower viscous dissipation within the liquid due to the generation of lower local vorticities.

Another interesting observation is the shape change of the droplet interface after applying the SAWs. For the aligned IDTs, the droplet tip is raised because of the upward flow patterns (red arrows in Figure 5-16(a)). Moreover, the initial circular solid-liquid interface is changed to an elliptical shape since the diameter of the solid-liquid interface is reduced in X-direction by SAW and as a result, expanded in Y-direction. For the IDTs with the offset design, the rotational flow changes the initial solid-liquid interface into a semi-rectangular shape with rounded edges. This is due to the deformation and motion of the TPCL in the areas affected by SAW. Meanwhile, the droplet tip height is lower than the aligned IDT cases since the droplet is spread on the planar surface. The same dynamics are observed in the experiments and are presented in Figure 5-17.

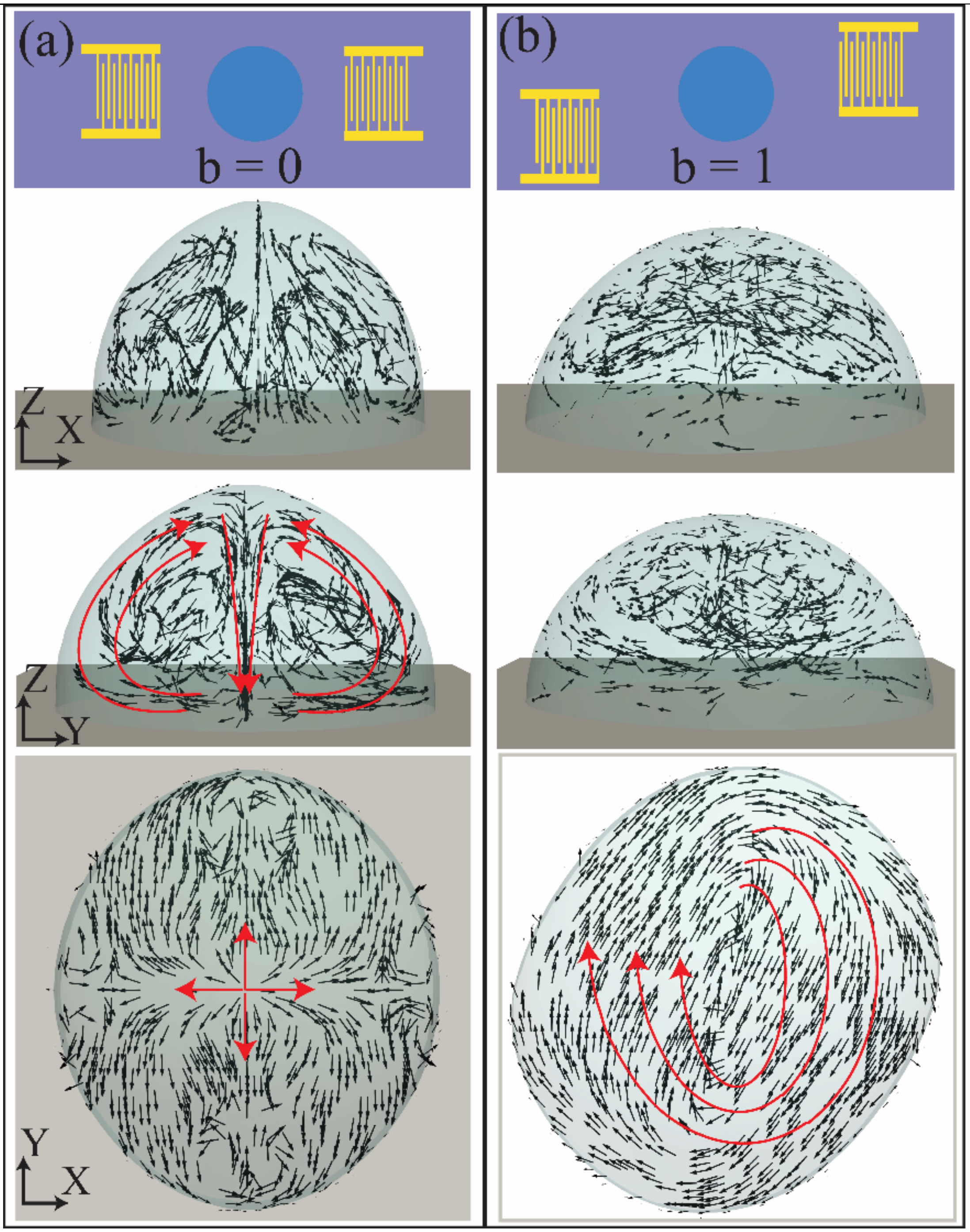

Figure 5-16: Internal streaming patterns for a droplet excited by a pair of (a) aligned IDTs, (b) offset IDTs. For both cases, a droplet with a volume of 2 µl is in place in the centre of the SAW device with a static contact angle of 104^o. Wave amplitude and frequency for both cases are 180 Å and 66.2 MHz, respectively. Internal streaming flow (red coloured lines) is presented after 42 ms of simulation to illustrate a fully developed flow,. XZ and YZ views are shown in 3D, and the XY view is the 2D view of the bottom plane.

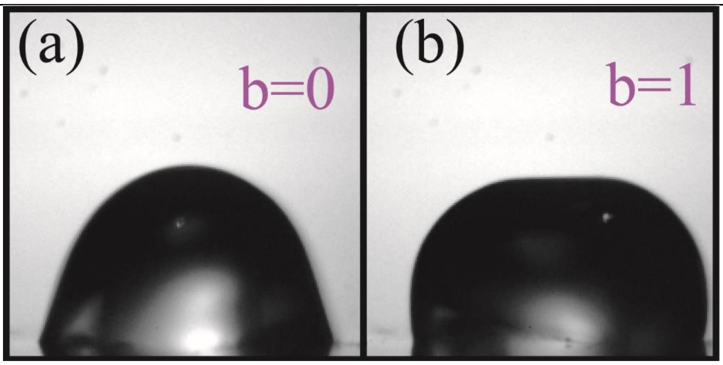

Figure 5-17: Experimental results of a 2 µl droplet internal streaming with a pair of (a) aligned IDTs, (b) adjacent IDTs. For both experiments, the applied power to the IDTs is 3.6 W.

Figures 5-18(a-b) compare the kinetic energy and viscous dissipation rate in the middle planes in XZ and YZ planes after 42 ms of simulation. The colour map indicates the kinetic energy per volume (right side) and viscous dissipation rate per volume (left side) enhanced by simulation results. The blue line illustrates the liquid-air interface. By comparison of the coloured maps, it is possible to follow the changes in dissipation rates of kinetic and viscous energies. Due to negligible motion in the liquid-air interface, the surface and gravitational energies changed are simulated to be less than 4 and 2 percent, respectively. Consequently, the applied SAW energy to the liquid medium is mostly converted into the kinetic energy, which creates an internal streaming flow. However, a part of this energy is dissipated due to the fluid viscosity.

For the aligned IDTs (see Figure 5-16(a)), since there is a downward flow in the droplet centre, the kinetic energy is high in this region in both XZ and YZ planes. In addition, at the edge of the droplet in XZ plane (where is excited by SAW), the flow is in the Rayleigh angle direction, and the kinetic energy per volume is high in that region. Besides, the viscous dissipation rate is high in the areas close to the liquid-gas and liquid-solid interfaces (see the left side of Figures 5-18(a-b)).

On the other hand, for the offset IDT configuration (see Figure 5-18(b)), most of the kinetic energy is concentrated in the area close to the liquid-air interface, which shows that the rotational flow velocity is higher in this region. Moreover, since lower vorticities are generated in the stream, the liquid viscous dissipation rate is lower. The viscous dissipation rate is relatively high in the areas close to the liquid-air interface. However, unlike the aligned IDTs,

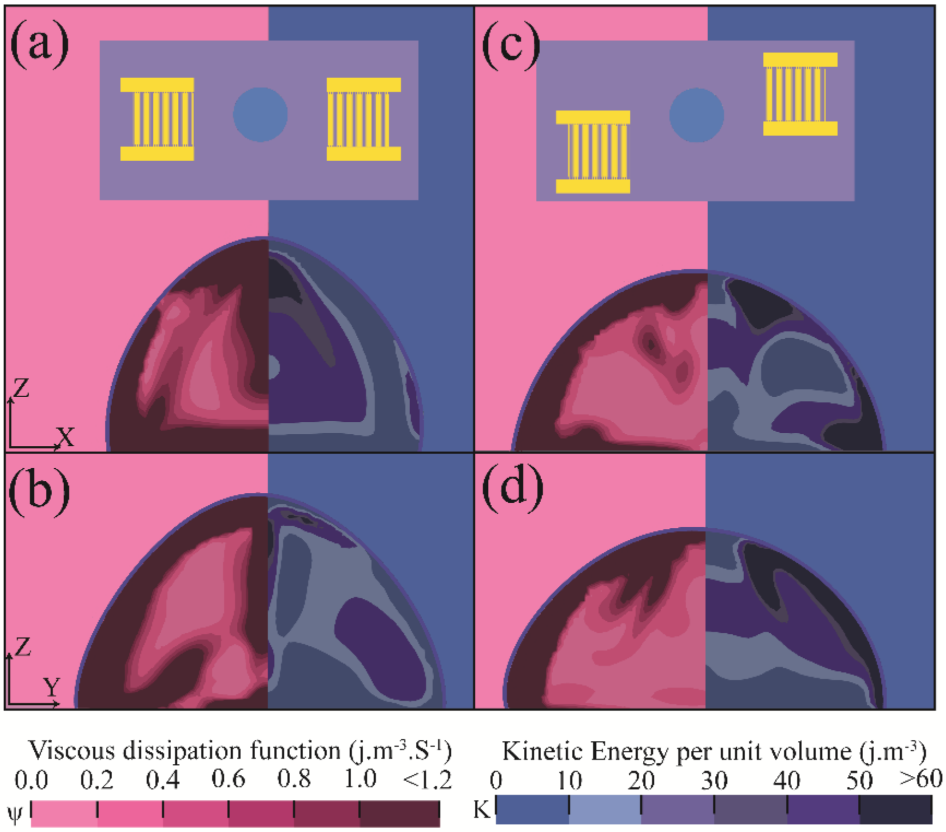

Figure 5-18: Kinetic energy and viscous dissipation rate fields for a droplet with internal streaming induced by a pair of aligned IDTs in (a) XZ-midplane and (b) YZ-midplane. Kinetic energy and viscous dissipation rates fields for a droplet with internal streaming induced by a pair of IDTs with offset (b=1), in (c) XZ-midplane and (d) YZ-midplane. The colour map in the left side depicts the viscous dissipation function per unit volume, and the right side shows the kinetic energy per volume. Fields are compared after 42 ms of simulation to make sure that the internal flow is steady.

viscous dissipation is much lower in the centre of the droplet. A comparison between the viscous dissipation rates in Figures 5-18(a-b) and (c-d) clearly illustrates that more energy is dissipated in the aligned IDT configuration. These results provide an important insight into the effect of the IDT configurations in the internal streaming patterns. The gradual changes of the IDT offset value, *b*, on energy terms of the droplet are further investigated to use the numerical results to optimise the IDT position design.

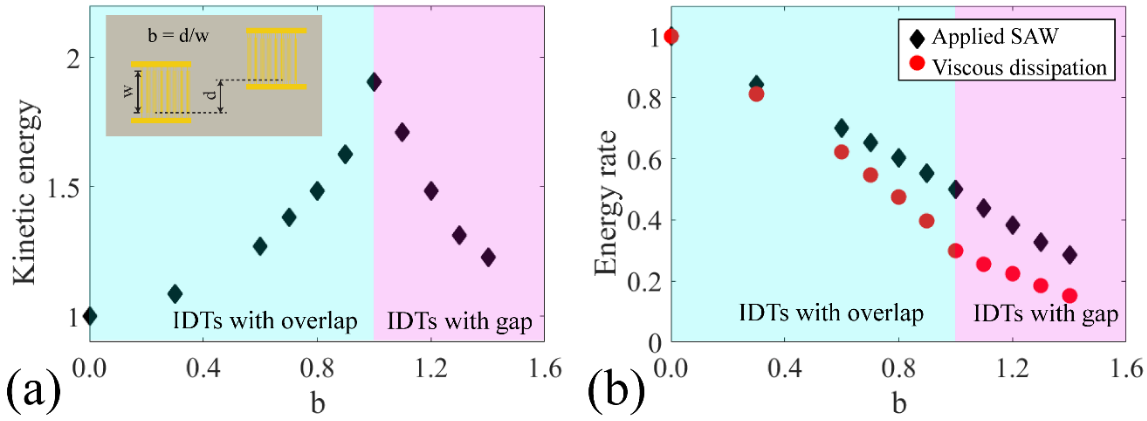

Figure 5-19: (a) Normalised total kinetic energy of the liquid medium after 42 ms of applying SAW as a function of IDT offset. (b) The normalised rate of applied SAW energy and viscous dissipation 42 ms after the start of SAW propagation. For all the cases, the SAW amplitude and droplet volume are kept constant at 180 Å, and 2 µl. in both graphs the values are normalised by the value of the aligned IDT case (i.e., *b=0*).

By progressively changing the value of b from 0 to 1.4, a series of simulations (keeping all other parameters constant) is ran, and energy terms are compared. The results are shown in Figure 5-19. All the energy terms are calculated after 42 ms of simulation and normalised by the aligned IDT device energy term (i.e., $d = 0$).

As shown in Figure 5-19(a), by increasing the value of b, the kinetic energy is increased until it reaches a peak at $b = 1$ (i.e., the IDTs are offset). The droplet kinetic energy for the offset IDTs case is ~1.9 times larger than the aligned IDTs for the same applied power to the SAW device. Meanwhile, For the IDTs overlapping between them (i.e., $b > 1$), the droplet kinetic energy is decreased. The kinetic energy of the fully developed flow illustrates the streaming velocity inside the liquid. For concentration or centrifugal applications, it is ideal for generating the maximum mixing velocity (i.e., maximum kinetic energy) by using the same applied SAW power[211]. Therefore, a SAW device with offset IDTs with b value of one is optimal for microscale mixing and separation applications.

As shown in Figure 5-19(b), with a successive increase in the value of b, a reduction in viscous dissipation (and thus diffusive mixing) is obtained. The reason for the decrease of viscous dissipation within the liquid could be the reduction in the local vortices by the generation of the swirl-like circular flow within the droplet. As expected, in SAW device with an IDT offset, the amount of SAW energy transferred to the liquid medium is decreased by increasing the value of b, since the solid-liquid interface induced by SAW is reduced. Thus, two aligned IDTs are optimal for mixing applications to obtain a fast and homogeneous mixing effect. The results in Figure 5-19 show that optimising an electrode configuration for various SAW device applications can be checked by performing these simulations before physically fabricating the SAW devices with different IDT configurations.

Examples of experimentally obtained droplet jetting images with a pair of IDTs with the offset design are presented in Figure 5-20. As shown by the red lines, SAW generates a swirl-like flow within the liquid droplet which deforms the droplet interface and triggers the liquid jetting. To explore the effect of the IDTs design on jetting by the developed numerical method, the simulation results of the jetting process of two different cases, e.g., with aligned and offset IDTs are compared. The amplitude of the applied SAW and droplet volume in all simulations are kept constant at 542 Å and 2 µl, respectively. Figure 5-21 illustrates the internal streaming patterns of the droplet during the jetting. For the aligned IDTs (see Figure 5-21(a)), after applying the SAWs, the liquid-solid interface forms a deformed oval shape from the top view as discussed above. During the jetting, this oval area is diminished until the droplet is separated from the surface.

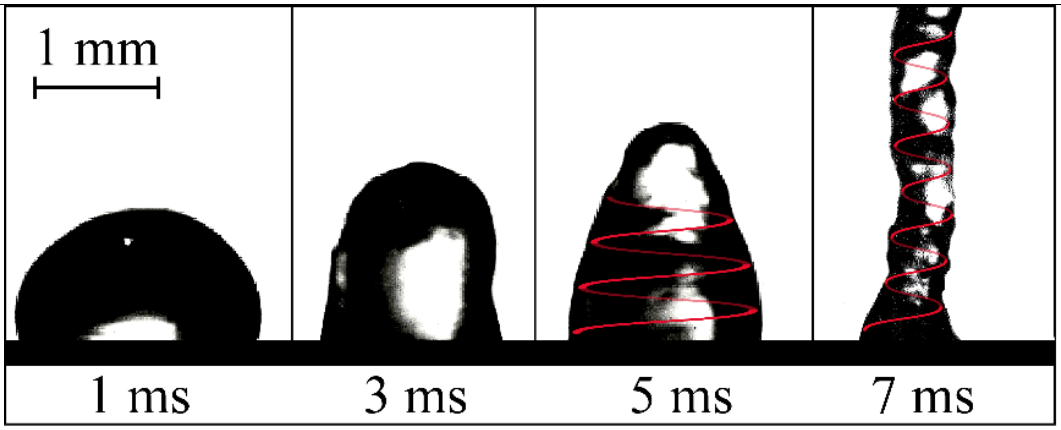

Figure 5-20: snapshots of 2 µl droplet jetting induced by a pair of IDTs with offset (b=1). The applied RF power to the IDTs is 9 W, and the SAW device frequency is 66.54 MHz

The top view of the velocity vectors illustrates that an upward flow is created inside the droplet, and this flow pushes the droplet in the vertical direction. The velocity vectors in the ZY-plane (i.e., $\boldsymbol{U}_{yz} = \boldsymbol{U}_{Y}.\boldsymbol{j}+\boldsymbol{U}_{Z}.\boldsymbol{k}$) shows that the area close to the liquid-gas interface has a stronger upward flow pattern compared to the centre of the droplet, which pushes the droplet jetting upwards.

The flow patterns for the offset IDT SAW device is presented in Figure 5-21(b). Similar to the internal streaming case, after SAW agitation, the solid-liquid interface is changed from its circular shape to a rectangular-like one with curved edges. Due to the IDTs offset, the liquid flow profile combines vertical jetting and swirling flow in XY-plane during the jetting process. The swirling velocity field (see the XY-plane in Figure 5-21(b)) illustrates that synchronous twisting and jetting can be obtained. This SAW platform with particular IDT configuration can be used in bioprinting applications to mix and jet the flow toward a particular target, simultaneously.

The kinetic energy and viscous dissipation rate for the liquid jet, 4 ms after the inset of SAW propagation in XZ and YZ mid-planes, are summarised in Figure 5-22. As shown in Figure 5-22(a), for the aligned IDTs, the kinetic energy is higher at the areas closer to the liquid-air interface compared to the centre of the droplet in both XZ and YZ mid planes. This shows that the applied SAW energy creates an upward momentum which has a higher value around the liquid-gas interface region, at which the flow is pushed upward along the Rayleigh angle. Moreover, due to the higher velocity gradients at this area, more energy is dissipated by viscosity. Both kinetic energy and viscous dissipation energy are lower around the Z-axis in the centre of the droplet.

On the other hand, due to the swirling flow pattern during the jetting induced by the offset IDTs, the kinetic energy and viscous dissipation for these cases are somewhat different. Unlike the internal streaming cases in Figure 5-18, the viscous dissipation is higher for the offset IDTs since the combined vertical jetting and twisting flows generate vorticities, promoting viscous dissipation. Also, for the offset IDT case, the region close to the droplet tip does not have the maximum kinetic energy.

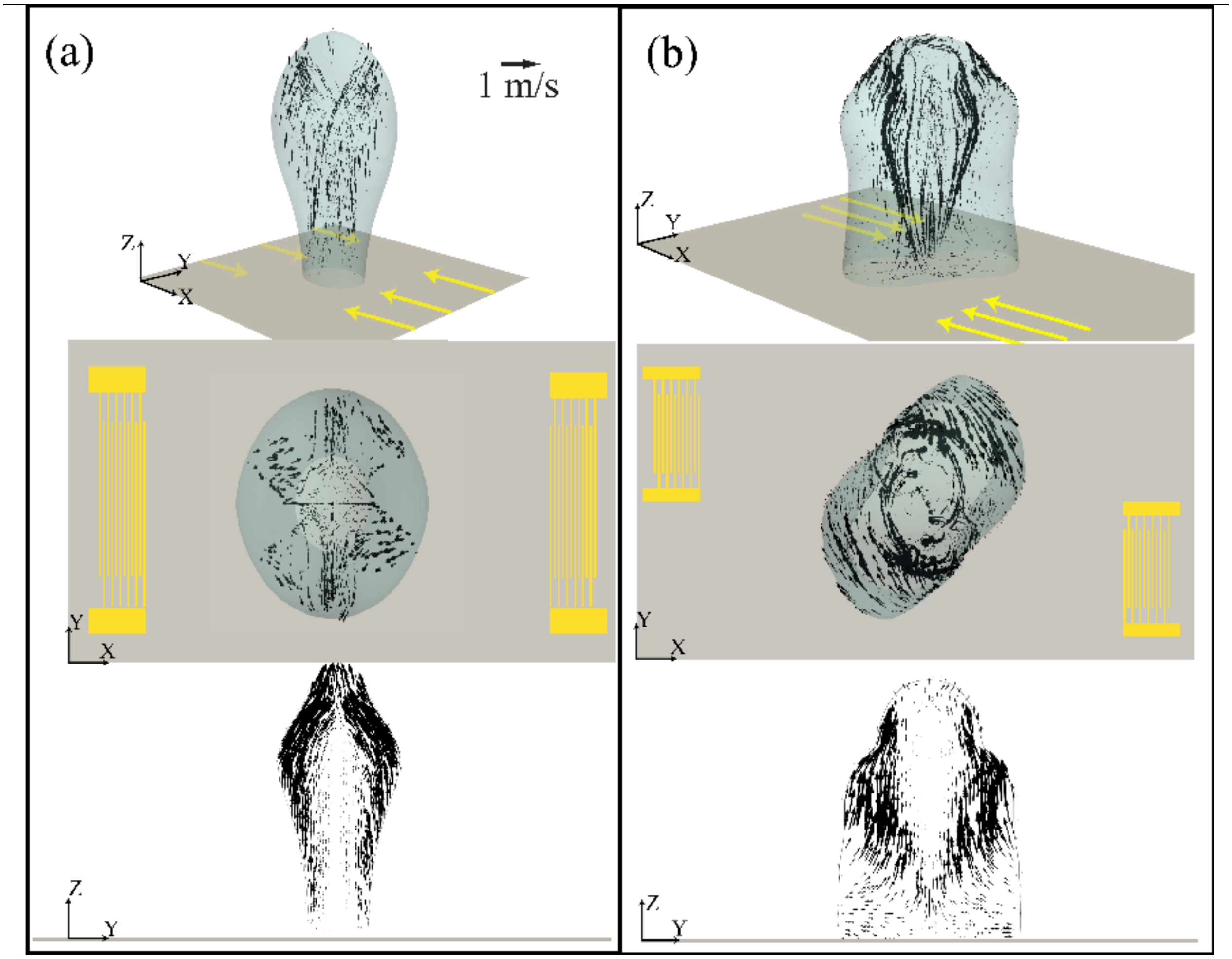

Figure 5-21: internal flow patterns during the jetting for a droplet excited by a pair of (a) aligned IDTs, (b) offset IDTs. For both cases, a droplet with a volume of 2 µl is in place in the centre of the SAW device with a static contact angle of 104°. Wave amplitude and frequency for both cases are 542 Å and 66.2 MHz, respectively. Internal streaming flow is compared after 4 ms of simulation. XZ and YZ views are shown in 3D, and the YZ view is the 2D view of the middle plane.

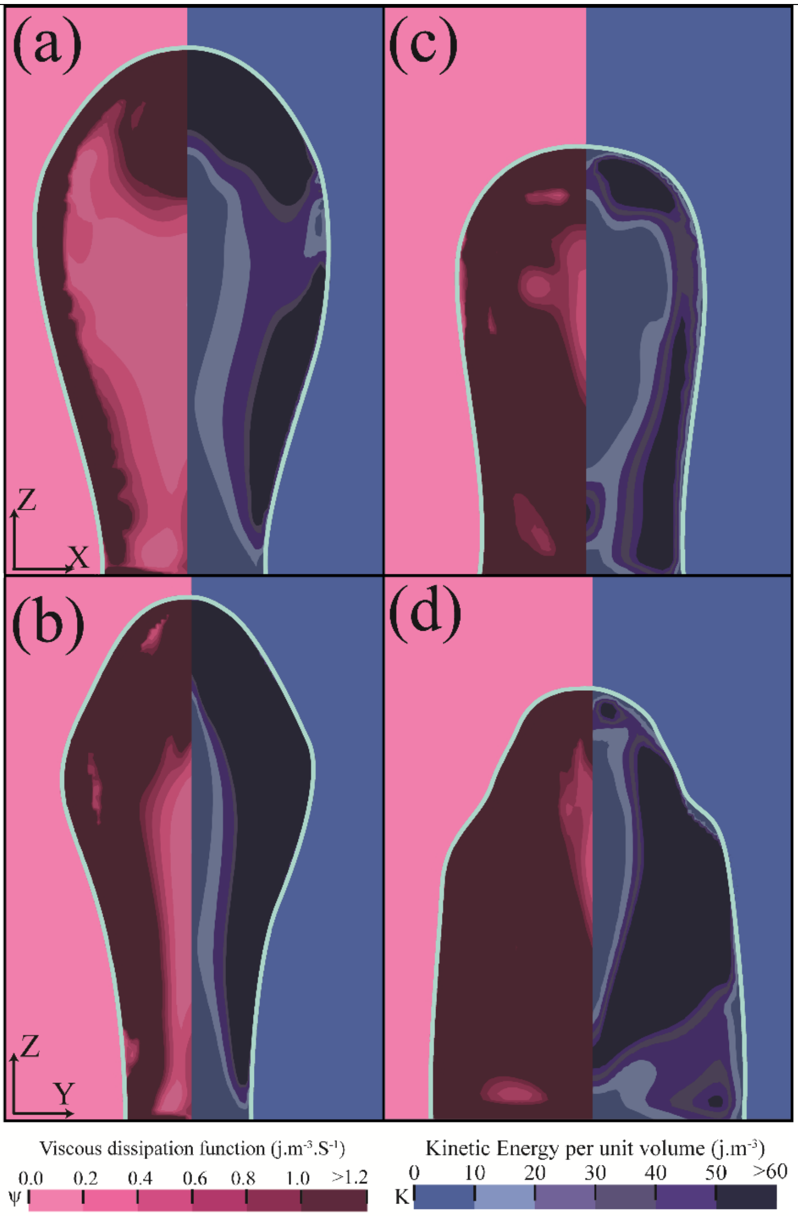

Figure 5-22: Kinetic energy and viscous dissipation rate fields for a droplet jetting triggered by a pair of aligned IDTs in (a) XZ-midplane and (b) YZ-midplane. Kinetic energy and viscous dissipation rates fields for a droplet with internal streaming induced by a pair of offset IDTs ($b=1$), in (c) XZ-midplane and (d) YZ-midplane. The colour map in the left side depicts the viscous dissipation function per unit volume, and the right side shows the kinetic energy per volume. For both cases, a droplet with a volume of 2 µl is in place in the centre of the SAW device with a static contact angle of 104^{o}. Wave amplitude and frequency for both cases are 542 Å and 66.2 MHz, respectively. Fields are compared after 4 ms of simulation.

Like internal streaming applications, numerical results can be used to compare the IDT design effect on the jetting phenomena. The jetting time (i.e., the time which it takes for all of the droplets to be removed from the surface) and the jetting velocity (i.e., the velocity of the droplet tip) are used as the design parameters in this section to investigate the effect of IDT configuration on droplet jetting. Droplet tip velocity and jetting time as a function of IDT offset ratio are shown in Figure 5-23(a). The simulation results show that with the increase of IDT offset, the tip velocity is decreased, and the jetting time is increased. Unlike the internal streaming cases, the solid-liquid interface area during droplet jetting is not (almost) constant. Thus, the total applied SAW energy to the liquid is a function of both the solid-liquid interface area and jetting time. The jetting time is increased by increasing the value of b since the total SAW energy transferred to the liquid medium is decreased, and the energy dissipation rate is increased (See Figure 5-23(b)). As shown in Figure 5-23(b), by increasing the IDT offset from 0 to 1.4, the applied SAW energy is decreased by ~42%, and the viscous dissipation is increased by 435%. As a result, the tip velocity is reduced by ~76%.

However, the comparison between the internal streaming patterns in Figure 5-20 illustrates that the swirl-like flow around the Z-axis (which is generated as a result of IDT offset) also affects the vertical jetting velocity. To understand the effect of the swirling on the droplet flow, the swirl number, *SN*, is defined and evaluated from the velocity components as[214]:

$$SN = \frac{\int \sqrt{U_X^2 + U_Y^2}\, dV}{\int \sqrt{U_Z^2}\, dV} \tag{5.10}$$

The simulation results can obtain the temporal evolutions of the SN for four of the IDT designs, which are presented in Figure 5-24. Numerical results show that after a transient time, the jetting flow is fully developed. Then the swirling numbers for all the cases remain almost a constant. The SN as a function of IDT offset is presented in Figure 5-23(c). By increasing the value of the b, the mixing flow in XY-plane becomes more dominant compared to the jetting flow along the Z-axis. Considering the results shown in Figures 5-23(a-c), one can explain the differences in the flow induced by the different SAW devices. By increasing the IDT offset, the solid-liquid interface area which is excited by SAW is decreased. Thus, much lower SAW energy is transferred to the droplet (see Figure 5-23(b)). For the SAW device with aligned IDTs (i.e., $b = 0$), the maximum SAW energy is applied to the droplet during the jetting time. However, as shown in Figure 5-23(c), the application of energy produces a flow along the Z-axis (maximum jetting velocity and minimum swirling). By increasing the IDT offset, less energy is transferred to the liquid medium during the jetting. Simultaneously the jetting velocity is decreased, and interestingly recirculation in the XY-plane is increased.

Another interesting observation based on the simulation results is the increase of viscous dissipation (and thus diffusive mixing) during the jetting. Figure 5-16 illustrate that viscous dissipation is negligible (compared to other energies) in jetting. However, for potential SAW-based jetting applications, which may require both synchronised jetting and mixing, it is essential to optimise the IDT design and configuration. As shown in Figure 5-23(b), by increasing *b* values in IDT design, the viscous dissipation is increased within the droplet, and consequently, diffusive mixing is enhanced.

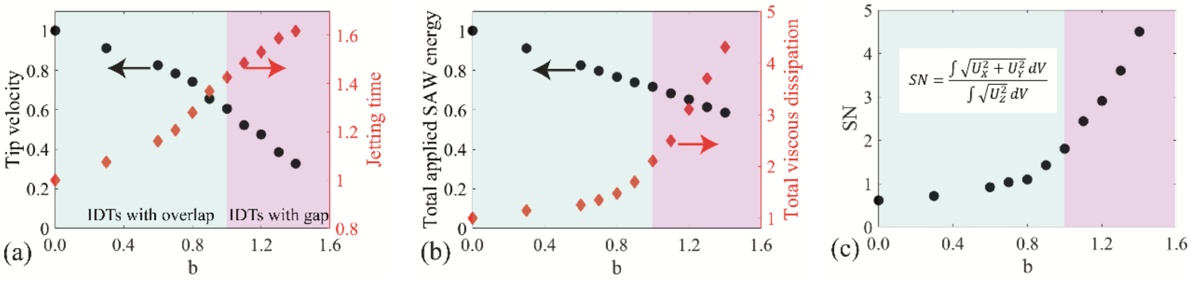

Figure 5-23: (a) Normalised tip velocity and jetting time as a function of IDT offset. (b) Normalised total applied SAW energy and viscous dissipation during the jetting time versus IDT offset. (c) Normalised swirl number (SN) versus IDT offset. For all the cases, SAW amplitude and droplet volume are kept constant at 542 Å and 2 µl. All the parameters are normalised by their respective value of the aligned IDT cases.

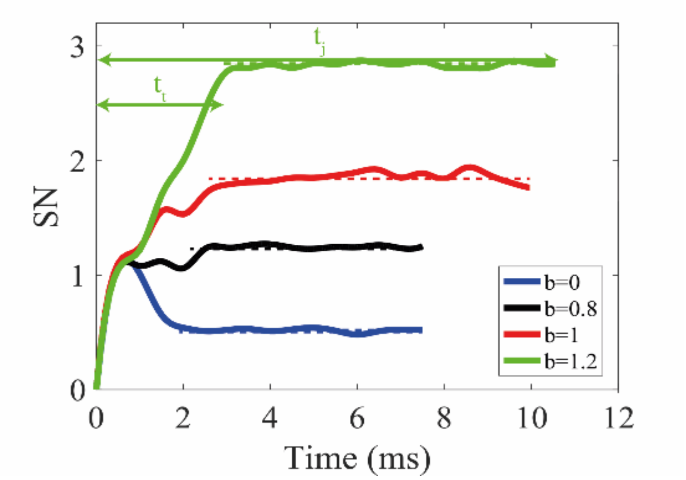

Figure 5-24: Temporal evolution of the Swirl number for four selected cases. For all the cases, the SAW amplitude and droplet volume are kept constant at 400 Å and 2 µl.

5.4 Summary

In this chapter, the numerical results were used to simulate the simulate droplet pumping and jetting scenarios. After doing mesh dependency tests for both cases, the experimental and simulation results are compared, and a good agreement was obtained. This chapter shows that the developed solver can be used to simulate different droplet actuation by SAWs cases.

After model validation, the simulation results are used to explain the physics of the droplet pumping and then the key factors affecting droplet movement by SAWs are investigated. Additionally, droplet jetting by TSAW and SSAW is explored by numerical results as well. The energy budget of the droplet during the jetting and internal streaming applications is explained. Additionally, the simulation results are used to optimize the IDT positions in the SAW device for various microfluidic applications such as mixing, separation and jetting.

In the next chapter, the use of SAWs to modify and control the droplet impact dynamics on solid surfaces is investigated.

Chapter 6. Droplet impact control by SAWs

In this chapter, a method is proposed to modify and control the droplet impact dynamics using SAWs. First, in section 6.1, SAWs are used to reduce the droplet contact time (CT) on flat surfaces and then this method is used to control the droplet impact dynamics on inclined surfaces in section 6.2. The results in sections 6.1 and 6.2 are published as research papers in Physical Review Applied and Langmuir.

6.1 Contact time reduction for droplet impact on flat surfaces

The need for manufacturing a textured surface with macrostructures to reduce the droplet impact time brings complexity for practical applications. Therefore, finding new methodologies to manipulate droplet impact on a smooth and non-textured surface with an extensive area coverage is crucial. In this section, the effect of applying SAWs during the droplet impingement process on the solid surface is investigated. It is expected that the CT of an impacting droplet would be reduced by remotely generating SAWs, which then propagate along a smooth and non-textured surface into the area where the droplet impact is occurring. Figure 6-1 illustrates the droplet impingement dynamics on the solid surface in the presence of a propagating SAW. The droplet contact width is characterised by $\beta = \delta/D_0$, which is the ratio of the contact width, δ, to the initial droplet diameter, D_0. The droplet interface asymmetry along the X-axis is expected to be observed, triggered by SAW energy conversion into the LSAWs and the resulting different internal streaming patterns inside the droplet. This would affect the various interfaces, which in turn could lead to different contact widths and dynamics during the impingement. It is reasonable to conjecture that the droplet may detach from the surface sooner and along a non-normal detachment angle, as shown in Figure 6-1.

This section aims to determine whether CT will be reduced by applying the SAW during the droplet impact on the solid surface based on the above hypothesis. A thin-film ZnO/Si SAW device with a resonant frequency of 66.2 MHz is used to achieve this. Two types of SAWs were applied during the impact, including (i) TSAWs, and (ii) SSAW during droplet impingement. The experimental results were compared with the conventional droplet free impact (DFI) on the solid surface in terms of contact width and contact time, as functions of SAW power and the *We* number.

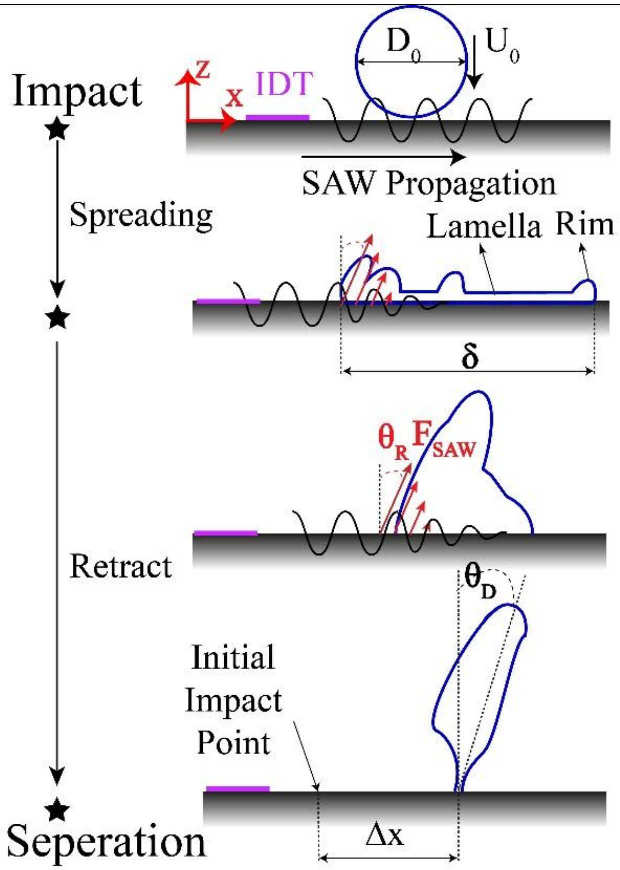

Figure 6-1: Anticipated time evolution of droplet impact on a solid surface with the presence of SAW propagating on the surface. SAWs can dissipate energy into the liquid droplet during its impact process and break-off the symmetry in droplet spreading and retracting phase leading to shorter contact time.

6.1.1 Experimental results

6.1.1.1 Device selection

SAW devices with resonant frequencies ranging from 22.04 to 110.84 MHz are used to investigate the droplet impact hydrodynamics in the presence of SAWs. The droplet impact dynamics on ZnO/Al and ZnO/Si SAW devices with the same wavelength are compared to see the Rayleigh angle effect on the droplet contact time. Table 6-1 lists the measured frequency of the fabricated ZnO/Al and ZnO/Si devices. As explained in Chapter 3, the SAW force (see Equation 3.8) is applied to the liquid medium along the Rayleigh angle, and the ratio of the components of the SAW force in X and Z directions is equal to the attenuation coefficient

($\frac{F_{SAWz}}{F_{SAWx}} = \alpha_1$)[66]. As shown in Table 6-1, due to lower sound velocity on the aluminium substrate, the Rayleigh angle is larger for Al-based SAW devices and thus α_1 is lower.

Consequently, the ratio of the $\frac{F_{SAWz}}{F_{SAWx}}$ is lower for the ZnO/Al device than the ZnO/Si device due to the larger Rayleigh angle. Experimental results of droplet CT on the surface of ZnO/Al and ZnO/Si SAW devices as a function of SAW power are illustrated in Figure 6-2(a). This graph shows that at lower SAW powers, the CT for the ZnO/Al SAW device is reduced up to 10% on the ZnO/Al device. However, by increasing the SAW power ($P > 20$ w), the CT starts to increase sharply. On the other hand, for the ZnO/Si device, the CT is decreased by increasing the SAW power. The experimental movies show that by applying TSAW to the droplet, it moves a certain distance along the X-direction during the impingement. The transition along the X-direction on the surface before separation, Δx, for both devices is compared in Figure 6-2(b). At higher SAW power, Δx is larger for the Al-based devices. The ZnO/Al SAW device has a lower attenuation constant than the ZnO/Si SAW device. Thus, the X-component of the SAW force is higher, driving the droplet on the surface in X-direction at high SAW powers before complete detachment. This, in turn, leads to a change in the CT for ZnO/Al SAW devices. Since this section investigates the CT reduction using SAWs, ZnO/Si SAW devices are chosen to be used for this purpose.

Table 6-1: Resonant frequency, Rayleigh angle, SCA, advancing contact angle, receding contact angle, and CAH for ZnO/Al SAW device. The contact angles are measured after the surface treatment with CYTOP. The contact time is measured for a 3.56 µl droplet with an impact velocity of 1.41m/s.

SAW Device	Resonant Frequency	Rayleigh Angle	α_1
ZnO/Al	40.40 (MHz)	34.75°	1.46
ZnO/Si	66.1 (MHz)	21.2°	2.47

Table 6-2: Measured frequencies and calculated sound velocities and liquid attenuation lengths, ζ, for ZnO/Si SAW devices

Wavelength (µm)	Frequency (MHz)	$v_S(\frac{m}{s})$	ζ/λ
36	110.82	3989.5	850
64	66.10	4230.4	1602
100	43.12	4312.0	2550
200	22.04	4407.5	5215

Four different ZnO/Si SAW devices with different IDT designs are used to explore the effect of the resonant frequency on droplet impact dynamics. Details of the used devices are presented in Table 6-2.

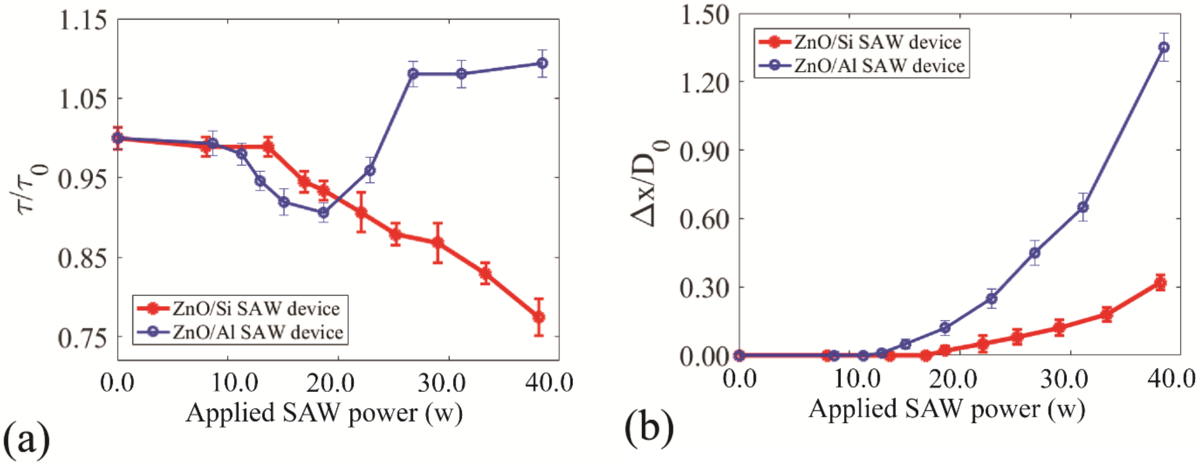

Figure 6-2: (a) Experimental results of normalized CT versus SAW power for ZnO/Si and ZnO/Al SAW devices. For both devices, the wavelength of the SAW is 64 µm, and a droplet with a volume of 3.56 µl is impacting the surface with a velocity of 1.4 m/s. CT, τ is normalized with the CT of DFI case, τ_0 for each device. (b) Experimental results of transition distance in x-direction before separation as a function of SAW power.

To compare the effect of frequency on the dynamics of the impacting droplet, the SAW wavelength, λ, is normalized with the attenuation length of the SAW in the liquid medium, ζ[13].

$$\zeta = \frac{\rho {v_L}^3}{4\pi^2\omega^2(\frac{4}{3}\mu + \mu')} \tag{6.1}$$

The effect of the SAW device resonant frequency on the CT of the droplet is illustrated in Figure 6-3. By increasing the wavelength, SAW propagates longer distances within the liquid medium before significant attenuation. For the devices with a higher resonant frequency, the interaction area between the SAW and liquid medium is decreased[71]. As a result, less momentum is transferred by SAW to the liquid medium during the impingement. As shown in Figure 6-3, the SAW device with a resonant frequency of 110.82 MHz cannot significantly reduce the CT.

On the other hand, by effectively transferring the SAW momentum to the droplet during the impingement, the CT can be significantly reduced by SAW devices with lower resonant frequencies (i.e. 66.10 MHz and lower). However, for the SAW devices with a resonant frequency of 43.12 MHz and 22.04 MHz, and at higher SAW powers ($P = 25\ W$ for 43.12MHz device and $P = 25\ W$ for 22.04MHz device), the droplet impact regime can be changed from complete rebound from the surface to break-up. In this case, a few sub-units are separated from the droplet during the retracting phase (See Figure 6-3). The attenuation length of the SAW can explain the droplet breakup mechanism in the liquid medium. At lower frequencies, the attenuation length of the liquid medium is higher, leading to higher SAW energy reaching the liquid-gas interface. This energy can overcome the surface tension at larger powers, and the droplet will break into smaller sub-units. Considering the effect of frequency on the droplet behaviour on the surface, SAW devices with a resonant frequency of 66.10 MHz are selected to perform our studies.

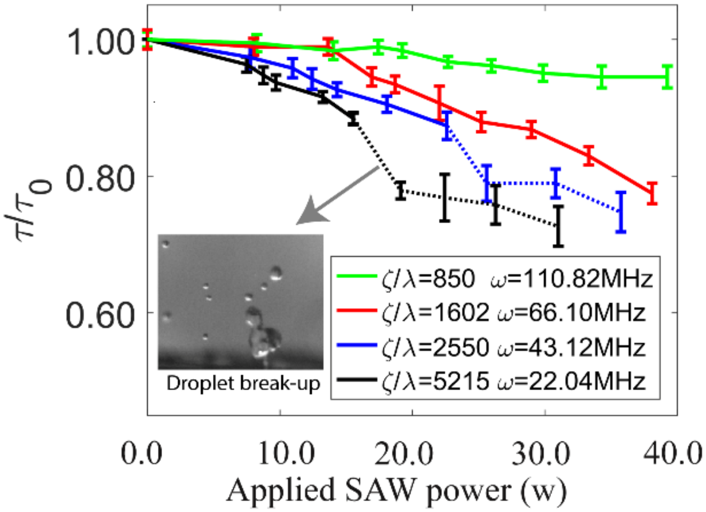

Figure 6-3: Experimental results of normalized CT versus wave power for SAW devices with different frequencies for a droplet with a volume of 3.56 μl and impact velocity of 1.4 m/s impacting the ZnO/Si SAW device surface with CYTOP surface treatment. Solid and dashed lines represent droplet rebounce and break-up regimes, respectively.

Based on this results, the ZnO/Si SAW device with a resonant frequency of 66.10 MHz is selected for CT reduction studies. Figures 6-4(a-c) show snapshots of the droplet impact images on the SAW device surface with the CYTOP surface treatment for three different DFI, TSAW, and SSAW cases, respectively. When the droplet impinges onto the solid surface in both the cases of the DFI and SSAW, it starts to spread into its maximum diameter before it starts to retract, and both the deformation patterns are relatively symmetric with respect to the Z-axis. In contrast, the TSAW shows a more irregular and asymmetric pattern (see Figure 6-4(b)), which is more significant during its maximum spreading and retraction/detachment periods. Figure 6-5(a) shows comparisons between experimental and simulation results as a function of the normalized contact width for all three impact cases. During the spreading and retracting stages (e.g., $t < 6$ ms), the dynamics are comparable for these three cases. The spreading time (τ_s) for all the cases is similar and can be given as $\tau_s/\tau \sim We^{-0.5215}$. The CT for the TSAW case is reduced by ~4.6 ms compared with the DFI case, mainly due to the shortening of the detachment period. Figure 6-5(b) shows the maximum contact width for both the TSAW and SSAW cases at different SAW powers. By increasing the SAW power, the maximum spreading diameter is decreased. As expected, this radius reduction during the impact is higher for the SSAW case, as the X-component of the SAW force from both directions restrain the contact line movement during its spreading phase.

Figure 6-5(c) shows the normalized CT of the droplet versus SAW power. For the TSAW cases, the CT is reduced by increasing the SAW power. Whereas at lower SAW powers (P < 15 w), the CT reduction is not significant, due to the lower energy transferred from the solid surface during the impingement. By increasing the normalized SAW power up to 40 w, the CT is significantly reduced by ~25%. For the SSAW case, the evolution of the CT can be divided into two stages. The CT reduction is observed at powers lower than 25 w, whereas the CT is increased at normalized powers higher than this value.

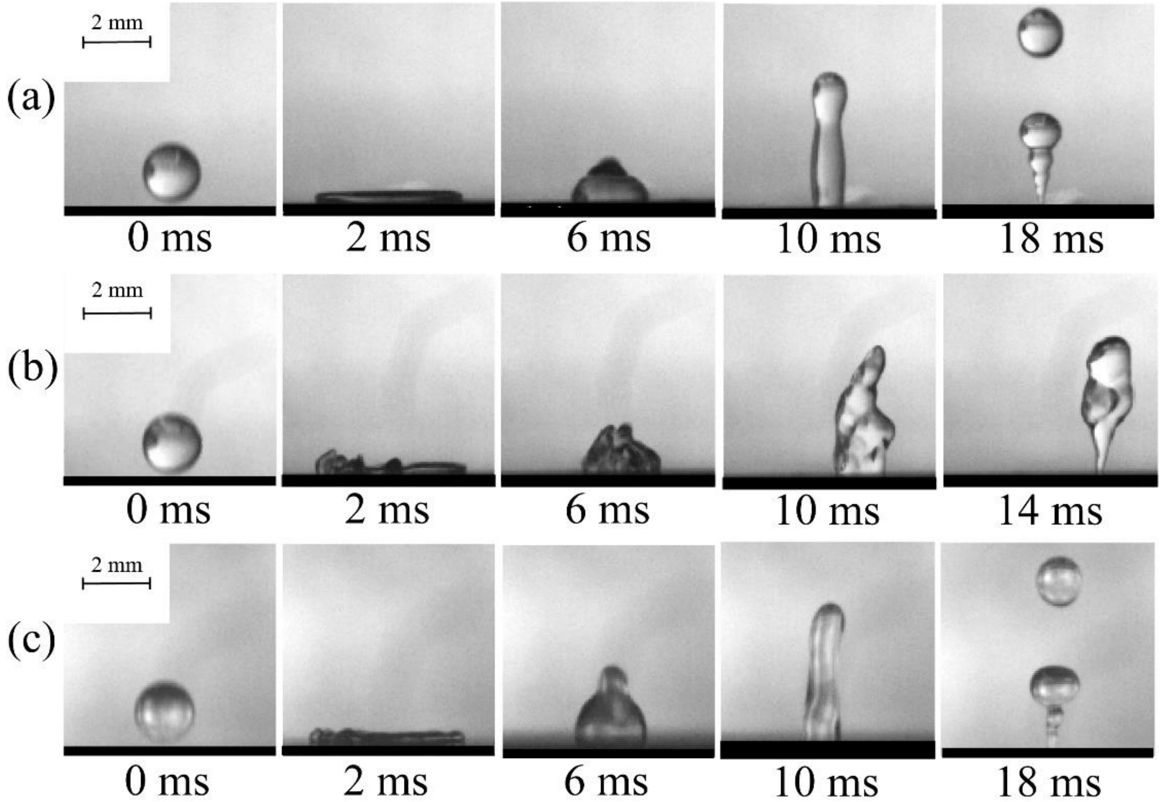

Figure 6-4: Experimental snapshots of a water droplet impinging on the solid surface. (a) Droplet free impact case without SAW applied, (b) impact on ZnO/Si surface with TSAW applied to propagate from left to right (c) impact on ZnO/Si surface while SSAW is applied to the surface. For all the experiments, the droplet impact velocity and volume are respectively 1.4 m/s and 3.56 µl. See Supplementary videos 1-3 for experimental movies.

The CT for the DFI scenarios is not a function of impact velocity[195,216]. Interestingly, the experimental results showed a threshold of droplet impact velocity for a complete rebound from the hydrophobic and non-textured surfaces. As shown in Figure 6-5(d), with the impact velocities lower than 1.26 m/s, the droplet initial kinetic energy is not high enough to detach the whole droplet from the surface at the end of the retract phase. The results in Figure 6-5(d) show that by applying the TSAW, the impact regime can be effectively changed from deposition to rebound for impact velocities lower than 1.26 m/s. Furthermore, applying the TSAW can reduce the CT by ~25% on average for higher impact velocities. The results in Figure 6-5(d) indicate that the CT of the droplet, regardless of the presence of SAW, is not a function of impact velocity. Additionally, the TSAW can change the nature of the untextured hydrophobic surface into a water-repellent surface.

6.1.1.2 Effect of surface wettability

Droplet impact tests with a volume of 3.56 µl and an impact velocity of 1.08 m/s are carried out on the surfaces with and without CYTOP treatments to investigate the effects of surface treatment and wettability on the impact dynamics. The same experiments were repeated in the presence of TSAW with a power of 27 W for both types of SAW devices. The devices' differences in contact angles after the surface treatments are listed in Table 6-1.

During the TPCL motion on the solid surface, CAH generates an adhesion force that resists the droplet motion and dissipates the droplet kinetic energy. To explain the effect of contact angles on droplet impact hydrodynamics, the work done by this adhesion force, W_{adh}, is analysed[195,217]:

$$W_{adh} \propto \frac{cos\theta_r - cos\theta_a}{1 - \cos\theta_a} \tag{6.2}$$

Equation 6.2 shows that during the impact, a higher ACA or a lower CAH can lead to lower energy dissipation during the TPCL motion.

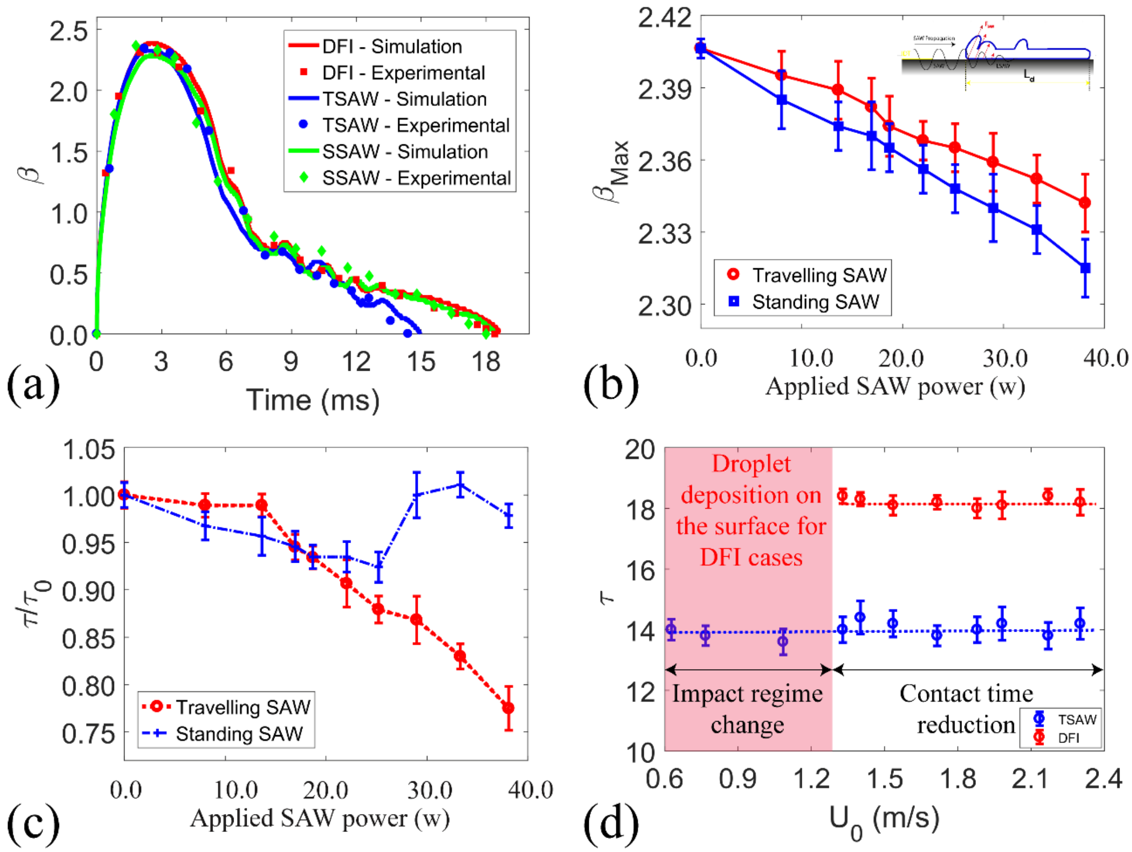

Figure 6-5: (a) Comparing numerical and experimental results for normalized contact width of droplet impact on SAW device for DFI, TSAW and SSAW scenarios. (b) Maximum contact width versus SAW power for both SSAW and TSAW cases. Impact experiments are carried out for a droplet with a volume of 3.56 µl and an impact velocity of 1.4 m/s. (c) Normalized CT as a function of SAW power for a droplet with a volume of 3.56 µl and impact velocity of 1.4 m/s impacting the ZnO/Si SAW device surface with CYTOP surface treatment. (d) CT versus impact velocity for a droplet with a volume of 3.56 µl for DFI and TSAW scenarios. The shaded area represents droplet deposition on the surface for DFI cases.

For the DFI case, due to the adhesion force large work on the surface without hydrophobic treatment, the droplet still stays on the surface after the impact. In the same DFI case, by treating the device surface with a layer of CYTOP, the CAH is decreased by ~35° while the ACA is increased by ~35°, thus reducing adhesion force work by 320%. Thus, a much lower value of kinetic energy loss by the adhesion force can be expected for the CYTOP coated surfaces, and partial rebound of the droplet is observed for the DFI cases on these surfaces. Due to the lower energy dissipation by the CAH resistance work, a sub-unit of the liquid has enough energy at the end of the retraction phase to overcome the surface tension and is separated from the droplet while the bulk droplet still remains on the surface.

However, for both the treated and non-treated surfaces, by applying the TSAW the droplet gains enough kinetic energy during the impingement to bounce off the surface, mainly due to the large vertical SAW momentum dissipated into the liquid by the Z-component of the SAW force. As shown in Figure 6-6, in the absence of SAW, the droplet stays on the surface at the end of the retraction phase. However, by applying the SAW, the droplet gains more energy during the impingement and is fully separated from the surface. Due to the lower energy loss induced by the resistive work for the surface with CYTOP coating, less kinetic energy is dissipated, leading to a faster detachment of the droplet from the surface. Figure 6-6 shows that applying a TSAW can significantly reduce the CT regardless of the surface treatment. Moreover, the droplet impact regime can be changed from deposition on the surface to complete rebound from the surface after applying the SAW.

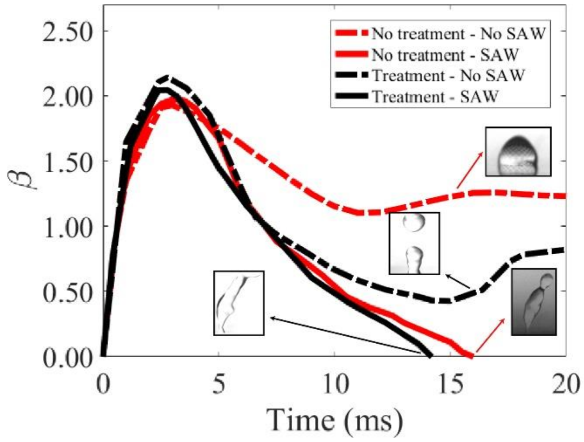

Figure 6-6: Temporal evolution of contact width for droplets impacting the SAW device surface with different wettability. In these experiments, a droplet volume and impact velocity are kept constants at 3.56µl and 1.08 m/s. For each surface coating, experiments are carried out for both DFI and TSAW scenarios. The applied RF power to the IDTs for the TSAW scenario is 27 W. Snapshots of the experimental results confirm that TSAW changes the droplet deposition (red dashed line) and break-up (black dashed line) on the surface to complete rebound (solid lines).

6.1.2 Numerical simulations

In this section, to gain a better insight into the physics of contact reduction by the SAW and to interpret the differences between droplet detachments for both the TSAW and SSAW cases, the SAW effect on the impingement dynamics is investigated using the numerical simulations.

Initially, a series of validation simulations are performed to reproduce the experimental results and test the capability of the developed numerical method. Agreements between the experimental and simulation results are achieved, which can be seen from the results shown in Figure 6-3(a). Since the simulation results can reveal the internal streaming patterns during the impingement process, the numerical results are used to understand the mechanism by which different SAW modes change the CT. As can be seen in Figure 6-7, while the velocity vectors for the DFI and SSAW cases demonstrate relatively regular and symmetric flow patterns, the results for the TSAW case (see Figure 6-7) involve an irregular flow pattern and a robust internal recirculation on the left-hand side.

As the process evolves in time, relatively regular flow patterns for both DFI and SSAW cases are developed. It is worth mentioning that both the DFI and SSAW cases exhibit a very similar spreading flow pattern with an almost identical maximum spreading diameter of 2.4 mm, while the apparent differences between these two cases are only observed at a much later stage, e.g., after 6 ms, which is during the retraction period.

The impingement behaviour of the droplet subjected to TSAW is entirely different (see Figure 6-8). Considering the shape of the interface in Figure 6-8 at a time of 3 ms, the initiation of an asymmetric deformation at the interface near the rim on the left-hand side (where it is subjected to the SAWs) is noticed. This deformation is not present on the right-hand side of this case, neither can be found in the results for DFI and SSAW cases. The same asymmetric deformation can be seen in Figure 6-4(b). This irregular deformation at the droplet interface, which the one-sided SAW has initially triggered at 2.5 ms during the spreading period, is rapidly developed during the retraction phase. The asymmetric retraction of the droplet, in turn, creates even more irregular deformations and instabilities at the interface and rapidly develops an asymmetric flow pattern with a different interface morphology as it can be seen in Figure 6-8 after 7 ms. At the end of the spreading phase, the streamlines around the droplet rims are toward the centre of the droplet, However, there fluid in the droplet centre is still flowing toward the rims. This flows in opposite directions, create a rather complex streamlines inside the liquid medium. Since the applied SAW increase the inward flow in the TSAW scenario, the streamline in this flow is directed toward the centre of the droplet after 3ms. It is expected that these complex flows would cause the flow inside the droplet to become temporary turbulent at some points which needs further investigations.

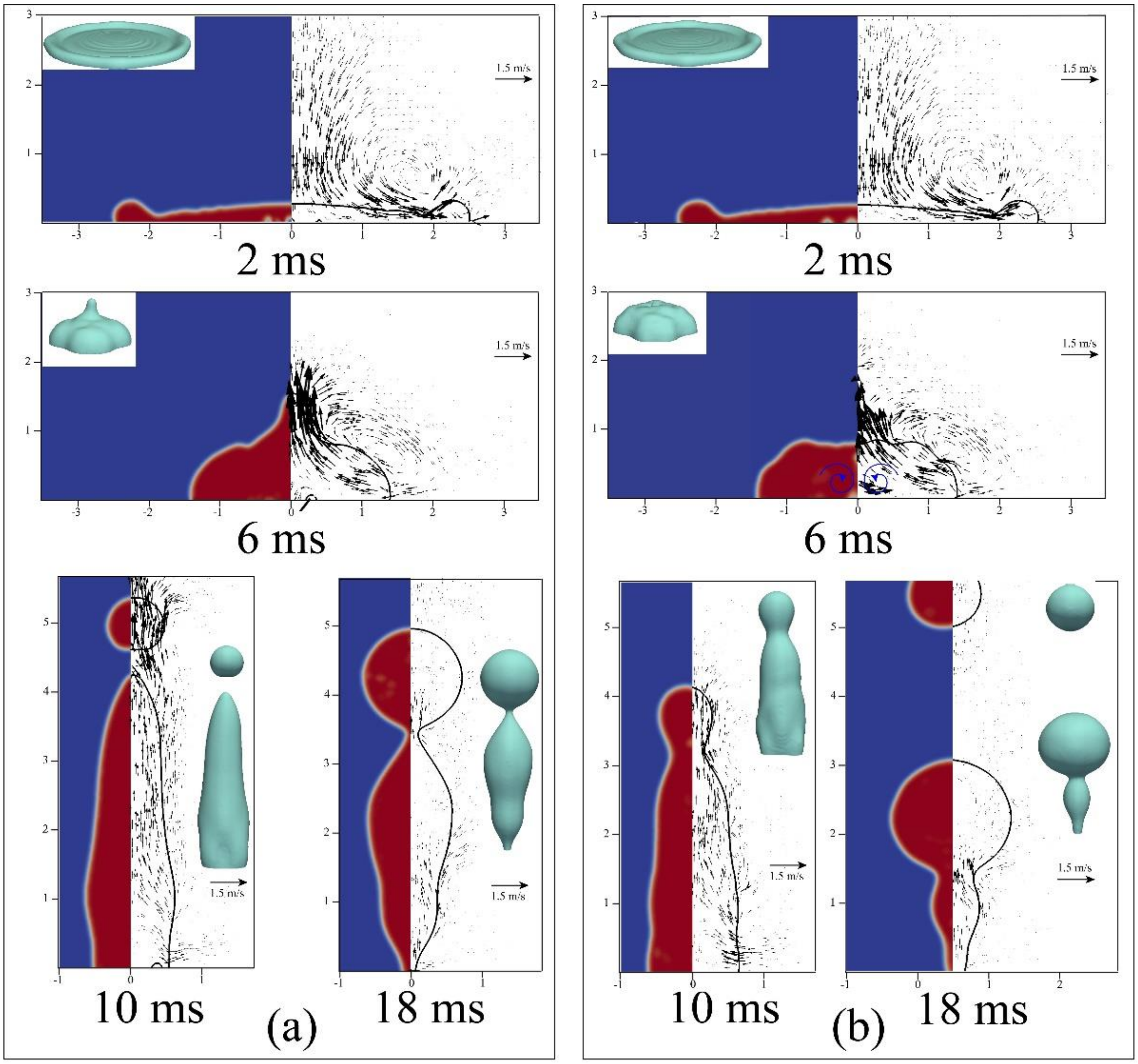

Figure 6-7: Time evolution images of the droplet impact dynamics obtained by numerical simulation. (a) DFI scenario. (b) SSAW propagation on the solid surface during the impact. In all the simulations, the droplet impact velocity and volume are 1.4 m/s and 3.56 µl subsequently.

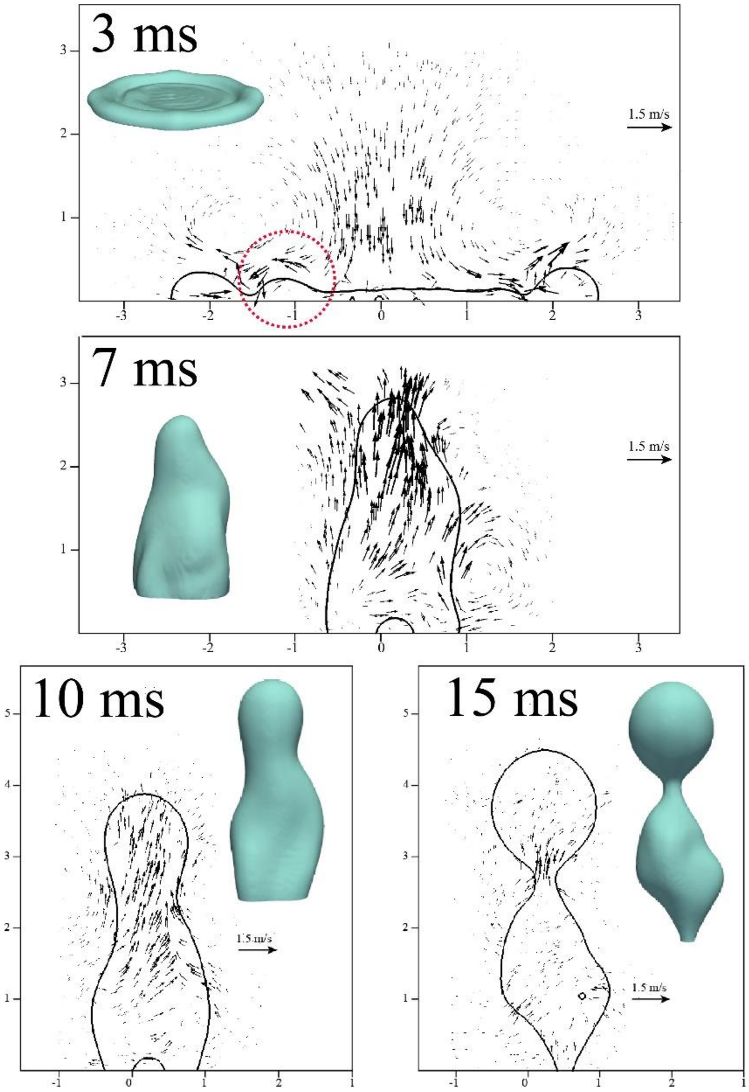

Figure 6-8: CFD snapshots of liquid phase overlaid by velocity vectors during the impingement process in the presence of TSAW propagating from left to right. The droplet impact velocity and volume are 1.4 m/s and 3.56 μl subsequently.

During the impingement process, there are continuous changes of gravitational, kinetic and the liquid-vapour-solid interfacial/surface energies. Furthermore, these energies are continuously dissipated during the impact because of viscous dissipation, wave generation on the interface and sub-unit separation[116,218]. The energy budget and the rates of conversion of the initial energy of the droplet, E_0 into the kinetic energy, potential energy and interfacial energy are analysed here to reveal the real mechanism of CT reduction in the TSAW case. The sum of the kinetic, gravitational, and interfacial energies are defined here as the total energy of the droplet:

$$E_t = \mathrm{K} + \mathrm{SE} + \mathrm{P}E \tag{6.3}$$

The normalized total energy of the droplet during the impingement, E_t/E_0, is illustrated in Figure 6-9(a). Interestingly, more than 70% of the total energy is dissipated within less than 0.5 ms after the onset of impact, which is consistent with the finding in references[116,118,219]. Since the potential energy is one order of magnitude smaller than kinetic and interfacial energy, it is not shown in Figure 6-9.

The variation of kinetic energy (normalized by E_0) shown in Figure 6-9(b), indicates its significant reduction in the first 0.5 ms of the impact time. Results in Figure 6-9(c) shows only 10% of the kinetic energy is stored in the form of interfacial energy during the spreading phase, and the rest of the kinetic energy is dissipated during the first 0.5 ms of impact. The stored interfacial energy at the end of the spreading phase starts to be converted into kinetic energy and causes retraction. The conversion of the interfacial energy into kinetic energy leads to an increase in the kinetic energy between 3-6 ms after the onset of the impact. This increase in the kinetic energy is more significant for the TSAW scenario since the kinetic energy is increased both by interfacial energy conversion and applied SAW energy. However, for the SSAT and DFI scenarios, due to droplet deformation symmetry, a relatively strong internal recirculation field is created within the droplet, which dissipates the kinetic energy.

More importantly, Figure 6-9(a-c) show that the energy conversion rates for all the cases during the spreading and retracting time, e.g., time < 6 ms, are almost identical. This implies that the total initial energy dissipation by viscous liquid and interaction between liquid and solid surfaces are the two dominant processes during the initial 6 ms. However, the differences between these cases begin to appear in the values of kinetic energy, after approximately 3.5 ms, because of the presence of SAW, which is shown in the magnified diagram in Figure 6-9(b). For example, the kinetic energy recovery rate from the interfacial energy between the durations of 3.5 ms and 6 ms, is ~37% higher for the TSAW case than that of the SSAW case. The droplet normalized vertical momentum by the initial momentum is shown in Figure 6-9(d). The differences in the kinetic energy, in turn, increases the vertical momentum of the droplet during the retraction phase. Also, the separation of each sub-unit from the main droplet leads to a sudden decrease in the momentum, which delays the droplet detachment from the surface.

Another interesting phenomenon obtained from Figure 6-9(c) is that while significant differences of the variation of kinetic energy between TSAW with those of SSAW and DFI are observed, the interfacial energy in all the cases is almost identical during the spreading and the retraction phases. This clearly shows that the dissipation rate for the TSAW case during the retraction period is 50% smaller than those of SSAW and DFI cases. Snapshots in Figure 6-7(a-b) reveal the mechanism responsible for such higher dissipation rates in SSAW and DFI cases. It can be seen in Figure 6-7(a-b) at 6 ms that the rather symmetric small-scale vortices have been formed for both the SSAW and DFI cases. Such small-scale vortices have not formed in the TSAW case due to its asymmetric and irregular flow patterns.

All the above results indicate that most energies in the SSAW and DFI cases during the retraction processes are dissipated by the symmetric and very stable internal flow recirculation. In contrast, they have been recovered into the kinetic energy more efficiently in the TSAW case since such an internal recirculation cannot be easily formed due to the asymmetric and the instabilities. This, in turn, leads to a much faster retraction and dispatching processes of the droplet from the surface in this TSAW case. Simulation results show that a shorter CT can be achieved by increasing asymmetry in the liquid flow during droplet impact under the TSAWs.

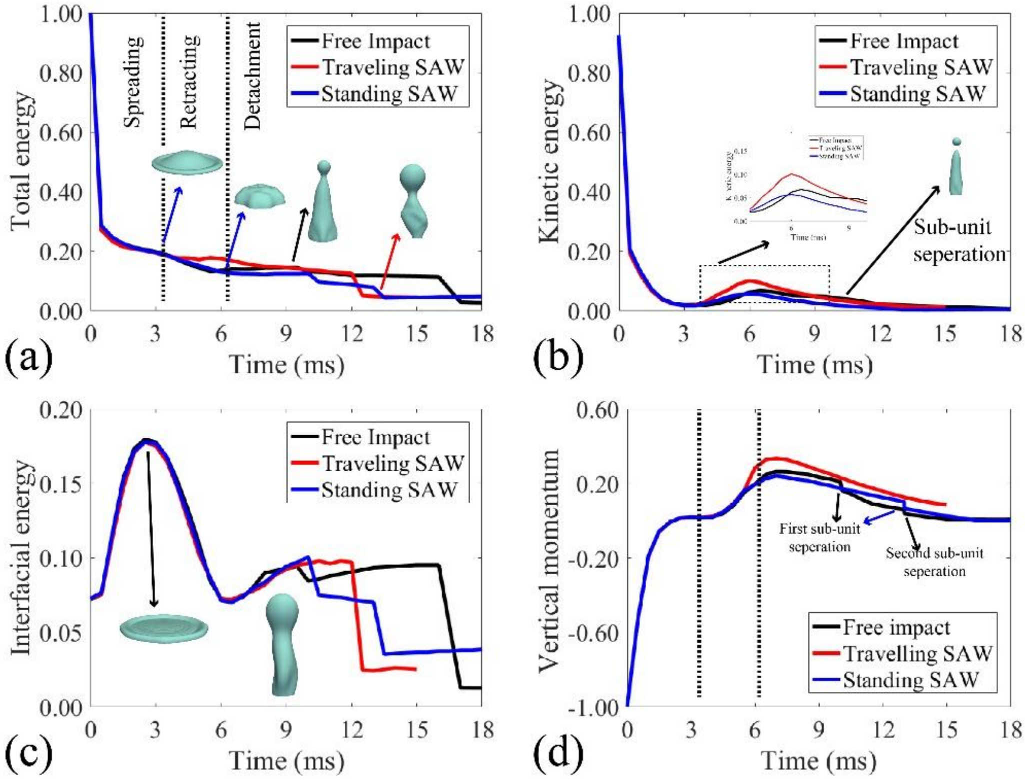

Figure 6-9: (a) Total energy, (b) Kinetic energy, (c) Interfacial energy for FI, TSAW, and SSAW scenarios. In the simulation, the droplet impact velocity and volume are 1.4 m/s and 3.56 µl subsequently. All the energies are normalized by kinetic energy at the onset of impact.

To further verify this idea, the droplet impact dynamics are further investigated using a perpendicular IDT design sample, which can generate two waves propagating in vertical directions into the droplets (see Figure 6-10). Three different cases were tested, and the results are illustrated in Figure 6-10(a). Depending on the droplet size, the CT can be reduced between 20-35%, if compared with the DFI case. Unlike the SSAW cases, in this IDT design, the applied SAWs from both sides create a kinetic energy field that breaks the symmetry of droplet deformation in both X and Y directions and speed up the detachment process of the bouncing droplet. Figure 6-10(b) shows the effects of the impact velocity for the droplet impact dynamics. At lower SAW powers, the CTs for all the cases do not show significant differences. However, at SAW powers greater than 20 w, the CT is considerably reduced with increased impact velocity. This is mainly due to the significant increase of the acoustic wave energy absorbed by the droplets. Results clearly confirm our prediction that by breaking the droplet symmetry along both the X and Y axis, the CT can be significantly reduced. However, the CT reduction achieved using this method is limited by the applied power to the IDTs. Applying powers higher than 50 w could damage the SAW device, and at such high powers, the droplet tends to break-up or splash during the spreading phase.

6.1.3 Discussion

Overall, the presented results clearly indicate that the droplet impact dynamics can be modified and controlled using the thin-film based SAW technique. The key features of the thin-film piezoelectric platform are its seamless, scalable, and localized SAW generation, which can then propagate across entire structural surfaces. Piezoelectric films can be deposited and applied locally on a component to generate vibrations without covering the whole structure surface with the piezoelectric film. The SAW direction and amplitude can also be controlled through electrode shapes and designs, and SAWs can also be generated wirelessly and remotely. Therefore, due to its high efficiency and wireless function, the SAW technique can be used in different engineering applications.

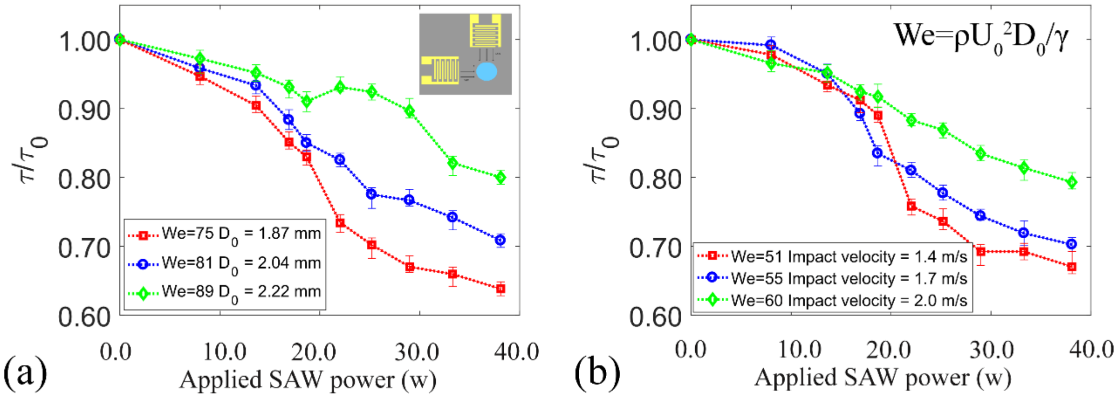

Figure 6-10: (a) Experimental results of normalized CT as a function of SAW power for droplets with the initial diameter of 1.87, 2.04 and 2.22 mm. Impact velocity for all the cases is kept constant at 1.7 m/s. (b) Experimental results of normalized CT as a function of SAW power for droplets with impact velocities of 1.4, 1.7, and 2.0 m/s. Droplet initial diameter is kept constant at 1.87 mm for the experiments presented in this graph. Error bars represent SD of CT.

6.2 Droplet impact control on inclined surfaces

In this section, the application of SAWs for the active control of droplet impact dynamics (including impact regime, contact time, and rebouncing angle) on inclined surfaces is investigated. The droplet impact regime can be effectively modified by applying SAWs with different propagation directions and powers on inclined surfaces. Additionally, different impact parameters such as CT, maximum spreading diameter, and rebouncing angle can be dramatically altered. It is expected that by applying upward SAW (USAW) or downward SAW (DSAW) and as a result of changing the energy budget within the liquid medium, the motion of the leading and tailing edges of the droplet (See Figure 6-11 for definitions) would be altered. Consequently, impact characteristics parameters such as CT, maximum spreading ($\beta_{Max} = L_{cl\,,max}/D_0$, where $L_{cl\,,max}$ is the maximum spreading width along the direction tangential to the surface), movement along the surface, (δ/D_0), and rebounce angle ($\theta_{Rebounce}$, which is defined as the angle between the surface normal vector and the line connecting the separation point to the droplet tip at the separation moment in an anticlockwise direction) could be altered in a programmable and controllable way. Definitions of all these parameters are illustrated in Figure 6-11.

To examine the effect of SAW on droplet impact, three scenarios are proposed, e.g., droplet free impact (DFI), droplet impact in the presence of USAW, and DSAW on the inclined surface, as illustrated in Figures 6-11(a-c). Using the developed CLSVOF mathematical model, first, the physics of the droplet impact on inclined surfaces is investigated. Later the effect of critical parameters such as inclination angle, impact velocity, SAW direction and power are experimentally investigated.

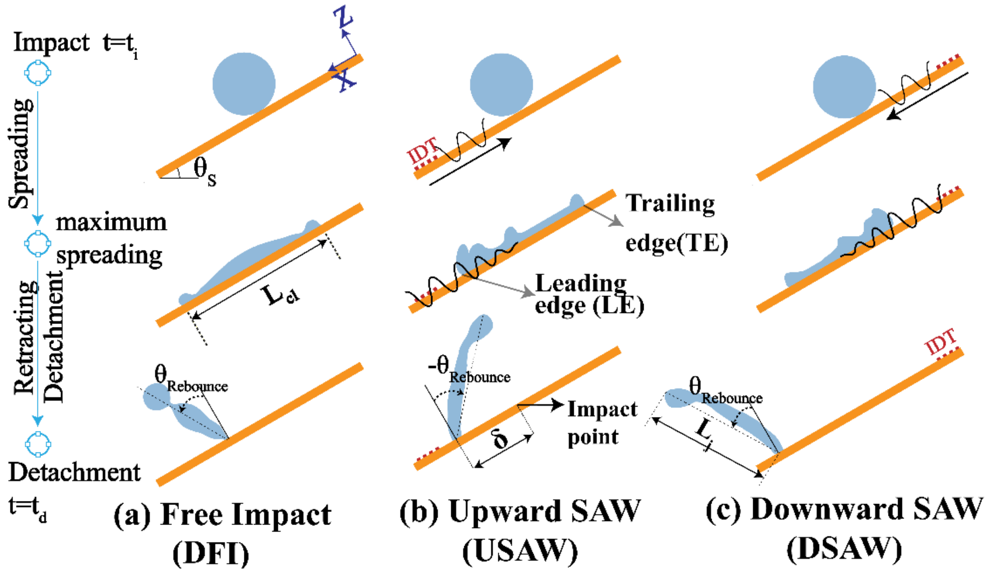

Figure 6-11: Schematic views of different scenarios of droplet impact on inclined surfaces. (a) Droplet free impact (FI), (b) Droplet impact in the presence of USAW, (c) Droplet impact in the presence of DSAW. The positive direction of the rebouncing angle is in the anticlockwise direction from the surface normal direction. (d) Schematic view of SAW and gravitational force interaction.

6.2.1 Impact mechanism based on numerical simulations.

First, droplet impact and bouncing dynamics of a spherical droplet on a solid surface with an inclination angle of 30^o for three cases of DFI, USAW, and DSAW scenarios are simulated. For all the simulation cases, the droplet volume and impact velocity are kept constants at 3.5 µl and 1.4 m/s, respectively. A set of experiments with the same parameters was performed to validate the numerical results. A quantitative comparison between experimental and simulation results for the droplet contact width during the impact is shown in Figure 6-12(a). A good agreement between the experimental and numerical results can be found, proving that simulation results can be precisely used to analyse the SAW effect on droplet impact. Moreover, to qualitatively validate the numerical findings, comparisons between the droplet interfaces from numerical and experimental results are presented in Figures 6-13. Both the quantitative and qualitative comparisons show that the developed numerical method can capture the interaction between the acoustic waves and liquid medium and the TPCL movements.

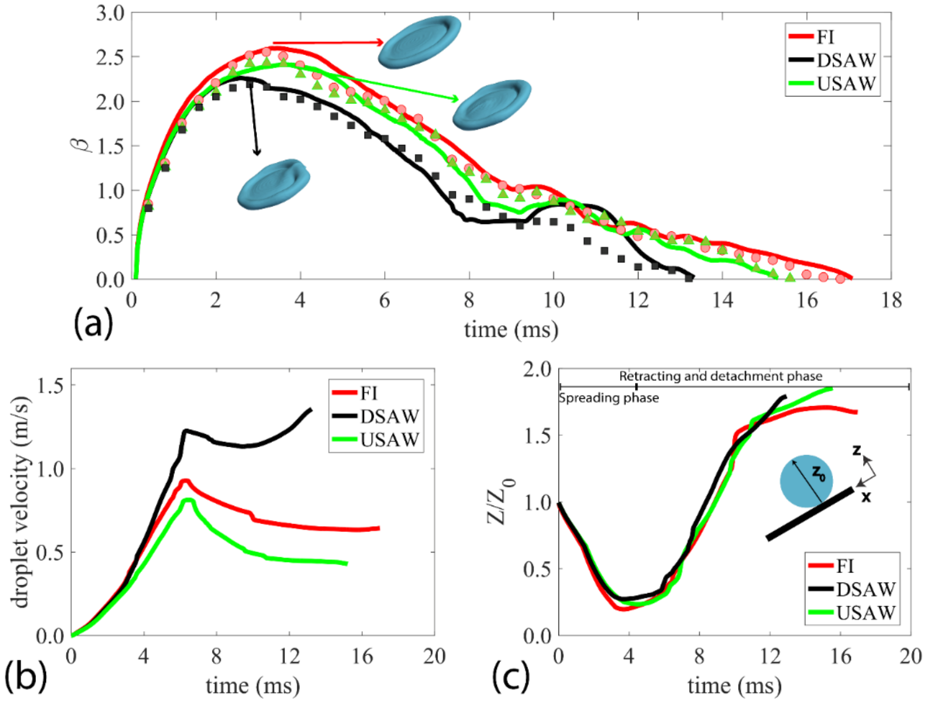

Figure 6-12: (a) A quantitative comparison between the simulation and experimental results for the droplet contact width evolution. (b) Temporal droplet velocity (i.e., an average of leading and tailing-edge velocities) in the X-direction. (c) Temporal evolution of normalized droplet tip height in Z-direction.

As shown in Figure 6-12(a), the droplet continuously spreads to its maximum diameter on the inclined surface for all three scenarios, and then the thickened rim starts to retract toward the centre of the liquid. For the DSAW (USAW) scenario, the applied SAW energy restricts the tailing-edge (leading-edge) from spreading. For the DFI scenario, the contact width reduces until the droplet is separated from the surface after 16.8 ms. By applying DSAW, the maximum spreading width and the time to reach this width are reduced (i.e., 2.4 ms compared to 3.6 ms for USAW and DFI cases). After reaching the maximum spreading width, the contact width is gradually reduced until 8 ms after the onset of the impact. Then, it stays nearly a constant for ~2.6 ms since the droplet is moving on the inclined surface. Afterwards, the contact width is reduced sharply until the droplet is separated from the surface after 13.6 ms. In the case of the USAW, during the whole retract phase, the contact width is lower (higher) than the DFI (DSAW) case. Moreover, the sharp reduction in spreading width is not observed at the end of the retracting phase for the USAW scenario.

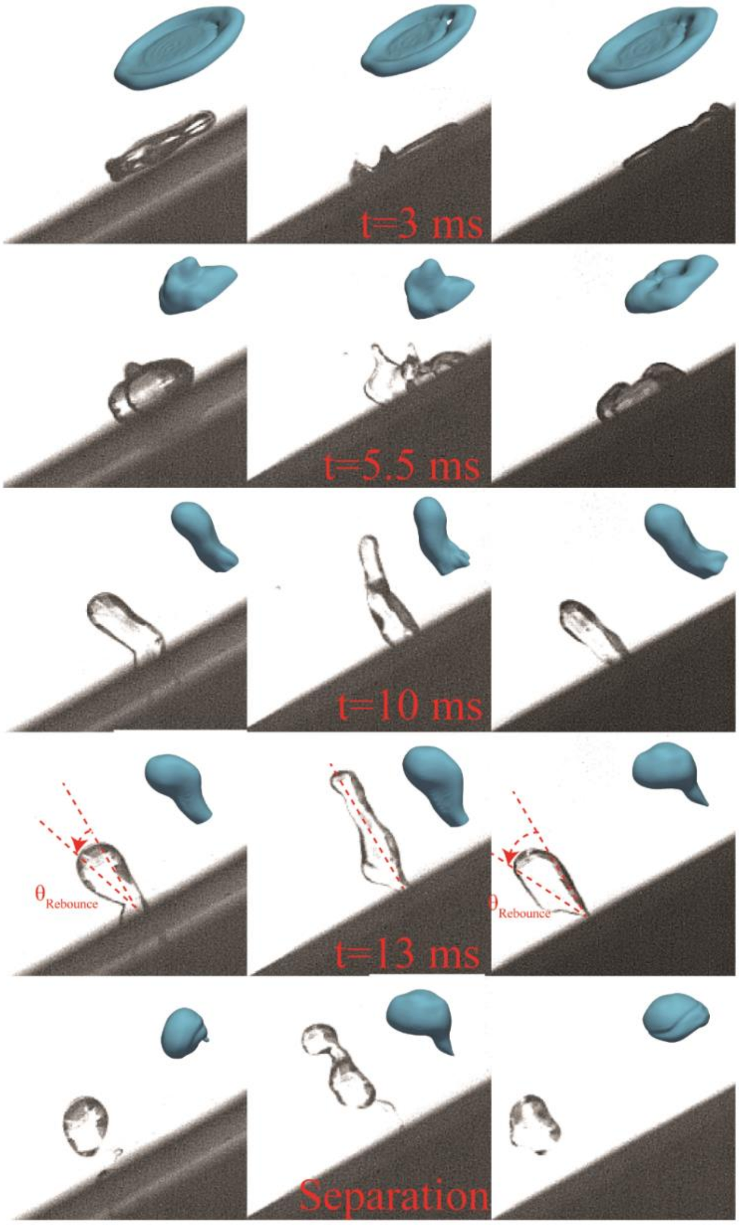

(b) DFI **(b) USAW** **(b) DSAW**

Figure 6-13: Comparisons between experimental and simulation results of the droplet interface during the impact on a surface with an inclination angle of 30^{o} for (a) FI scenario, (b) USAW scenario, and (c) DSAW scenario. In both simulation and experiments, a droplet with a volume of 3.5 µl and *We* number of 50 is impacting on the surface.

Figure 6-12(b) shows the average droplet velocity along the X-direction for the three cases. During the spreading phase, the velocities do not show considerable differences. After ~2.8 ms from the onset of impact, the droplet in the DSAW scenario starts to accelerate much faster than the other two scenarios. In general, since the applied DSAW (USAW) energy promotes (restricts) the droplet motion in the X-direction, the droplet has a higher (lower) average velocity compared to the DFI scenario. The ratio of the droplet tip height (highest point in Z-direction in liquid medium), Z, to its initial value, Z_0 (see Figure 6-12(c)) shows that the droplet tip heights have a rather similar behaviour during the impact. However, since the maximum spreading diameter of the droplet is larger for the DFI scenario than those of USAW and DSAW scenarios, the droplet tip position is lower for this case at its maximum spreading.

The internal streaming patterns within the liquid medium during the impingement for the designed three scenarios is are investigated. Snapshots of internal streaming patterns in the middle plane of the droplet are illustrated in Figure 6-14. For the DFI case, 2 ms after the onset of the impact, there is a strong velocity field in the region close to the leading-edge. However, due to viscous dissipation, this velocity field is not apparent in the tailing-edge, as shown in Figure 6-14(a). After 6 ms, while the leading-edge has moved ~1.4 mm on the inclined surface, the tailing-edge has moved as large as 3 mm, resulting in a significant internal flow generation in the tailing-edge area (see Figure 6-14(a)). After 16 ms, near the last moment of the impingement, the droplet contact width is minimized, and the internal streaming pattern is faded compared to previous snapshots.

By applying USAW, after 2 ms from the onset of the impact, a hunch is noticeable in the centre of the spreading droplet on the inclined surface. Since the USAW is restricting the droplet to spread downward, the velocity field around the leading edge is much weaker than that of the DFI case. After 6 ms, the tailing-edge has moved ~2.6 mm. In the liquid medium close to the tailing-edge, a velocity field along the X-direction is generated. A strong streaming pattern along Z-direction is observed near the centre of the droplet because of applied SAW energy, which can push the droplet upwards. Finally, after 15 ms, the droplet is separated from the surface with a faded internal streaming pattern in the area close to the droplet tip and a rather weak internal streaming field in the droplet root, mostly along the Z-direction.

For the DSAW scenario (see Figure 6-14(c)), during the spreading phase, the SAW energy causes the restriction of spreading from the tailing-edge, and a strong streaming pattern is created in the area close to the tailing-edge. After 6 ms, the droplet tip height is 21% larger than that of the DFI case (see Figure 6-14(c)), and the internal streaming pattern in the droplet root is almost disappeared. However, a strong velocity field is created in the droplet tip area. After 12.5 ms, the droplet is at its final moments of impingement, and the liquid medium has a relatively strong velocity field inside.

The simulation results clearly show that the energy of SAW has changed the internal recirculation patterns upon the droplet impinging onto the inclined surfaces. By applying the USAW, the velocity field (especially in the leading-edge area) is slightly rotated toward Z-direction in all the impact stages. However, the intensity of the internal streaming patterns looks similar to that of the DFI scenario. On the other hand, in the DSAW scenario, it is apparent that the liquid medium has a much stronger internal recirculation pattern during the impact.

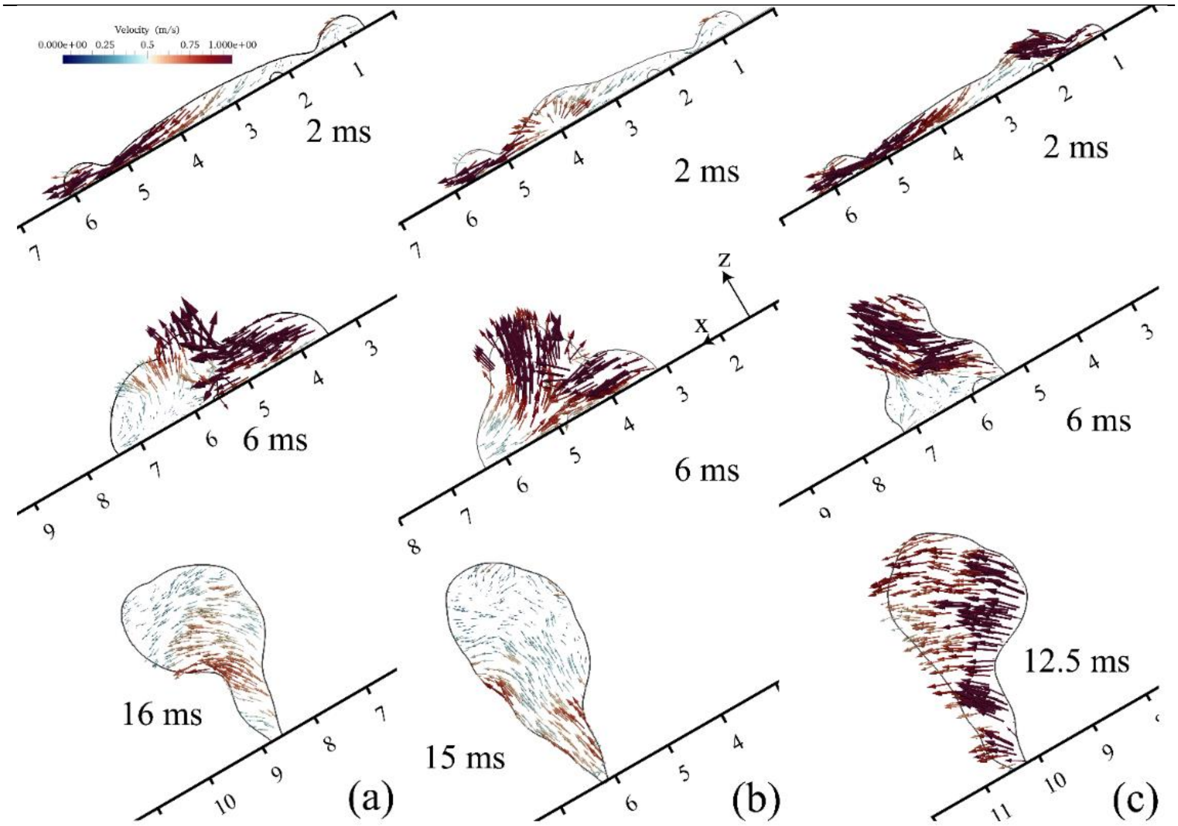

Figure 6-14: CFD snapshots of droplet interface overlaid by velocity vectors at spreading, retracting, and detachment stages for (a) FI scenario, (b) USAW scenario, and (c) DSAW scenario. For all the cases, a droplet with a volume of 3.5µl and *We* number of 50 is impacting on a surface with an inclination angle of 30^{o}.

To quantitively analyse the applied SAW energy effect, we further investigate the energy budget during the designed scenarios' impact. Results of the evolution of energies for the simulated three scenarios are presented in Figure 6-15. The initial energy of the droplet normalizes all the energies in Figure 6-15 at the onset of the impact (e.g., $E_0 = \frac{1}{2}V_{Dr}u^2 + \gamma_{lv}s_{a0}$). Figure 6-15(b) shows that the gravitational energy occupies less than ~2 % of the total energy during the impingement for all the cases; therefore, it is not considered in the following analysis. Figure 6-15(c) illustrates the total energy dissipation from the impact moment.

For the DFI scenario at the onset of the droplet impact, 79% of its total energy is in the form of kinetic energy, and during the spreading phase (e.g., the blue area in Figures 6-15(a-c)), the kinetic energy is converted to the surface energy or dissipated by viscosity and capillary dissipation. During the droplet spreading, surface energy is increased by 18%, and ~44% of the system energy is dissipated. At the end of the spreading phase, there is a transient time when the surface energy stays almost a constant. During the retraction phase, the surface energy is converted back to kinetic energy (e.g., the red area in Figures 6-15(a-c)). At the end of the retraction phase, the surface energy is decreased by 23.3% from its maximum, and the kinetic energy is increased by 7%. After ~7 ms, the droplet kinetic energy starts to decrease due to the energy dissipation, and the droplet is separated from the surface after ~16.8 ms.

By applying the DSAW, the X-component of the SAW force along the inclined surface prevents the tailing-edge from spreading, and thus, the maximum surface energy is ~4.2% lower than the DFI case. On the other hand, during the impingement, the total SAW energy, which is transferred to the liquid medium (as shown in the small graph in Figure 6-15(a)), is as much as 66% of the initial energy of the droplet. The droplet kinetic energy at the end of the spreading phase is decreased to ~20%, and the energy dissipation is ~60%. However, due to applied SAW energy and conversion of the surface energy, the kinetic energy of the droplet starts to increase sharply. Once all the energy stored as surface energy is converted back to kinetic energy (i.e., after ~8 ms), the kinetic energy stays almost constant, meaning that the applied SAW energy is dissipated during this period. Due to the relatively higher kinetic energy after the spreading stage, the droplet detaches from the surface after ~13.6 ms, which is 20% shorter in contact time than the DFI case.

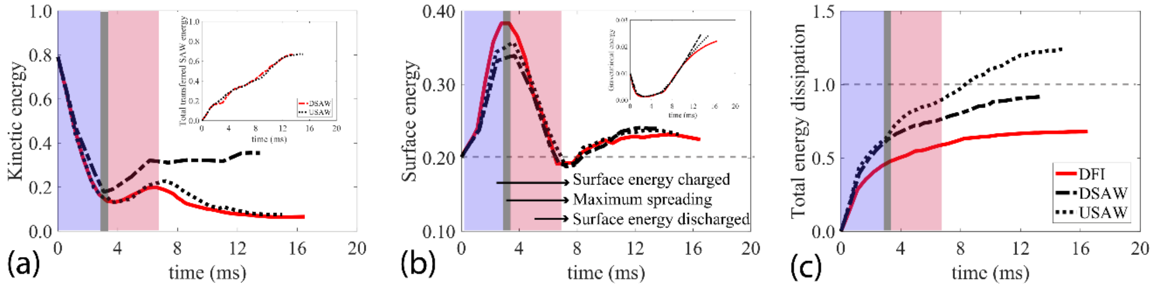

Figure 6-15: Simulation results of the effect of SAW on the temporal evolution of energy. (a) The normalized kinetic energy of the liquid medium. The embedded graph represents the total energy of the droplet. (b) The normalized surface energy of the liquid. Normalized gravitational energy is presented in the embedded graph. (c) Energy dissipation during the impingement. Blue and red areas represent the droplet spreading and retracting, respectively. All the energies are normalized with the total droplet energy at the inset of the impact.

For the USAW case, during the 6 ms after the onset of the impact, the kinetic energy has a rather similar trend to the DFI scenario. Nevertheless, between 6-10 ms after the impact, the droplet kinetic energy is ~5% higher on average than that of the DFI case. The results indicate that despite the applied SAW energy to the droplet for both USAW and DSAW scenarios are equal (see the embedded graph in Figure 6-15(a)), the droplet gains less kinetic energy in the USAW cases due to significant energy dissipation. This can be explained by the fact that the X-component of the SAW force is in the opposite direction of the component of gravitational force, and thus (as a result of interaction between these forces in a 3D pattern) a rather strong internal recirculation field with vortices is generated within the liquid medium, thus dissipating more energy. Interestingly, for the USAW case, the amount of dissipated energy by viscosity is higher than the initial droplet energy. The ratio of the total dissipated energy for USAW and DSAW cases, $\frac{E_{dis,USAW}}{E_{dis,DSAW}}$ is ~1.35. This result is significant since it shows that by changing the SAW propagation direction, energy dissipation within the liquid and kinetic energy can be modified.

By comparing the simulation results from the above three scenarios on the inclined angled plate, it is concluded that by changing the direction of the applied SAW, the amount of kinetic energy and energy dissipation during the impingement can be altered to control impact parameters such as contact time, and droplet movement on the surface during the impact. After understanding the physics behind the effect of SAW on the droplet impact on the inclined surface, the effects of SAWs on the impact dynamics are experimentally investigated in the next section.

6.2.2 Experimental investigation of droplet impact on inclined surfaces

Figure 6-16 shows snapshot examples of the impact of a droplet with a volume of 3.5 µl and a Weber number of ~30.3 on a surface with an inclination angle of 15^o, for the designed three scenarios. For the DFI case (see Figure 6-16(a)), the droplet first spreads to its maximum diameter forming a crater shape, and then the rim starts to retract toward the centre. In this case, the droplet kinetic energy at the end of the retraction phase is not large enough to detach the whole droplet from the surface, leading to deposition of the droplet after a series of vibration on the surface.

On the other hand, numerical results revealed that by applying the USAWs or DSAW onto the inclined devices, the droplet energy budget is changed (depending on the SAW power), and the correspondingly the droplet dynamics and impact regime are changed. As shown in Figure 6-16(b), the applied USAW deforms the leading-edge of the droplet during the spreading phase, and after ~6 ms, a liquid beam starts to form at the end of retracting phase. As discussed in the numerical results, the USAW can slightly increase the kinetic energy of the droplet during the impingement process. As a result, the droplet is detached from the surface after ~18 ms in a rotating sphere shape (see Figure 6-16(b)). More interestingly, by applying DSAW, the tailing-edge is deformed during the spreading phase, and the kinetic energy of the liquid is intensively increased, leading to a liquid beam formation after ~10 ms. The enhanced jet is separated from the surface along a rebouncing angle of 41° after ~17 ms. The time evolution plot of the droplet contact line width is illustrated in Figure 6-17. The comparisons between these three cases show that by applying the SAWs, critical parameters of droplet impact such as the contact time, impact regime, and rebouncing angle can practically be modified.

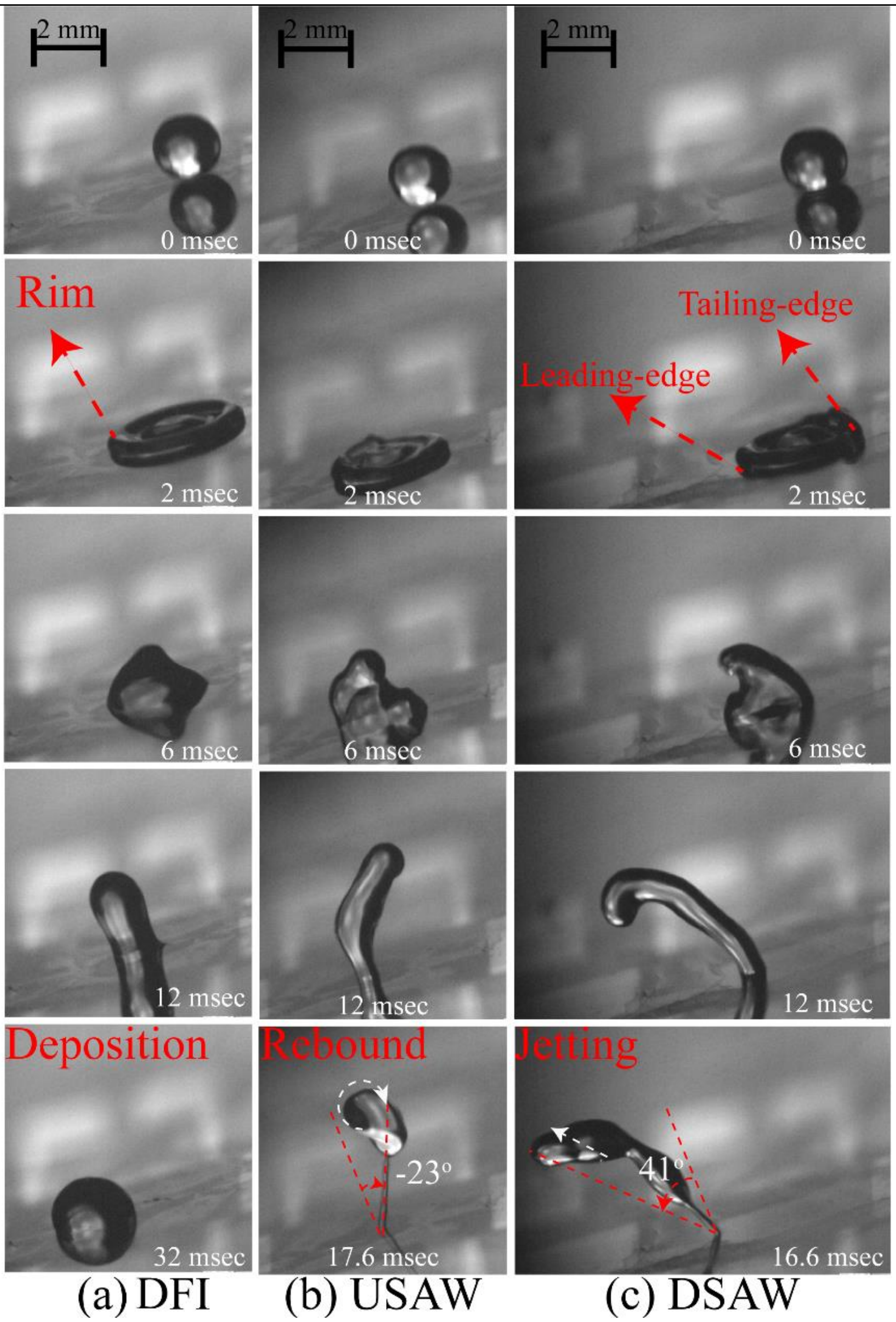

Figure 6-16: Sequential snapshots of a water droplet impacting on the solid surface with an inclination angle of 15° and a Weber number of 30.3 for (a) FI scenario, (b) USAW scenario with the power of 15 *W* applied to the IDTs, (c) DSAW with the power of 15 *W* applied to the IDTs. In all the scenarios, DI water droplet with a volume of 3.5 µl is impacting on the hydrophobic surface of the SAW device. See the supplementary videos V4-V6 for the experimental movies.

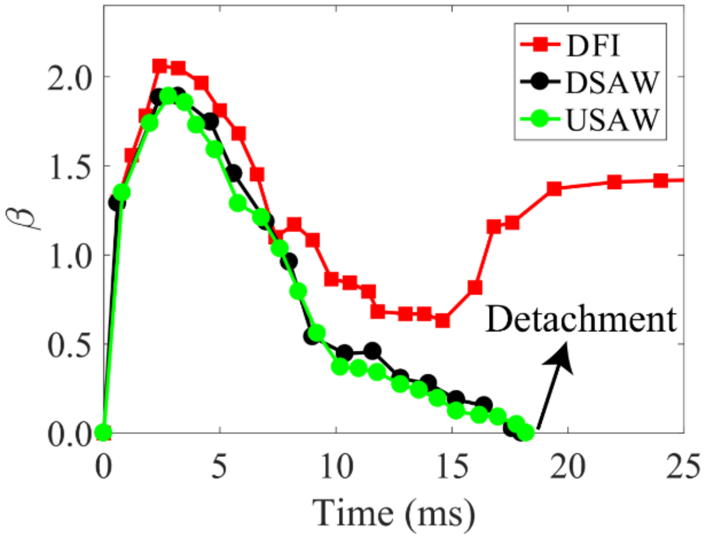

Figure 6-17: (a) Droplet normalized contact width versus time for the experimental cases presented in Figure 6-16. Lines are provided as a guide for the eyes.

6.2.2.1 Effects of Inclination Angle on Impact Dynamics

A set of experiments are conducted using the DI water droplets with a volume of 3.5 µl and an impact velocity of 1.4 m/s to understand the effects of inclination angle on the impact dynamics in the presence of SAW. The obtained distribution maps of droplet impact regimes for the cases of USAW and DSAW are shown in Figures 6-18(a-b), respectively. The impact regimes are categorized into droplet deposition, partial and complete rebound, jetting rebound, and break up (see Figure 6-19).

In the absence of SAW and at a low inclination angle (e.g., 15° and less in this study), the droplet cannot be detached from the surface after the impact. However, by increasing the inclination angle above 15°, the droplet can be fully detached from the DFI scenarios' surface. As the inclination angle increases, the tangential component of the gravitational force is increased. Accordingly, the droplet has more kinetic energy during the retracting phase, which results in full detachment of the droplet from the surface.

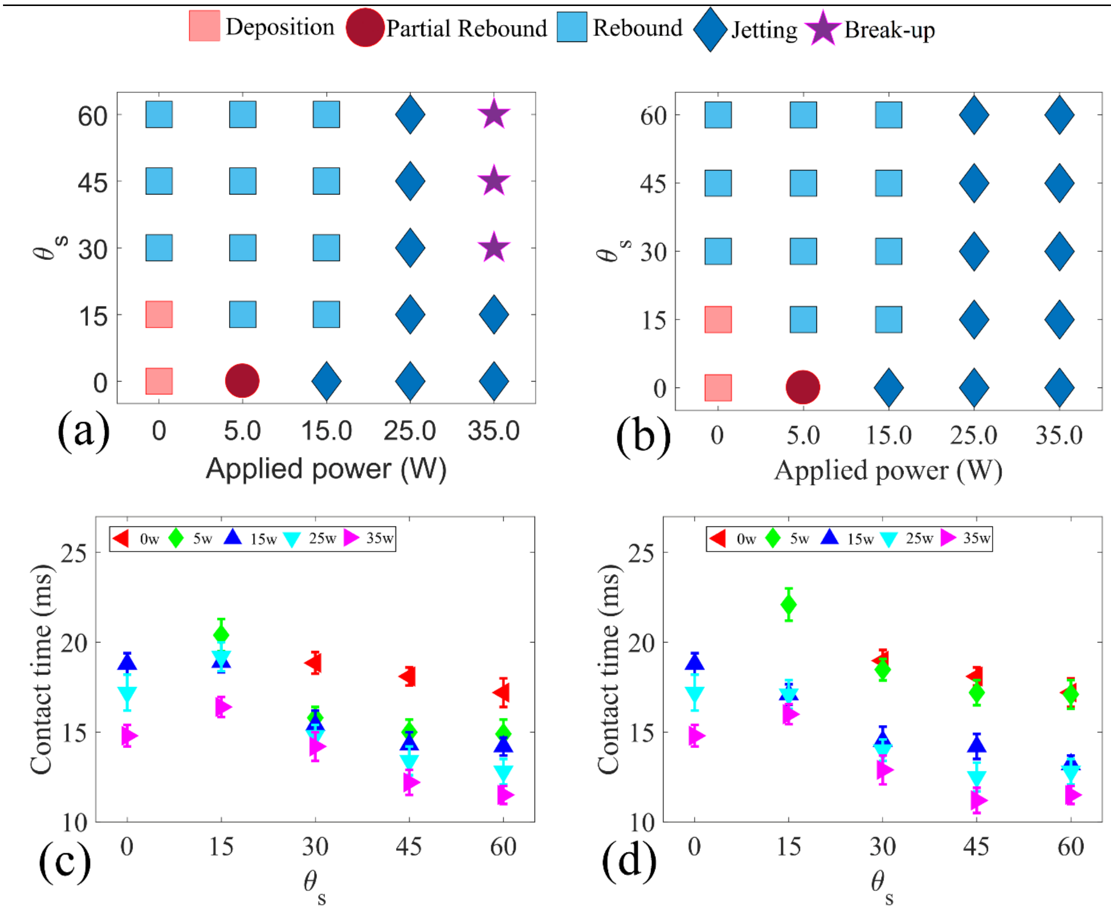

Figure 6-18: (a) Droplet impact regime map as a factor of applied SAW power and surface inclination angle for (a) USAW, and (b) DSAW scenarios. Contact time versus inclination angle for different applied SAW powers for (c) USAW, and (d) DSAW scenarios. Note that the contact time is not shown for the deposition and partial rebound cases. In all the cases, the droplet with a volume of 3.5μl and Weber number of 50 impacts on the ZnO/Si SAW device.

By applying SAWs during the droplet impacting inclined surfaces, the impact regime can be changed among rebound, jetting, or droplet break-up with the gradual increase of applied powers. For the DSAW cases, by applying SAWs with high powers (i.e., with powers higher than 25 *W* applied to the IDTs), the liquid droplet is bounced off the solid surface as a thin beam. However, droplet break-up into several sub-units is sometimes observed in the USAW cases at very high applied powers. In these cases, the droplet starts to break-up after reaching the maximum diameter since the surface tension force cannot overcome the applied SAW momentum, which has been transferred into the liquid medium.

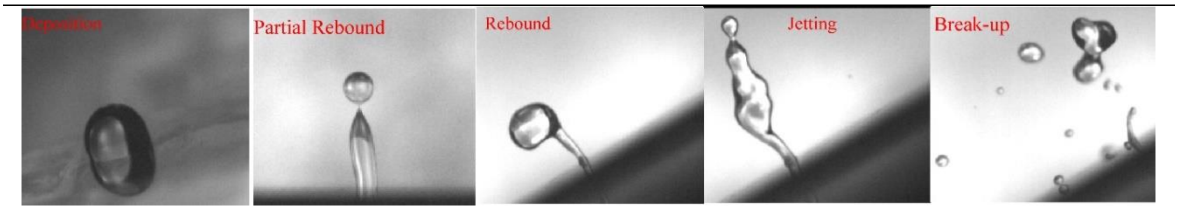

Figure 6-19: obtaining diverse impact regimes on the inclined surfaces by applying SAW

The corresponding contact times for the designed experiments are presented in Figure 6-18(c-d). As discussed, for inclination angles of 0^{o} and 15^{o}, the droplet stays stationary on the inclined surface at the end of the retract phase, and thus the contact time is defined as indefinite for these cases. Nevertheless, SAWs can change the droplet impact regime from deposition to complete rebound or jetting from the surface. Moreover, by increasing the applied SAW power at each fixed inclination angle, the droplet contact time is reduced. The detailed analysis shows that the contact time can be effectively reduced by applying SAW. For instance, as shown in Figure 6-18(d), for the surface inclination angle of 45^{o} by applying DSAW with the power of 35 W, the contact time can be reduced as much as 30% compared to the DFI scenario. From the simulation results, it is known that by applying SAWs (both the USAW and DSAW), the energy budget of the droplet is changed, and the droplet gains more kinetic energy during the retract phase to bounce off the inclined surface.

Figure 6-20 presents the effect of inclination angle on maximum spreading diameter β_{max}, rebounding angle, and movement along the surface. As shown in Figures 6-20(a) and (d), by increasing the inclination angle for the DFI scenarios, the value of β_{max} increases. For all the scenarios, by increasing the inclination angle, the tangential component of the gravitational force, $mgsin\theta_{s}$, enhances the spreading of the droplet front but suppresses the spreading of the back of the droplet. However, when the SAWs are applied, the tangential component of the SAW force, $f_{SAW}sin\theta_{R}$, limits the spreading of the droplet (e.g., the leading edge for USAW and the tailing edge for DSAW). At a lower inclination angle, the SAW force is dominated in limiting the spreading of the droplet. However, by increasing the inclination angle, the gravitational force becomes dominant, which leads to larger values of the maximum spreading diameters. The maximum spreading is reduced more so by applying USAW compared to DSAW for all the angles.

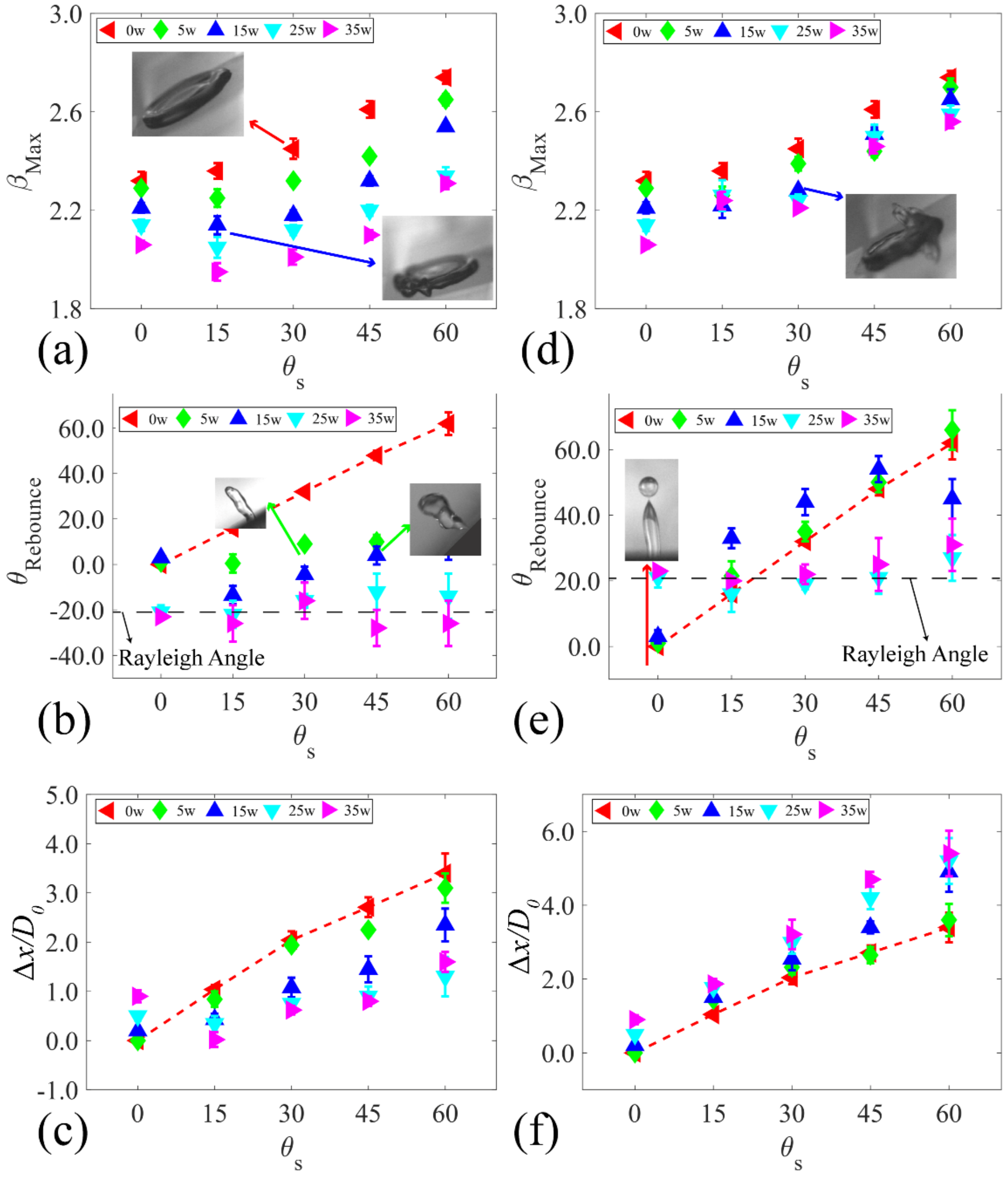

Figure 6-20: Effect of surface inclination angle on (a) maximum spreading, (b) Rebounding angle, and (c) Droplet movement along X direction for USAW scenario. Effect of surface inclination angle on (d) maximum spreading, (e) Rebounding angle, and (f) Droplet movement along X direction for DSAW scenario. In all the cases, the droplet with a volume of 3.5µl and a Weber number of 50 is impacted on a ZnO/Si SAW device.

Results of the droplet rebounding angles (see Figure 6-11 for definition) are illustrated in Figures 6-20(b) and 7(e). In general, the interaction between the applied SAW force and the gravitational force determines the droplet rebouncing angle. For the DFI scenarios, since the only force redirecting the droplet during the rebouncing is gravity, the rebouncing angle of the droplet has a nearly linear trend as a function of inclined angle (see the dashed red line in Figure 6-20(b) and 6-20(e)). However, by applying lower SAW powers to the IDTs (i.e., 5-15 W), the interactions among these forces and the corresponding rebouncing angles are modified compared to those of DFI cases. At higher powers, the droplet is fully detached from the surface along the Rayleigh angle. The results show that at higher powers, the SAW force is large enough compared to the gravitational force and will drive the droplet as a jet along the Rayleigh angle of the SAW device along the inclined solid surface regardless of the inclination angle. These results show that, by changing the SAW power and direction on any inclination angle, the droplet rebouncing angle can be changed. To examine the repeatability of the jet redirecting by SAW, droplet impact with *We* number of 50 on a surface with an inclination angle of 15^o was repeated 16 times, while a power of 25 W was applied to the IDTs. The histogram results of the tests are presented in Figure 6-21, which showed good repeatability.

Figures 6-20(c) and 6-20(f) show the results of distances for droplet movements along the X-direction, between the impact and detachment. As explained by the simulation results, for the DSAW cases, the tangential components of SAW and gravitational force tend to move forward the droplet in the X-direction by increasing the SAW power or inclination angle, the value of δ increases. However, in the USAW cases, the tangential components of gravitational and SAW forces work against each other, and the value of δ is decreased by increasing the SAW power.

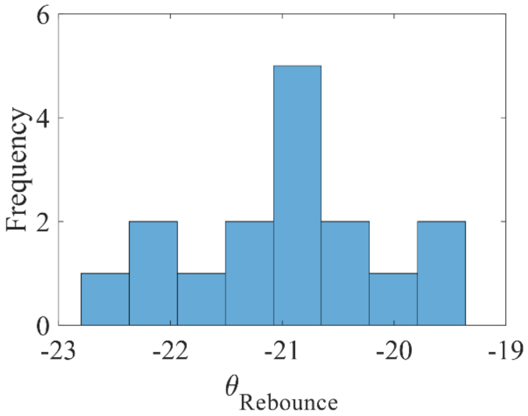

Figure 6-21: Frequency of droplet rebouncing angle for 16 experiments on a surface with an inclination angle of 15° and droplet impact velocity of 1.4 m/s. The experiments war repeated four times a day in 5 consecutive days to test the repeatability of the droplet rebouncing angle. During the impact, USAW with the power of 35 W was propagating on the surface.

6.2.2.2 Effect of Droplet Impact Velocity

Figures 6-22(a-b) present the impact regime map results as a function of *We* number and SAW applied power, with the droplet volume and inclination angle of the surface fixed at 3.5 μL and 15°. For the DI cases and at lower *We* numbers (i.e., 10 and 30), the droplet stays stationary on the surface after the impact, and the contact time is indefinite. By increasing the *We* number to 50, since the droplet initial kinetic energy is increased, part of the droplet gains enough energy at the end of the retract phase to be detached from the surface. However, the droplet root still stays in contact with the surface. At higher *We* numbers, the liquid kinetic energy at the end of the retract phase is high enough to detach the whole droplet from the solid surface, so a complete rebound is observed.

For both the USAW and DSAW scenarios, jetting rebounce is observed when the applied SAW power is larger than 20 *W*. At these larger SAW powers, the kinetic energy induced by the SAWs is much higher than the dissipation energy due to the liquid viscosity. Correspondingly, the droplet has enough energy to be separated from the solid surface at the end of the retract phase. Conversely, for the USAW scenario and the applied SAW power of 15 W, a complete rebound of the droplet from the surface is observed for all the *We* numbers except the *We* number of 70. This inconsistency is due to the relatively more viscous dissipation in this case, where the opposite directions of the momentums generated by gravitational and SAW forces during the spreading phase cause significant vortices within the droplet. These vortices, in turn, dissipated the kinetic energy of the droplet. Therefore, the droplet kinetic energy might not be high enough at the retract phase to detach the liquid phase from the solid surface.

The droplet contact times as a function of *We* numbers were obtained To investigate the effect of SAWs on droplet dynamics, and the results are presented in Figure 6-22(c-d). Comparisons of these two graphs with Figure 6-22(a-b) reveal that the droplet is deposited on the surface for the impacts with *We* number lower than 70 and DFI scenarios. However, by applying SAWs with powers higher than 25 W, regardless of the SAW direction, a complete detachment of the droplet from the surface is observed. Interestingly, results show that the droplet contact time can be reduced by the factor of a maximum of 48.5% by increasing the SAW power to 35 W.

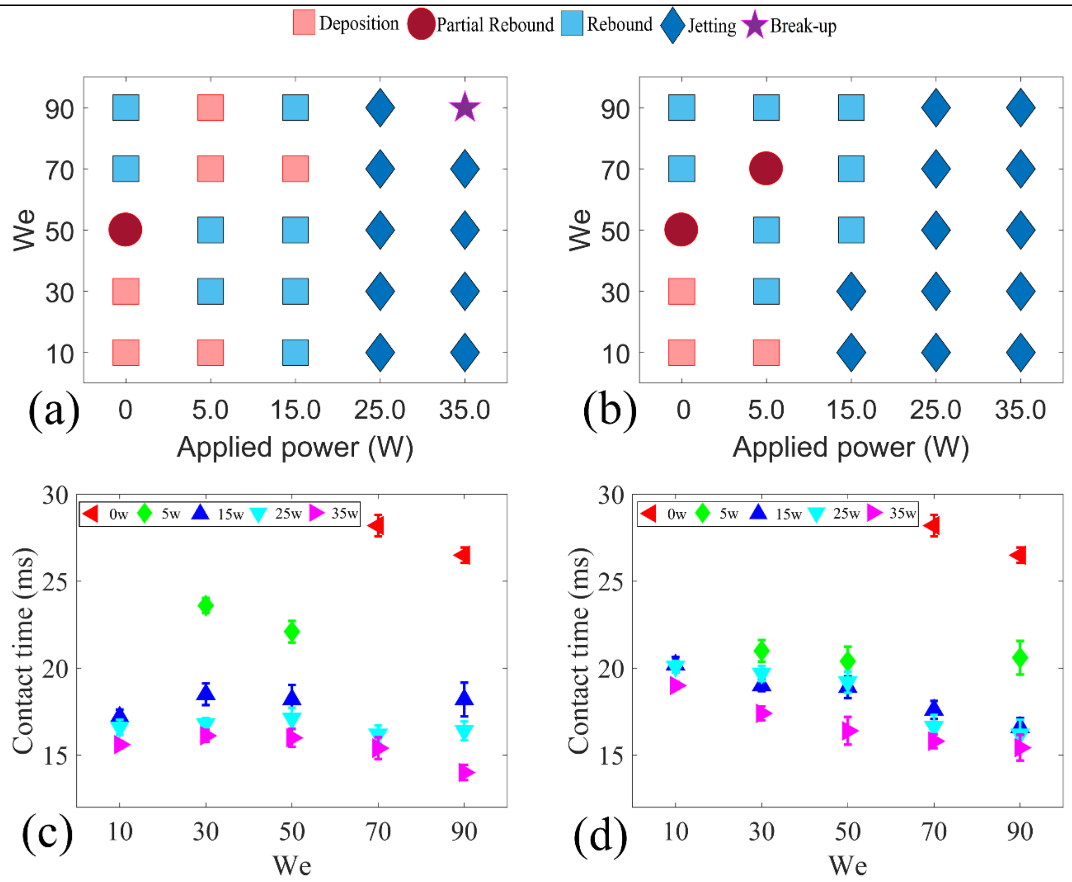

Figure 6-22: Droplet impact regime map as functions of applied SAW power and *We* number for (a) USAW, and (b) DSAW cases. Contact time versus *We* number for different applied SAW powers for (c) USAW, and (d) DSAW scenarios. In all the experiments, a droplet with a volume of 3.5μl is impacting on a ZnO/Si SAW device with an inclination angle of 15°.

Figures 6-23(a) and 6-23(d) show the effects of *We* number on maximum spreading widths of the droplet during the impact for the scenarios. Due to increased initial kinetic energy, the value of β_{Max} for DFI scenarios is increased as *We* number is increased. However, by applying the SAWs, the droplet spreading width is limited, and thus the value of $\beta_{Max}$is decreased. For both USAW and DSAW scenarios and regardless of the *We* number, the maximum spreading distance is decreased by increasing the applied SAW power. This is due to the contact line motion restriction by the applied SAW spreading area.

The effect of We number on rebounding angle is illustrated in 6-23(b) and 6-23(e). From these figures, it is apparent that by changing the SAW direction, the detached droplet direction is changed. As expected, for the DSAW case, by increasing the applied SAW power, the rebounding angle is increased. On the contrary, for the USAW cases, the rebounding angle is decreased significantly by changing the applied power. It is interesting to observe that a wide-range of the rebouncing angle up to 110º (e.g., from -60º to 50º) can be achieved by changing the applied SAW power and direction.

Figures 6-23(c) and 6-23(f) show the effect of We number on the values of displacement δ. For the DFI scenario, with the successive increases in the We number, as a result of the increase in the tangential component of the gravitational force, the value of δ, increases linearly. After applying the DSAW, the tangential component of the SAW force enhances the droplet movement in the X-direction, and the value of distance δ, increases significantly. For the USAW scenarios, the tangential components of the gravitational and SAW forces are in opposite directions, and the interaction between these forces determines the displacement of δ, values. Here, using a standard equation of $\delta = AWe^{B}$ the regression fitting for the movement of the droplet on the surface in DFI scenarios are obtained with $A = 0.1$ and $B = 0.61$, as shown by the dashed lines in Figure 6-23(c) and 6-23(f).

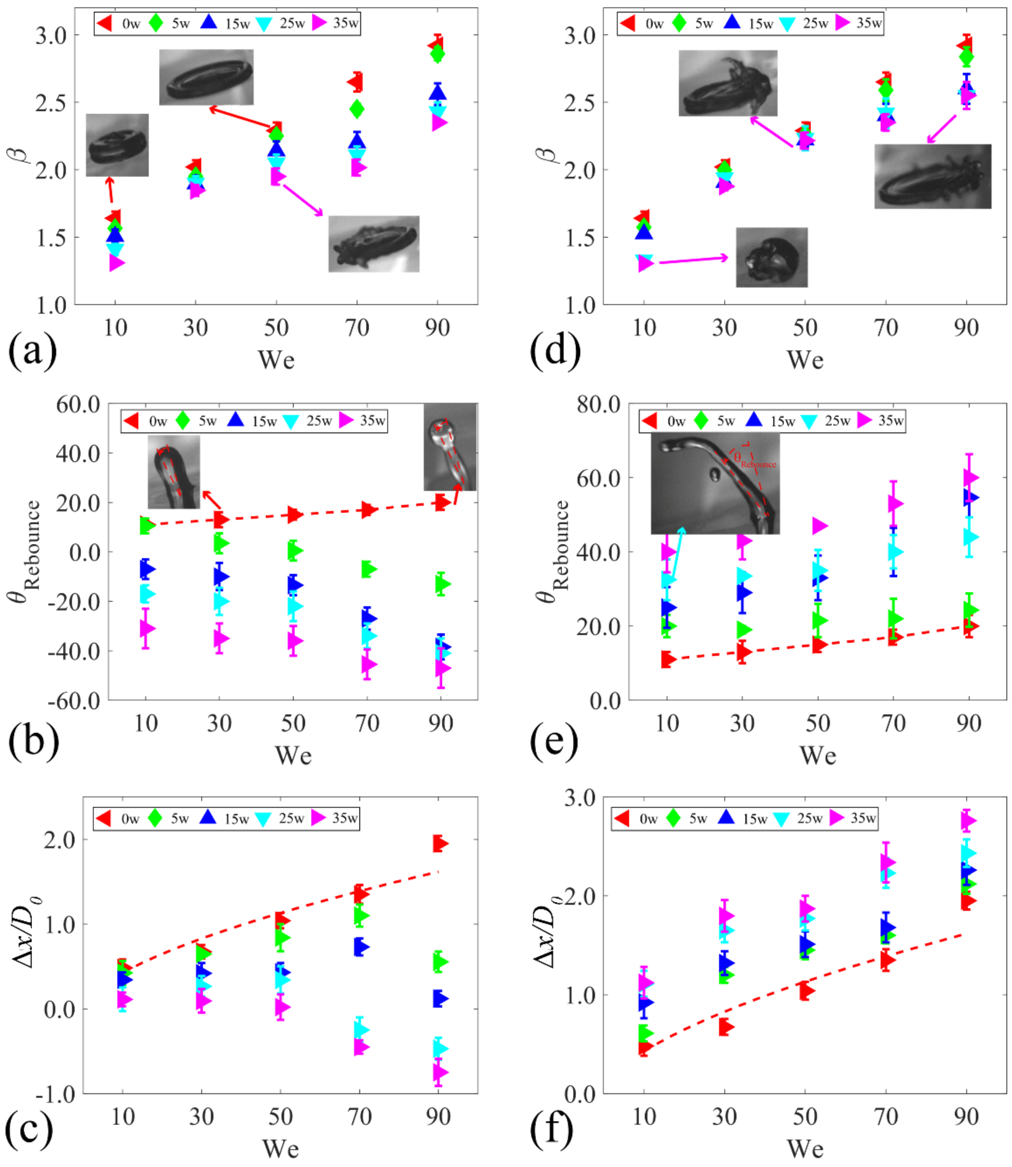

Figure 6-23: Effect of impact velocity on (a) maximum spreading, (b) Rebounding angle, and (c) Droplet movement along X direction for USAW scenario. Effect of impact velocity on (d) maximum spreading, (e) Rebounding angle, and (f) Droplet movement along X direction for DSAW scenario. In all the cases, the droplet with a volume of 3.5μl impacts a ZnO/Si SAW device with a surface inclination angle of 15°.

6.3 Summary

In this chapter, a new method to control and modify the droplet impact dynamics was introduced and explored. SAW-based microfluidic devices showed that they could be used to change the characteristic parameters of impact, such as impact regime and contact time on flat and inclined surfaces. Droplet impact time was reduced up to 30% using TSAW on flat surfaces. The numerical results show that the reduction in contact time is due to breaking the symmetry in internal flow. Furthermore, by changing the SAW power and direction on inclined surfaces, the droplet impact can be controlled. This new application of SAWs could provide a new approach in the design of smart water-repellent surfaces. Moreover, it also offers new methods to control the droplet impact dynamics actively.

Chapter 7. Conclusions and future work

7.1 Conclusion

SAW technology has become a significant platform in droplet-based microfluidics. In the last two decades, research has focused on investigating the potential of this technology for various applications. However, due to the complexity of the liquid and acoustic wave interaction, the underlying physics remains elusive.

The main goal of the present study was to use numerical and experimental methods to investigate the droplet actuation by surface acoustic waves. A 3D computational model based on the coupled level set volume of the fluid method was developed to simulate the large deformations of liquid interface subjected to SAWs. Additionally, a boundary condition was implemented to simulate the solid-liquid interaction during the SAW excitation. The developed model and boundary condition have been validated using the experimental results. In this study, the physics behind the different droplet actuation phenomena such as pumping and jetting was simulated and explained using the developed numerical model.

The key factors affecting droplet translation were numerically investigated to understand the physics of droplet pumping. Simulation results showed that although droplet pumping velocity decreased (at the same SAW power) for droplets with higher volumes, the droplet moved on the solid surface with larger interface deformations. Additionally, the simulation results of droplet pumping showed that following the increase in SAW device frequency, the attenuation length of the SAW decreases, and thus, less energy was transferred to the liquid medium. As a result, at higher frequencies, more SAW power was needed to push the droplet forward (the same physics was observed in the experiments). Another outcome of the CFD simulation of droplet pumping by SAW was calculating the minimum power required (for various SAW devices) to achieve droplet pumping and jetting. Accordingly, an equation was proposed based on the computational results to calculate the wave amplitude from the SAW device RF power to predict the minimum power to start droplet transportation and jetting.

Moreover, the numerical simulations were used to explore droplet jetting by one or a pair of IDTs. After analysing the physics of the droplet jetting by SAWs, the droplet energy budget was analysed. The results showed that during the droplet jetting by SAWs, both kinetic and surface energies play the primary role in the jetting dynamics, whereas viscous dissipation effects can be neglected. To be more precise, ~50% of the applied SAW energy is converted to kinetic energy and ~45% of the SAW energy is spent on the droplet deformation. The obtained results are not easily measured using the experimental methods, and this shows the importance of the CFD simulations.

On the contrary, for the droplet internal streaming, viscous dissipation plays the central role, and surface energy variations during the application are negligible. Due to creating an internal streaming field inside the droplet, the droplet kinetic energy is raised.

Besides, for the first time, the numerical results in this study showed that by changing the SAW device configuration and design, the device efficiency for different applications could be improved. The energy budget analysis was used to optimise the position of the IDTs for diverse microfluidic applications. For micromixing applications of the SAW device, aligned IDT configuration is optimal. The rate of viscous dissipation for this configuration is 500% higher than SAW devices with offset IDTs. Also, a pair of aligned IDTs enhance the maximum jetting velocity and minimum jetting time, which is essential for a wide range of applications such as 3D printing and tissue engineering.

In contrast, for microdroplet separation applications, a pair of IDTs with an offset value of one can generate the maximum internal circulation velocity. The numerical results showed that the droplet kinetic energy is increased by 100% if the IDT configuration is changed from aligned to offset. These results, which are identified by numerical simulations, will be helpful for the fabrication of more efficient LOC devices.

Another significant finding to emerge from this study was the application of SAWs to manipulate and actively control the droplet impact on smooth surfaces. The experimental evidences of this study showed that droplet behaviour during the short impact time on the solid surfaces could be effectively altered. The experimental results of droplet impact on flat surfaces showed that the droplet contact time could be reduced up to 35%. Moreover, by applying SAWs to the droplet, the impact regime can be modified, and droplet deposition on the surface can be effectively avoided by applying SAWs to an impacting droplet to achieve a complete rebound from the surface. This is the first study reporting the efficiency of SAWs in droplet impact control.

Additionally, analysis of droplet impact in the presence of SAW by numerical methods has extended the knowledge of physics of the phenomena. Using CFD results, the details of the flow during the impact in the presence of SAWs is revealed. Although experimental methods do not capture the flow details, simulation results show that the internal streaming flow for both the droplet free impact and standing SAW cases is almost symmetrical. On the other hand, it shows that applying the travelling SAW creates an irregular flow field, which breaks the symmetry of internal streaming and reduces contact time.

Numerical simulations were also carried out on various droplet impact scenarios on inclined surfaces. These results verified that SAWs could alter the impacting droplet energy budget and modify the impact dynamics on inclined surfaces. It is well known that more than 60% of the droplet initial kinetic energy is dissipated during the droplet spreading on the solid surface. However, Applying the DSAW to the surface during the impingement process increases the droplet kinetic energy, leading to a faster detachment from the surface. On the other hand, by applying the USAW, the energy dissipation of the liquid medium is increased compared to those for the DSAW and FI scenarios. The slightly increased kinetic energy causes a faster detachment from the surface.

A set of experimental investigations were also carried out to analyse the effect of various parameters on droplet impact control. Accordingly, the effect of impact velocity, SAW direction and power, and surface inclination angle, and surface structure on the droplet impact were studied. Various impact parameters such as droplet impact regime, contact time, maximum spreading radius, rebouncing angle, and droplet movement on the surface during the impact were chosen to analyse the droplet impact control by SAWs in details. In general, the results showed that applying the SAWs, regardless of their direction, can avoid the droplet deposition on the inclined surface after the impact. This result showed that SAW-based droplet impact control has several potential practical applications in the fabrication of anti-icing, anti-erosion and self-cleaning surfaces. In addition, through the application of high power SAW to the surface during the droplet impact, the liquid can be pushed as a beam toward a particular target. Droplet impact time and motion on the surface can also be manipulated by SAWs, showing their great potential in smart cooling surfaces. The time and area of liquid-solid interaction can be controlled by applying SAWs, which is the critical parameter in spray cooling applications.

SAWs can be generated remotely from a drop impact location and can be switched on and off. Moreover, research has shown that SAW can propagate on flexible and curved surfaces. Thus, the concept of using SAWs to control the droplet impact can be applied to a wide range of real-world applications, especially the development of smart surfaces. This research could provide a base for future studies of droplet impact control on smart surfaces.

7.2 Future work

The presented research in this study can be explored further. Following are some recommendations for future work:

- One of the major issues with multiphase flow methods such as CLSVOF is the high computational cost and time due to the need for a small grid size. To reduce the computational costs, the adaptive and dynamic mesh should be used during the simulations. Using dynamic mesh, only the cells around the interfaces are refined, and thus, the number of cells in the simulation domain is significantly reduced. Therefore, computational costs and time could be significantly reduced.
- Further work can be carried out on the direct solution of the sound wave propagation under the droplet (although the computational costs would be much more). To do so, instead of using the body force (which adds the effect of SAW energy on liquid medium), the sound wave equations can be directly solved on the solid surface and then be used as the velocity (and pressure) boundary conditions for the liquid medium which can lead to more accurate solution results for this complex multi-physics problem.
- Another direction for future works is to use the critical point theory to analyse the numerical results to examine viscous flow patterns around the rigid boundaries.
- In addition to numerical methods to investigate the droplet actuation with SAW, theoretical/mathematical works could be carried out to understand the energy transfer from the surface of the SAW device to the liquid medium

- Although the actuation of Newtonian liquids (and mainly water) by SAWs has been studied in the present work, this method could be applied to non-Newtonian fluids, particularly pseudoplastic fluids, to investigate their behaviours subjected to SAWs. Since most LOC devices are used to do analysis using the blood products (which is a shear-thinning non-Newtonian liquid), it is imperative to develop mathematical models that can simulate such liquids' behaviours. Since performing experiments with human blood cannot be easily performed (compared to water), CFD simulations can produce information about such liquids' behaviour. To develop such models, empirical equations that calculate the liquid viscosity as a function of shear rate in the flow would be used in simulations. Using such equations can significantly increase the computational time; thus, using dynamic mesh and cost-effective methods would be beneficial.

- Another possible area of future research would be experimental investigations of new applications of SAWs. It may be possible to use the SAWs as an effective and active anti-icing method on solid surfaces. This study shows that SAWs could efficiently modify the droplet impact dynamics on solid surfaces. The ability to reduce the droplet contact time can also be used to control heat transfer between a solid and liquid or for de-icing and anti-icing applications in aeroplane wings or wind-turbine surfaces. Also, the capability of SAWs to control the droplet impact dynamics on various types of surface treatments could be investigated to increase the efficiency and reliability of this method.

- Further research regarding the heating effect of SAW would be worthwhile. Although a few studies have been carried out to investigate droplet heating by SAWs experimentally, numerical simulations are needed to understand SAW-based heating better[62]. The energy equation could be added to the numerical model to simulate the heating effects of the SAWs. The effect of heat transfer on the liquid generated by SAWs can be important for some anti-icing applications.

Appendix A DCA model validation

To develop an accurate DCA model, a set of droplet jetting and pumping experiments were performed by a SAW device with a resonant frequency of 66.2 MHz. Various volumes of the droplet were used in the experiments. The experimental results of the droplet contact angle as a TPCL velocity function are compared with the numerical results obtained from Equation 3-32 and 3-33 in Figure A1.

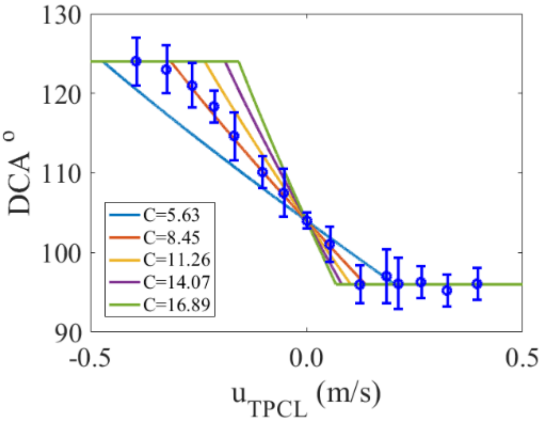

Figure A1: The DCA variation as a function TPCL velocity for different values of fitting coefficient, C. The blue circles are the experimental results obtained from the water droplet translation experiments on the ZnO/Si SAW device surface treated with CYTOP.

As shown in Figure A1, by choosing the value of the fitting factor, C, equal to 8.45, the numerical results curve almost fits the experimental results. Thus, in all the simulations, the value of the C is set to be 8.45.

References

(1) Bruus, H. *Theoretical Microfluidics*; Oxford University Press, 2008; Vol. 45. https://doi.org/10.5860/choice.45-5602.

(2) Mao, Z.; Xie, Y.; Guo, F.; Ren, L.; Huang, P. H.; Chen, Y.; Rufo, J.; Costanzo, F.; Huang, T. J. Experimental and Numerical Studies on Standing Surface Acoustic Wave Microfluidics. *Lab Chip* **2016**, *16* (3), 515–524. https://doi.org/10.1039/c5lc00707k.

(3) Petersson, F.; Åberg, L.; Swärd-Nilsson, A. M.; Laurell, T. Free Flow Acoustophoresis: Microfluidic-Based Mode of Particle and Cell Separation. *Anal. Chem.* **2007**, *79* (14), 5117–5123. https://doi.org/10.1021/ac070444e.

(4) Alghane, M. M. Surface Acoustic Wave Streaming in a Microfluidic System, Heriot-Watt University, 2013.

(5) Sritharan, K.; Strobl, C. J.; Schneider, M. F.; Wixforth, A.; Guttenberg, Z. Acoustic Mixing at Low Reynold's Numbers. *Appl. Phys. Lett.* **2006**, *88* (5), 1–3. https://doi.org/10.1063/1.2171482.

(6) Wixforth, A.; Strobl, C.; Gauer, C.; Toegl, A.; Scriba, J.; Guttenberg, Z. V. Acoustic Manipulation of Small Droplets. *Anal. Bioanal. Chem.* **2004**, *379* (7–8), 982–991. https://doi.org/10.1007/s00216-004-2693-z.

(7) Fu, Y. Q.; Luo, J. K.; Nguyen, N. T.; Walton, A. J.; Flewitt, A. J.; Zu, X. T.; Li, Y.; McHale, G.; Matthews, A.; Iborra, E.; Du, H.; Milne, W. I. Advances in Piezoelectric Thin Films for Acoustic Biosensors, Acoustofluidics and Lab-on-Chip Applications. *Prog. Mater. Sci.* **2017**, *89*, 31–91. https://doi.org/10.1016/j.pmatsci.2017.04.006.

(8) Yeo, L. Y.; Friend, J. R. Surface Acoustic Wave Microfluidics. *Annu. Rev. Fluid Mech.* **2014**, *46* (1), 379–406. https://doi.org/10.1146/annurev-fluid-010313-141418.

(9) Fu, Y. Q.; Luo, J. K.; Du, X. Y.; Flewitt, A. J.; Li, Y.; Markx, G. H.; Walton, A. J.; Milne, W. I. Recent Developments on ZnO Films for Acoustic Wave Based Bio-Sensing and Microfluidic Applications: A Review. *Sensors Actuators, B Chem.* **2010**,

143 (2), 606–619. https://doi.org/10.1016/j.snb.2009.10.010.

(10) Fu, C.; Quan, A. J.; Luo, J. T.; Pang, H. F.; Guo, Y. J.; Wu, Q.; Ng, W. P.; Zu, X. T.; Fu, Y. Q. Vertical Jetting Induced by Shear Horizontal Leaky Surface Acoustic Wave on 36° Y-X LiTaO3. *Appl. Phys. Lett.* **2017**, *110* (17), 173501. https://doi.org/10.1063/1.4982073.

(11) Destgeer, G.; Sung, H. J. Recent Advances in Microfluidic Actuation and Micro-Object Manipulation via Surface Acoustic Waves. *Lab Chip* **2015**, *15* (13), 2722–2738. https://doi.org/10.1039/c5lc00265f.

(12) Fu, Y. Q.; Garcia-Gancedo, L.; Pang, H. F.; Porro, S.; Gu, Y. W.; Luo, J. K.; Zu, X. T.; Placido, F.; Wilson, J. I. B.; Flewitt, A. J.; Milne, W. I. Microfluidics Based on ZnO/Nanocrystalline Diamond Surface Acoustic Wave Devices. *Biomicrofluidics* **2012**, *6* (2). https://doi.org/10.1063/1.3699974.

(13) Connacher, W.; Zhang, N.; Huang, A.; Mei, J.; Zhang, S.; Gopesh, T.; Friend, J. Micro/Nano Acoustofluidics: Materials, Phenomena, Design, Devices, and Applications. *Lab Chip* **2018**, *18* (14), 1952–1996. https://doi.org/10.1039/c8lc00112j.

(14) Barani, A.; Paktinat, H.; Janmaleki, M.; Mohammadi, A.; Mosaddegh, P.; Fadaei-Tehrani, A.; Sanati-Nezhad, A. Microfluidic Integrated Acoustic Waving for Manipulation of Cells and Molecules. *Biosens. Bioelectron.* **2016**, *85*, 714–725. https://doi.org/10.1016/j.bios.2016.05.059.

(15) Jangi, M.; Luo, J. T.; Tao, R.; Reboud, J.; Wilson, R.; Cooper, J. M.; Gibson, D.; Fu, Y. Q. Concentrated Vertical Jetting Mechanism for Isotropically Focused Zno/Si Surface Acoustic Waves. *Int. J. Multiph. Flow* **2019**, *114,* 1–8. https://doi.org/10.1016/j.ijmultiphaseflow.2019.02.002.

(16) Rayleigh, Lord. On Waves Propagated along the Plane Surface of an Elastic Solid. *Proc. London Math. Soc.* **1885**, *s1-17* (1), 4–11. https://doi.org/10.1112/plms/s1-17.1.4.

(17) Love, A. E. H. *Theory of the Propagation of Seismic Waves*; Cornell University Library, 1911.

(18) Atanasoff, J. V.; Hart, P. J. Dynamical Determinitation of the Elastic Constants and Their Temperature Coefficients for Quartz. *Phys. Rev.* **1941**, *59* (1), 85–96. https://doi.org/10.1103/PhysRev.59.85.

(19) Dieulesaint, E.; Hartemann, P. *Acoustic Surface Wave Filters*; Academic Press, 1973; Vol. 11. https://doi.org/10.1016/0041-624X(73)90507-6.

(20) Gronewold, T. M. A. Surface Acoustic Wave Sensors in the Bioanalytical Field: Recent Trends and Challenges. *Anal. Chim. Acta* **2007**, *603* (2), 119–128. https://doi.org/10.1016/j.aca.2007.09.056.

(21) Mark, D.; Haeberle, S.; Roth, G.; Stetten, F. Von; Zengerle, R. Microfluidic Lab-on-a-Chip Platforms: Requirements, Characteristics and Applications. *Chem. Soc. Rev.* **2010**, *39* (3), 1153–1182. https://doi.org/10.1039/b820557b.

(22) Gopinath, S. C. B.; Tang, T. H.; Citartan, M.; Chen, Y.; Lakshmipriya, T. Current Aspects in Immunosensors. *Biosens. Bioelectron.* **2014**, *57*, 292–302. https://doi.org/10.1016/j.bios.2014.02.029.

(23) Mokhtari, S.; Skelly, K. D.; Krull, E. A.; Coughlan, A.; Mellott, N. P.; Gong, Y.; Borges, R.; Wren, A. W. Copper-Containing Glass Polyalkenoate Cements Based on SiO2–ZnO–CaO–SrO–P2O5 Glasses: Glass Characterization, Physical and Antibacterial Properties. *J. Mater. Sci.* **2017**, *52* (15), 8886–8903. https://doi.org/10.1007/s10853-017-0945-5.

(24) Gantner, A.; Hoppe, R. H. W.; Köster, D.; Siebert, K.; Wixforth, A. Numerical Simulation of Piezoelectrically Agitated Surface Acoustic Waves on Microfluidic Biochips. *Comput. Vis. Sci.* **2007**, *10* (3), 145–161. https://doi.org/10.1007/s00791-006-0040-y.

(25) Arzt, R. M.; Salzmann, E.; Dransfeld, K. Elastic Surface Waves in Quartz at 316 MHz. *Appl. Phys. Lett.* **1967**, *10* (5), 165–167. https://doi.org/10.1063/1.1754894.

(26) Lighthill, S. J. Acoustic Streaming. *J. Sound Vib.* **1978**, *61* (3), 391–418. https://doi.org/10.1016/0022-460X(78)90388-7.

(27) Biroun, M. H.; Rahmati, M. T.; Jangi, M.; Tao, R.; Chen, B. X.; Fu, Y. Q.

Computational and Experimental Analysis of Droplet Transportation/Jetting Behaviours Driven by Thin Film Surface Acoustic Waves. *Sensors Actuators, A Phys.* **2019**, *299*, 111624. https://doi.org/10.1016/j.sna.2019.111624.

(28) Ding, X.; Li, P.; Lin, S. C. S.; Stratton, Z. S.; Nama, N.; Guo, F.; Slotcavage, D.; Mao, X.; Shi, J.; Costanzo, F.; Huang, T. J. Surface Acoustic Wave Microfluidics. *Lab Chip* **2013**, *13* (18), 3626–3649. https://doi.org/10.1039/c3lc50361e.

(29) Wey-Yen, K. An Investigation of the Temperature Discontinuity at the Boundary Between a Solid and Superfluid Helium. *Jetp* **1962**, *15* (4), 635.

(30) Shiokawa, S.; Matsui, Y.; Moriizumi, T. Experimental Study on Liquid Streaming by SAW. *Jpn. J. Appl. Phys.* **1989**, *28* (S1), 126–128. https://doi.org/10.7567/JJAPS.28S1.126.

(31) Shiokawa, S.; Matsui, Y.; Ueda, T.; Measurement, T.; Ito, S.; Sugimoto, M.; Device, A. W.; Murochi, N.; Sugimoto, M.; Microfluidic, C. D.; Fukaya, T.; Kondoh, J. Related Content Experimental Study on Liquid Streaming by SAW. **1989**.

(32) Moroney, R. M.; White, R. M.; Howe, R. T. Microtransport Induced by Ultrasonic Lamb Waves. *Appl. Phys. Lett.* **1991**, *59* (7), 774–776. https://doi.org/10.1063/1.105339.

(33) Wixforth, A. Acoustically Driven Planar Microfluidics. *Superlattices Microstruct.* **2003**, *33* (5–6), 389–396. https://doi.org/10.1016/j.spmi.2004.02.015.

(34) Wixforth, A. Acoustically Driven Programmable Microfluidics for Biological and Chemical Applications. *J. Lab. Autom.* **2006**, *11* (6), 399–405. https://doi.org/10.1016/j.jala.2006.08.001.

(35) Li, H.; Friend, J. R.; Yeo, L. Y. Surface Acoustic Wave Concentration of Particle and Bioparticle Suspensions. *Biomed. Microdevices* **2007**, *9* (5), 647–656. https://doi.org/10.1007/s10544-007-9058-2.

(36) Shilton, R.; Tan, M. K.; Yeo, L. Y.; Friend, J. R. Particle Concentration and Mixing in Microdrops Driven by Focused Surface Acoustic Waves. *J. Appl. Phys.* **2008**, *104* (1). https://doi.org/10.1063/1.2951467.

(37) Frommelt, T.; Kostur, M.; Wenzel-Schäfer, M.; Talkner, P.; Hänggi, P.; Wixforth, A. Microfluidic Mixing via Acoustically Driven Chaotic Advection. *Phys. Rev. Lett.* **2008**, *100* (3), 034502. https://doi.org/10.1103/PhysRevLett.100.034502.

(38) Tao, R.; Mchale, G.; Reboud, J.; Cooper, J. M.; Torun, H.; Luo, J. T.; Luo, J.; Yang, X.; Zhou, J.; Canyelles-Pericas, P.; Wu, Q.; Fu, Y. Hierarchical Nanotexturing Enables Acoustofluidics on Slippery yet Sticky, Flexible Surfaces. *Nano Lett.* **2020**, *20* (5), 3263–3270. https://doi.org/10.1021/acs.nanolett.0c00005.

(39) Lim, H.; Back, S. M.; Choi, H.; Nam, J. Acoustic Mixing in a Dome-Shaped Chamber-Based SAW (DC-SAW) Device. *Lab Chip* **2020**, *20* (1), 120–125. https://doi.org/10.1039/c9lc00820a.

(40) Shilton, R. J.; Yeo, L. Y.; Friend, J. R. Quantification of Surface Acoustic Wave Induced Chaotic Mixing-Flows in Microfluidic Wells. *Sensors Actuators, B Chem.* **2011**, *160* (1), 1565–1572. https://doi.org/10.1016/j.snb.2011.09.007.

(41) Shilton, R. J.; Travagliati, M.; Beltram, F.; Cecchini, M. Nanoliter-Droplet Acoustic Streaming via Ultra High Frequency Surface Acoustic Waves. *Adv. Mater.* **2014**, *26* (29), 4941–4946. https://doi.org/10.1002/adma.201400091.

(42) Liang, W.; Zhang, F.; Yang, G.; Wang, Z. Separation of Water from a Microliter Oil/Water Mixed Drop Using Lamb Waves on an Inclined Glass Plate. *Microfluid. Nanofluidics* **2017**, *21* (10), 2–5. https://doi.org/10.1007/s10404-017-2002-8.

(43) Hsu, J. C.; Lin, Y. D. Microparticle Concentration and Separation inside a Droplet Using Phononic-Crystal Scattered Standing Surface Acoustic Waves. *Sensors Actuators, A Phys.* **2019**, *300*. https://doi.org/10.1016/j.sna.2019.111651.

(44) Raghavan, R. V.; Friend, J. R.; Yeo, L. Y. Particle Concentration via Acoustically Driven Microcentrifugation: MicroPIV Flow Visualization and Numerical Modelling Studies. *Microfluid. Nanofluidics* **2010**, *8* (1), 73–84. https://doi.org/10.1007/s10404-009-0452-3.

(45) Collins, D. J.; Ma, Z.; Ai, Y. Highly Localized Acoustic Streaming and Size-Selective Submicrometer Particle Concentration Using High Frequency Microscale Focused Acoustic Fields. *Anal. Chem.* **2016**, *88* (10), 5513–5522.

https://doi.org/10.1021/acs.analchem.6b01069.

(46) Wang, K.; Zhou, W.; Lin, Z.; Cai, F.; Li, F.; Wu, J.; Meng, L.; Niu, L.; Zheng, H. Sorting of Tumour Cells in a Microfluidic Device by Multi-Stage Surface Acoustic Waves. *Sensors Actuators, B Chem.* **2018**, *258*, 1174–1183. https://doi.org/10.1016/j.snb.2017.12.013.

(47) Guttenberg, Z.; Müller, H.; Habermüller, H.; Geisbauer, A.; Pipper, J.; Felbel, J.; Kielpinski, M.; Scriba, J.; Wixforth, A. Planar Chip Device for PCR and Hybridization with Surface Acoustic Wave Pump. *Lab Chip* **2005**, *5* (3), 308–317. https://doi.org/10.1039/b412712a.

(48) Renaudin, A.; Tabourier, P.; Camart, J. C.; Druon, C. Surface Acoustic Wave Two-Dimensional Transport and Location of Microdroplets Using Echo Signal. *J. Appl. Phys.* **2006**, *100* (11), 116101. https://doi.org/10.1063/1.2388725.

(49) Beyssen, D.; Le Brizoual, L.; Elmazria, O.; Alnot, P. Microfluidic Device Based on Surface Acoustic Wave. *Sensors Actuators, B Chem.* **2006**, *118* (1–2), 380–385. https://doi.org/10.1016/j.snb.2006.04.084.

(50) Du, X. Y.; Swanwick, M. E.; Fu, Y. Q.; Luo, J. K.; Flewitt, A. J.; Lee, D. S.; Maeng, S.; Milne, W. I. Surface Acoustic Wave Induced Streaming and Pumping in 128° Y-Cut LiNbO 3 for Microfluidic Applications. *J. Micromechanics Microengineering* **2009**, *19* (3), 035016. https://doi.org/10.1088/0960-1317/19/3/035016.

(51) Brunet, P.; Baudoin, M.; Matar, O. B.; Zoueshtiagh, F. Droplet Displacements and Oscillations Induced by Ultrasonic Surface Acoustic Waves: A Quantitative Study. *Phys. Rev. E - Stat. Nonlinear, Soft Matter Phys.* **2010**, *81* (3). https://doi.org/10.1103/PhysRevE.81.036315.

(52) Baudoin, M.; Brunet, P.; Matar, O. B.; Herth, E. Low Power Sessile Droplets Actuation via Modulated Surface Acoustic Waves. *Appl. Phys. Lett.* **2012**, *100* (15), 154102. https://doi.org/10.1063/1.3701725.

(53) Travagliati, M.; Simoni, G. De; Lazzarini, C. M.; Piazza, V.; Beltram, F.; Cecchini, M. Interaction-Free, Automatic, on-Chip Fluid Routing by Surface Acoustic Waves. *Lab Chip* **2012**, *12* (15), 2621–2624. https://doi.org/10.1039/c2lc40396j.

(54) Ai, Y.; Marrone, B. L. Droplet Translocation by Focused Surface Acoustic Waves. *Microfluid. Nanofluidics* **2012**, *13* (5), 715–722. https://doi.org/10.1007/s10404-012-0990-y.

(55) Collignon, S.; Friend, J.; Yeo, L. Planar Microfluidic Drop Splitting and Merging. *Lab Chip* **2015**, *15* (8), 1942–1951. https://doi.org/10.1039/c4lc01453g.

(56) Bussonnière, A.; Baudoin, M.; Brunet, P.; Matar, O. B. Dynamics of Sessile and Pendant Drops Excited by Surface Acoustic Waves: Gravity Effects and Correlation between Oscillatory and Translational Motions. *Phys. Rev. E* **2016**, *93* (5). https://doi.org/10.1103/PhysRevE.93.053106.

(57) Zhang, A. L.; Wu, Z. Q.; Xia, X. H. Transportation and Mixing of Droplets by Surface Acoustic Wave. *Talanta* **2011**, *84* (2), 293–297. https://doi.org/10.1016/j.talanta.2011.01.017.

(58) Wang, Y.; Tao, X.; Tao, R.; Zhou, J.; Zhang, Q.; Chen, D.; Jin, H.; Dong, S.; Xie, J.; Fu, Y. Q. Acoustofluidics along Inclined Surfaces Based on AlN/Si Rayleigh Surface Acoustic Waves. *Sensors Actuators, A Phys.* **2020**, *306*, 111967. https://doi.org/10.1016/j.sna.2020.111967.

(59) Luo, J. T.; Geraldi, N. R.; Guan, J. H.; McHale, G.; Wells, G. G.; Fu, Y. Q. Slippery Liquid-Infused Porous Surfaces and Droplet Transportation by Surface Acoustic Waves. *Phys. Rev. Appl.* **2017**, *7* (1), 014017. https://doi.org/10.1103/PhysRevApplied.7.014017.

(60) Sriphutkiat, Y.; Kasetsirikul, S.; Ketpun, D.; Zhou, Y. Cell Alignment and Accumulation Using Acoustic Nozzle for Bioprinting. *Sci. Rep.* **2019**, *9* (1), 17774. https://doi.org/10.1038/s41598-019-54330-8.

(61) Castro, J. O.; Ramesan, S.; Rezk, A. R.; Yeo, L. Y. Continuous Tuneable Droplet Ejection via Pulsed Surface Acoustic Wave Jetting. *Soft Matter* **2018**, *14* (28), 5721–5727. https://doi.org/10.1039/c7sm02534c.

(62) Lee, D.; Lee, N.; Choi, G.; Cho, H. H. Heat Transfer Characteristics of a Focused Surface Acoustic Wave (F-SAW) Device for Interfacial Droplet Jetting. *Inventions* **2018**, *3* (2), 38. https://doi.org/10.3390/inventions3020038.

(63) Padilla-Martinez, J. P.; Ramirez-San-Juan, J. C.; Berrospe-Rodriguez, C.; Korneev, N.; Aguilar, G.; Zaca-Moran, P.; Ramos-Garcia, R. Controllable Direction of Liquid Jets Generated by Thermocavitation within a Droplet. *Appl. Opt.* **2017**, *56* (25), 7167. https://doi.org/10.1364/ao.56.007167.

(64) Obreschkow, D.; Kobel, P.; Dorsaz, N.; De Bosset, A.; Nicollier, C.; Farhat, M. Cavitation Bubble Dynamics inside Liquid Drops in Microgravity. *Phys. Rev. Lett.* **2006**, *97* (9). https://doi.org/10.1103/PhysRevLett.97.094502.

(65) Go, D. B.; Atashbar, M. Z.; Ramshani, Z.; Chang, H. C. Surface Acoustic Wave Devices for Chemical Sensing and Microfluidics: A Review and Perspective. *Anal. Methods* **2017**, *9* (28), 4112–4134. https://doi.org/10.1039/c7ay00690j.

(66) Shiokawa, S.; Matsui, Y.; Ueda, T. Study on Saw Streaming and Its Application to Fluid Devices. *Jpn. J. Appl. Phys.* **1990**, *29* (S1), 137–139. https://doi.org/10.7567/JJAPS.29S1.137.

(67) Bennès, J.; Alzuaga, S.; Ballandras, S.; Chérioux, F.; Bastien, F.; Manceau, J. F. Droplet Ejector Using Surface Acoustic Waves. In *Proceedings - IEEE Ultrasonics Symposium*; IEEE, 2005; Vol. 2, pp 823–826. https://doi.org/10.1109/ULTSYM.2005.1602976.

(68) Friend, J.; Tan, M.; Yeo, L. Unraveling Interfacial Jetting Phenomena Induced by Focused Surface Acoustic Waves. In *Proceedings - IEEE Ultrasonics Symposium*; IEEE, 2009; Vol. 024501, pp 811–814. https://doi.org/10.1109/ULTSYM.2009.5441559.

(69) Bhattacharjee, P. K.; McDonnell, A. G.; Prabhakar, R.; Yeo, L. Y.; Friend, J. Extensional Flow of Low-Viscosity Fluids in Capillary Bridges Formed by Pulsed Surface Acoustic Wave Jetting. *New J. Phys.* **2011**, *13*. https://doi.org/10.1088/1367-2630/13/2/023005.

(70) Pang, H. F.; Fu, Y. Q.; Garcia-Gancedo, L.; Porro, S.; Luo, J. K.; Placido, F.; Wilson, J. I. B.; Flewitt, A. J.; Milne, W. I.; Zu, X. T. Enhancement of Microfluidic Efficiency with Nanocrystalline Diamond Interlayer in the ZnO-Based Surface Acoustic Wave Device. *Microfluid. Nanofluidics* **2013**, *15* (3), 377–386.

https://doi.org/10.1007/s10404-013-1155-3.

(71) Guo, Y. J.; Lv, H. B.; Li, Y. F.; He, X. L.; Zhou, J.; Luo, J. K.; Zu, X. T.; Walton, A. J.; Fu, Y. Q. High Frequency Microfluidic Performance of LiNbO3 and ZnO Surface Acoustic Wave Devices. *J. Appl. Phys.* **2014**, *116* (2). https://doi.org/10.1063/1.4885038.

(72) Darmawan, M.; Byun, D. Focused Surface Acoustic Wave Induced Jet Formation on Superhydrophobic Surfaces. *Microfluid. Nanofluidics* **2015**, *18* (5–6), 1107–1114. https://doi.org/10.1007/s10404-014-1503-y.

(73) Zhou, J.; Pang, H. F.; Garcia-Gancedo, L.; Iborra, E.; Clement, M.; De Miguel-Ramos, M.; Jin, H.; Luo, J. K.; Smith, S.; Dong, S. R.; Wang, D. M.; Fu, Y. Q. Discrete Microfluidics Based on Aluminum Nitride Surface Acoustic Wave Devices. *Microfluid. Nanofluidics* **2015**, *18* (4), 537–548. https://doi.org/10.1007/s10404-014-1456-1.

(74) Lei, Y.; Hu, H.; Chen, J.; Zhang, P. Microfluidic Jetting Deformation and Pinching-off Mechanism in Capillary Tubes by Using Traveling Surface Acousticwaves. *Actuators* **2020**, *9* (1), 5. https://doi.org/10.3390/act9010005.

(75) Lei, Y.; Hu, H.; Chen, J.; Zhang, P. Microfluidic Jetting Deformation and Pinching-off Mechanism in Capillary Tubes by Using Traveling Surface Acousticwaves. *Actuators* **2020**, *9* (1). https://doi.org/10.3390/act9010005.

(76) Kurosawa, M.; Futami, A.; Higuchi, T. Characteristics of Liquids Atomization Using Surface Acoustic Wave. In *International Conference on Solid-State Sensors and Actuators, Proceedings*; IEEE, 1997; Vol. 2, pp 801–804. https://doi.org/10.1109/sensor.1997.635221.

(77) Lai, Y.; Tang, Y.; Gong, J.; Gong, D.; Chi, L.; Lin, C.; Chen, Z. Transparent Superhydrophobic/Superhydrophilic TiO 2-Based Coatings for Self-Cleaning and Anti-Fogging. *J. Mater. Chem.* **2012**, *22* (15), 7420–7426. https://doi.org/10.1039/c2jm16298a.

(78) Mishchenko, L.; Hatton, B.; Bahadur, V.; Taylor, J. A.; Krupenkin, T.; Aizenberg, J. Design of Ice-Free Nanostructured Surfaces Based on Repulsion of Impacting Water

Droplets. *ACS Nano* **2010**, *4* (12), 7699–7707. https://doi.org/10.1021/nn102557p.

(79) Kreder, M. J.; Alvarenga, J.; Kim, P.; Aizenberg, J. Design of Anti-Icing Surfaces: Smooth, Textured or Slippery? *Nature Reviews Materials*. Nature Publishing Group January 11, 2016. https://doi.org/10.1038/natrevmats.2015.3.

(80) Cao, L.; Jones, A. K.; Sikka, V. K.; Wu, J.; Gao, D. Anti-Icing Superhydrophobic Coatings. *Langmuir* **2009**, *25* (21), 12444–12448. https://doi.org/10.1021/la902882b.

(81) Zhang, L.; Wu, J.; Hedhili, M. N.; Yang, X.; Wang, P. Inkjet Printing for Direct Micropatterning of a Superhydrophobic Surface: Toward Biomimetic Fog Harvesting Surfaces. *J. Mater. Chem. A* **2015**, *3* (6), 2844–2852. https://doi.org/10.1039/c4ta05862c.

(82) Sakurada, S.; Sole-Gras, M.; Christensen, K.; Wallace, D. B.; Huang, Y. Liquid-Absorbing System-Assisted Intersecting Jets Printing of Soft Structures from Reactive Biomaterials. *Addit. Manuf.* **2020**, *31*. https://doi.org/10.1016/j.addma.2019.100934.

(83) Boland, T.; Xu, T.; Damon, B.; Cui, X. Application of Inkjet Printing to Tissue Engineering. *Biotechnology Journal*. September 2006, pp 910–917. https://doi.org/10.1002/biot.200600081.

(84) Wu, L.; Dong, Z.; Kuang, M.; Li, Y.; Li, F.; Jiang, L.; Song, Y. Printing Patterned Fine 3D Structures by Manipulating the Three Phase Contact Line. *Adv. Funct. Mater.* **2015**, *25* (15), 2237–2242. https://doi.org/10.1002/adfm.201404559.

(85) Boukhalfa, H. H.; Massinon, M.; Belhamra, M.; Lebeau, F. Contribution of Spray Droplet Pinning Fragmentation to Canopy Retention. *Crop Prot.* **2014**, *56*, 91–97. https://doi.org/10.1016/j.cropro.2013.11.018.

(86) Zheng, L.; Cao, C.; Cao, L.; Chen, Z.; Huang, Q.; Song, B. Bounce Behavior and Regulation of Pesticide Solution Droplets on Rice Leaf Surfaces. *J. Agric. Food Chem.* **2018**, *66* (44), 11560–11568. https://doi.org/10.1021/acs.jafc.8b02619.

(87) Breitenbach, J.; Roisman, I. V.; Tropea, C. From Drop Impact Physics to Spray Cooling Models: A Critical Review. *Exp. Fluids* **2018**, *59* (3), 55.

https://doi.org/10.1007/s00348-018-2514-3.

(88) Bjørge, J. S.; Bjørkheim, S. A.; Metallinou, M. M.; Log, T.; Frette, Ø. Influence of Acetone and Sodium Chloride Additives on Cooling Efficiency of Water Droplets Impinging onto Hot Metal Surfaces. *Energies* **2019**, *12* (12), 2358. https://doi.org/10.3390/en12122358.

(89) Yang, Q.; Luo, Z.; Jiang, F.; Luo, Y.; Tan, S.; Lu, Z.; Zhang, Z.; Liu, W. Air Cushion Convection Inhibiting Icing of Self-Cleaning Surfaces. *ACS Appl. Mater. Interfaces* **2016**, *8* (42), 29169–29178. https://doi.org/10.1021/acsami.6b10165.

(90) Blossey, R. Self-Cleaning Surfaces - Virtual Realities. *Nat. Mater.* **2003**, *2* (5), 301–306. https://doi.org/10.1038/nmat856.

(91) Wisdom, K. M.; Watson, J. A.; Qu, X.; Liu, F.; Watson, G. S.; Chen, C. H. Self-Cleaning of Superhydrophobic Surfaces by Self-Propelled Jumping Condensate. *Proc. Natl. Acad. Sci. U. S. A.* **2013**, *110* (20), 7992–7997. https://doi.org/10.1073/pnas.1210770110.

(92) Wang, N.; Xiong, D.; Deng, Y.; Shi, Y.; Wang, K. Mechanically Robust Superhydrophobic Steel Surface with Anti-Icing, UV-Durability, and Corrosion Resistance Properties. *ACS Appl. Mater. Interfaces* **2015**, *7* (11), 6260–6272. https://doi.org/10.1021/acsami.5b00558.

(93) Mohamed, A. M. A.; Abdullah, A. M.; Younan, N. A. Corrosion Behavior of Superhydrophobic Surfaces: A Review. *Arabian Journal of Chemistry*. Elsevier 2015, pp 749–765. https://doi.org/10.1016/j.arabjc.2014.03.006.

(94) Chen, Y.; Chen, S.; Yu, F.; Sun, W.; Zhu, H.; Yin, Y. Fabrication and Anti-Corrosion Property of Superhydrophobic Hybrid Film on Copper Surface and Its Formation Mechanism. *Surf. Interface Anal.* **2009**, *41* (11), 872–877. https://doi.org/10.1002/sia.3102.

(95) Solomatin, Y.; Shlegel, N. E.; Strizhak, P. A. Atomization of Promising Multicomponent Fuel Droplets by Their Collisions. *Fuel* **2019**, *255*. https://doi.org/10.1016/j.fuel.2019.115751.

(96) Tang, C.; Qin, M.; Weng, X.; Zhang, X.; Zhang, P.; Li, J.; Huang, Z. Dynamics of Droplet Impact on Solid Surface with Different Roughness. *Int. J. Multiph. Flow* **2017**, *96*, 56–69. https://doi.org/10.1016/j.ijmultiphaseflow.2017.07.002.

(97) Kavale, M. S.; Mahadik, D. B.; Parale, V. G.; Wagh, P. B.; Gupta, S. C.; Rao, A. V.; Barshilia, H. C. Optically Transparent, Superhydrophobic Methyltrimethoxysilane Based Silica Coatings without Silylating Reagent. *Appl. Surf. Sci.* **2011**, *258* (1), 158–162. https://doi.org/10.1016/j.apsusc.2011.08.023.

(98) Barati Darband, G.; Aliofkhazraei, M.; Khorsand, S.; Sokhanvar, S.; Kaboli, A. Science and Engineering of Superhydrophobic Surfaces: Review of Corrosion Resistance, Chemical and Mechanical Stability. *Arab. J. Chem.* **2020**, *13* (1), 1763–1802. https://doi.org/10.1016/j.arabjc.2018.01.013.

(99) De Ruiter, J.; Soto, D.; Varanasi, K. K. Self-Peeling of Impacting Droplets. *Nat. Phys.* **2018**, *14* (1), 35–39. https://doi.org/10.1038/NPHYS4252.

(100) Damak, M.; Mahmoudi, S. R.; Hyder, M. N.; Varanasi, K. K. Enhancing Droplet Deposition through In-Situ Precipitation. *Nat. Commun.* **2016**, *7*. https://doi.org/10.1038/ncomms12560.

(101) Wang, H.; Liu, C.; Zhan, H.; Liu, Y. Droplet Asymmetric Bouncing on Inclined Superhydrophobic Surfaces. *ACS Omega* **2019**, *4* (7), 12238–12243. https://doi.org/10.1021/acsomega.9b01348.

(102) Hao, C.; Li, J.; Liu, Y.; Zhou, X.; Liu, Y.; Liu, R.; Che, L.; Zhou, W.; Sun, D.; Li, L.; Xu, L.; Wang, Z. Superhydrophobic-like Tunable Droplet Bouncing on Slippery Liquid Interfaces. *Nat. Commun.* **2015**, *6*. https://doi.org/10.1038/ncomms8986.

(103) Liu, C.; Ju, J.; Ma, J.; Zheng, Y.; Jiang, L. Directional Drop Transport Achieved on High-Temperature Anisotropic Wetting Surfaces. *Adv. Mater.* **2014**, *26* (35), 6086–6091. https://doi.org/10.1002/adma.201401985.

(104) Li, J.; Hou, Y.; Liu, Y.; Hao, C.; Li, M.; Chaudhury, M. K.; Yao, S.; Wang, Z. Directional Transport of High-Temperature Janus Droplets Mediated by Structural Topography. *Nat. Phys.* **2016**, *12* (6), 606–612. https://doi.org/10.1038/nphys3643.

(105) Chantelot, P.; Mazloomi Moqaddam, A.; Gauthier, A.; Chikatamarla, S. S.; Clanet, C.; Karlin, I. V.; Qu;ré, D. Water Ring-Bouncing on Repellent Singularities. *Soft Matter* **2018**, *14* (12), 2227–2233. https://doi.org/10.1039/c7sm02004j.

(106) Pack, M. Y.; Yang, A.; Perazzo, A.; Qin, B.; Stone, H. A. Role of Extensional Rheology on Droplet Bouncing. *Phys. Rev. Fluids* **2019**, *4* (12). https://doi.org/10.1103/PhysRevFluids.4.123603.

(107) Tran, T.; Staat, H. J. J.; Prosperetti, A.; Sun, C.; Lohse, D. Drop Impact on Superheated Surfaces. *Phys. Rev. Lett.* **2012**, *108* (3). https://doi.org/10.1103/PhysRevLett.108.036101.

(108) Liu, F.; Ghigliotti, G.; Feng, J. J.; Chen, C. H. Self-Propelled Jumping upon Drop Coalescence on Leidenfrost Surfaces. *J. Fluid Mech.* **2014**, *752*, 22–38. https://doi.org/10.1017/jfm.2014.319.

(109) Antonini, C.; Bernagozzi, I.; Jung, S.; Poulikakos, D.; Marengo, M. Water Drops Dancing on Ice: How Sublimation Leads to Drop Rebound. *Phys. Rev. Lett.* **2013**, *111* (1). https://doi.org/10.1103/PhysRevLett.111.014501.

(110) Quintero, E. S.; Riboux, G.; Gordillo, J. M. Splashing of Droplets Impacting Superhydrophobic Substrates. *J. Fluid Mech.* **2019**, *870*, 175–188. https://doi.org/10.1017/jfm.2019.258.

(111) Schutzius, T. M.; Graeber, G.; Elsharkawy, M.; Oreluk, J.; Megaridis, C. M. Morphing and Vectoring Impacting Droplets by Means of Wettability-Engineered Surfaces. *Sci. Rep.* **2014**, *4*, 7029. https://doi.org/10.1038/srep07029.

(112) Bouwhuis, W.; Van Der Veen, R. C. A.; Tran, T.; Keij, D. L.; Winkels, K. G.; Peters, I. R.; Van Der Meer, D.; Sun, C.; Snoeijer, J. H.; Lohse, D. Maximal Air Bubble Entrainment at Liquid-Drop Impact. *Phys. Rev. Lett.* **2012**, *109* (26). https://doi.org/10.1103/PhysRevLett.109.264501.

(113) Josserand, C.; Thoroddsen, S. T. Drop Impact on a Solid Surface. *Annu. Rev. Fluid Mech.* **2016**, *48* (1), 365–391. https://doi.org/10.1146/annurev-fluid-122414-034401.

(114) Khojasteh, D.; Kazerooni, M.; Salarian, S.; Kamali, R. Droplet Impact on

Superhydrophobic Surfaces: A Review of Recent Developments. *Journal of Industrial and Engineering Chemistry*. October 2016, pp 1–14. https://doi.org/10.1016/j.jiec.2016.07.027.

(115) Rioboo, R.; Tropea, C.; Marengo, M. Outcomes from a Drop Impact on Solid Surfaces. *At. Sprays* **2001**, *11* (2), 155–165. https://doi.org/10.1615/atomizspr.v11.i2.40.

(116) Ma, H.; Liu, C.; Li, X.; Huang, H.; Dong, J. Deformation Characteristics and Energy Conversion during Droplet Impact on a Water Surface. *Phys. Fluids* **2019**, *31* (6). https://doi.org/10.1063/1.5099228.

(117) Chen, B.; Wang, B.; Mao, F.; Wen, J.; Tian, R.; Lu, C. Experimental Study of Droplet Impacting on Inclined Wetted Wall in Corrugated Plate Separator. *Ann. Nucl. Energy* **2020**, *137*. https://doi.org/10.1016/j.anucene.2019.107155.

(118) Lee, J. B.; Derome, D.; Dolatabadi, A.; Carmeliet, J. Energy Budget of Liquid Drop Impact at Maximum Spreading: Numerical Simulations and Experiments. *Langmuir* **2016**, *32* (5), 1279–1288. https://doi.org/10.1021/acs.langmuir.5b03848.

(119) Cionti, C.; Taroni, T.; Meroni, D. Bouncing Droplets: A Hands-On Activity to Demonstrate the Properties and Applications of Superhydrophobic Surface Coatings. *J. Chem. Educ.* **2019**. https://doi.org/10.1021/acs.jchemed.9b00406.

(120) Liang, G.; Guo, Y.; Shen, S.; Yu, H. A Study of a Single Liquid Drop Impact on Inclined Wetted Surfaces. *Acta Mech.* **2014**, *225* (12), 3353–3363. https://doi.org/10.1007/s00707-014-1110-8.

(121) Liu, Y.; Moevius, L.; Xu, X.; Qian, T.; Yeomans, J. M.; Wang, Z. Pancake Bouncing on Superhydrophobic Surfaces. *Nat. Phys.* **2014**, *10* (7), 515–519. https://doi.org/10.1038/nphys2980.

(122) Bird, J. C.; Dhiman, R.; Kwon, H. M.; Varanasi, K. K. Reducing the Contact Time of a Bouncing Drop. *Nature* **2013**, *503* (7476), 385–388. https://doi.org/10.1038/nature12740.

(123) Abolghasemibizaki, M.; Mohammadi, R. Droplet Impact on Superhydrophobic

Surfaces Fully Decorated with Cylindrical Macrotextures. *J. Colloid Interface Sci.* **2018**, *509*, 422–431. https://doi.org/10.1016/j.jcis.2017.09.030.

(124) Liu, Y.; Andrew, M.; Li, J.; Yeomans, J. M.; Wang, Z. Symmetry Breaking in Drop Bouncing on Curved Surfaces. *Nat. Commun.* **2015**, *6*. https://doi.org/10.1038/ncomms10034.

(125) Zhang, R.; Hao, P.; He, F. Drop Impact on Oblique Superhydrophobic Surfaces with Two-Tier Roughness. *Langmuir* **2017**, *33* (14), 3556–3567. https://doi.org/10.1021/acs.langmuir.7b00569.

(126) Eckart, C. Vortices and Streams Caused by Sound Waves. *Phys. Rev.* **1948**, *73* (1), 68–76. https://doi.org/10.1103/PhysRev.73.68.

(127) Nyborg, W. L. Acoustic Streaming Due to Attenuated Plane Waves. *J. Acoust. Soc. Am.* **1953**, *25* (1), 68–75. https://doi.org/10.1121/1.1907010.

(128) Westervelt, P. J. The Theory of Steady Rotational Flow Generated by a Sound Field. *J. Acoust. Soc. Am.* **1953**, *25* (1), 60–67. https://doi.org/10.1121/1.1907009.

(129) Mitome, H. The Mechanism of Generation of Acoustic Streaming. *Electron. Commun. Japan, Part III Fundam. Electron. Sci. (English Transl. Denshi Tsushin Gakkai Ronbunshi)* **1998**, *81* (10), 1–8. https://doi.org/10.1002/(SICI)1520-6440(199810)81:10<1::AID-ECJC1>3.0.CO;2-9.

(130) Riley, N. Steady Streaming. *Annu. Rev. Fluid Mech.* **2001**, *33* (1), 43–65. https://doi.org/10.1146/annurev.fluid.33.1.43.

(131) Wiklund, J.; Shahram, I.; Stading, M. Methodology for In-Line Rheology by Ultrasound Doppler Velocity Profiling and Pressure Difference Techniques. *Chem. Eng. Sci.* **2007**, *62* (16), 4277–4293. https://doi.org/10.1016/j.ces.2007.05.007.

(132) Köster, D. Numerical Simulation of Acoustic Streaming on Surface Acoustic Wave-Driven Biochips. *SIAM J. Sci. Comput.* **2007**, *29* (6), 2352–2380. https://doi.org/10.1137/060676623.

(133) Riaud, A.; Baudoin, M.; Bou Matar, O.; Thomas, J. L.; Brunet, P. On the Influence of Viscosity and Caustics on Acoustic Streaming in Sessile Droplets: An

Experimental and a Numerical Study with a Cost-Effective Method. *J. Fluid Mech.* **2017**, *821*, 384–420. https://doi.org/10.1017/jfm.2017.178.

(134) Endoh, G.; Hashimoto, K. Y.; Yamaguchi, M. Surface Acoustic Wave Propagation Characterisation by Finite-Element Method and Spectral Domain Analysis. *Jpn. J. Appl. Phys.* **1995**, *34* (5S), 2638–2641. https://doi.org/10.1143/JJAP.34.2638.

(135) Chung, G. S.; Phan, D. T. Finite Element Modeling of Surface Acoustic Waves in Piezoelectric Thin Films. *J. Korean Phys. Soc.* **2010**, *57* (3), 446–450. https://doi.org/10.3938/jkps.57.446.

(136) Tan, M. K.; Friend, J. R.; Matar, O. K.; Yeo, L. Y. Capillary Wave Motion Excited by High Frequency Surface Acoustic Waves. *Phys. Fluids* **2010**, *22* (11). https://doi.org/10.1063/1.3505044.

(137) Antil, H.; Glowinski, R.; Hoppe, R. H. W.; Linsenmann, C.; Pan, T. W. Modeling, Simulation, and Optimization of Surface Acoustic Wave Driven Microfluidic Biochips. *J. Comput. Math.* **2010**, *28* (2), 149–169. https://doi.org/10.4208/jcm.2009.10-m1001.

(138) Vanneste, J.; Bühler, O. Streaming by Leaky Surface Acoustic Waves. *Proc. R. Soc. A Math. Phys. Eng. Sci.* **2011**, *467* (2130), 1779–1800. https://doi.org/10.1098/rspa.2010.0457.

(139) Schindler, M.; Talkner, P.; Hänggi, P. Computing Stationary Free-Surface Shapes in Microfluidics. *Phys. Fluids* **2006**, *18* (10). https://doi.org/10.1063/1.2361291.

(140) Sankaranarayanan, S. K. R. S.; Cular, S.; Bhethanabotla, V. R.; Joseph, B. Flow Induced by Acoustic Streaming on Surface-Acoustic-Wave Devices and Its Application in Biofouling Removal: A Computational Study and Comparisons to Experiment. *Phys. Rev. E - Stat. Nonlinear, Soft Matter Phys.* **2008**, *77* (6), 1–19. https://doi.org/10.1103/PhysRevE.77.066308.

(141) Sankaranarayanan, S. K.; Bhethanabotla, V. R. Numerical Analysis of Wave Generation and Propagation in a Focused Surface Acoustic Wave Device for Potential Microfluidics Applications. *IEEE Trans. Ultrason. Ferroelectr. Freq. Control* **2009**, *56* (3), 631–643. https://doi.org/10.1109/TUFFC.2009.1079.

(142) Alghane, M.; Chen, B. X.; Fu, Y. Q.; Li, Y.; Luo, J. K.; Walton, A. J. Experimental and Numerical Investigation of Acoustic Streaming Excited by Using a Surface Acoustic Wave Device on a 128° YX-LiNbO3 Substrate. *J. Micromechanics Microengineering* **2011**, *21* (1), 015005. https://doi.org/10.1088/0960-1317/21/1/015005.

(143) Shah, I.; Uddin, E.; Mubashar, A.; Sajid, M.; Younis, M. Y.; Samad, H.; Choi, K. H. Numerical Investigation of Surface Acoustic Wave (SAW) Interacting with a Droplet for Point-of-Care Devices. *Int. J. Acoust. Vib.* **2019**, *24* (4), 632–637. https://doi.org/10.20855/ijav.2019.24.41312.

(144) Sheikholeslam Noori, S. M.; Taeibi Rahni, M.; Shams Taleghani, S. A. Numerical Analysis of Droplet Motion over a Flat Plate Due to Surface Acoustic Waves. *Microgravity Sci. Technol.* **2020**, *32* (4), 647–660. https://doi.org/10.1007/s12217-020-09784-1.

(145) Johansson, N. Implementation of a Standard Level Set Method for Incompressible Two-Phase Flow Simulations. **2011**.

(146) Unverdi, S. O.; Tryggvason, G. A Front-Tracking Method for Viscous, Incompressible, Multi-Fluid Flows. *J. Comput. Phys.* **1992**, *100* (1), 25–37. https://doi.org/10.1016/0021-9991(92)90307-K.

(147) Albadawi, A. On the Assessment of Numerical Interface Capturing Methods for Two Fluid Flow Applications. **2014**, No. July.

(148) Dianat, M.; Skarysz, M.; Garmory, A. A Coupled Level Set and Volume of Fluid Method for Automotive Exterior Water Management Applications. *Int. J. Multiph. Flow* **2017**, *91*, 19–38. https://doi.org/10.1016/j.ijmultiphaseflow.2017.01.008.

(149) Zhang, Y. L.; Yeo, K. S.; Khoo, B. C.; Wang, C. 3D Jet Impact and Toroidal Bubbles. *J. Comput. Phys.* **2001**, *166* (2), 336–360. https://doi.org/10.1006/jcph.2000.6658.

(150) Best, J. P. The Formation of Toroidal Bubbles upon the Collapse of Transient Cavities. *J. Fluid Mech.* **1993**, *251*, 79–107. https://doi.org/10.1017/S0022112093003349.

(151) Ding, H.; Spelt, P. D. M. Wetting Condition in Diffuse Interface Simulations of Contact Line Motion. *Phys. Rev. E - Stat. Nonlinear, Soft Matter Phys.* **2007**, *75* (4), 046708. https://doi.org/10.1103/PhysRevE.75.046708.

(152) Jacqmin, D. Calculation of Two-Phase Navier-Stokes Flows Using Phase-Field Modeling. *J. Comput. Phys.* **1999**, *155* (1), 96–127. https://doi.org/10.1006/jcph.1999.6332.

(153) Cahn, J. W. On Spinodal Decomposition. *Acta Metall.* **1961**, *9* (9), 795–801. https://doi.org/10.1016/0001-6160(61)90182-1.

(154) Shan, X.; Chen, H. Lattice Boltzmann Model for Simulating Flows with Multiple Phases and Components. *Phys. Rev. E* **1993**, *47* (3), 1815–1819. https://doi.org/10.1103/PhysRevE.47.1815.

(155) Yang, Z. L.; Dinh, T. N.; Nourgaliev, R. R.; Sehgal, B. R. Numerical Investigation of Bubble Growth and Detachment by the Lattice-Boltzmann Method. *Int. J. Heat Mass Transf.* **2001**, *44* (1), 195–206. https://doi.org/10.1016/S0017-9310(00)00101-0.

(156) Hirt, C. W.; Nichols, B. D. Volume of Fluid (VOF) Method for the Dynamics of Free Boundaries. *J. Comput. Phys.* **1981**, *39* (1), 201–225. https://doi.org/10.1016/0021-9991(81)90145-5.

(157) Hirt, C. W.; Nichols, B. D. Volume of Fluid (VOF) Method for the Dynamics of Free Boundaries. *J. Comput. Phys.* **1981**, *39* (1), 201–225. https://doi.org/10.1016/0021-9991(81)90145-5.

(158) Rider, W. J.; Kothe, D. B. Reconstructing Volume Tracking. *J. Comput. Phys.* **1998**, *141* (2), 112–152. https://doi.org/10.1006/jcph.1998.5906.

(159) Muzaferija, S.; Peric, M.; Sames, P.; Schellin, T. *Twenty-Second Symposium on Naval Hydrodynamics*; SYMPOSIUM ON NAVAL HYDRODYNAMICS; National Academy Press, 1999. https://doi.org/10.17226/9771.

(160) Davanipour, M.; Javanmardi, H.; Goodarzi, N. Chaotic Self-Tuning PID Controller Based on Fuzzy Wavelet Neural Network Model. *Iran. J. Sci. Technol. - Trans. Electr. Eng.* **2018**, *42* (3), 357–366. https://doi.org/10.1007/s40998-018-0069-1.

(161) Kothe, D. B.; Mjolsness, R. C. RIPPLE - A New Model for Incompressible Flows with Free Surfaces. *AIAA J.* **1992**, *30* (11), 2694–2700. https://doi.org/10.2514/3.11286.

(162) Youngs, D. L. Time-Dependent Multi-Material Ow with Large Uid Distortion. *Numer. methods uid Dyn.* **1982**, *1* (1), 41–51.

(163) Aulisa, E.; Manservisi, S.; Scardovelli, R. A Mixed Markers and Volume-of-Fluid Method for the Reconstruction and Advection of Interfaces in Two-Phase and Free-Boundary Flows. *J. Comput. Phys.* **2003**, *188* (2), 611–639. https://doi.org/10.1016/S0021-9991(03)00196-7.

(164) López, J.; Hernández, J.; Gómez, P.; Faura, F. A Volume of Fluid Method Based on Multidimensional Advection and Spline Interface Reconstruction. *J. Comput. Phys.* **2004**, *195* (2), 718–742. https://doi.org/10.1016/j.jcp.2003.10.030.

(165) Ginzburg, I.; Wittum, G. Two-Phase Flows on Interface Refined Grids Modeled with VOF, Staggered Finite Volumes, and Spline Interpolants. *J. Comput. Phys.* **2001**, *166* (2), 302–335. https://doi.org/10.1006/jcph.2000.6655.

(166) Rudman, M. Volume-Tracking Methods for Interfacial Flow Calculations. *Int. J. Numer. Methods Fluids* **1997**, *24* (7), 671–691. https://doi.org/10.1002/(SICI)1097-0363(19970415)24:7<671::AID-FLD508>3.0.CO;2-9.

(167) Lafaurie, B.; Nardone, C.; Scardovelli, R.; Zaleski, S.; Zanetti, G. *Modelling Merging and Fragmentation in Multiphase Flows with SURFER*; Academic Press, 1994; Vol. 113, pp 134–147. https://doi.org/10.1006/jcph.1994.1123.

(168) Aulisa, E.; Manservisi, S.; Scardovelli, R.; Zaleski, S. Interface Reconstruction with Least-Squares Fit and Split Advection in Three-Dimensional Cartesian Geometry. *J. Comput. Phys.* **2007**, *225* (2), 2301–2319. https://doi.org/10.1016/j.jcp.2007.03.015.

(169) Scardovelli, R.; Zaleski, S. Interface Reconstruction with Least-Square Fit and Split Eulerian-Lagrangian Advection. *Int. J. Numer. Methods Fluids* **2003**, *41* (3), 251–274. https://doi.org/10.1002/fld.431.

(170) López, J.; Hernández, J. Analytical and Geometrical Tools for 3D Volume of Fluid

Methods in General Grids. *J. Comput. Phys.* **2008**, *227* (12), 5939–5948. https://doi.org/10.1016/j.jcp.2008.03.010.

(171) Cervone, A.; Manservisi, S.; Scardovelli, R.; Zaleski, S. A Geometrical Predictor-Corrector Advection Scheme and Its Application to the Volume Fraction Function. *J. Comput. Phys.* **2009**, *228* (2), 406–419. https://doi.org/10.1016/j.jcp.2008.09.016.

(172) Zalesak, S. T. Fully Multidimensional Flux-Corrected Transport Algorithms for Fluids. *J. Comput. Phys.* **1979**, *31* (3), 335–362. https://doi.org/10.1016/0021-9991(79)90051-2.

(173) Ubbink, O.; Issa, R. I. A Method for Capturing Sharp Fluid Interfaces on Arbitrary Meshes. *J. Comput. Phys.* **1999**, *153* (1), 26–50. https://doi.org/10.1006/jcph.1999.6276.

(174) Sussman, M.; Puckett, E. G. A Coupled Level Set and Volume-of-Fluid Method for Computing 3D and Axisymmetric Incompressible Two-Phase Flows. *J. Comput. Phys.* **2000**, *162* (2), 301–337. https://doi.org/10.1006/jcph.2000.6537.

(175) Enright, D.; Fedkiw, R.; Ferziger, J.; Mitchell, I. A Hybrid Particle Level Set Method for Improved Interface Capturing. *J. Comput. Phys.* **2002**, *183* (1), 83–116. https://doi.org/10.1006/jcph.2002.7166.

(176) Osher, S.; Sethian, J. A. Fronts Propagating with Curvature-Dependent Speed: Algorithms Based on Hamilton-Jacobi Formulations. *J. Comput. Phys.* **1988**, *79* (1), 12–49. https://doi.org/10.1016/0021-9991(88)90002-2.

(177) Sussman, M. A Level Set Approach for Computing Solutions to Incompressible Two-Phase Flow. *J. Comput. Phys.* **1994**, *114* (1), 146–159. https://doi.org/10.1006/jcph.1994.1155.

(178) Sussman, M.; Fatemi, E.; Smereka, P.; Osher, S. An Improved Level Set Method for Incompressible Two-Phase Flows. *Comput. Fluids* **1998**, *27* (5–6), 663–680. https://doi.org/10.1016/S0045-7930(97)00053-4.

(179) Losasso, F.; Fedkiw, R.; Osher, S. Spatially Adaptive Techniques for Level Set Methods and Incompressible Flow. *Comput. Fluids* **2006**, *35* (10), 995–1010.

https://doi.org/10.1016/j.compfluid.2005.01.006.

(180) Harten, A.; Engquist, B.; Osher, S.; Chakravarthy, S. R. Uniformly High Order Accurate Essentially Non-Oscillatory Schemes, III. *J. Comput. Phys.* **1987**, *71* (2), 231–303. https://doi.org/10.1016/0021-9991(87)90031-3.

(181) Liu, X. D. Weighted Essentially Non-Oscillatory Schemes. *J. Comput. Phys.* **1994**, *115* (1), 200–212. https://doi.org/10.1006/jcph.1994.1187.

(182) Sussman, M.; Almgren, A. S.; Bell, J. B.; Colella, P.; Howell, L. H.; Welcome, M. An Adaptive Level Set Approach for Incompressible Two-Phase Flows. *Am. Soc. Mech. Eng. Fluids Eng. Div. FED* **1996**, *238* ((5-6)), 355–360.

(183) Mulder, W.; Osher, S.; Sethian, J. A. Computing Interface Motion in Compressible Gas Dynamics. *J. Comput. Phys.* **1992**, *100* (2), 209–228. https://doi.org/10.1016/0021-9991(92)90229-R.

(184) Sussman, M.; Puckett, E. G. A Coupled Level Set and Volume-of-Fluid Method for Computing 3D and Axisymmetric Incompressible Two-Phase Flows. *J. Comput. Phys.* **2000**, *162* (2), 301–337. https://doi.org/10.1006/jcph.2000.6537.

(185) Son, G.; Hur, N. A Coupled Level Set and Volume-of-Fluid Method for the Buoyancy-Driven Motion of Fluid Particles. *Numer. Heat Transf. Part B Fundam.* **2002**, *42* (6), 523–542. https://doi.org/10.1080/10407790260444804.

(186) Paykani, A.; Kakaee, A. H.; Rahnama, P.; Reitz, R. D. Effects of Diesel Injection Strategy on Natural Gas/Diesel Reactivity Controlled Compression Ignition Combustion. *Energy* **2015**, *90*, 814–826. https://doi.org/10.1016/j.energy.2015.07.112.

(187) Campbell, J. J.; Jones, W. R. A Method for Estimating Optimal Crystal Cuts and Propagation Directions for Excitation of Piezoelectric Surface Waves. *IEEE Trans. Sonics Ultrason.* **1968**, *15* (4), 209–217. https://doi.org/10.1109/T-SU.1968.29477.

(188) Kalifa, R. Ben; Hamza, S. Ben; Saïd, N. M.; Bournot, H. Fluid Flow Phenomena in Metals Processing Operations: Numerical Description of the Fluid Flow Field by an Impinging Gas Jet on a Liquid Surface. *Int. J. Mech. Sci.* **2020**, *165*, 105220.

https://doi.org/10.1016/j.ijmecsci.2019.105220.

(189) Brackbill, J. U.; Kothe, D. B.; Zemach, C. A Continuum Method for Modeling Surface Tension. *J. Comput. Phys.* **1992**, *100* (2), 335–354. https://doi.org/10.1016/0021-9991(92)90240-Y.

(190) Sussman, M.; Puckett, E. G. A Coupled Level Set and Volume-of-Fluid Method for Computing 3D and Axisymmetric Incompressible Two-Phase Flows. *J. Comput. Phys.* **2000**, *162* (2), 301–337. https://doi.org/10.1006/jcph.2000.6537.

(191) Damián, S. M.; Nigro, N. M. An Extended Mixture Model for the Simultaneous Treatment of Small-Scale and Large-Scale Interfaces. *Int. J. Numer. Methods Fluids* **2014**, *75* (8), 547–574. https://doi.org/10.1002/fld.3906.

(192) Snoeijer, J. H.; Andreotti, B. Moving Contact Lines: Scales, Regimes, and Dynamical Transitions. *Annu. Rev. Fluid Mech.* **2013**, *45* (1), 269–292. https://doi.org/10.1146/annurev-fluid-011212-140734.

(193) Manservisi, S.; Scardovelli, R. A Variational Approach to the Contact Angle Dynamics of Spreading Droplets. *Comput. Fluids* **2009**, *38* (2), 406–424. https://doi.org/10.1016/j.compfluid.2008.05.001.

(194) Aussillous, P.; Quéré, D. Liquid Marbles. *Nature* **2001**, *411* (6840), 924–927. https://doi.org/10.1038/35082026.

(195) Shen, Y.; Tao, J.; Tao, H.; Chen, S.; Pan, L.; Wang, T. Relationship between Wetting Hysteresis and Contact Time of a Bouncing Droplet on Hydrophobic Surfaces. *ACS Appl. Mater. Interfaces* **2015**, *7* (37), 20972–20978. https://doi.org/10.1021/acsami.5b06754.

(196) Familie, M. Numerical Modeling and Investigation of Boiling Phenomena. *Thesis* **2011**, No. September, 137.

(197) Shen, C.; Zhang, C.; Gao, M.; Li, X.; Liu, Y.; Ren, L.; Moita, A. S. Investigation of Effects of Receding Contact Angle and Energy Conversion on Numerical Prediction of Receding of the Droplet Impact onto Hydrophilic and Superhydrophilic Surfaces. *Int. J. Heat Fluid Flow* **2018**, *74,* 89–109.

https://doi.org/10.1016/j.ijheatfluidflow.2018.09.015.

(198) Malgarinos, I.; Nikolopoulos, N.; Marengo, M.; Antonini, C.; Gavaises, M. VOF Simulations of the Contact Angle Dynamics during the Drop Spreading: Standard Models and a New Wetting Force Model. *Adv. Colloid Interface Sci.* **2014**, *212*, 1–20. https://doi.org/10.1016/j.cis.2014.07.004.

(199) Cox, R. G. The Dynamics of the Spreading of Liquids on a Solid Surface. Part 1. Viscous Flow. *J. Fluid Mech.* **1986**, *168* (1), 169–194. https://doi.org/10.1017/S0022112086000332.

(200) Rose, J. L.; Nagy, P. B. Ultrasonic Waves in Solid Media. *J. Acoust. Soc. Am.* **2000**, *107* (4), 1807–1808. https://doi.org/10.1121/1.428552.

(201) Afkhami, S.; Zaleski, S.; Bussmann, M. A Mesh-Dependent Model for Applying Dynamic Contact Angles to VOF Simulations. *J. Comput. Phys.* **2009**, *228* (15), 5370–5389. https://doi.org/10.1016/j.jcp.2009.04.027.

(202) Yokoi, K.; Vadillo, D.; Hinch, J.; Hutchings, I. Numerical Studies of the Influence of the Dynamic Contact Angle on a Droplet Impacting on a Dry Surface. *Phys. Fluids* **2009**, *21* (7), 1–12. https://doi.org/10.1063/1.3158468.

(203) Legendre, D.; Maglio, M. Comparison between Numerical Models for the Simulation of Moving Contact Lines. *Comput. Fluids* **2015**, *113*, 2–13. https://doi.org/10.1016/j.compfluid.2014.09.018.

(204) Renardy, Y. Y.; Cristini, V. Effect of Inertia on Drop Breakup under Shear. *Phys. Fluids* **2001**, *13* (1), 7–13. https://doi.org/10.1063/1.1331321.

(205) The Open Source CFD Toolbox User Guide https://www.openfoam.com/documentation/.

(206) Aminzadeh, M.; Maleki, A.; Firoozabadi, B.; Afshin, H. On the Motion of Newtonian and Non-Newtonian Liquid Drops. *Sci. Iran.* **2012**, *19* (5), 1265–1278. https://doi.org/10.1016/j.scient.2011.09.022.

(207) Tian, J. M.; Chen, B. Dynamic Behavior of Non-Evaporative Droplet Impact on a Solid Surface: Comparative Study of R113, Water, Ethanol and Acetone. *Exp. Therm.*

Fluid Sci. **2019**, *105*, 153–164. https://doi.org/10.1016/j.expthermflusci.2019.03.024.

(208) Tan, M. K.; Friend, J. R.; Yeo, L. Y. Interfacial Jetting Phenomena Induced by Focused Surface Vibrations. *Phys. Rev. Lett.* **2009**, *103* (2), 024501. https://doi.org/10.1103/PhysRevLett.103.024501.

(209) Biroun, M. H.; Li, J.; Tao, R.; Rahmati, M.; McHale, G.; Dong, L.; Jangi, M.; Torun, H.; Fu, Y. Q. Acoustic Waves for Active Reduction of Contact Time in Droplet Impact. *Phys. Rev. Appl.* **2020**, *14* (2), 1–18. https://doi.org/10.1103/PhysRevApplied.14.024029.

(210) Sreenivasan, K. R. Turbulent Mixing: A Perspective. *Proceedings of the National Academy of Sciences of the United States of America*. National Academy of Sciences September 10, 2019, pp 18175–18183. https://doi.org/10.1073/pnas.1800463115.

(211) Alghane, M.; Fu, Y. Q.; Chen, B. X.; Li, Y.; Desmulliez, M. P. Y.; Walton, A. J. Streaming Phenomena in Microdroplets Induced by Rayleigh Surface Acoustic Wave. *J. Appl. Phys.* **2011**, *109* (11). https://doi.org/10.1063/1.3586040.

(212) Sadhal, S. S. Acoustofluidics 13: Analysis of Acoustic Streaming by Perturbation Methods. *Lab Chip* **2012**, *12* (13), 2292–2300. https://doi.org/10.1039/c2lc40202e.

(213) Ding, X.; Li, P.; Lin, S. C. S.; Stratton, Z. S.; Nama, N.; Guo, F.; Slotcavage, D.; Mao, X.; Shi, J.; Costanzo, F.; Huang, T. J. Surface Acoustic Wave Microfluidics. *Lab Chip* **2013**, *13* (18), 3626–3649. https://doi.org/10.1039/c3lc50361e.

(214) Al-Zurfi, N.; Turan, A. A Numerical Simulation of the Effects of Swirling Flow on Jet Penetration in a Rotating Channel. *Flow, Turbul. Combust.* **2015**, *94* (2), 415–438. https://doi.org/10.1007/s10494-014-9586-9.

(215) Yun, S. Bouncing of an Ellipsoidal Drop on a Superhydrophobic Surface. *Sci. Rep.* **2017**, *7* (1), 17699. https://doi.org/10.1038/s41598-017-18017-2.

(216) Richard, D.; Clanet, C.; Quéré, D. Surface Phenomena: Contact Time of a Bouncing Drop. *Nature* **2002**, *417* (6891), 811. https://doi.org/10.1038/417811a.

(217) Pasandideh-Fard, M.; Qiao, Y. M.; Chandra, S.; Mostaghimi, J. Capillary Effects during Droplet Impact on a Solid Surface. *Phys. Fluids* **1996**, *8* (3), 650–659.

https://doi.org/10.1063/1.868850.

(218) Bisighini, A.; Cossali, G. E.; Tropea, C.; Roisman, I. V. Crater Evolution after the Impact of a Drop onto a Semi-Infinite Liquid Target. *Phys. Rev. E - Stat. Nonlinear, Soft Matter Phys.* **2010**, *82* (3), 036319. https://doi.org/10.1103/PhysRevE.82.036319.

(219) Erkan, N. Full-Field Spreading Velocity Measurement inside Droplets Impinging on a Dry Solid-Heated Surface. *Exp. Fluids* **2019**, *60* (5), 88. https://doi.org/10.1007/s00348-019-2735-0.